UNIVERSITEIT VAN PRETORIA
UNIVERSITY OF PRETORIA
YUNIBESITHI YA PRETORIA

EFFECTS OF SOIL STRENGTH ON PROPAGATION MECHANISMS ABOVE DEEP TRAPDOORS

CATHERINE PURCHASE

A dissertation submitted in partial fulfilment of the requirements for the degree of

MASTER OF ENGINEERING (GEOTECHNICAL ENGINEERING)

In the

FACULTY OF ENGINEERING, BUILT ENVIRONMENT AND INFORMATION TECHNOLOGY

UNIVERSITY OF PRETORIA

May 2019

DISSERTATION SUMMARY

EFFECTS OF SOIL STRENGTH ON PROPAGATION MECHANISMS ABOVE DEEP TRAPDOORS

C PURCHASE

Supervisor: Professor S.W. Jacobsz

Co-Supervisor: Professor D.N. Wilke

Department: Civil Engineering

University: University of Pretoria

Degree: Master of Engineering (Geotechnical Engineering)

Approximately a quarter of South Africa's Gauteng Province is underlain by dolomite, a carbonate rock which is susceptible to dissolution and therefore sinkhole formation. Current design codes for developing on dolomitic land are known to be conservative, resulting in areas of land which are uninhabitable due to the often-unfeasible construction costs associated with large sinkhole sizes. The Gauteng Province is the heart of South Africa's economy and, as such, there is a need to investigate and understand the propagation mechanisms associated with sinkhole formation, as well as the factors that govern these mechanisms as cavities propagate from depth to the ground surface. A better understanding of cavity propagation mechanisms will enable design standards to be improved to optimise the utilisation of dolomitic land.

Trapdoor experiments have been used extensively in the past to investigate soil arching and the associated material behaviour. More recently, cavity propagation associated with sinkhole formation has been investigated by means of deep trapdoor experiments. With the advent of Graphical Processing Unit (GPU)-based Discrete Element Method (DEM) codes, the DEM numerical method has become a popular tool for investigating the rheology of granular materials. This research study therefore focused on utilising physical deep trapdoor experiments, complemented by DEM, to investigate the relationship between the shear strength of a material and the soil deformation mechanisms during cavity propagation.

Deep trapdoor experiments were undertaken at the University of Pretoria geotechnical centrifuge facility with three materials, namely a fine-grained sand, a coarse-grained sand and 2 mm glass beads.

These tests were conducted to observe the different deformation mechanisms, at field stress conditions, associated with materials of distinctly different shear strengths. The trapdoor experiment with glass beads was further used to calibrate a numerical DEM model with spherical particles. The calibration procedure of the DEM trapdoor experiment included a sensitivity analysis of the numerical model input parameters, as well as validation by comparing displacement contours, particle displacement trajectories and maximum shear strain plots. Once satisfactorily calibrated, the model was used to investigate the effect of material strength, as a result of particle shape, on the material deformation mechanisms during trapdoor lowering, simulating cavity propagation. Particle shape was initially simulated by means of polyhedral particles. These simulations did not run successfully as the required time step at the calibrated particle stiffness was not feasible within the single precision DEM code for polyhedral particles. Furthermore, a reduction in the stiffness of the particles, yielding a greater required time step, was not suited to the high stresses within the material model. Varying rolling resistance and friction coefficients were therefore applied to the particles to simulate the effect of particle shape.

Based on the maximum shear strain results from both the physical (centrifuge) and numerical (DEM) trapdoor results, it was found that an elongated ellipsoidal deformation mechanism governs behaviour for materials with a low shear strength. Whereas for materials with a comparatively high shear strength cavity propagation occurs between two vertical shear bands. The DEM models demonstrated that the greater the shear strength of the overburden material, the greater the tendency of the shear bands and cavity propagation towards verticality. It was further observed that for both sets of tests, the deformation mechanisms widen at the surface. The lower the material shear strength, the wider the zone of influence at the surface.

ACKNOWLEDGEMENTS

I would like to thank Jesus Christ, my Lord and Saviour, for the incredible opportunity of undertaking my master's degree and for granting me the strength, wisdom and perseverance needed to complete this research study (Isaiah 41:10).

I further wish to express my sincere appreciation to the following persons and organisations who made this dissertation possible:

a) Prof. S.W. Jacobsz for his time, enthusiasm and encouragement – especially during the more trying times of the study. This dissertation would not have been possible without his guidance and motivation. I count myself privileged to have been able to work with and learn from him.

b) Prof. D.N Wilke for his time and effort, specifically with reference to the Blaze-DEM simulations with polyhedral particles. Hopefully we will have better luck next time.

c) Rian Lauwrens for his love, patience and encouragement. I cannot thank you enough for your incredible support throughout this study, including the use of your electronic resources, your endless supply of study snacks, as well as your prayers and much-needed pep talks.

d) My parents, John and Esté Purchase, for their continuous motivation, love and support. Thank you for believing in me.

e) Jennifer Purchase, my sister, for the use of her laptop and just for being wonderful and selfless.

f) The post-graduate group of 2017/2018 for their motivation and positivity. A special word of thanks to André Broekman for his technical support and encouragement, as well as to Sachin Ravjee for his guidance in using Blaze-DEM.

g) Mr Jan Vermaak for his practical assistance and persistence with the trapdoor experiments in the centrifuge facility.

h) Ms Heather Davis for proof-reading sections of this dissertation.

i) Jones and Wagener (Pty) Ltd for their financial support.

j) Mr Dawie Erasmus and Mr Kostas Rontiris (SMEC South Africa (Pty) Ltd) for supporting me in my request to undertake my master's degree.

k) Last, but not least, my friends for their love, grace, support and prayers.

TABLE OF CONTENTS

LIST OF TABLES

LIST OF FIGURES

LIST OF SYMBOLS AND ABBREVIATIONS

a	Acceleration
B	Trapdoor width
c'	Cohesion
c_n	Normal damping coefficient
c_t	Tangential damping coefficient
CC_{ZNCC}	Zero-Normalised Cross-Correlation Coefficient
CPU	Core Processing Unit
$CSIR$	Council for Scientific and Industrial Research
CST	Constant Strain Triangle
D_{50}	Mean particle size
DEM	Discrete Element Method
DIC	Digital Image Correlation
$e\ or\ COR$	Coefficient of Restitution
e	Void ratio
e_{max}	Reference void ratio of soil at minimum index density
e_{min}	Reference void ratio of soil at maximum index density
E	Young's Modulus
EBP	Equal Bounding Perimeter
EV	Equal Volume
f_{fluid}	Interaction forces between fluid and particles
F_n	Normal contact force
f_{nc}	Normal inter-particle contact forces exerted by neighbouring particles
$F_s\ or\ F_t$	Tangential (shear) contact force
f_{tc}	Tangential inter-particle contact forces exerted by neighbouring particles
G	Shear Modulus
g	Gravitational acceleration
GPU	Graphical Processing Unit
H/B	Ratio of model height to trapdoor width
I	Moment of inertia
I_D	Relative density
I_R	Relative density index
IHC	Inherent Hazard Class
K	Coefficient of lateral earth pressure

K_0	Coefficient of lateral earth pressure at rest
k_n	Normal particle contact stiffness
k_r	Rolling particle contact stiffness
$k_t \ or \ k_s$	Tangential particle contact stiffness
$LVDT$	Linear Variable Differential Transformer
m	Mass
M_r	Rolling resistant moment
M_p	Maximum rolling moment
MPS	Maximum Potential Size
NCC	Normalised Correlation Coefficient
p'	Mean effective stress level
p	Load measured on the trapdoor
p_0	Theoretical geostatic load on trapdoor
p_{min}	Minimum load applied to the trapdoor during trapdoor lowering
p_{ult}	Final asymptotic load applied to the trapdoor
PIV	Particle Image Velocimetry
q	Surcharge at the soil surface
q'	Deviator stress
r	Average particle radius
r_c	Vector from the particle mass centre to the contact point
R	Particle radius
RG	Reliability Guided
RoI	Region of Interest
s'	Maximum normal stress
t'	Maximum shear stress
S	Sphericity
SA	Surface Area
$SABS$	South African Bureau of Standards
SEM	Scanning Electron Microscope
$SIMD$	Single Instruction Multiple Data
SM	Streaming Multiprocessor
v	Velocity
v_n	Normal inter-particle relative velocity
v_t	Tangential inter-particle relative velocity
V	Volume

WAD	Weathered Altered Dolomite
x	Position of particle centroid
γ	Unit weight of soil
β	Qualitative surface settlement (Physical trapdoor experiments)
β	Coefficient of rolling stiffness (Discrete Element Method)
δ, Δ	Trapdoor displacement
δ/B	Relative trapdoor displacement
Δt	DEM time step
Δt_c	Critical time step
Δp_{max}	Maximum error between the reference and target subsets (PIV)
Δs, Δn	Particle-particle overlap in DEM
Δn_n	Normal inter-particle overlap
Δn_t	Tangential inter-particle overlap
$\Delta\theta_r$	Relative rotational angle between two particles
ϵ_a	Axial strain
ϵ_v	Volumetric strain
μ	Particle-particle friction coefficient
μ_k	Kinetic friction coefficient
$\mu_r \; or \; \eta$	Rolling resistance coefficient
μ_s	Static friction coefficient
ν	Poisson's Ratio
ρ	Density
$\rho_{d\,max}$	Maximum dry density
$\rho_{d\,min}$	Minimum dry density
σ_v	Vertical stress
σ_h	Horizontal stress
φ'	Friction angle
φ'_p	Peak friction angle
φ'_{cs}	Critical state friction angle
ψ, ν	Dilation angle
ψ_{max}	Peak angle of dilation
ω	Angular velocity
$2D$	Two-dimensional
$3D$	Three-dimensional

*The effective equivalent entities have been denoted with an asterisk (*) in the text

Constant Strain Triangle Application (Finite Element Method)

B	Strain-displacement matrix
E_{Biot}	Biot strain matrix
F	Deformation matrix
I	Identity matrix
J	Jacobian matrix
L	Displacement gradient matrix
q	Displacement matrix
U	Stretch matrix
$\gamma_{log,max}$	Maximum natural shear strain
γ_{xy}	Engineering shear strain
ε	Strain matrix
$\varepsilon_{eng,I}$ $\varepsilon_{eng,II}$	Principal engineering strains
$\varepsilon_{eng,xx}$ $\varepsilon_{eng,yy}$	Engineering linear strains
$\varepsilon_{log,I}$ $\varepsilon_{log,II}$	Natural principal strains

1. INTRODUCTION

1.1. BACKGROUND

South Africa's Gauteng Province derives its name from the Sotho name "Gauta", meaning gold. The name alludes to the significance of the province as South Africa's economic hub as it contributes approximately a third of the country's gross domestic product. Despite being the smallest province and representing only about 1.5% of the country's area, the province is home to roughly a quarter of the country's population, with this percentage increasing by an average of 0.3% per year as people are drawn to the wealth and employment opportunities in the province (Statistics South Africa, 2017). Approximately 25% of the Gauteng Province is underlain by dolomite and therefore susceptible to sinkhole formation. The disastrous effects associated with sinkhole formation are well-known and include severe damage to infrastructure, as well as the loss of life. Given the social and economic significance of the Gauteng Province, an astute understanding of the mechanisms associated with sinkhole formation, as a result of cavity propagation, is essential to ensure the optimal utilisation of land.

The South African standard for developing infrastructure on dolomitic land advocates the use of a "rational assessment" to determine the maximum potential size of a sinkhole (SANS 1936-2, 2012). It further presents Buttrick & van Schalkwyk's (1995) funnel method as a "deemed to satisfy" method for determining the maximum potential development space of a sinkhole (Jacobsz, 2016). As illustrated in Figure 1-1, the maximum surface diameter of a sinkhole is primarily dependent on both the depth of the subsurface cavity, as well as the selected angle of draw assigned to each of the blanket materials through which the sinkhole propagates. This implies that for subsurface cavities at great depths, the resulting maximum potential development space would be substantial, resulting in large areas of

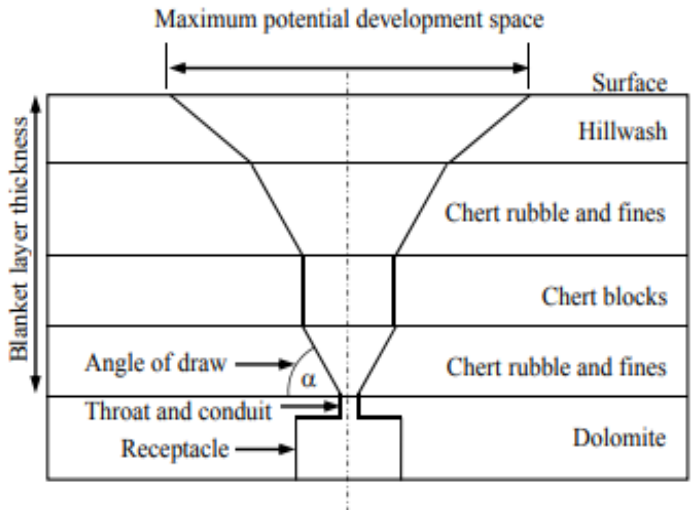

Figure 1-1: Estimation of the maximum potential development space of a sinkhole (Jacobsz, 2016, adapted from Buttrick & Van Schalkwyk, 1995)

uninhabitable land. This method is further known to predict conservatively large sinkhole sizes thereby compromising the effective utilisation of land (Jacobsz, 2016).

Sinkhole formation in South African dolomitic profiles is typified by the collapse of a stable arch, spanning the throat of an underlying cavity in dolomitic residuum. The spanning mechanism, known as arching, refers to the redistribution of stresses within the overburden material as load is transferred to the abutments of the arch with the loss of subsurface support. A natural or man-made disturbing agent such as water ingress, groundwater level fluctuation or ground vibrations, is required to alter the equilibrium of the stable arch, causing the cavity to propagate towards the surface and ultimately resulting in the formation of a sinkhole (Jennings et al., 1965). Soil arching occurs when stresses are transferred from the yielding part of the soil mass, for example the activated material which flows through the throat of a subsurface cavity (receptacle), to the adjacent rigid part of the soil mass. Karl Terzaghi, widely known as the father of modern soil mechanics, first investigated the arching mechanism in soil by means of a trapdoor experiment in 1936. It has since been regarded as the classical experimental setup to investigate arching in soils.

Due to the discontinuous nature of soils, complex formulations are required to numerically model cavity propagation resulting in sinkhole formation. One of the most suitable numerical methods that can be used to study sinkhole development is Discrete Element Modelling. The Discrete Element Method (DEM) is becoming an increasingly popular numerical method to investigate the mechanical properties of geomaterials. In the past, work related to DEM simulations of granular material has been restricted due to the limited computing capabilities of conventional Core Processing Unit (CPU)-based DEM codes. With the advent of Graphical Processing Unit (GPU)-based DEM codes, and their parallel processing ability, the application of DEM simulations in geotechnics has become almost regular practice (Donze et al., 2009). The discrete nature of the DEM is suited to study the flow of granular material as these materials are inherently discontinuous (Belheine et al., 2009). The DEM is therefore considered to be the ideal tool for the investigation of large soil deformations associated with cavity propagation during sinkhole formation.

The primary objective of this research project was to investigate the effect of varying material shear strength properties on the soil deformation mechanisms during cavity propagation. This would lead to a better understanding of sinkhole formation and the associated potential size of a sinkhole, with far-reaching impacts, both socially and economically. Given the significance of the trapdoor experiment in investigating soil arching, as well as the application of DEM to large strain problems in geotechnics, trapdoor experiments were modelled physically, in a centrifuge facility to replicate typical soil stresses in the field, as well as numerically, using DEM. These models were used to simulate and investigate the deformation mechanisms associated with cavity propagation of materials with different shear strength properties.

1.2. OBJECTIVES OF THE STUDY

The primary objective of this study was to investigate the relationship between the soil strength of non-cohesive materials, as a function of simulated particle shape effects, and the corresponding propagation mechanism initiated during deep trapdoor experiments simulating the loss of subsurface support during sinkhole formation.

In addition, the study includes the following objectives:

- Investigate the effect of material shear strength on the qualitative characteristic material behaviour associated with deep trapdoor experiments (H/B > 2), from literature, for the following material characteristics:
    - Trapdoor load-displacement behaviour
    - Deformation mechanisms at the initial, intermediate and final stages of trapdoor displacement
    - Surface settlement characteristics
- Establish the influence of the DEM input parameters when modelling trapdoor experiments.
- To determine whether Blaze-DEM, the DEM code used during this study, is an appropriate tool for investigating cavity propagation in the classical trapdoor experiment.

1.3. SCOPE OF THE STUDY

The scope of the study was limited to the following aspects:

- The research project included two primary components: Physical modelling of deep trapdoor experiments in a centrifuge facility and numerical modelling of trapdoor experiments using DEM.
- The geomaterials used in the physical testing were dry, cohesionless materials. Dense to very dense, homogenous soil models were prepared in the laboratory for all the centrifuge trapdoor experiments.
- The deformation mechanisms, trapdoor load-displacement behaviour and surface settlement characteristics were investigated for the physical trapdoor experiments.
- The second part of the study entailed numerical modelling of trapdoor experiments using Blaze-DEM, a three-dimensional research code developed for Graphical Processing Unit (GPU) architecture. The calibrated particle parameters were limited to those required as input parameters in Blaze-DEM.
- The discrete particles were single-sized and as with the physical experiments, a homogenous material model was prepared.

- For the numerical experiments, material shear strength was imposed by applying a range of inter-particle rolling resistance and friction coefficients. The effect of the varying material strength on the deformation mechanisms associated with trapdoor displacement was then investigated.
- Trapdoor load-displacement and surface settlement characteristics were not investigated in the numerical modelling portion of this research project.
- Force chains within the DEM simulation were not investigated in this study.

1.4. METHODOLOGY

Cavity propagation was investigated by means of both deep physical trapdoor experiments, conducted in a centrifuge facility, as well as deep numerical trapdoor experiments using the Discrete Element Method. In comparison to physical experiments, DEM simulations allow for greater control over individual particle parameters as well as ease of individual parameter variation.

The following methodology was applied to achieve the objectives set for this research study:

- A literature review of sinkhole formation and characterisation, previous trapdoor experiments, soil arching, as well as the fundamentals and application of the Discrete Element Method was undertaken. A review of the relevant literature stressed the importance of the study objectives and provided the necessary background information to commence with the study.
- Three granular materials were tested in the centrifuge facility, namely a fine-grained sand, a coarse-grained sand and 2 mm glass beads (ballotini). The three materials were used to investigate the relationship between soil strength and the associated deformation mechanism during cavity propagation. The trapdoor experiments were conducted at an elevated acceleration in the University of Pretoria's centrifuge facility to simulate typical field stress conditions for sinkhole formation.
- The physical trapdoor experiment with glass beads was used as baseline to calibrate the DEM numerical trapdoor experiment. The parameters of the spherical particles used in the DEM experiment were calibrated by means of a sensitivity study to ensure that the material behaviour of the DEM model corresponded to that of the physical model with glass beads (spherical particles).
- Once the DEM model was calibrated, the shear strength of the material was varied to determine the effect of soil strength on shear band propagation during sinkhole formation. Initially, the aim of the study was to simulate various material shear strengths by changing only the particle shape and consequently the friction angle of the material (i.e. from spherical to various polyhedral particle shapes). As a result of a numerical constraint inherent to the DEM code used in the research project, a full simulation with polyhedral particles could not be simulated.

Coetzee (2017) lists two methods in which particle shape can be simulated in DEM, namely the application of non-spherical particles and the application of a rolling resistance parameter. The methodology was subsequently changed to simulate particle shape effects by applying a rolling resistance coefficient, in combination with an increased friction coefficient, to the particles in the DEM experiments. Material (soil) shear strength was varied by increasing the above-mentioned coefficients incrementally.

- Finally, the results of both the physical and numerical trapdoor experiments were evaluated to determine the effect of material shear strength on the associated soil deformation mechanisms associated with cavity propagation.

1.5. ORGANISATION OF THE REPORT

The report consists of the following chapters and appendices:

- **Chapter 1** serves as an introduction to the report and highlights the significance of the research. The chapter further provides an overview of the objectives, scope and methodology of the project.
- **Chapter 2** presents a review of literature applicable to this study including sinkhole formation in South Africa, trapdoor experiments, the discrete element method and its application to geotechnics, as well as numerical modelling of trapdoor experiments using DEM.
- **Chapter 3** describes the experimental setup for the physical trapdoor experiments undertaken in the centrifuge facility. It includes a physical description of the three materials used during testing, as well as an overview of the analysis techniques and instrumentation used to quantify material behaviour.
- **Chapter 4** presents the results of the physical trapdoor experiments. The results are analysed and discussed in terms of the applicable literature.
- **Chapter 5** describes the methodology employed to investigate the effect of simulated particle shape, corresponding to a change in material shear strength, using the DEM. The numerical trapdoor model setup, calibration, validation and application is described.
- **Chapter 6** presents the results of the calibration and validation procedures applied to prepare a numerical trapdoor model, using DEM, which is comparable to the physical trapdoor experiment undertaken with glass beads.
- **Chapter 7** includes a discussion and analysis of the results of the numerical trapdoor experiments. The unforeseen limitations of the DEM model are detailed, and significant findings are presented.
- **Chapter 8** contains the primary conclusions and recommendations of this study.

- **Chapter 9** provides a list of references used during the course of the research project.

- **Appendix A** contains a summary of the calculations used in the initial angle of shear band propagation analysis.
- **Appendix B** contains the DEM simulation logs for particle pluviation, model "spin-up" (increased model acceleration), as well as model calibration and application.
- **Appendix C** presents the python scripts used to analyse the DEM results for calibration, validation and application purposes.
- **Appendix D** presents the results of the DEM particle and PIV subset displacement trajectory validation exercise

2. LITERATURE REVIEW

2.1. INTRODUCTION

As introduction to the chapter, an overview of sinkhole formation in dolomitic ground conditions in South Africa is presented. The significance of the current design standards associated with dolomitic land is further highlighted. Classical arching theory, related to cavity propagation in dolomitic soils, is then discussed in combination with the renowned geotechnical trapdoor experiment and its attributes. Following an overview of recent arching studies by means of trapdoor experiments, the fundamentals of the Discrete Element Method (DEM) and its application to geotechnics are presented. A description and validation of the DEM code used in this study are detailed followed by a review of studies in which trapdoor experiments were simulated using numerical models. The chapter concludes with a summary of the literature review in which the significance of the presented material is highlighted and a hypothesis for the study formulated.

2.2. SINKHOLE FORMATION IN DOLOMITIC REGIONS

2.2.1 Dolomite geology

A karst topography refers to a distinctive terrain established on soluble carbonate rock, such as dolomite and limestone, in which the dissolution of the rock results in underground drainage systems. These are often characterised by sinkholes and complex natural cave passages (Waltham & Fookes, 2003). Carbonate rocks are classified as sedimentary rocks and are primarily composed of carbonate minerals such as dolomite, magnesite and calcite. The two primary carbonate rock types are limestone, which is dominated by calcite, and dolomite, in which the dolomite mineral is predominant. The lattice structure of the dolomite mineral consists of alternating layers of calcium (Ca) and magnesium (Mg), separated by layers of carbonate trioxide (CO_3), and is represented by the following stoichiometric chemical composition: $CaMg(CO_3)_2$ (Warren, 2000).

Over geological time, dolomite rock may be subjected to the process of dissolution when it encounters weakly-acidic groundwater in the form of a carbonic acid. This weak carbonic acid forms when atmospheric carbon dioxide dissolves in rain or ground water. When dolomite rock reacts with this weak acidic water as it percolates along fractures, faults and rock joints in the karst landscape, calcium and magnesium bicarbonates are leached from the rock and removed by the circulating ground water (Department of Water Affairs, 2009).

Residual dolomitic soils, which form as a result of the dissolution process of dolomite rock, include WAD (Weathered Altered Dolomite) and chert gravel. WAD is a low strength, fine-grained, residual material consisting primarily of manganese oxide, whereas chert is a residual dolomitic rock comprised

almost entirely of silica (SiO_2). In dolomitic soil profiles chert is present in the form of chert rubble or gravel. These are residual products of the chert bands commonly found in dolomite bedrock. Buttrick and van Schalkwyk (1998) describe residual dolomitic materials as porous and compressible and attribute these properties to the difference in grading between WAD and chert rubble, as well as to the leaching process described above. As a result of natural compaction as well as a characteristic ferricrete formation near the ground surface, the vertical profile of residual dolomitic materials often reflects a decrease in strength and increase in both porosity and permeability with depth (Oosthuizen & Richardson, 2011). This is contrary to most geological formations.

Figure 2-1, from Wagener and Day (1986), depicts a typical soil profile on dolomite. Characteristically, the site is covered by a blanket of transported material, underlain by a pebble marker which separates the transported material from the residuum. The dolomitic bedrock is characterised by irregular pinnacles and boulders or "floaters". In chert-rich dolomite, the residual materials usually grade from relatively competent coarse, angular chert gravel to fine, compressible WAD and clay before reaching solid dolomite at bedrock level. The residual materials are often collectively referred to as the blanketing layer (Buttrick & Van Schalkwyk, 1995). As shown in the figure below, cavities may be found in the lower residuum between pinnacles with solution caverns often manifesting in the upper layers of the dolomitic bedrock.

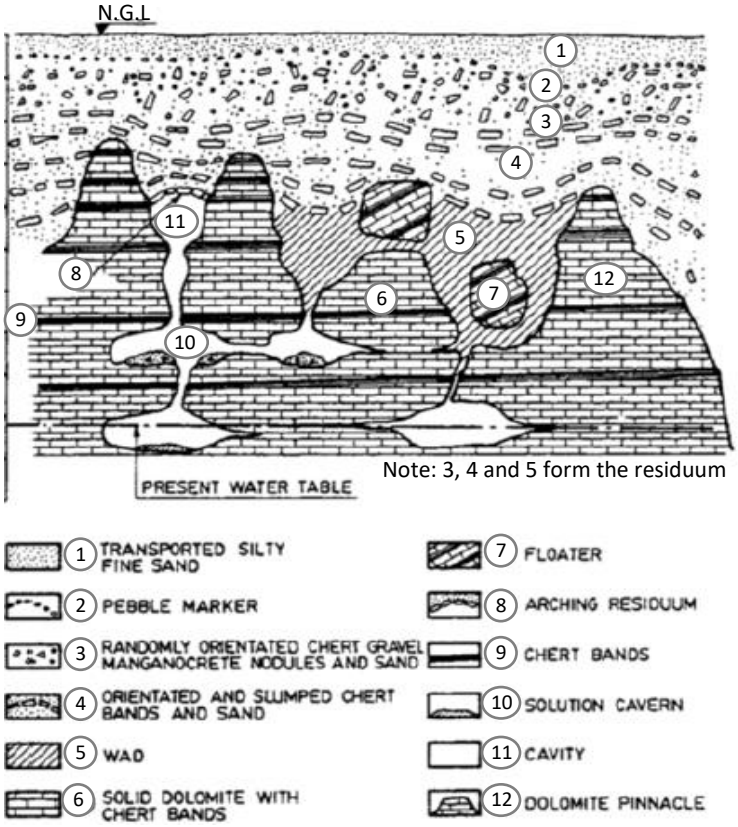

Figure 2-1: Typical soil profile on dolomite (Wagener & Day, 1986)

2.2.2 Mechanisms of sinkhole formation

Trollip (2006) defines a sinkhole as a feature of karst-related ground movement which forms suddenly and manifests itself as a hole in the ground. Waltham & Fookes (2003) categorise sinkholes into six different types, based on the mechanisms associated with ground failure, but emphasise that subsidence sinkholes are the primary sinkhole hazard in civil engineering practice. A 'subsidence sinkhole' is a term used to describe sinkholes formed in soil cover, overlying bedrock. In cohesive overburden material, a dropout, or cover-collapse, sinkhole forms when a mobilising agent causes a subsurface void, above an opening in the underlying bedrock, to propagate to the surface (Tharp, 1999; Buttrick & Van Schalkwyk, 1998). Suffosion sinkholes are formed in non-cohesive soil cover when these granular soils wash into the receptacles in the underlying dolomite. Dropout and suffosion sinkholes are referred to collectively as subsidence sinkholes. Waltham & Fookes (2003) illustrate the two types of subsidence sinkholes in Figure 2-2.

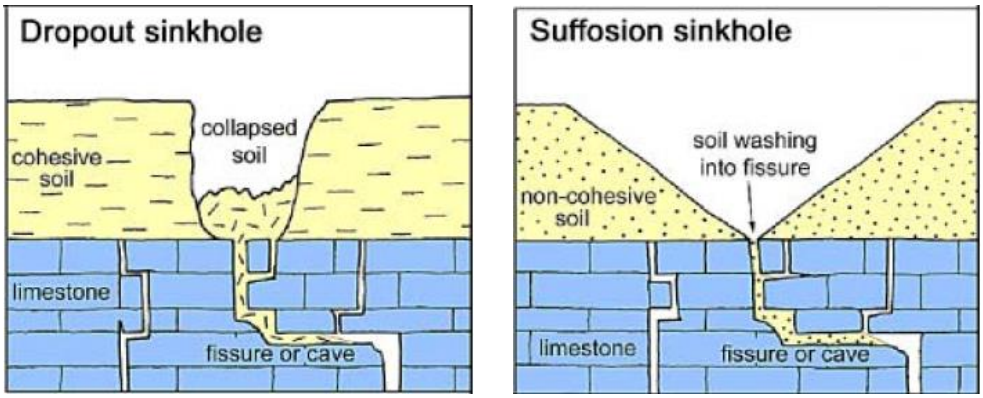

(a) (b)

Figure 2-2: Subsidence sinkhole classification: (a) Dropout sinkhole (cohesive soil) and (b) Suffosion sinkhole (non-cohesive soil) (Waltham & Fookes, 2003)

Jennings et al. (1965) postulated that five concurrent conditions must exist for sinkhole formation to occur. These well-referenced prerequisites are as follows:

1. There must be a stiff material on either side of the void to act as the abutments to the material spanning the void. The abutments may be dolomite pinnacles or the sides of subsurface canyons. The span between abutments must be appropriate to the properties of the bridging material. An arch will not form if the overlying material is too weak to span the distance between abutments.

2. An arching mechanism must be initiated within the residuum, in which the load of the overburden material is transferred to the abutments of the arch.

3. A void must exist or develop below the arched material.

4. A reservoir must exist below the arch in order to accept material from the arch as the void propagates upwards. It is also essential that a means of transporting this material exists.

5. A disturbing agent is required to collapse the roof of the void once equilibrium of the stable arch has formed.

Figure 2-3 presents a diagram showing sinkhole formation. All five prerequisites, listed above, are detailed in the figure. A leaking pipe acts as the mobilising agent in Figure 2-3.

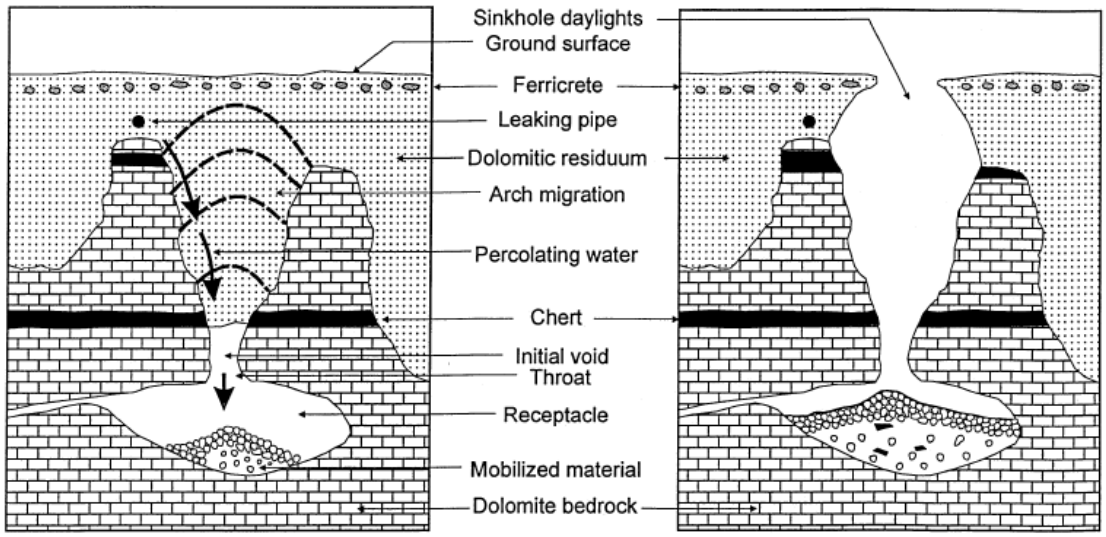

Figure 2-3: Schematic representation of a sinkhole formation (Buttrick & Van Schalkwyk, 1998)

The "disturbing agent" referred to by Jennings et al. (1965) may take the form of both natural and man induced mobilising agencies. In terms of natural triggers, Tharp (1999) noted the common occurrence of newly formed sinkholes during and after rains, or even after modest rain following a prolonged drought.

Although sinkholes may occur naturally, the generally accepted principle that man-induced mobilising agencies, as a result of land development, expedite sinkhole formation by many orders of magnitude is supported by Schoning (1990) who reported that 94% of the 375 sinkholes recorded south of Pretoria had, at that time, had occurred on developed land. A similar figure of 96% is reported for all sinkhole and subsidence occurrences to date (SANS 1936-4, 2012). Buttrick & Van Schalkwyk (1998) list the following as the primary man-induced trigger mechanisms for sinkhole formation, as they alter the natural geological environment:

- Concentrated water ingress
- Lowering of the groundwater level
- Ground vibrations

2.2.3 Effects of sinkhole formation

In the absence of risk mitigation, the effects of sinkhole formation can be devastating. Buttrick & Van Schalkwyk (1998) report that 38 sinkhole related deaths had occurred since 1968 as well as infrastructure damage amounting to hundreds of millions of Rand.

Although it is South Africa's smallest province, representing only 1.2% of the country's area, the Gauteng Province is known as the South Africa's commercial, mining and manufacturing hub and it is responsible for more than a third of the country's Gross Domestic Product (GDP) (Statistics South Africa, 2018).

It is estimated that 25% of the Gauteng Province is located on dolomite land and that between four and five million South Africans either work or live on land underlain by dolomite. Prohibiting any development of dolomite land is not practical and requirements for the development of dolomite land were therefore employed to ensure acceptably safe living and working environments, while allowing development on dolomitic land where the loss of assets is within reasonable limits and the risk of sinkhole formation is mitigated (SANS 1936-4, 2012). Figure 2-4 presents an aerial photograph of a sinkhole that formed near Bapsfontein, north-east of Johannesburg, in the Gauteng Province.

Figure 2-4: Aerial image of a sinkhole formation near Bapsfontein, Gauteng (Oosthuizen & Richardson, 2011)

2.2.4 Development on dolomite land in South Africa

In 2012 the South African Bureau of Standards (SABS) published a set of standards for developing infrastructure on dolomitic land, these are recorded in the SANS-1936 (2012) four-part document. One of the general requirements listed in the Part 1 of the document is to determine the Inherent Hazard Class (IHC) of the site. Based on the site's IHC, as well as the type of intended land usage, a dolomite area designation is assigned to the site. This designation governs the precautionary measures necessitated for infrastructure development on the site. The inherent hazard classification system characterises a site based on both the likelihood of a sinkhole (or subsidence) occurring, as well as by the predicted size of the sinkhole (SANS 1936-1, 2012). Although the method of determining the IHC is not specified explicitly, the standard supports the method of scenario supposition, or the approach of a "rational assessment" to classify the IHC of a site (SANS 1936-2, 2012).

The maximum potential development space for a sinkhole can be predicted by extrapolating a funnel-shaped failure zone from the subsurface cavity to the surface, based on typical angle of draw for the overburden material (Buttrick & Van Schalkwyk, 1995). This method is "deemed to satisfy" the rational assessment method (Jacobsz, 2016) and forms part of the more comprehensive scenario supposition method for determining the IHC of a site.

Buttrick & Van Schalkwyk (1998) state that the following factors should be used to characterise the risk of sinkhole formation, as well as to determine the maximum potential size of a sinkhole: The total thickness of the blanketing layer, the thickness of each of the horizons within the blanketing layer as well as their respective angles of draw. Further, the maximum available space for a sinkhole to form can only be utilised if the materials within the blanketing layer have mobilisation potential and if the mobilising agency is capable of mobilising this material. Finally, the volume of the receptacle needs to be large enough to accommodate the mobilised material. It is further noted that these factors cannot be determined with certainty during a site investigation, and that the maximum potential size is therefore assumed in the hazard classification procedure (Buttrick & Van Schalkwyk, 1998). Based on typical angles of draw presented in Buttrick & Van Schalkwyk (1995), the maximum potential sinkhole size, quantified in terms of surface diameter, can be determined. Figure 2-5 demonstrates the maximum potential sinkhole sizes (MPS) for scenario (a) and (b) based on the factors listed above.

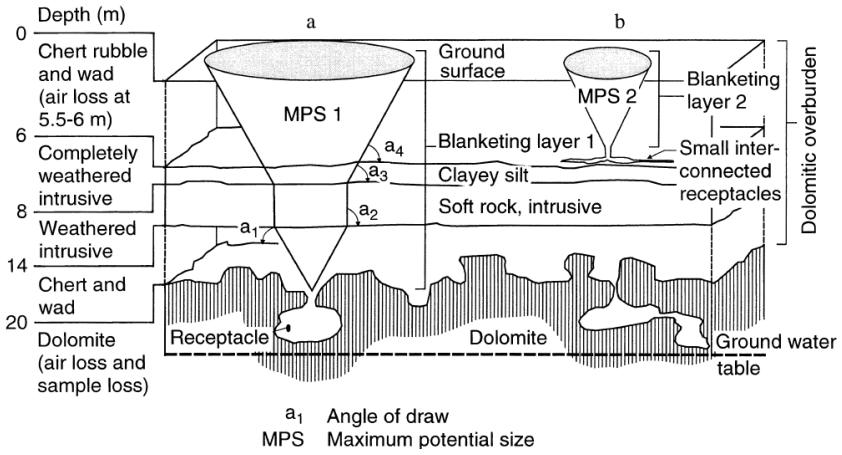

Figure 2-5: Schematic of the components of a dolomitic ground profile and their influence on the maximum potential sinkhole size (Buttrick & Van Schalkwyk, 1998)

A classification of sinkhole sizes, recommended by Buttrick & Van Schalkwyk (1995), is shown in Table 2-1. They further note that using the maximum potential size of the sinkhole to determine the IHC of a site is considering the worst-case scenario, as in reality the receptacle may be too small to accommodate all of the mobilised material. Figure 2-6 presents an example of the case where only a fraction of the maximum potential sinkhole space has been utilised. However, as no technique exists to accurately determine the volume of the receptacles, the maximum potential sinkhole size should be used to determine the IHC of the site (Buttrick & Van Schalkwyk, 1995).

Table 2-1: Suggested scale for size of sinkholes (Buttrick & Van Schalkwyk, 1995)

Suggested terminology	Maximum diameter on surface (m)
Small sinkhole	< 2
Medium-size sinkhole	2 – 5
Large sinkhole	5 – 10
Very large sinkhole	> 10

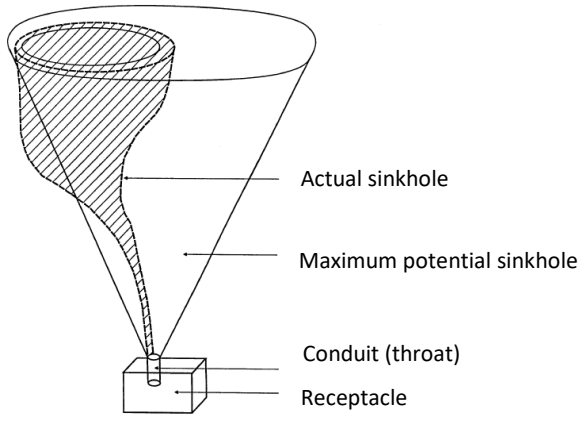

Figure 2-6: Diagram of a sinkhole formation where the maximum potential size has not been used (Buttrick & Van Schalkwyk, 1995)

The second part of the Inherent Hazard Classification system is the likelihood of sinkhole occurrence. According to Buttrick & Van Schalkwyk (1998), this aspect is dependent on the mobilisation potential of the blanketing layer and the nature of potential mobilising agencies. The mobilising agencies are in turn governed by the future land use of the site. The inherent hazard associated with the likelihood of the occurrence of an event is quantified in terms of the average number of ground surface damage events, such as dolines or sinkholes, per hectare, in a 20-year period, after an initial 20-year period. Table 2-2 presents the inherent hazard classification associated with the probability of sinkhole or subsidence formation. Using the classification systems presented in Table 2-1 and Table 2-2, a site is assigned an IHC which then determines its dolomite area designation development potential (SANS 1936-1, 2012).

Table 2-2: Inherent hazard classification for likelihood of occurrence (Buttrick & Van Schalkwyk, 1998)

Inherent hazard class	Typical number of ground movement events (per ha per 20-year period)
Low	0
Medium	0.1
High	> 1

2.3. TRAPDOOR EXPERIMENTS

2.3.1 Arching mechanism

The arching mechanism is known to be one of the most prevalent soil mechanisms observed in both naturally occurring soils, as well as in experimental/laboratory models. Arching of soil is activated when part of the bulk material mass yields, while the adjacent material remains intact and rigid. Shear stresses resist the movement of the yielding material which results in a redistribution of stresses within both the yielding and rigid parts of the material mass (Terzaghi, 1943).

A description of the arching mechanism by Iglesia et al. (1990), relates it to the redistribution of stresses that occurs when an inclusion, or subsurface structure, is present within a ground mass. The stress distribution and deformation of the soil around, or above, the inclusion will differ to that experienced by the soil mass adjacent to the inclusion. The redistribution of stresses further influences the load transferred onto the subsurface inclusion or structure. The primary factors affecting the portion of load transferred onto the subsurface structure are the physical properties of the structure, most notably its stiffness and geometry, the ability of the surrounding soil to transfer load during soil deformation and lastly, the stress profile of the soil that would exist if there were no inclusions (McNulty, 1965).

Two distinct types of arching mechanisms exist, namely active and passive arching. Active arching occurs when the surrounding soil mass is stiffer than the inclusion. This causes a redistribution of

stresses in the soil mass, resulting in a stress reduction on the inclusion and an increase in the stress magnitude in the adjacent ground mass. Conversely, passive arching occurs when the surrounding soil mass has a greater compressibility than the subsurface inclusion. A stress increase is applied to the inclusion, while the stresses in the adjacent soil mass decrease (Einstein et al., 1990). Figure 2-7 (a) and (b) illustrate the typical stress distributions for active and passive arching, respectively.

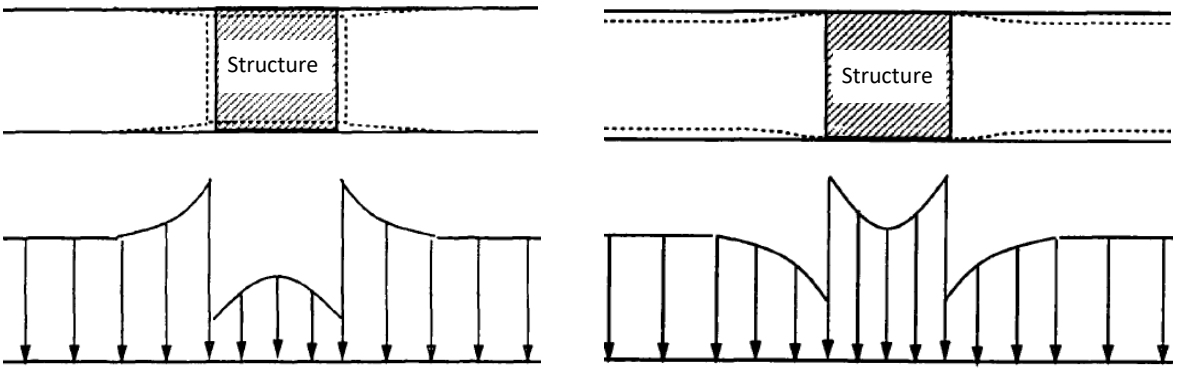

(a) (b)

Figure 2-7: Typical stress distributions that occur during (a) active and (b) passive arching (adopted from Iglesia et al. 1990)

The primary applications of the arching effect in geotechnics are associated with arching and related failure mechanisms engaged during the formation of sinkholes and dolines, as well as the design and construction of man-made structures such as tunnels and buried conduits (Tien, 1996). As described in the previous section, the formation of a sinkhole occurs when a subsurface cavity propagates to the surface due to the instability of the overburden material. Although Tien (1996) acknowledges the roles of both cohesion and the arching effect on the failure strength of a cavern roof in cohesive material, he postulates that for a cohesionless granular material the primary factor contributing to the failure characteristics of the cavity overburden is the arching mechanism. The need to understand the arching mechanism in granular materials is therefore emphasised when studying the strength of subsurface cavity roofs with non-cohesive overburden material.

Rui et al. (2016-b) report that recent research, used to investigate the arching effect in soils, has focussed on centrifuge modelling of trapdoor experiments and the implementation of Particle Image Velocimetry (PIV) to investigate shear strains and deformation mechanisms generated during trapdoor lowering. They further note that the significant increase in the application of Discrete Element Modelling (DEM) for granular materials has resulted in DEM being used to investigate the arching effect in soils.

2.3.2 Classical arching theory

Chevalier et al. (2012) state that the complexity of the stress redistribution, caused by the arching effect, makes it difficult to formulate design solutions which incorporate the expected arching effect around

geotechnical structures in the field. The trapdoor experiment is a method which has been used extensively to investigate the mechanisms associated with arching. Iglesia et al. (2014) describe the trapdoor experiment as “the classic experimental setup to investigate arching”.

The trapdoor experiment setup generally consists of a vertically translating horizontal strip, overlain by geomaterial. Downward displacement of the trapdoor results in a reduction in the soil stresses directly above the trapdoor and an increase in stress in the soil mass adjacent to the trapdoor. Active arching is simulated by this downward displacement of the trapdoor, whereas passive arching is simulated by an upward displacement of the trapdoor, resulting in an increase in the soil stresses directly above the trapdoor and a reduction in the stresses of the soil mass neighbouring the trapdoor. The downward displacement of the trapdoor can be used to simulate the deflection of a flexible support, relative to the adjacent soil mass, or it can be used to replicate grain silo discharge or sinkhole formation (Iglesia et al., 2014). Two different trapdoor systems exist, namely a deep and shallow trapdoor system. A deep trapdoor system has an H/B ratio greater than two, where H is the height of the overburden and B is the trapdoor width. Conversely, if the H/B ratio is less than two, the position of the trapdoor is deemed to be shallow (McNulty, 1965; Dewoolkar et al., 2007, and others).

Although the first trapdoor experiment can be attributed to the work done by Engesser (1882), Tien (1996) and Evans (1983) regard the experimental arching investigation undertaken by Terzaghi (1936 and 1943) to be the original and most renowned trapdoor experiment for geotechnical applications. The following aspects were investigated during the original trapdoor experiment and (with the exception of the surface settlement characteristics) have been shown to be the primary points of investigation in recent trapdoor experiments:

- Load-displacement characteristics of the system
- Lateral stress ratio (K-value)
- Failure mechanisms and sliding surfaces within the soil mass

Terzaghi’s (1936) trapdoor experiment consisted of a sandbox with a trapdoor located below the sand, which was level with the base of the sandbox. The height of the sand was 31 cm, the trapdoor width was 7.3 cm (2B) and the length of the sandbox was 46.3 cm (L). The displacement of the trapdoor as well as the load on the trapdoor were measured during trapdoor translation. Additionally, indirect measurements of the horizontal and vertical stresses were taken at various heights above the trapdoor (Tien, 1996).

2.3.2.1 Trapdoor load versus displacement

The trapdoor load-displacement characteristics determined by Terzaghi (1936), and revised by Evans (1983), are presented in Figure 2-8. The force measured on the trapdoor during its downward translation is normalised by the force acting on the trapdoor before lowering commenced. The graph shows a rapid

decrease in the normalised force during initial translation of the trapdoor. The minimum normalised force is less than 10% of the original overburden load and occurs at a displacement of only 1% of the trapdoor width. It is further noted that the minimum normalised force is lower for dense sand than for loose sand. After the minimum normalised force is attained and displacement of the trapdoor continues, the normalised force tends to increase to a constant value of approximately 12.5% of the initial overburden force, for both dense and loose sands. Terzaghi believed that the increase in load on the trapdoor, before reaching the constant value of 12.5%, could be attributed to the disintegration of the "structure" that had formed within the sand (Tien, 1996). The constant normalised force value occurred at displacements exceeding 10% of the trapdoor width.

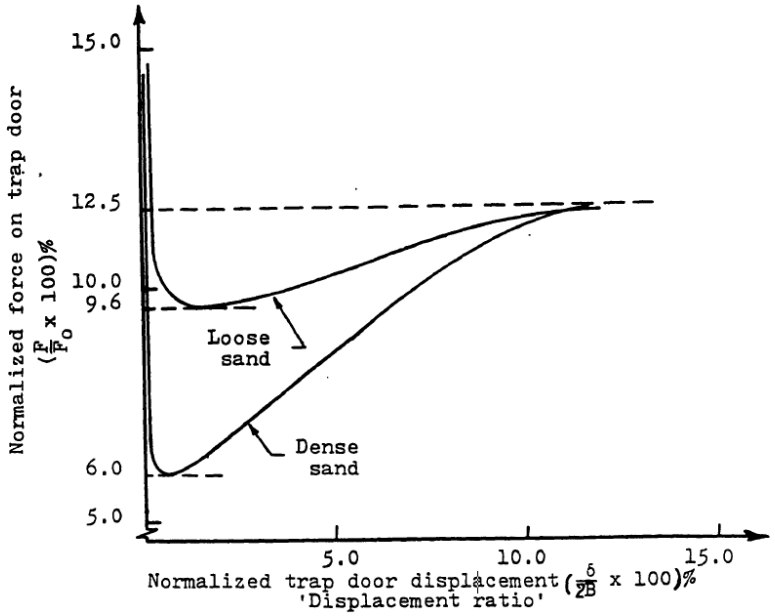

Figure 2-8: Trapdoor load-displacement curves from Terzaghi's trapdoor experiment (Terzaghi 1936, revised by Evans, 1983)

2.3.2.2 Lateral stress ratio (K)

Typical vertical and horizontal stress distributions, measured in the soil during trapdoor lowering, are shown in Figure 2-9 (a) and (b), respectively. Linearly increasing stress conditions with depth, corresponding to zero displacement of the trapdoor, are represented by the solid lines. The dotted lines in both graphs depict the respective stress distributions at trapdoor displacements of 1% and 10% of the trapdoor width. The primary difference between the two plots is that the horizontal stress distribution shows stress values slightly greater than the geostatic values recorded for zero displacement of the trapdoor, whereas a reduction in vertical stress is recorded throughout the soil profile depth. This is indicative of the stress redistribution associated with the arching effect (Terzaghi, 1936 and Tien, 1996).

Values for the coefficient of lateral stress (K) were obtained from these stress distribution profiles and are presented in Figure 2-9 (c). As expected, an increase in the lateral stress ratio is noted in the area

above the trapdoor, but it starts reducing to a value of K_o (describing material at rest) from a height of approximately 2.5B above the trapdoor, where the trapdoor width is defined as 2B.

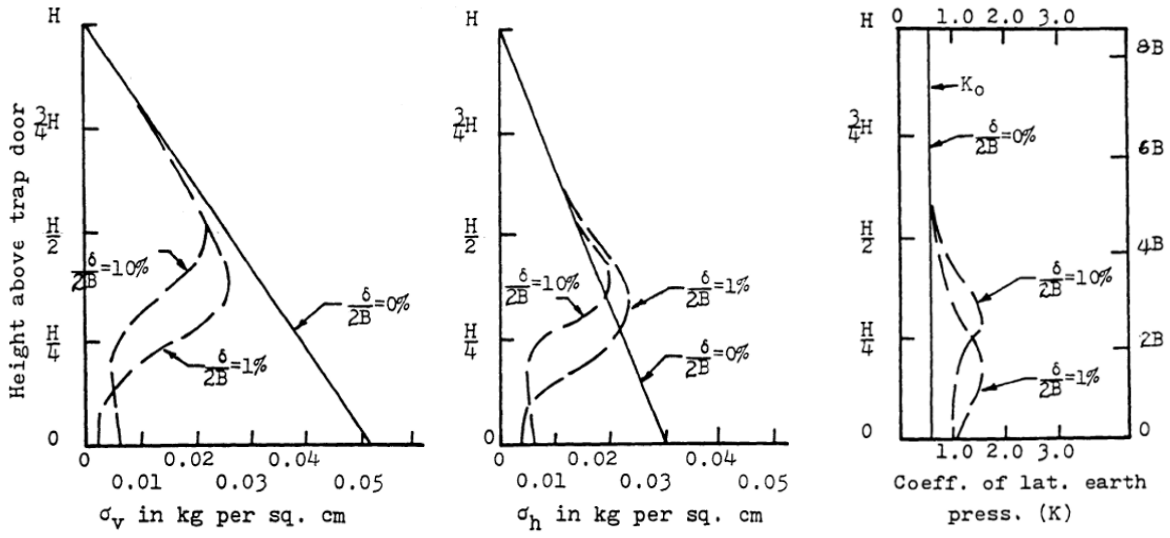

(a) (b) (c)

Figure 2-9: Terzaghi's trapdoor experiment results for the (a) vertical stress profile (b) horizontal stress profile and (c) coefficient of lateral earth pressure (K) variation with depth (Terzaghi, 1936, revised by Evans, 1983)

Terzaghi (1943) attempted to quantify the experimental results theoretically by adopting vertical sliding surfaces, propagating from the edges of the trapdoor. The actual sliding surfaces were, however, curved and extended beyond the trapdoor edges at the surface of the soil. He further assumed that vertical stresses were uniform across the entire horizontal section of the soil profile and that the coefficient of lateral earth pressure (K) was constant. Figure 2-10 (a) shows both the actual and adopted sliding surfaces for Terzaghi's trapdoor experiments undertaken in sand under plane strain conditions. Tien (1996) summarised the derivation of Terzaghi's arching theory based on the free body diagram of a slice of soil in the yielding material above the trapdoor. The free body diagram is illustrated in Figure 2-10 (b).

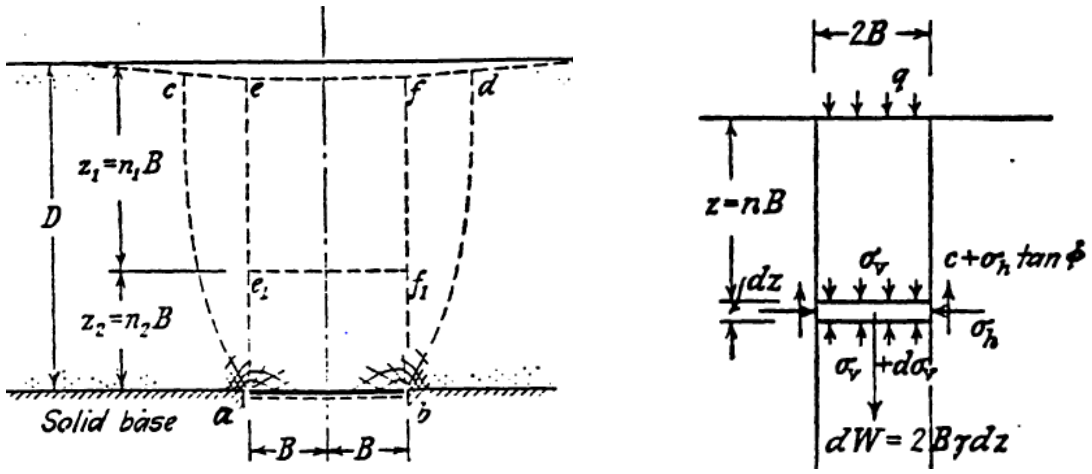

(a) (b)

Figure 2-10: (a) Vertical sliding surfaces and (b) free body diagram of a slice of soil adopted for the theoretical derivation of the arching effect (Terzaghi, 1943)

Equation 2-1 describes the vertical equilibrium for the slice of soil detailed in Figure 2-10 (b).

$$2B\gamma dz = 2B(\sigma_v + d\sigma_v) - 2B\sigma_v + 2dz(c + \sigma_h \tan \emptyset) \quad \text{Equation 2-1}$$

Where:

$2B =$ Trapdoor width

$z =$ Depth

$\gamma =$ Unit weight of soil

$\sigma_v =$ Vertical stress

$\sigma_h =$ Horizontal stress ($\sigma_v K$)

$K =$ Coefficient of lateral stress

$c =$ Cohesion

$\emptyset =$ Friction angle

At the surface of the soil profile (z = 0), the vertical stress is equal to the surcharge. Given this boundary condition and solving for vertical stress in the vertical equilibrium equation, Equation 2-2 is derived:

$$\sigma_v = \frac{B\left(\gamma - \frac{c}{B}\right)}{K.\tan \emptyset}\left(1 - e^{-K.\tan \emptyset.\left(\frac{z}{B}\right)}\right) + q.e^{-K.\tan \emptyset\left(\frac{z}{B}\right)} \quad \text{Equation 2-2}$$

Where:

$q =$ Surcharge at the soil surface

Terzaghi (1936 & 1943) found that the soil stresses at an elevation greater than 5B above the trapdoor were not affected by the trapdoor movement. It was therefore assumed that shear resistance of the soil was only mobilised in the lower portion of the sliding mass, along sliding planes ae_1 and bf_1 in Figure 2-10 (a). As the material above an elevation of 5B did not contribute to the stress redistribution in the soil mass, it was regarded as surcharge. The surcharge is therefore represented by the prism e_1eff_1, in the same figure. If $z_1 = n_1B$ is the depth of the surcharge prism and $z_2 = n_2B$ is the depth of the prism resisting shear along its vertical boundaries, then the revised equation for the vertical stress on a trapdoor during displacement is then given Equation 2-3:

$$\sigma_v = \frac{B\left(\gamma - \frac{c}{B}\right)}{K.\tan\emptyset}\left(1 - e^{-K.n_2.\tan\emptyset.}\right) + \gamma.B.n_1.e^{-K.n_2.\tan\emptyset} \qquad \text{Equation 2-3}$$

Evans (1983) described the arching effect theoretically, by applying basic plasticity theory principles. He applied traditional elasticity theory (Hooke's Law) to the elastic zones in the soil, but the Coulomb failure criterion and corresponding plastic flow rule was used to predict soil behaviour in the plastic zones. The deformation mechanisms were found to be governed by the direction of the trapdoor movement as well as the soil's angle of dilation (v). The angle of dilation is the angle of the plastic potential with respect to the horizontal and the plastic potential is defined as the curve perpendicular to all plastic strain increment vectors. Figure 2-11 (a) presents a graphical representation of the angle of dilation and plastic potential.

Based on the plasticity theory, as well as laboratory experiment results, Evans (1983) concluded that a triangular prism formed above the trapdoor during active arching, when the angle of dilation of the soil was greater than zero. However, a rectangular prism formed above the trapdoor for the case of zero dilation. Evans (1983) noted that the angle of dilation could be approximated by determining the angle at which shear bands propagate during trapdoor translation. Figure 2-11 (b) displays a free-body diagram used to illustrate the application of plasticity theory to active arching in plane strain conditions for an angle of dilation greater than zero (Evans, 1983).

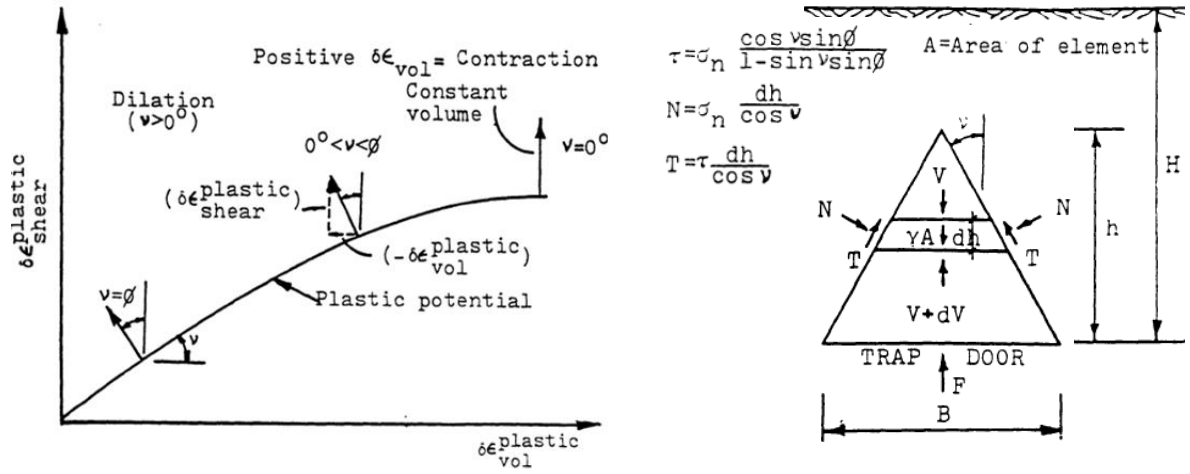

(a) (b)

Figure 2-11: Plasticity theory applied to arching: (a) plastic flow rule (b) free body diagram for ν > 0° (Evans, 1983)

2.3.3 Deformation mechanisms (shear band formation)

(Wang & Kong, 2011) define a shear band as a narrow failure zone that forms when a geomaterial is subjected to compressive loading. In this area of strain localisation, the material may soften as a result of plastic flow, however, outside of this band, the material generally exhibits elastic or slightly plastic behaviour. According to Stone & Wood (1992), the soil mass between two failure surfaces remains fairly rigid and does not contribute to the deformation process. Finally, Stone & Wood (1992) as well as Santichaianaint (2002) concluded that soil density, soil particle size and stress confinement of the soil are the three factors which have the greatest effect on the soil's angle of dilation and resulting pattern of failure surfaces. Dewoolkar et al. (2007), Costa et al. (2009), Iglesia et al. (2014) and Rui et al. (2016-a) have been at the forefront of investigating the soil deformation mechanisms associated with trapdoor lowering in recent times; their results are summarised below.

2.3.3.1 Trapdoor deformation mechanisms: Dewoolkar et al. (2007)

Dewoolkar et al. (2007) conducted a series of trapdoor experiments under normal gravitational conditions, as well as in the centrifuge at an elevated gravitational acceleration of 75g. The stress profile of the trapdoor experiments undertaken under normal gravitational conditions (at 1g) was found to be uniform and of comparatively low magnitude. Straight shear bands, associated with constant dilatancy behaviour, was observed as a result of the uniform stress levels. For tests conducted in the centrifuge, a significant difference exists between stresses at the bottom and top of the soil profile. As the shear bands propagated upwards, to zones of lower stress, these strain localisations tended towards the centre of the model at a greater angle of inclination, corresponding to the higher angles of dilatancy. The stark differences noted between the shear band propagation results for tests undertaken at 1g and 75g

highlight the importance of undertaking centrifuge testing when overburden stress effects are significant.

From Evans (1983), it is assumed that the angle of dilation is directly related to the angle formed by the shear band to the vertical. Figure 2-12 (a) presents a shear strain localisation pattern, representative of the trapdoor experiment results obtained by Dewoolkar et al. (2007), from tests conducted in the centrifuge at an H/B ratio of two. For tests undertaken in the centrifuge, the corresponding stress profile of the soil is shown in Figure 2-12 (b).

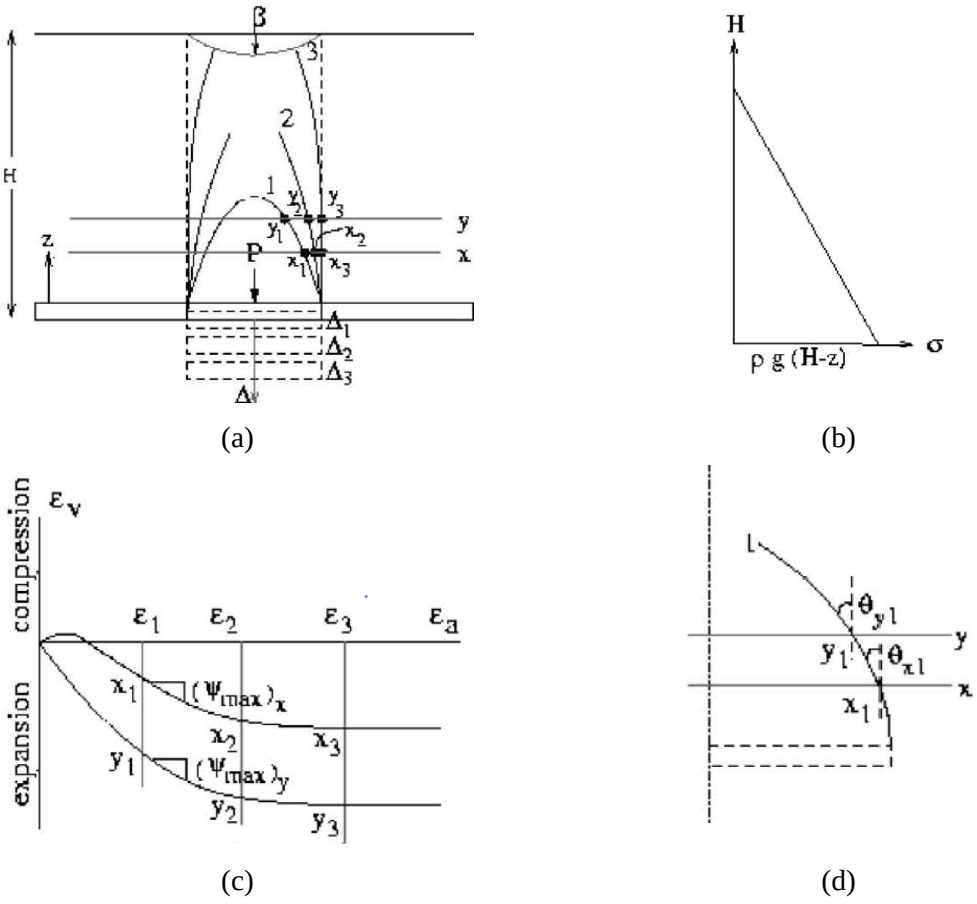

Figure 2-12: Qualitative results for a trapdoor experiment undertaken in the centrifuge: (a) shear strain deformation pattern (b) corresponding stress profile (c) triaxial test results at confined stresses corresponding to points x and y and (d) magnification of the angle between the shear band and the vertical (Dewoolkar et al., 2007)

The variables in Figure 2-12 (a), x and y, represent locations in the soil profile and were chosen, as such, to investigate the effects of the stress level on the shape of the shear bands as the angle of dilation is known to reduce with an increase in stress level (Bolton, 1986). Dewoolkar et al. (2007) noted that the secondary shear band only initiated after the first shear band had stopped propagating and therefore deduced that the shear strains at all points along the shear band are of approximately equal magnitude. The graph in Figure 2-12 (c) plots the volumetric (ϵ_v) versus shear strain (ϵ_a) results obtained from triaxial tests undertaken at confining stresses corresponding to positions x and y. For the initial shear

band, at a trapdoor displacement of Δ_1, the corresponding shear strain is ϵ_1. From Figure 2-12 (c), the dilatancy angles, given by the tangent gradient of ϵ_a:ϵ_v, show that for x_1 and y_1, at the respective stresses for positions x and y, the angle of dilation at the point y_1 is greater than the angle of dilation at point x_1 due to the significant stress difference between the two points in the soil profile. Furthermore, the lower stress value at y_1 corresponds to a greater inclination of the shear band than at x_1 as shown in Figure 2-12 (d).

As the trapdoor is lowered to Δ_2, the shear strain in the shear band corresponds to ϵ_2 and the secondary shear band appears to expand towards the vertical. The angles of dilation observed for x_2 and y_2 correspond to the reduced angle of inclination of the secondary shear band to the vertical. When zero dilatancy is recorded at the critical state of the soil, no volumetric change is noted. Zero soil dilation corresponds to the final shear band which should theoretically be vertical but may show slight curvature as observed and depicted in Figure 2-12 (a) (Dewoolkar et al., 2007).

In summary, the development of failure surfaces which form as a result of shear displacement during trapdoor lowering, as shown in Figure 2-12 (a), bring the soil along the failure zone to critical state. This corresponds to a reduction in the dilation angle from x_1 at the commencement of trapdoor lowering, to x_3 or zero, for large trapdoor displacements.

Figure 2-13 (a) represents the load-displacement behaviour of the trapdoor, corresponding to the trapdoor displacement and shear bands presented in Figure 2-12 (a). At a trapdoor displacement of Δ_1, corresponding to the first shear band, the load on the trapdoor drops from the geostatic load, corresponding to zero trapdoor displacement, to the minimum load (P_{min}) applied to the trapdoor during the trapdoor lowering exercise. This state is referred to as *maximum arching* and it occurs at relative trapdoor displacements (δ/B or Δ/B) of approximately 1 to 2%. As the trapdoor is lowered to Δ_2, a redistribution of stresses in the soil takes place, while maintaining a kinematically admissible mechanism. A slight increase in the load on the trapdoor is measured as a greater soil mass is influenced by the trapdoor displacement, as shown by the second shear band in Figure 2-12 (a). After considerable trapdoor displacement (Δ_3), the soil mass displaces along with the trapdoor, forming vertical shear bands which propagate from the edge of the trapdoor. This final state is termed *minimum arching* and it coincides with the final asymptotic load value (P_{ult}) in Figure 2-13 (a).

A qualitative surface settlement (β) vs trapdoor displacement (Δ) graph, with two distinct gradients indicating the rate of change in surface settlement with an increase in trapdoor displacement, is presented in Figure 2-13 (b). Dewoolkar et al. (2007) reported that the two surface settlement gradients are separated by a deflection point (or point of slope change) corresponding to Point 3 in Figure 2-13 (a). The shallow gradient $\left(\frac{\delta\beta}{\delta\Delta}\right)_1$ corresponds to the portion of the experiment where shear bands have not reached the surface whereas the second, steeper gradient $\left(\frac{\delta\beta}{\delta\Delta}\right)_2$ represents the increase in surface

settlement after the two vertical shear bands, propagating from the edges of the trapdoor, have formed and propagated to the surface of the overburden material (Point 3 in Figure 2-12 (a)).

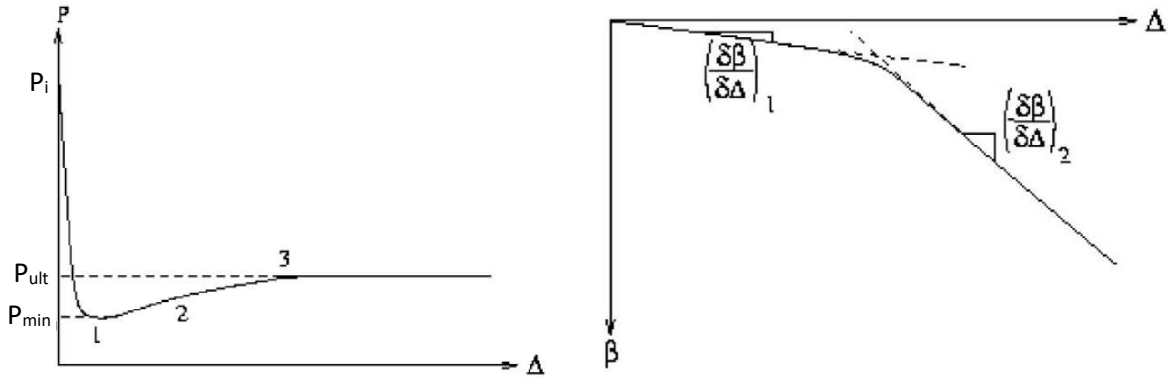

(a) (b)

Figure 2-13: Qualitative (a) load-displacement and (b) surface settlement behaviour during a trapdoor experiment (Dewoolkar et al., 2007)

2.3.3.2 Trapdoor deformation mechanisms: Costa et al. (2009)

Costa et al. (2009) conducted several trapdoor experiments to investigate the failure mechanisms associated with a deep trapdoor, in both the longitudinal and transverse directions of the model. For the investigation of failure patterns generated in the longitudinal direction, six trapdoor experiments were undertaken at a relative soil density of 85%. Three of the tests were conducted in a centrifuge at 45g (Figure 2-14 (a) to (c)) and three were conducted under normal gravity (Figure 2-14 (d) to (f)), at relative trapdoor displacements of 14%, 29% and 57% for both sets of tests. The relative trapdoor displacement is given by trapdoor displacement (δ) divided by the maximum trapdoor width (B_{max} = 35 mm).

The results in Figure 2-14 show that a single failure surface propagates from the corners of the trapdoor, at the soil's angle of dilation to the vertical, for each of the six stress and displacement combinations. It is further observed that the failure surfaces for the tests carried out at 1g show much greater curvature (and therefore larger variations of θ_i) than those conducted in the centrifuge. Costa et al. (2009) attribute this finding to the larger difference between peak and residual angles of dilation for a soil at a lower confining stress than for those at a higher confining stress. The straight failure curves observed in the centrifuge failure patterns are also accredited to the comparatively small variations in the dilatancy ratio (de_v / de_a) recorded for confining stresses greater than 35 kPa. Significantly larger values for the dilatancy ratio are recorded at lower confining pressures. The angle between the failure surface and the vertical at the trapdoor edge (θ_i) decreases with increasing displacement of the trapdoor. Conversely, the maximum height of the failure surface (h_v) increases with increasing trapdoor displacement. This was found to correspond to the results reported by Dewoolkar et al. (2007) which show that the effects of dilation decrease with an increase in shearing of the material as the trapdoor displaces downwards.

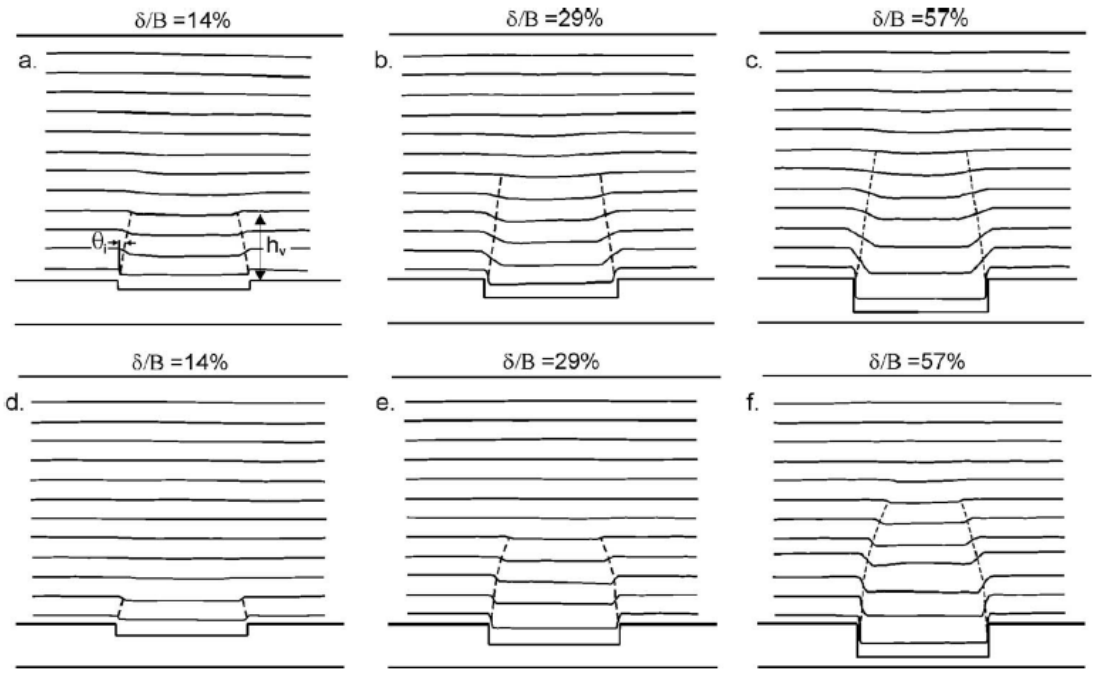

Figure 2-14: Failure surfaces in the longitudinal direction of the models (Costa et al., 2009)

Figure 2-15 (a) shows a plan view of the trapdoor model setup and the central transverse section is indicated by cross-section S1. Upon investigation of the failure patterns formed in the transverse direction, along section S1, Costa et al. (2009) noted that larger displacements of the trapdoor result in the development of failure surfaces beyond the vertical failure surface propagating from the trapdoor edge. These failure surfaces are depicted as 'external failure surfaces' in Figure 2-15 (b). As the trapdoor undergoes relatively large displacements, simulating the migration of soil into the cavity below, the soil adjacent to the trapdoor edge becomes unstable resulting in the development of external failure surfaces. As previously noted, the soil's dilatancy decreases with increasing shear strain (see Figure 2-12). Due to the significant shearing at Point O, the initial inclination of surface OD to the horizontal ($\theta_{e\text{-}OD}$) is greater than the angle between surface OE and the horizontal ($\theta_{e\text{-}OE}$). During trapdoor lowering this angle gradually decreases until it reaches the critical state friction angle (ϕ'_{cr}), which represents the shearing resistance of the soil at its loosest state. This angle also corresponds to the angle of repose of the soil (Costa et al., 2009).

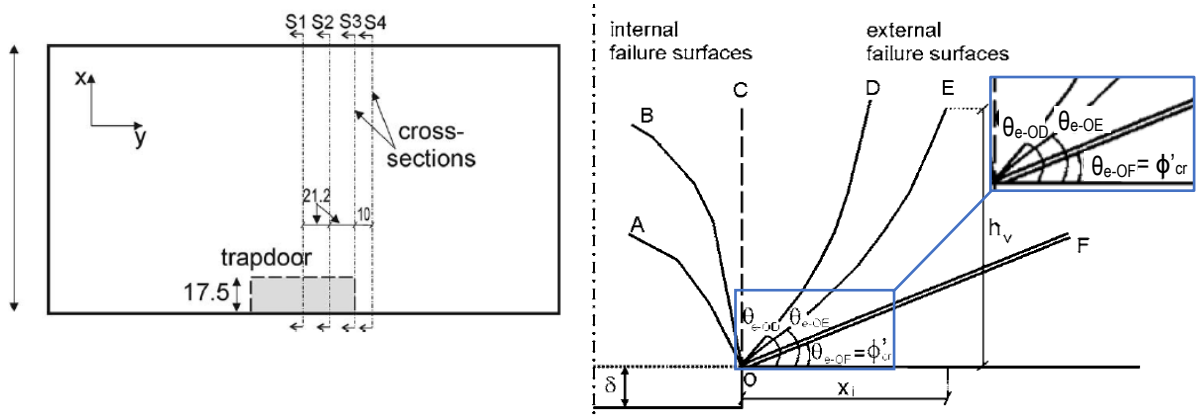

(a) (b)

Figure 2-15: (a) Plan view of trapdoor setup; (b) transverse direction shear failure patterns at S1 (Costa et al., 2009)

Figure 2-16 shows the transverse failure surfaces observed for a trapdoor test undertaken at gravitational accelerations of 45g (a) and 1g (b). A comparison of these two figures shows that a steeper external failure surface was observed under normal gravity than at elevated stress levels, which Costa et al. (2009) attributed to greater soil dilatancy observed at lower stress levels. External failure surfaces, which are evident in the failure patterns for the transverse direction, were recorded at an equivalent relative displacement of 114%. The maximum height (h_v) of the failure surfaces in the transverse direction were also found to be greater than the corresponding heights of the failure patterns in the longitudinal direction. It was therefore concluded that the differences in the failure patterns observed for the longitudinal and transverse sections of the model were due to the variation of the trapdoor width.

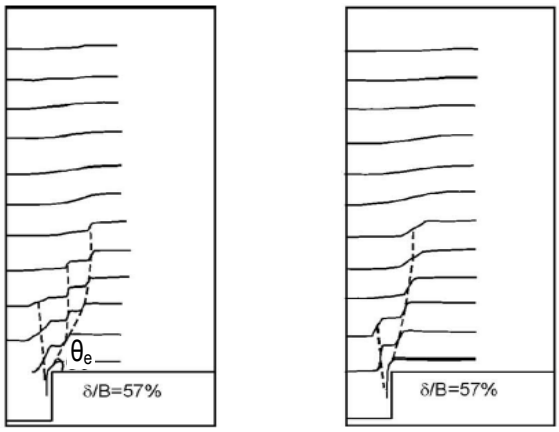

(a) (b)

Figure 2-16: Transverse shear band propagation at (a) 45g and (b) 1g (Costa et al., 2009)

A further investigation of the failure patterns was conducted with loose backfill, at a relative density of 42%, and dense backfill, at a relative density of 85%. Costa et al. (2009) found that the extent of the horizontal projection of the outer failure surface from the trapdoor edge (x_i) was almost three times

greater for the loose backfill than for the dense backfill, indicating that wider failure zones are expected for loose overburden material.

2.3.3.3 Trapdoor deformation mechanisms: Iglesia et al. (2014)

A plane strain, deep trapdoor experiment was carried out by Iglesia et al. (2014), to investigate the arching effect in granular material at an elevated acceleration. Based on the results of their own study, as well as those from literature, they proposed that small relative displacements of the trapdoor result in the formation of a curved arch. A triangular arch shape develops during medium relative trapdoor displacement, whereas large trapdoor displacements result in a rectangular arch where the entire rectangular prism above the trapdoor displaces downwards with the trapdoor along vertical failure surfaces. Figure 2-17 illustrates the progression of the simplified soil deformation patterns observed during increasing relative trapdoor displacement.

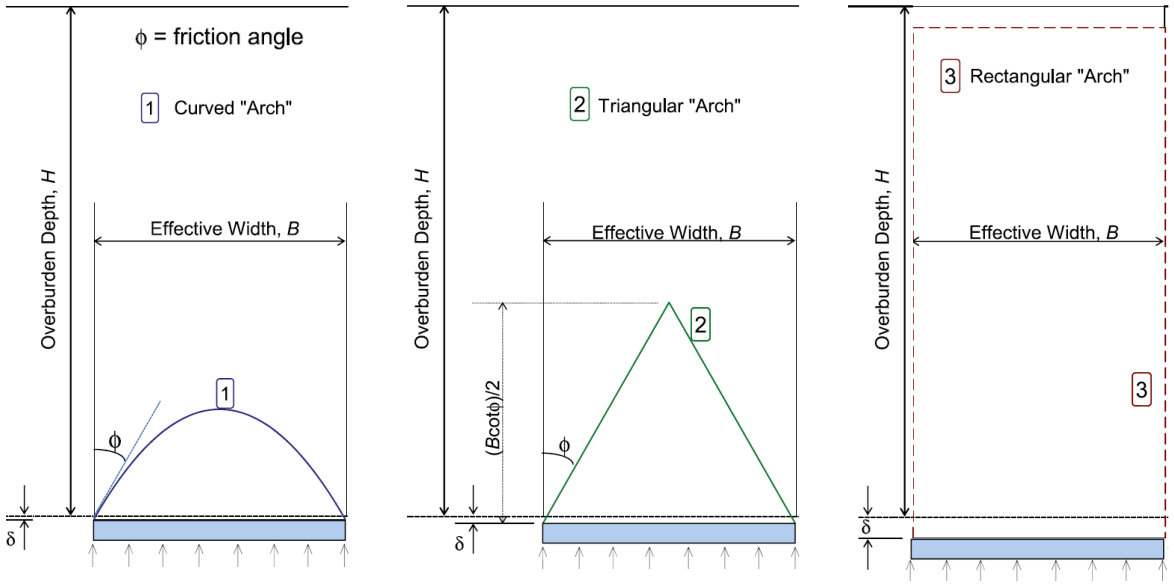

Figure 2-17: Typical failure patterns for (a) small (b) medium and (c) large relative trapdoor displacements (adapted from Iglesia et al., 2014)

2.3.3.4 Trapdoor deformation mechanisms: Rui et al. (2016-a)

Rui et al. (2016-a) conducted a study of load transfer in the fill of piled embankments by undertaking trapdoor experiments with multiple trapdoors. The overburden height, grain size, as well as trapdoor and pile widths were varied to investigate soil arching mechanisms and the related development of failure patterns. As reported by Dewoolkar et al. (2007) and several other researchers, triangular slip surfaces formed at very small displacements of the trapdoor. The testing programme implemented by Rui et al. (2016-a) included 16 tests, each comprising a different combination of variable parameters. The dimensional variables are denoted as follows:

H = Overburden/fill height

$s - a$ = Net spacing (equivalent to trapdoor width, B)

a = Pile width

$H/(s-a)$ = Relative trapdoor height (equivalent H/B ratio)

$(s-a)/a$ = Relative trapdoor width (equivalent B/a ratio)

Three development patterns were found to evolve from the initial triangular slip surfaces depending on the relative trapdoor width and relative trapdoor depth, as defined above. A tower-shaped development pattern was observed when $H/B \geq 2$ (i.e. deep trapdoor) and $B/a \leq 2$. These tower-shaped surfaces rise with increasing settlement of the trapdoor as shown in Figure 2-18 (a). Figure 2-18 (b) illustrates the triangular expanding pattern in which the initial triangular slip surfaces expand towards the vertical, while remaining straight lines. Both the tower-shaped and triangular expanding patterns result in vertical slip surfaces once sufficient settlement of the trapdoor has taken place. The final failure pattern is termed the equal settlement pattern and is shown in Figure 2-18 (c). This pattern occurs when $B/a >$ 3 and is characterised by vertical triangular surfaces which form immediately after the initial triangular ones. The fill material above the vertical and triangular slip surfaces tends to settle uniformly.

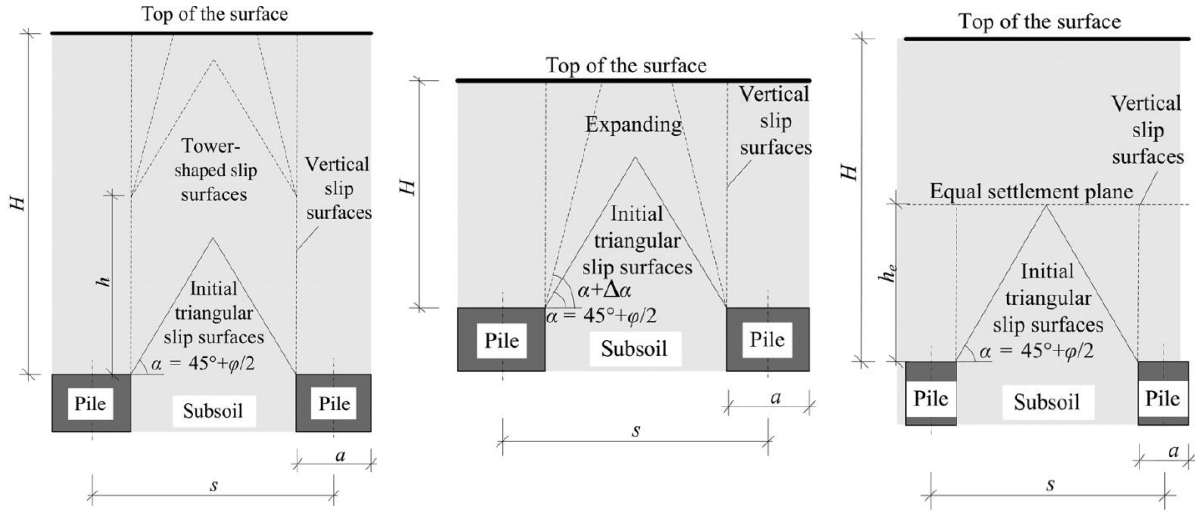

(a) (b) (c)

Figure 2-18: Soil failure patterns observed for unreinforced piled embankments: (a) tower-shaped development, (b) triangular expanding, and (c) equal settlement (Rui et al. 2016-a)

2.3.4 Shear band width

Roscoe (1970) reported that failure surfaces have a thickness of approximately ten times the mean particle size of the soil (D_{50}). Muir Wood (2002) recorded t/D_{50} ratios ranging between 7.3 and 18.5 for various experimental conditions, whereas Vardoulakis,et al. (1981) and Santichaianaint (2002) found that for shallow trapdoor systems the failure surface thickness yielded t/D_{50} values of between 10 and 21. Costa et al. (2009), however, observed that the measured t/D_{50} ratios for the longitudinal sections of

the models exceeded 30 for all the tests conducted; the only exception being the tests undertaken under normal gravitational conditions in dense backfill. It was further noted that the failure surface thickness increases with increasing displacement of the trapdoor. During shearing of the soil in the failure surface, dilatancy decreases which in turn results in the activation of some of the surrounding soil particles during the deformation process, thereby creating a wider shear band (Costa et al., 2009).

2.4. THE DISCRETE ELEMENT METHOD

2.4.1 Description and overview

The Discrete Element Method (DEM) is an explicit numerical method developed by Cundall & Strack (1979) to describe the mechanical response of an assembly of discrete elements (individual particles) to an applied force or disturbance. The classical DEM algorithm, used to describe the kinematics of each particle, can be divided into two primary stages. A force-displacement contact law is applied during the first phase to determine the interaction forces between particles at all inter-particle contacts. During the second stage of the algorithm the resulting acceleration of each particle is computed by applying Newton's second law of motion. These two stages, and their associated computations, are then alternated for the duration of the simulation. The bulk material response is directly related to the input parameters assigned to the individual particles in the assembly of elements and the discontinuous nature of granular assemblies is adequately represented by the particle boundaries (Donze et al., 2009). O'Sullivan (2011) notes that the method in inherently non-linear, even if the selected constitutive contact model (or force-displacement contact law described above) is linear. This is due to the change in contact conditions during the simulation.

2.4.2 Basic computational process

When a disturbance is applied to an assembly of discrete particles, the DEM is used to describe the propagation of the disturbance through the assembly, thus modelling the assembly's response to the disturbance. The speed and extent of the propagation through the assembly of particles is directly dependent on the input parameters assigned to the individual particles, which are used to describe the physical properties of the discrete particles. An important assumption when applying the DEM is that the particle accelerations are assumed to be constant within a single time step. The time step therefore needs to be small enough to ensure that the disturbance does not propagate beyond the immediate neighbour of the particle in question. This assumption facilitates numerical modelling of a dynamic problem using the DEM and ensures that particles do not pass through one another in highly dynamic simulations, such as a ball mill. The resultant force on a particle can therefore be determined solely by its interaction with its neighbouring particles (Cundall & Strack, 1979).

The fundamental procedure employed during a single time step of a DEM simulation is illustrated in Figure 2-19, followed by the associated computational sequence pioneered by Cundall & Strack (1979).

The figure depicts two discs, labelled X and Y, confined between two rigid walls at time step zero (t_0). A disturbance is applied to the system causing the walls to move towards each other at a constant velocity.

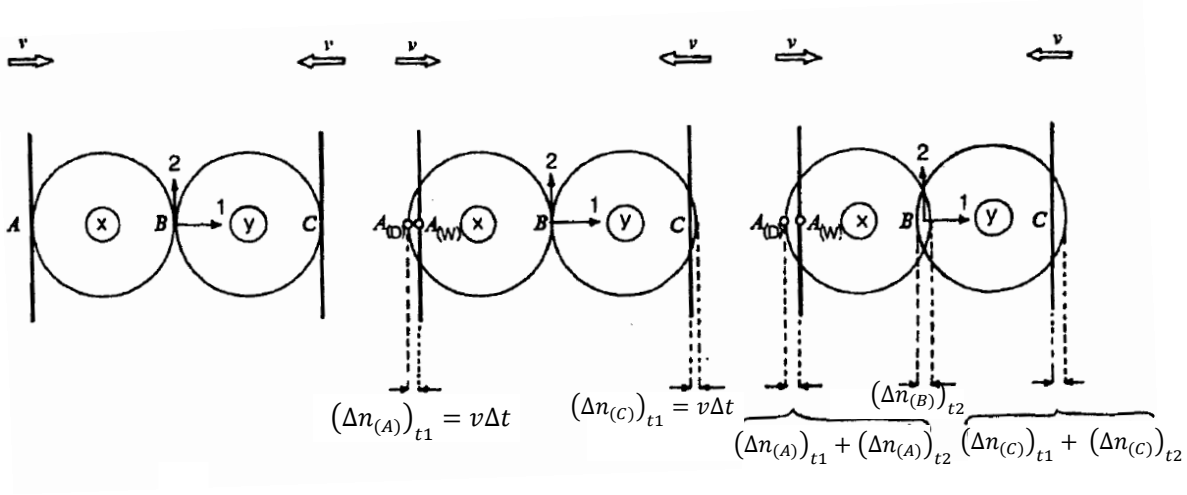

(a) (b) (c)

Figure 2-19: Calculation cycle for two discs compressed between rigid walls (the overlaps are exaggerated) at timesteps: (a) $t = t_0$; (b) $t = t_1 = t_0 + \Delta t$; and (c) $t = t_2 = t_0 + 2\Delta t$ (Cundall & Strack, 1979)

Step 1: At t_0, shown in Figure 2-19 (a), the discs are in contact with each other and with the walls adjacent to them. However, no contact forces exist between any of the elements.

Step 2: During the first time step, from t_0 to t_1, the walls move towards each other at a constant velocity, v. Figure 2-19 (b) represents the dynamic state of the discs at time step t_1 (where: $t_1 = t_0 + \Delta t$). The walls have moved, but the discs remained stationary as a result of the assumption that a disturbance cannot travel beyond a single element in one time step. The discs are assumed to be rigid and allow a small amount of overlap between particles to simulate the relative deformation of the particle surfaces. An overlap (Δn) is evident at the particle-wall contact points denoted by A and C, the magnitude of which is calculated by integrating the wall's velocity (v) over the duration of the time step (Δt), as shown in Equation 2-4 and Equation 2-5 for constant and linear variation in particle velocity, respectively.

$$(\Delta n)_{t1} = v.\Delta t \qquad \text{Equation 2-4}$$

$$(\Delta n)_{t1} = \int_{t_0}^{t_1} v.dt \qquad \text{Equation 2-5}$$

Step 3: A force-displacement law is used to derive the contact forces from the calculated displacements of the walls. The resulting normal force (F_n) is dependent on the normal stiffness (k_n) of the discs, as

indicated by the force-displacement law presented in Equation 2-6 and applied in Cundall & Strack's DEM formulation.

$$F_n = k_n.(\Delta n)_{t1} = k_n.v.\Delta t \qquad \text{Equation 2-6}$$

Step 4: From the resulting forces, the accelerations of discs X and Y are calculated by applying Newton's second law of motion, described in Equation 2-7, which states that the force experienced by an object is the product of its mass (m) and acceleration (a).

$$a = \frac{F_n}{m} \qquad \text{Equation 2-7}$$

Step 5: Equation 2-8 shows that the accelerations of the discs are then integrated over the time step interval to determine their new velocities at time step t_2. Similarly, a double integral of the disc accelerations yields the relative disc displacement increments at t_2.

$$(v)_{t2} = \left(\frac{F_n}{m}\right).\Delta t \qquad \text{Equation 2-8}$$

The example above describes the fundamental principles applied in the DEM for translational motion, based on only two particles. Where the numerical model contains an assembly of particles, the resultant force on each particle is equal to the vectoral sum of its contact forces. Additionally, a shear force (F_s) is introduced between particles as the resultant force may not act through the particle centroid, thereby creating a moment between the particles and initiating particle rotation. A force-displacement law, similar to that used to derive the normal contact forces, is used to calculate the shear or tangential contact forces, as described in Section 2.4.4. Once both normal and shear forces have been determined, Newton's second law of motion is used to calculate particle accelerations from the sum of the contact forces as well as the Moment of Inertia from the sum of the inter-particle moments (Cundall & Strack, 1979). Rotational particle motion is therefore introduced. Particle motion according to Newton's second law of motion, as well as selected contact models (force-displacement laws) used to calculate particle-particle interactions in DEM, are discussed in Section 2.4.3 and 2.4.4, respectively.

2.4.3 Particle motion

The fundamental DEM computational process described in the previous section shows that particle mechanics is essentially governed by Newton's second law of motion, as well as a force-displacement law or contact model. Based on Newton's second law of motion the resultant force acting on a particle determines its translational motion, as shown in Equation 2-9. The rotational motion of a particle is

governed by Equation 2-10 which can be used to calculate the resultant moment acting on a particle (Zhao, 2017).

$$m_i \frac{d^2}{dt^2}\overrightarrow{x_i} = m_i\vec{g} + \sum_{N_c}\left(\overrightarrow{f_{nc}} + \overrightarrow{f_{tc}}\right) + \overrightarrow{f_{fluid}} \quad \text{Equation 2-9}$$

$$I_i \frac{d}{dt}\overrightarrow{\omega_i} = \sum_{Nc} \overrightarrow{r_c} \times \overrightarrow{f_{tc}} + \overrightarrow{M_r} \quad \text{Equation 2-10}$$

Where:

m_i = Mass of particle *i*

$\overrightarrow{x_i}$ = Position of particle *i* centroid

$\vec{g}$ = Gravitational acceleration

$\overrightarrow{f_{nc}}$ = Normal inter-particle contact forces exerted by neighbouring particles

$\overrightarrow{f_{tc}}$ = Tangential inter-particle contact forces exerted by neighbouring particles

N_c = Number of neighbouring particles contacts of particle *i*

f_{fluid} = Interaction forces between fluid and particles

I_i = Moment of inertia about particle *i* centroid

$\overrightarrow{\omega_i}$ = Angular velocity of particle *i*

$\overrightarrow{r_c}$ = Vector from the particle mass centre to the contact point

$\overrightarrow{M_r}$ = Rolling resistant moment

2.4.4 Contact model

A force-displacement law or contact model is used to calculate the inter-particle contact forces based on the displacement, or overlap increment, representing the deformation of the rigid particles during contact (Wang, 2017). The effective stress within a cohesionless soil mass governs the behaviour of the material (Goldsmith, 1960). This stress is simulated by the inter-particle contact forces in DEM and therefore emphasises the importance of force-displacement law selection.

It is well-known that the basic contact model applied in DEM simulations is the linear spring-dashpot model shown in Figure 2-20 (Jiang & Yu, 2006 and Wang, 2017). The spring represents the elastic contact force between the two particles during a collision. The damping force, used to simulate energy dissipation due to collisions of the particles not being perfectly elastic, is represented by the dashpot. The damping force is also applied to maintain equilibrium in a quasi-static simulation (Yousefi & Ng, 2017). Figure 2-20 (a) and (b) illustrate the linear-spring dashpot contact model for two rigid particles in the normal and tangential directions, respectively. However, the maximum value of the shear force

is limited according to the Coulomb friction law, represented by the slider in Figure 2-20 (b). This contact model was adopted in Cundall & Strack's (1979) DEM formulation described in Section 2.4.2.

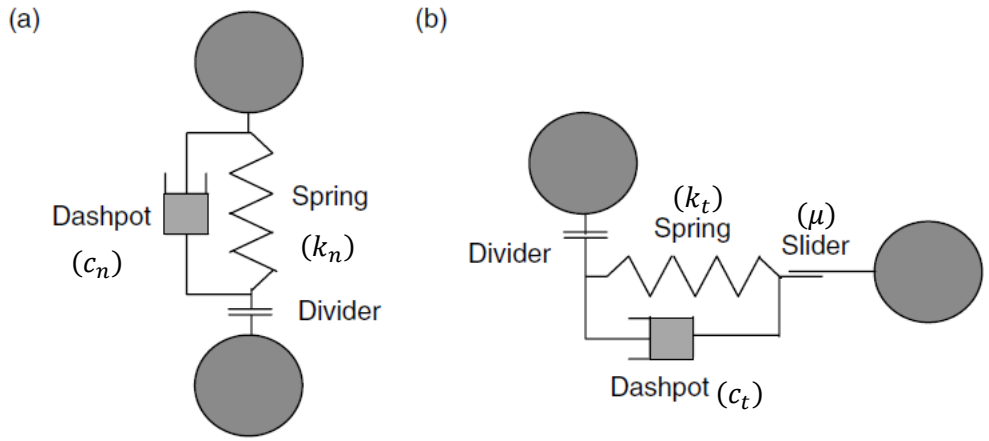

Figure 2-20: Standard contact models of two rigid discs used in DEM for the (a) normal direction and (b) tangential direction (adapted from Jiang & Yu, 2006)

The linear spring-dashpot or Hooke contact model assumes that the contact force increases linearly with an increase in inter-particle overlap. The normal and tangential inter-particle force formulations for the linear spring-dashpot model are described by Equation 2-11 and Equation 2-12, respectively. When inter-particle sliding of particle occurs, the tangential contact force is calculated incrementally according to Equation 2-12 up to a maximum tangential force according to Coulomb's friction law. The inter-particle friction coefficient, or slider in Figure 2-20 (b), dictates this maximum tangential contact force as denoted in Equation 2-13 (Wang, 2017).

$$F_n = -k_n.\Delta n_n + c_n.v_n \qquad \text{Equation 2-11}$$

$$F_t = \int_{t_0}^{t} k_t\,\Delta v_t.dt + c_t.\Delta v_t \qquad \text{Equation 2-12}$$

$$F_t \leq \mu F_n \qquad \text{Equation 2-13}$$

Where:

F_n = Normal contact force

F_t = Tangential contact (shear) force

k_n = Normal contact stiffness

k_t = Tangential contact stiffness

Δn_n = Normal inter-particle deformation (overlap)

c_n = Normal damping coefficient

c_t = Tangential damping coefficient

v_n = Normal inter-particle relative velocity

v_t = Tangential inter-particle relative velocity

μ = Inter-particle friction coefficient

The mechanical response of the linear spring dashpot contact model is illustrated in Figure 2-21 below. Figure 2-21 (a) presents the normal contact model and Figure 2-21 (b) the tangential contact model.

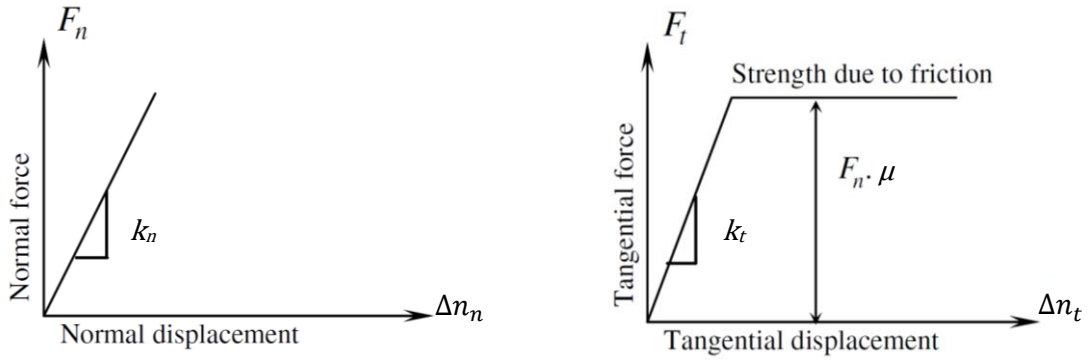

(a) (b)

Figure 2-21: (a) Normal and (b) tangential contact models (adapted from Belheine et al., 2009)

In addition to the linear spring-dashpot model, a second commonly used model is the non-linear Hertz-Mindlin contact model. Both contact models are included in most DEM software packages used to model the behaviour of cohesionless granular material, including LIGGGHTS (Kloss & Goniva, 2011) and EDEM (EDEM Software, 2012). According to Jimenez-Herrera et al. (2018) the non-linear Hertz-Mindlin contact model applies a normal contact force based on Hertz (1882) contact theory. Work by Mindlin & Deresiewicz (1953), which simplifies the Hertz contact theory, is used to derive the tangential contact force. The physical material properties, including the Young's Modulus, Poisson's Ratio and particle radius, are used as input parameters for the normal and shear inter-particle forces, as shown in Equation 2-14 and Equation 2-15 respectively. The normal damping coefficient, defined in

Equation 2-16, and the tangential damping coefficient are a function of the overlap (displacement) between particles, as well as the coefficient of restitution of the material (Wang, 2017).

$$F_n = \frac{2\sqrt{2}}{3} R^2 E^* \left(\frac{\Delta n_n}{R}\right)^{3/2} \quad \text{Equation 2-14}$$

$$F_t = \int_{t_0}^{t} 8G^* \sqrt{\frac{R\Delta n_n}{2}} \Delta v_t . dt \quad \text{Equation 2-15}$$

$$c_n = -\sqrt{\frac{10}{3}} \frac{ln(e_r)}{\sqrt{ln^2(e_r) + \pi^2}} \sqrt{E^* m} \left(\frac{R\Delta n_n}{2}\right)^{1/4} \quad \text{Equation 2-16}$$

Where:

F_n = Normal contact force
R = Particle radius
E^* = Effective Young's Modulus
Δn_n = Normal inter-particle deformation (overlap)
F_t = Tangential contact force (or F_s = Shear contact force)
G^* = Effective shear modulus
Δv_t = Tangential inter-particle relative velocity
c_n = Normal coefficient of damping
e_r = Coefficient of restitution
m = Particle mass

The linearity difference of the normal forces for the two force-displacement relationships is illustrated in Figure 2-22. Based on a review of the literature, there is no consensus on which contact model to employ when investigating the behaviour of granular material using DEM. Renzo & Maio (2004) used three contact models to simulate the elastic collision of a sphere with a flat wall, two of which were the linear spring-dashpot (LD) and Hertz-Mindlin (HM) contact models. They found that the macroscopic behaviour was best simulated by the simple linear model, but on the microscopic scale, the normal and tangential forces were better represented by the HM model.

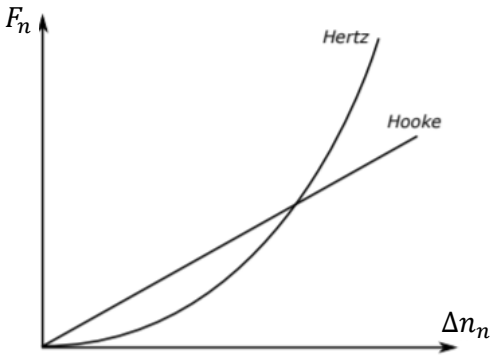

Figure 2-22: Force-displacement law comparison (normal force) (Wang, 2017)

2.4.5 Application of DEM in geotechnics

Continuum-based numerical models, such as the Finite Element or Finite Difference Methods (FEM or FDM, respectively), are often used to investigate the behaviour of geomaterials (Cundall, 2001). These methods assign a constitutive law to the soil continuum to describe its stress-strain response to an external force or disturbance. Granular materials are, however, inherently discontinuous and inhomogeneous in nature. The constituents of a soil fabric may include particles of varying size and shape, macropores, micropores and pore fluids which are all connected through inter-particle bonding (Jiang & Yu, 2006). O'Sullivan (2011) states that no single constitutive law can be used to model all states of a granular material, due to the complexity and range of physical regimes that these materials may exhibit.

Over and above the fact that a suitable stress-strain constitutive law for continuum modelling may not exist, it may also require numerous input parameters to define the relationship, thereby making it too complicated for application. The description of a discontinuity or localisation in a soil continuum is a complex problem. Progress has been made in this regard by explicitly including discontinuities in the model, however, remeshing and convergence challenges still occur during modelling (O'Sullivan, 2011). The primary limitations of including discontinuities in a continuum arise during large-scale slip of the materials (flow) or when the propagation of several cracks or fissures are expected to occur naturally (fragmentation), i.e. the position of the discontinuity cannot be predetermined (Donze et al., 2009).

The Discrete Element Method (DEM) is a non-linear dynamic analysis numerical method used to simulate the discontinuous nature of soil by assuming a simple force-displacement contact model and assigning parameters to each particle at particle-level (O'Sullivan, 2011). As the method is inherently non-linear, the complex physical and dynamic behaviour of a granular soil medium may therefore be captured without applying complex constitutive laws. An additional advantage of the DEM over experimental and other numerical models is that information regarding each particle's displacement and force can be obtained at any given point in time. A significant disadvantage of DEM is that it is

computationally expensive to simulate granular problems, particularly over long time periods or at large scales, where a large number of particles need to be modelled. Windows-Yule et al. (2016) regard the requirement of modelling assumptions, such as particle shape and contact model, as an additional disadvantage of applying DEM (Windows-Yule et al., 2016).

2.4.6 Critical time step and model calibration

In DEM, the time step refers to the time increment between each iteration of the calculation cycle in which the dynamic equilibrium of the individual particles is maintained. O'Sullivan (2011) highlights the importance of limiting the duration of the time step to ensure numerical stability of the system. Additionally, the duration of the time step should be small enough to restrict the influence of a particle's motion to its direct neighbours, as well as capture the changing contact conditions (in the form of moments and forces created during contact formation and separation). According to Malone & Xu (2008) the time step required to ensure numerical stability is usually expressed as a fraction of the natural frequency of an equivalent mass-spring system. The relationship used to determine this natural frequency, as well as the exact fraction required to ensure numerical stability, is, however, known to differ between researchers.

The critical time step is related to the particle stiffness and density when the linear spring-dashpot contact model is used. However, if a non-linear contact model is used, such as the Hertz-Mindlin model, the critical time step cannot be predetermined (Li et al., 2005). A formulation of the critical time step was derived by Thornton and Randall (1988) under the assumption that all energy in the system is transferred by means of Rayleigh waves. This formulation is presented in Equation 2-17.

$$\Delta t_c = \frac{\pi R^*}{0.8766 + 0.163v}\sqrt{\frac{\rho}{G}} \qquad \text{Equation 2-17}$$

Where:

Δt_c = Critical time step

R^* = Average particle radius

v = Poisson's Ratio

ρ = Particle density

G = Particle shear modulus

The small time step required to avoid numerical instability of a DEM simulation equates to a computationally expensive and time consuming numerical model. Three primary scaling techniques are often employed to reduce the computational cost of the simulation by artificially increasing the time

step (Yousefi & Ng, 2017). The scaling techniques include density, size and stiffness scaling. According to the critical time step defined in Equation 2-17, the time step increases with an increase in both particle density (ρ), or mass, as well as particle size (R*). Roessler & Katterfeld (2018) list exact scaling, coarse graining and scalping as three size scaling approaches used to reduce computational effort. Both the particle and system size are increased when the exact scaling approach is employed. The required critical time step will therefore increase due to the greater particle radius. In coarse graining, however, only the particle size is increased; the system size remains the same. Fewer particles are therefore modelled and the particle contacts are adapted to take the new geometrical setup into consideration. For the scalping approach, coarse graining is applied to the finer fraction of a bulk material. The particle size distribution is 'scalped' at a specific particle diameter. However, the coarser particles are modelled at realistic sizes.

When employing the linear spring-dashpot contact model, it is common practice to reduce the particle spring stiffness (which is related to the shear modulus) to reduce the critical time step. This causes the inter-particle overlap, or displacement, to increase. Based on a review of literature, Malone & Xu (2008) showed that the effect of an increase in particle overlap is dependent on the system being modelled. For example, for hopper discharge, Yuu et al. (1995) found very little difference in bulk material behaviour when varying the particle stiffness from 7.0E+03 to 70.0E+06 N/m. In contrast, the effect of reducing the particle stiffness (and increasing the particle overlap) was found to be significant when modelling the flow behaviour of cohesive powders (Moreno-Atanasio et al., 2007). In addition to these scaling techniques, the particle shape is often simplified by modelling spherical particles (3D) or discs in 2D simulations (Marigo & Stitt, 2015).

The input particle parameters for DEM need to be carefully selected for granular material behaviour to be predicted accurately. Windows-Yule et al. (2016) state that DEM simulations, and their results, are only of value to research and industry if they have been validated through a comparison of the results with the corresponding 'real-world' system results. Calibration is necessary due to the idealisations made in terms of particle shape, size and stiffness to reduce computational effort of a simulation (Coetzee, 2017). Coetzee (2017) compiled a review of the calibration techniques used to validate the particle parameters selected for a DEM simulation. He found that two primary approaches were used to calibrate models, namely the direct measurement approach, where the physical material properties are measured at contact level, and the bulk material measurement approach, where a trial-and-error iterative process is used to match the DEM results to experimental results. It was recommended that a combined approach be used where possible. He also highlighted the importance of selecting a validation experiment to which the relevant particle parameter would be sensitive. Li et al. (2015) and Marigo & Stitt (2015) noted that the calibration process should be carried out at the same stress conditions and flow regime as that of the granular material system being investigated.

2.5. DEM APPLICATION

2.5.1 CPU vs GPU: Computing power comparison

In addition to the scaling methods discussed in the previous section, the computational time restriction of DEM has also been mitigated by advances in the algorithm development and execution phases of discrete simulations. Windows-Yule et al. (2016) report that significant advances have been made in the development of contact detection algorithms used in DEM, as well as in the execution phase by utilising parallelised Graphical Processing Unit (GPU) clusters.

The GPU was originally developed to relieve the Core Processing Unit (CPU) of executing the computationally expensive graphic rendering process. During rendering millions of pixels are manipulated simultaneously to create realistic images on a computer screen. The primary constituents of a GPU are Arithmetic Logic Units or ALUs, which are designed to perform simple arithmetic operations. The GPU therefore has the capacity to perform simple arithmetic tasks in bulk. The purpose of the CPU, on the other hand, is to process complex logical operations needed to run the operating system (Govender et al., 2015 and NVIDIA, 2012).

A Streaming Multiprocessor (SM) in a GPU is the equivalent of a core in a CPU. A single SM on a Kepler GK110 GPU (used as an example) has the capacity to launch 2048 threads, each with the capability of performing a single arithmetic task or 'Single Instruction Multiple Data' (SIMD). This is opposed to a standard CPU core which can only launch two threads simultaneously. The threads launched by the CPU can, however, perform various complex tasks. The computing capacity of a multi-core CPU architecture is restricted due to the limited number of high-performance computing cores, usually 8 to 16, each of which are only able to launch two threads. The parallelism of the GPU architecture refers to its parallel processing capabilities when using the available threads on an SM, simultaneously. In order to access and take advantage of the parallelism of the GPU framework, the DEM algorithm needs to be completely decoupled and expressed as an SIMD task, so that identical instructions can be executed on each available thread. If the algorithm is not decoupled, the GPU would only be able to process one task per SM (Govender et al., 2015). Figure 2-23 (a) and (b) present a comparison of the processing capabilities of a CPU and GPU for different and identical incoming tasks, respectively.

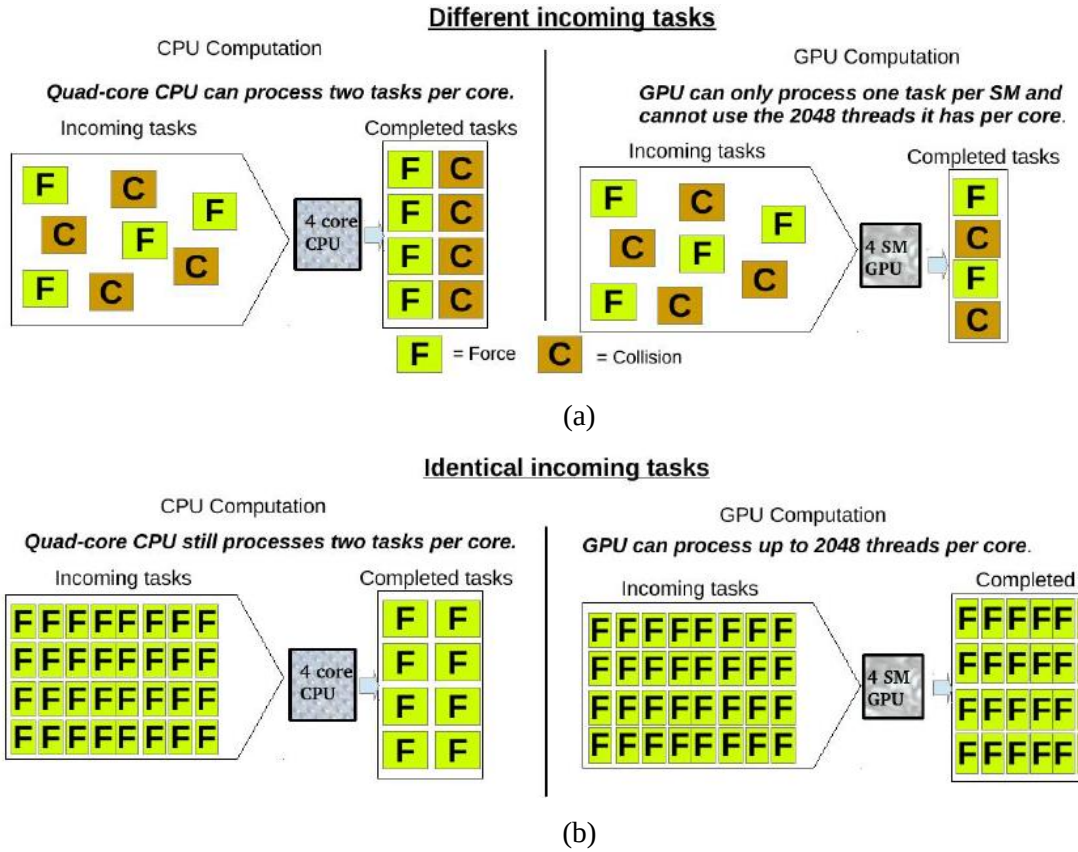

Figure 2-23: Comparison between CPU and GPU task processing for the case of (a) different incoming tasks and (b) identical incoming tasks (Govender et al., 2015)

2.5.2 Blaze-DEM

Blaze-DEM is a modular high-performance DEM research code that was developed by Govender (2015) at the University of Pretoria and at the Council for Scientific and Industrial Research (CSIR). The Blaze-DEM framework was developed for GPU architecture and therefore utilises the parallelism of a GPU cluster. Blaze-DEM is a three-dimensional (3D) simulation code that supports both spherical and polyhedral particles. Govender et al. (2015) emphasises the improved accuracy of a 3D simulation over a 2D simulation, as the moment of particles in the axial direction are considered in 3D, which is not the case for a 2D simulation. As a result of the GPU-based framework, a greater number of particles, as well as a variety of particle shapes, can be simulated using Blaze-DEM, improving the accuracy of its representation of reality. Single precision arithmetic is, however, used to conduct Blaze-DEM simulations on the GPU thereby limiting the range of values in a single calculation to $< 1 \times 10^{-6}$ (Govender et al., 2016).

The following assumptions are adopted in the Blaze-DEM code to ensure that the algorithm is completely decoupled, and that the parallel computing efficiency of the GPU framework can be accessed (Govender et al., 2014):

1. The discrete particles are rigid bodies, modelled as soft particles, with a single point of contact. In reality, no particle is completely rigid, and each particle would undergo local deformation during contact, but at a much smaller time scale than is necessary to simulate the bulk material behaviour. The application of a force-displacement constitutive law, at a greater timescale, is therefore deemed to be sufficient to model particle behaviour.
2. Two particles have a single point of contact, called a binary contact, at any given time.
3. The interactions are local and short-range. It is assumed that the particles are similar in size and that particle displacements during a single time step are very small. The resultant force acting on a particle may therefore be derived from the sum of the binary contact forces acting on the particle by its nearest neighbours during a single time step, as illustrated in Figure 2-24.
4. The assigned friction model is history independent and therefore non-incremental.
5. Particles are of a similar size.

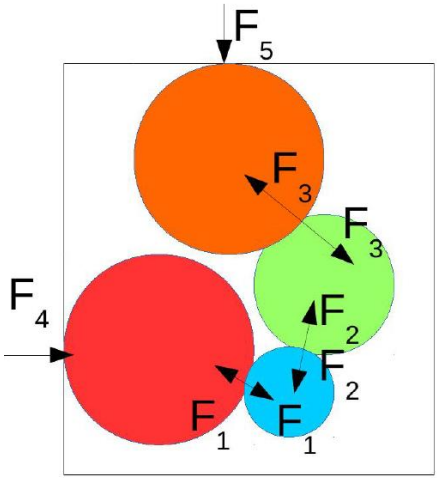

Figure 2-24: Blaze-DEM binary contact and force summation assumption (Govender et al., 2015)

The implementation procedure followed by the Blaze-DEM algorithm is summarised in Figure 2-25, below. Govender et al. (2015) attribute the bulk of the computational time to the neighbour search and collision detection. The collision detection phase is sub-divided into the broad and narrow phase contact detection methods, the latter being applied solely in the case of polyhedral particles. During the broad contact phase, a detection grid is used to identify particles which are potentially in contact, after which the narrow phase contact is implemented to determine whether actual contact was made. The collision is verified by determining the type of contact made and whether the resulting intersection volume is greater than zero. For polyhedral particles, contact types include vertex-face, face-face and edge-edge contact, amongst others (Govender et al., 2016).

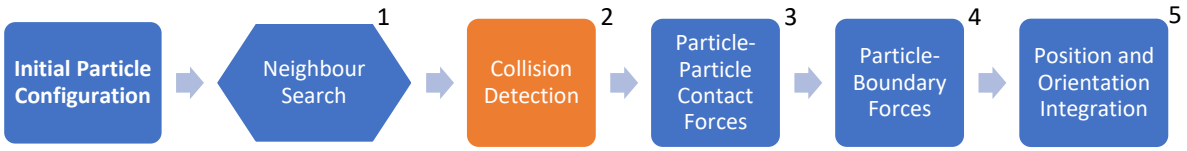

Figure 2-25: Blaze-DEM simulation procedure (adapted from Govender et al., 2014)

Figure 2-26 illustrates two of the primary contact modes experienced by convex polyhedral particles in DEM. Govender et al. (2014) as well as other authors (Mack et al., 2011; Nassauer & Liedke, 2013 and Boon et al., 2012) have all reported that the narrow phase contact detection accounts for approximately 70% of the simulation time in the DEM.

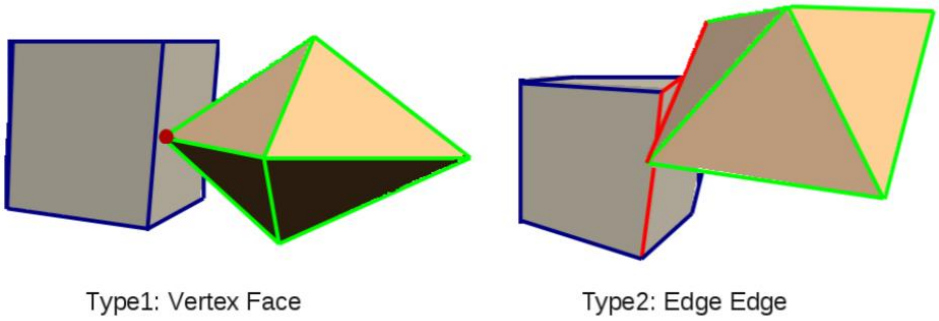

Figure 2-26: Two primary polyhedral particle contact types (Govender et al., 2014)

2.5.3 Verification of Blaze-DEM code

Govender et al. (2014) demonstrated the validity of the Blaze-DEM code by capturing and comparing the flow patterns of glass marbles in a plexiglass hopper to the flow patterns of an equivalent numerical simulation using Blaze-DEM. A total of 836 marbles were placed in the hopper, in alternating layers of green and blue marbles, with 132 marbles in each of the bottom five layers and 176 in the top layer. Due to the stochastic nature of the initial particle packing, the physical experiment could not be replicated exactly, however, a representative layout could be simulated to investigate qualitative similarities between the two experiments. Figure 2-27 shows the flow patterns of both experiments at one second intervals after the hopper was opened. They concluded that there was good agreement between the physical and numerical bulk flow behaviour results.

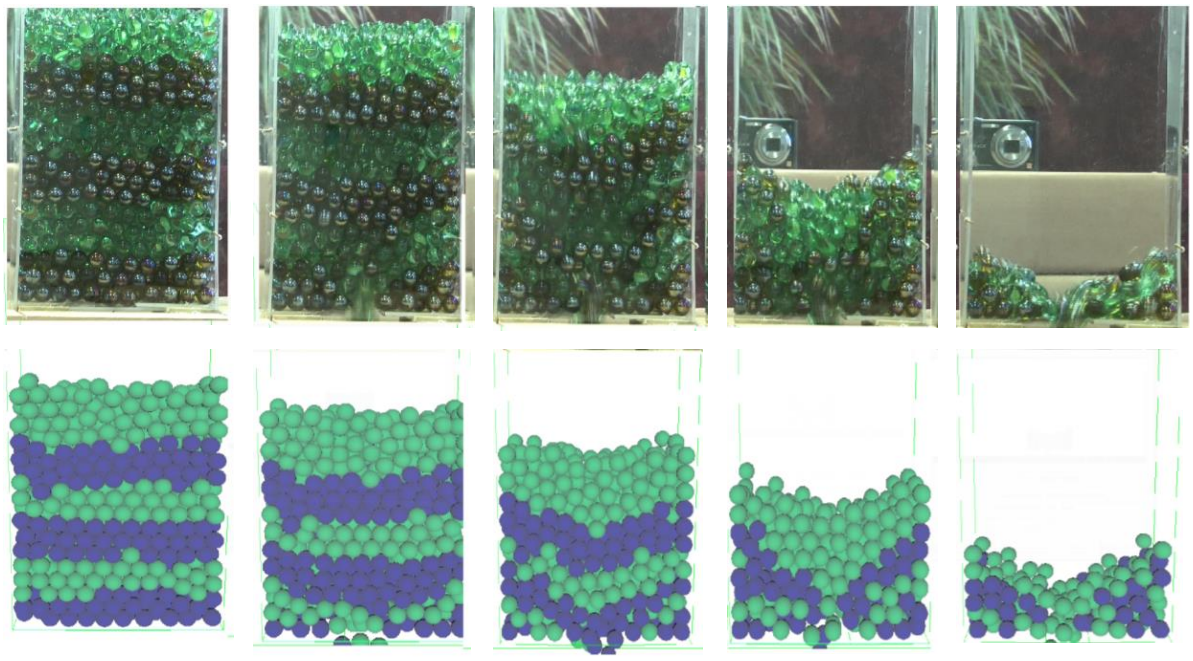

(a) (b) (c) (d) (e)

Figure 2-27: Validation of Blaze-DEM by means of experimental hopper flow comparisons at (a) t = 0 (b) t = 1.0 (c) t = 2.0 (d) t = 3.0 and (e) t = 5.0 seconds (Govender et al., 2014)

Further validation of the GPU-based Blaze-DEM is presented by Govender et al. (2015). The DEM simulation of a mill charge was undertaken using both 2D and 3D versions of the code. Mill charge profiles and power draw comparisons were made using Millsoft (a CPU-base DEM code) and pilot scale physical experiments. Figure 2-28 presents a comparison of 2D charge profile results for a 55 cm diameter mill and steel balls with a radius of 2.2 cm, at 40.81 rpm, which is 70% of the critical mill speed. The charge profiles shown in Figure 2-28 indicate good agreement between the Blaze-DEM, Millsoft and experimental results.

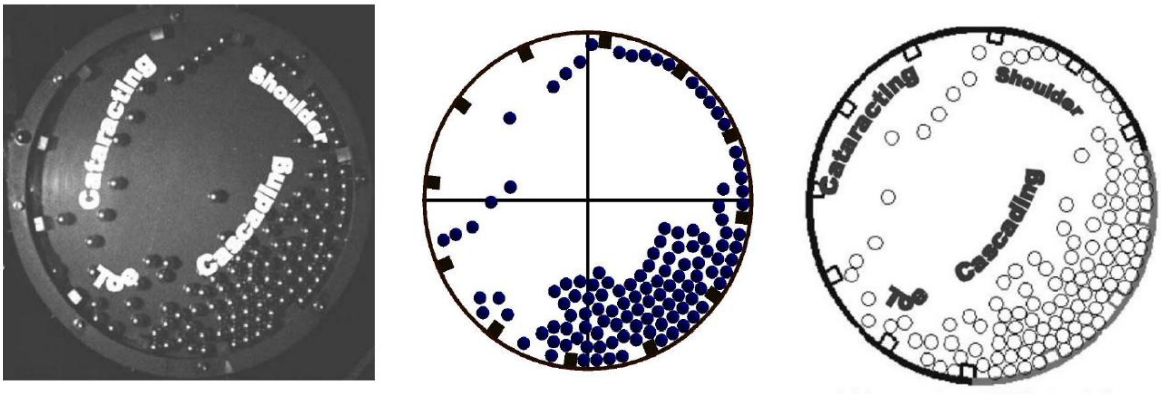

(a) (b) (c)

Figure 2-28: Comparison of mill charge profiles for (a) Physical experiment (b) Blaze-DEM (GPU) and (c) Millsoft (CPU) (Govender et al., 2015)

The results from Figure 2-27 and Figure 2-28 illustrate the findings of two of the experiments used to validate the Blaze-DEM code developed for a GPU framework. Govender et al. (2016) conclude that Blaze-DEM has been validated successfully against both physical experiments and established CPU DEM codes.

Govender et al. (2016) states that the primary benefits of Blaze-DEM are: (1) Increasing the number of particles in a simulation and (2) modelling of polyhedral particles, all within a reasonable time frame. Table 2-3 lists a comparison of computational times required by various codes for a gravity stacking simulation. The computational advantage of using a GPU-based code is emphasised in the results below.

Table 2-3: CPU and GPU DEM codes comparisons for polyhedral particles (Govender et al., 2016)

Author	Physics Fidelity	No. of Particles	Computational Time
BLOCKS (2013) - CPU	Highest	5 000	186 days
iDEM (2013) - CPU	Low	500 000	2.8 days
Blaze-DEM - GPU	High	32 000 000	32 minutes

2.5.4 Particle shape effects

Particle shape is computationally demanding to model using the DEM. The application of spherical particles is often favoured due to the ease and efficiency with which contact detection can be determined, as well as the fact that particle orientation is irrelevant and therefore does not need to be considered (Coetzee, 2017). When modelling granular materials with spherical particles, Belheine et al. (2009) emphasise that the shear strength will be too low, and results will not be realistic. Coetzee (2017) lists two methods in which particle shape can be simulated in DEM. The first is the application of a contact rolling friction parameter, also referred to as rolling resistance, and the second is the application of non-spherical particles, both of which simulate a greater shear strength of the bulk material.

Iwashita & Oda (1998) describe rolling resistance as the resistance to the relative rotation between two particles with a common contact. Ai et al. (2011) state that the terms ‘rolling friction model’ and ‘rolling resistance model’ are typically used when conducting dynamic and pseudo-static simulations, respectively. They further state that despite the name variation, both models can be expressed as a pair of torques which are applied at the contact. As detailed by both Ai et al. (2011) and Wensrich & Katterfeld (2012), several rolling resistance models can be applied in DEM.

Due to the irregular particle shape of real soil grains, the particle-particle contact point simulated in DEM (when spherical particles used) may differ significantly from the real contact point of the irregular shaped particles. The resultant rolling resistant moment (M_r) from the normal contact force opposes the direction of relative rotation of the two particles in contact (Zhao, 2017) as illustrated in Figure 2-29.

Zhao (2017) notes that the rolling moment component acts as an additional contact model to normal and tangential contact models during particle-particle interaction.

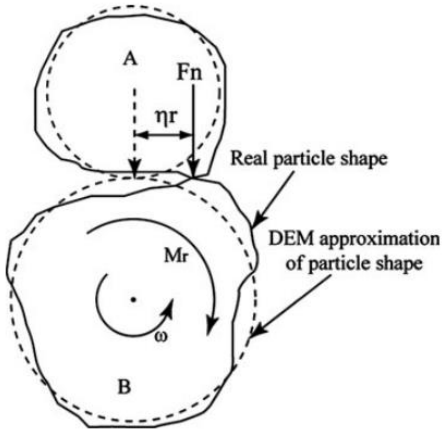

Figure 2-29: Real grain contact approximation using DEM (Zhao, 2017)

Figure 2-30 demonstrates the kinematics of two disks at time t and t +dt. The resisting moment (M_r) is a function of the incremental relative rotational angles ($d\theta_i$ and $d\theta_j$), as well as the rolling stiffness (k_r), as detailed by Equation 2-18 (Zhao, 2017 and Ai et al., 2011). Furthermore, Equation 2-19 describes the rolling stiffness parameter which governs the relationship between rolling resistance and relative particle rotation.

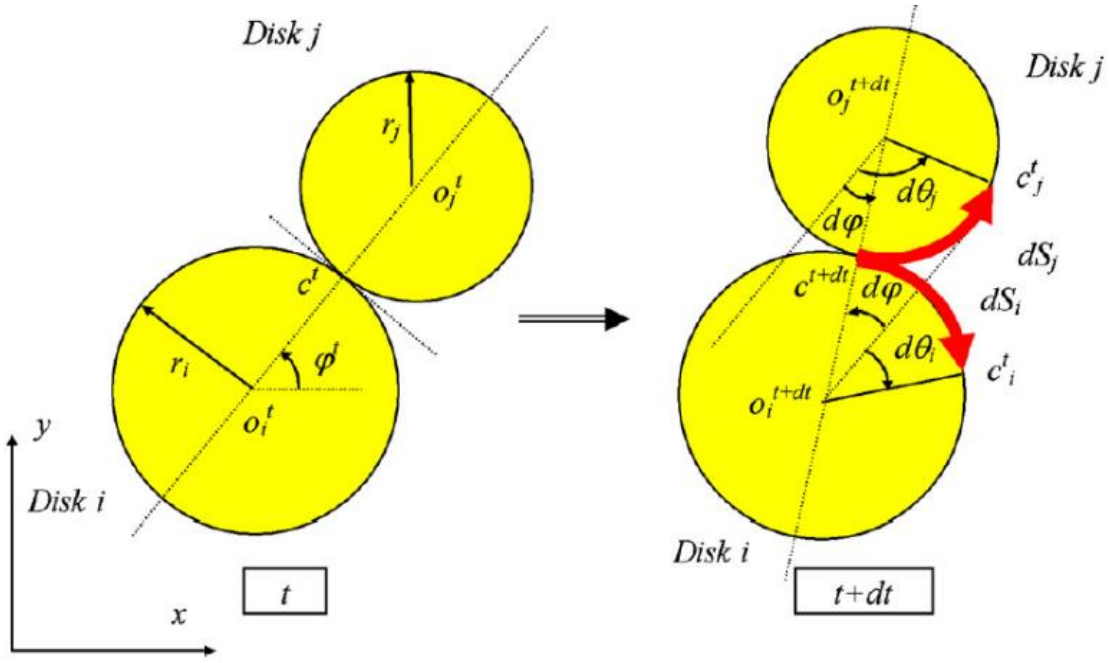

(a)

Figure 2-30: Kinematics of two disks at time t and t + dt (Ai et al, 2011; adapted from Jiang et al., 2005)

$$M_r^n = M_r^{n-1} + k_r.\Delta\theta_r$$ Equation 2-18

Where:

$$k_r = \beta k_s r^2$$ Equation 2-19

and:

M_r^n = Rolling moment at current iteration step

M_r^{n-1} = Rolling moment at previous iteration step

k_r = Rolling stiffness

k_s = Shear (or tangential, k_t) stiffness

β = Coefficient of rolling stiffness

$\Delta\theta_r$ = Relative rotational angle between two particles

r = Average particle radius at contact ($r = \frac{(r_i + r_j)}{2}$)

Figure 2-31 illustrates the contact model for rolling resistance. The rolling resistant moment is related to the relative rotational angle (see Figure 2-30) and therefore increases gradually as two particles come into contact and roll over one another, as indicated in Equation 2-18. As shown in Figure 2-31 and detailed in Equation 2-20, the maximum rolling moment (M_p) is dictated by the coefficient of plastic moment (η), also termed the coefficient of rolling friction or rolling resistance (Iwashita & Oda, 1998 and Ai et al., 2011).

$$M_p = \eta.r.|F_n|$$ Equation 2-20

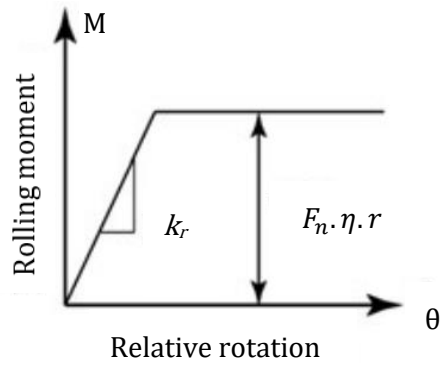

Figure 2-31: Rolling contact model (Zhao, 2017; adapted from Belheine et al., 2009)

Kozicki et al. (2014) applied rolling friction to the spherical particles in a DEM simulation of a drained triaxial compression test with cohesionless sand. They found that the bulk behaviour of the sand was

closely reproduced in the elastic, contraction, dilation and critical state/failure phases of the triaxial test, despite simplifications made in terms of particle shape, size and particle size distribution. Wensrich & Katterfeld (2012) also endorsed the application of rolling friction as a means of introducing shape-like behaviour but concluded that there is no physical basis for the value selected and assigned to this parameter. Their attempt to correlate the rolling friction to particle eccentricities was deemed unsuccessful. They attributed this to the fact that rolling friction always resists particle rotation, whereas particle shape may cause, as well as prohibit, rotation. A study was undertaken by Zhou et al. (2013) in which the macro- and micro-behaviour of 2D discs with rolling friction was compared to that of clumped 2D particles. They found that both materials exhibited greater shear strength and dilatancy (macroscopically), but distinct differences in the localisation patterns between the two materials were observed. These observations coincide with Obermayr et al. (2011) who stated that the application of rolling friction to spherical particles may produce realistic bulk material behaviour, but that the reliability of the micro-mechanical model results, in terms of shear band propagation, would be compromised.

The primary forms of non-spherical particles employed in DEM simulations are ellipsoids, super-quadrics, clumps (which comprise of clusters of spheres) and polyhedra (Coetzee, 2017). Figure 2-32 (a) to (d) illustrates examples of the above-mentioned particle shapes. The figures were adapted from: (a) Markauskas et al. (2010), (b) Sinnott & Cleary (2016), (c) Coetzee (2016) and (d) Höhner et al. (2013).

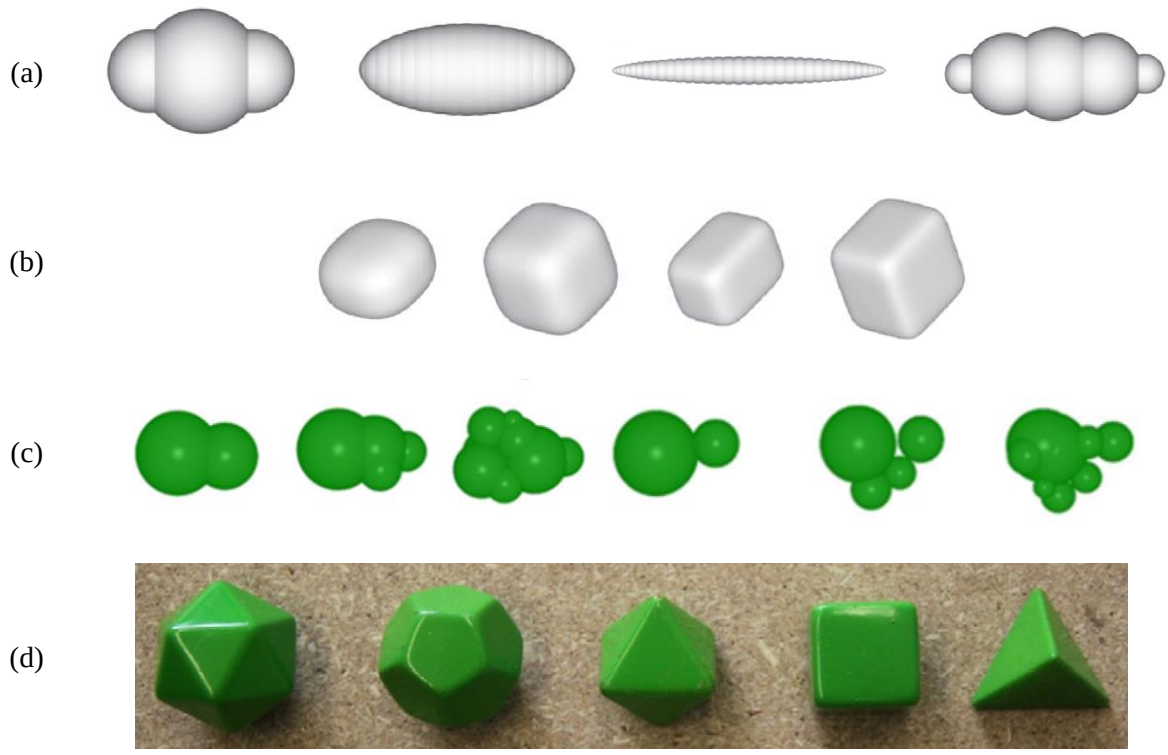

Figure 2-32: Primary particle shapes used in DEM: (a) Ellipsoids (b) Super-quadrics (c) Clumps and (d) Polyhedra (Coetzee, 2017)

In terms of computational effort, clumps have a great computational effort advantage over polyhedral particles, as the same efficient algorithms used for the contact detection and contact point processing of spheres are applied to clumps (Coetzee, 2017). As discussed in Section 2.5.2, DEM modelling with polyhedra is computationally expensive due to the narrow phase detection effort required resulting from the range of possible contact types. Polyhedral particles are often used to simulate the sharp edges and flat faces common to granular material particles. These particle attributes can also be simulated with clumps, however, a large number of spheres will be required to replicate them, which would increase the computational time significantly (Coetzee, 2017).

Höhner et al. (2013) investigated the difference in hopper flow behaviour between polyhedra with smoothed edges and those with sharp edges. He found that both particle types showed good agreement with the experimental results and that both types could therefore be used to simulate non-spherical particles within a DEM code. Further analysis of their results indicated that the sharp-edged polyhedral particles yielded higher angles of repose along the walls of the hopper and a greater resistance to hopper flow. This is in agreement with Govender et al. (2014) who demonstrated that the hopper discharge rate was much greater for spherical particles than for sharp-edged polyhedral particles. Höhner et al. (2013) deduced that the material with sharp-edged particle shapes, akin to angular sand grains, displayed a greater 'microstructural' or apparent shear strength.

2.6. NUMERICAL MODELLING OF TRAPDOOR EXPERIMENTS

A significant increase in the number of publications related to studying granular flow using the DEM has been recorded in recent times (Siegmann et al., 2017). Bym et al. (2013) indicate that the value of DEM lies in its ability to generate material behaviour results relating to both strains and stresses of the model material. In the past decade alone, the DEM has been used to investigate the deformation mechanisms of soil in response to tunnelling (Bym et al., 2013), reverse fault slip (Chang et al., 2013) and trapdoor experiments, including piled embankment applications (Rui et al., 2016-b), amongst others. A further application of the DEM has been to assess the accuracy of postulates inherent to continuum models (Rycroft et al., 2009) and the development of new, more applicable, constitutive models based on these results (Kamrin, 2010).

2.6.1 DEM deformation mechanisms (shear band formation)

Studies of the deformation mechanisms associated with trapdoor lowering, using both DEM and physical trapdoor experiments, have been undertaken by Chevalier et al. (2007 and 2012) and Rui et al. (2016-b) and are discussed below. Similarly, Bym et al. (2013) investigated the potential of using the DEM to study the ground deformation mechanisms associated with tunnelling. This research is briefly discussed as it also relates to subsurface cavity propagation and the arching mechanisms of soil.

2.6.1.1 Trapdoor deformation mechanisms: Chevalier et al. (2007 and 2012)

In their 2007 paper, Chevalier et al. investigated the application of the DEM to deformation mechanism and load-displacement characteristics associated with a trapdoor experiment. From their physical experiments, they observed three distinct soil deformation phases related to load transfer during trapdoor lowering. These phases are presented in Figure 2-33 and are related to the (a) maximum arching, (b) transitional phase and (c) final phase of load transfer. These three soil deformation phases correspond to the typical failure patterns observed by Iglesia et al. (2014) for small, medium and large trapdoor displacements (Section 2.3.3). The corresponding DEM displacement vectors, for the three phases, are illustrated in Figure 2-34 (a), (b) and (c), respectively, and were considered to validate the application of DEM to the study of trapdoor experiments.

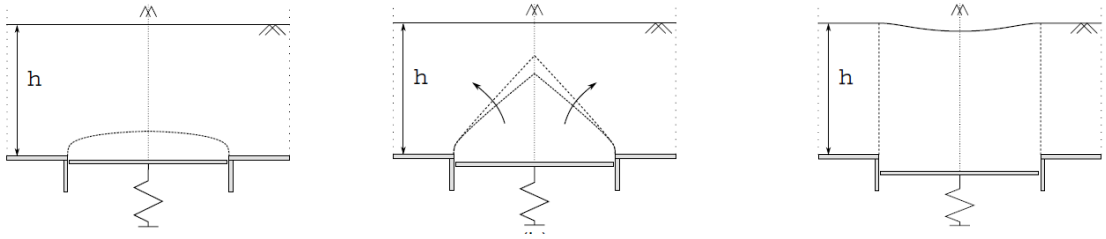

(a) (b) (c)

Figure 2-33: Physical trapdoor experiment failure patterns for (a) maximum arching (b) transitional phase and (c) final phase of load transfer for a shallow trapdoor (H/B = 1) (Chevalier et al., 2007)

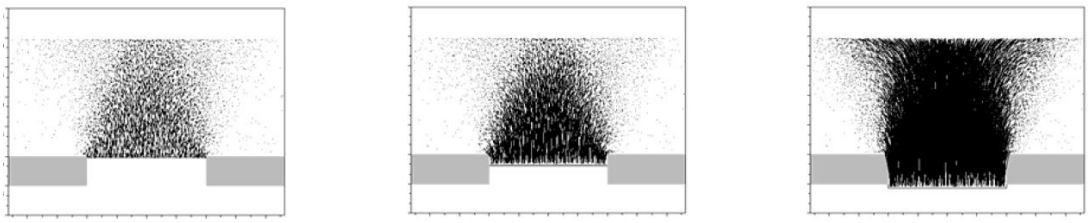

(a) (b) (c)

Figure 2-34: Displacement vector fields for the three phases of load transfer: (a) first phase (δ = 6 mm), (b) transitional phase (δ = 19 mm) and (c) final phase (δ = 57 mm) (Chevalier et al., 2007)

Using the DEM with spherical particles, Chevalier et al. (2007) also investigated the effect of both particle size and friction angle on the trapdoor load-displacement characteristics of the material. They found that there was virtually no difference in the load transfer mechanisms between the two materials with a particle size ratio (ratio of maximum to minimum particle diameter) of 1 to 1.25. However, a greater load reduction, i.e. greater arching, was observed for a material with a peak friction angle of 46.2° in comparison to a material with a peak friction angle of only 35.2°. They conclude that maximum arching related to transferral of load onto the trapdoor, observed at small trapdoor displacements, is related to the peak friction angle of the material. A greater reduction in load on the trapdoor will be

measured for a material with a greater peak friction angle than for that of a material with a comparatively smaller peak friction angle.

In a subsequent paper published by Chevalier et al. (2012), the effect of varying particle shape by means of clumps and friction angle were investigated, again in a shallow trapdoor setup with H/B = 1. The particle shapes used are displayed in Figure 2-35 and the variable *d* was used to denote the particle diameter. C-20 was used to refer to the clustered particle where the distance between the centroids of the two constituent particles is 20% of the particle diameter, the same derivation was used for C-95. Table 2-4 presents the physical and mechanical properties of the particle assemblies used in the particle shape and friction angle investigation.

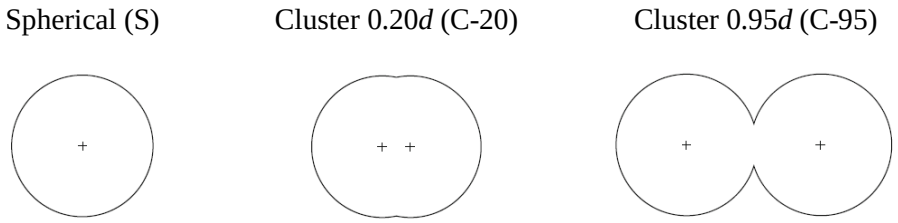

Figure 2-35: Particle shapes used in the study by Chevalier et al. (2012)

Table 2-4: Properties of the particle assemblies used in the particle shape and friction angle investigation (extracted from Chevalier et al., 2012)

Particle Assembly	**S1**	**S3**	**C-20-1**	**C-20-2**	**C-95-1**	**C-95-2**
Porosity, η	0.401	0.355	0.354	0.3	0.405	0.405
Young's Modulus, E (MPa)	3.39	7.25	7.09	13.78	4.95	5.88
Peak friction angle, ϕ_p (°)	24.5	37.1	37.2	49.0	35.2	46.2
Friction coefficient, μ	1.466	1.466	1.466	1.466	0.521	1.466

Figure 2-36 presents a comparison of the arching deformation patterns of particle types S3, C-20-1, and C-95-1, at maximum arching (first phase of load transfer). Significantly, the peak friction angles of the materials were almost identical. It was observed that no significant difference in the arch shape was evident with a given peak friction angle, regardless of the varying particle shape.

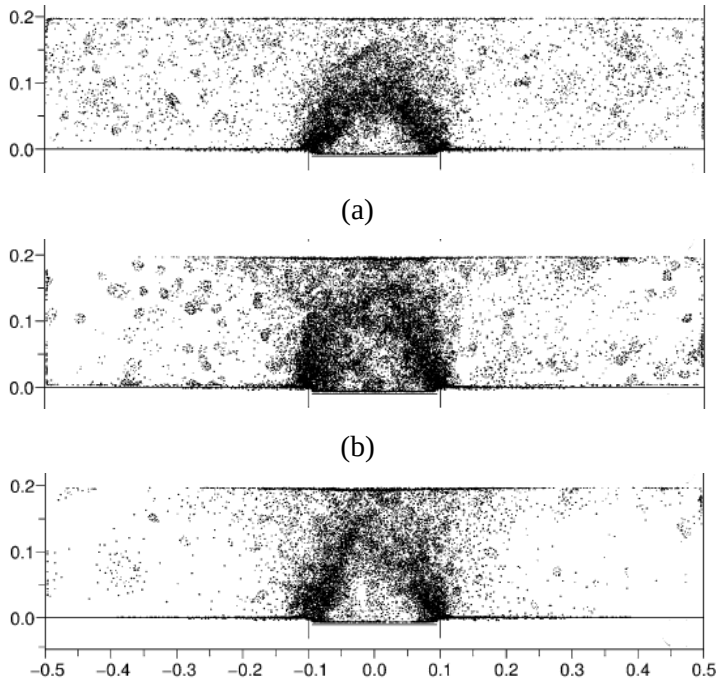

Figure 2-36: First phase deformation patterns for (a) C-95-1 with ϕ_p = 35.2°, (b) C-20-1 with ϕ_p = 37.2° and (c) S3 with ϕ_p = 37.1° (Chevalier et al., 2012)

Figure 2-37 presents a similar comparison using materials S1, C-95-1, and C-20-2. These deformation patterns present the maximum arching (i.e. first phase deformation patterns) of materials with peak friction angles which vary distinctly. Chevalier et al. (2012) noted that significant differences in both the arch geometry and shear band width of the three plots were observed as the arch of the material with the low friction angle yielded a higher arch with wider shear bands. The material with the highest peak friction angle had a comparatively narrower arch (shear bands) and the upper layers of the material were unaffected by the lowering of the trapdoor (i.e. cavity propagation had not reached the surface).

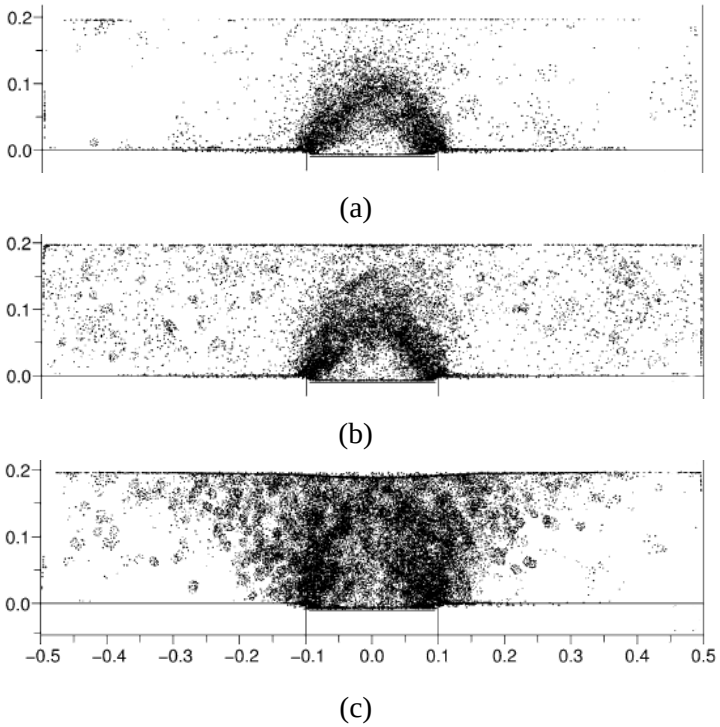

Figure 2-37: First phase deformation patterns for (a) C-20-2 with ϕ_p = 49.0°, (b) C-95-1 with ϕ_p = 35.2° and (c) S1 with ϕ_p = 24.5° (Chevalier et al., 2012)

Figure 2-38 illustrates the distribution of normal contact forces between particles at a trapdoor displacement of 10 mm (i.e. at the point of maximum arching). Small values of normal forces correspond to the thin black lines, whereas the thick white lines represent large normal forces between particles. From the figure below, as well as plots of the shear strains and principal stress directions presented in their paper, Chevalier et al. (2012) observed that an arch formed across the trapdoor and was grounded on the fixed base plate on either side of the trapdoor. The arch formation corresponded to the directions of the major principal stresses, varying from horizontal to vertical with depth, as proposed by Handy (1985), as well as the primary zones of shear strain.

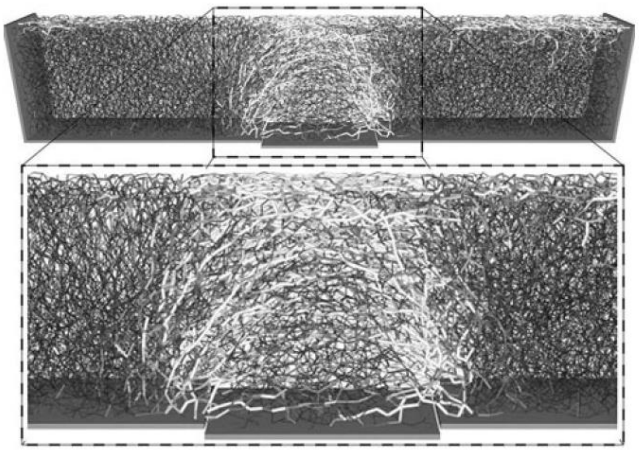

Figure 2-38: Force chain network for C-20 particle assemblies at 10 mm trapdoor displacement (Chevalier et al., 2012)

Chevalier et al. (2012) concluded that particle shape was a significant contributor to the shear strength of a material and therefore influenced the material's response to trapdoor lowering. However, the effect of different particle shapes on material response to trapdoor lowering was negligible when the materials had similar shear strength properties. They further noted that a stronger soil would arch sooner, resulting in a smaller arch geometry and narrower shear band width.

2.6.1.2 Trapdoor deformation mechanisms: Rui et al. (2016-b)

A similar study was undertaken by authors Rui et al. (2016-b). However, this discussion details the application of 2D DEM simulations undertaken by the authors to investigate the evolution of soil arching for a piled embankment. The aim of the study was to determine whether the DEM results support the observations from the physical multi-trapdoor experiment results, which show that three primary modes of soil arching exist and are governed by the geometric conditions of the test, namely the trapdoor width, beam width and fill height (see Section 2.3.3 for clarification of these dimensions). Figure 2-39 illustrates the three arching evolution patterns, namely the (a) triangular expanding pattern, (b) the tower-shaped evolution pattern and (c) the equal settlement pattern.

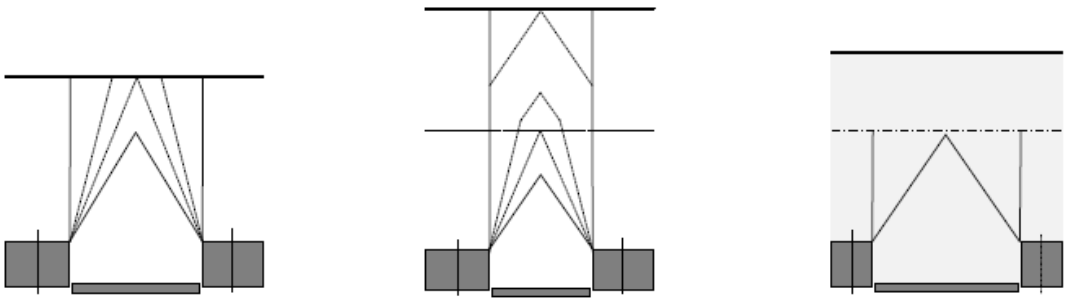

(a) (b) (c)

Figure 2-39: Soil arching evolution patterns for multi-trapdoor systems: (a) triangular expanding, (b) tower-shaped evolution and (c) equal settlement (Rui et al., 2016-b)

To reduce computational time, the particle size used in the 2D DEM simulations was made at least six times greater than that of the natural granular material (sand) used in the physical experiments. As the high shear strength of the natural sand could not be simulated using spherical particles, non-circular particle clumps comprising three (triangular particle clump) or four (square-shape particle clump) circular discs were used to simulate particle shape effects and achieve the required material strength.

Figure 2-40 presents three sets of results, each representing one of the soil arching evolution patterns shown in Figure 2-39, above. In each set of results, three arching evolution images are shown. These illustrate: (i) photos of the physical experiment results, (ii) PIV analysis results of the physical experiment, and the corresponding (iii) DEM simulation results for a fixed geometric setup and trapdoor displacement of 30 mm.

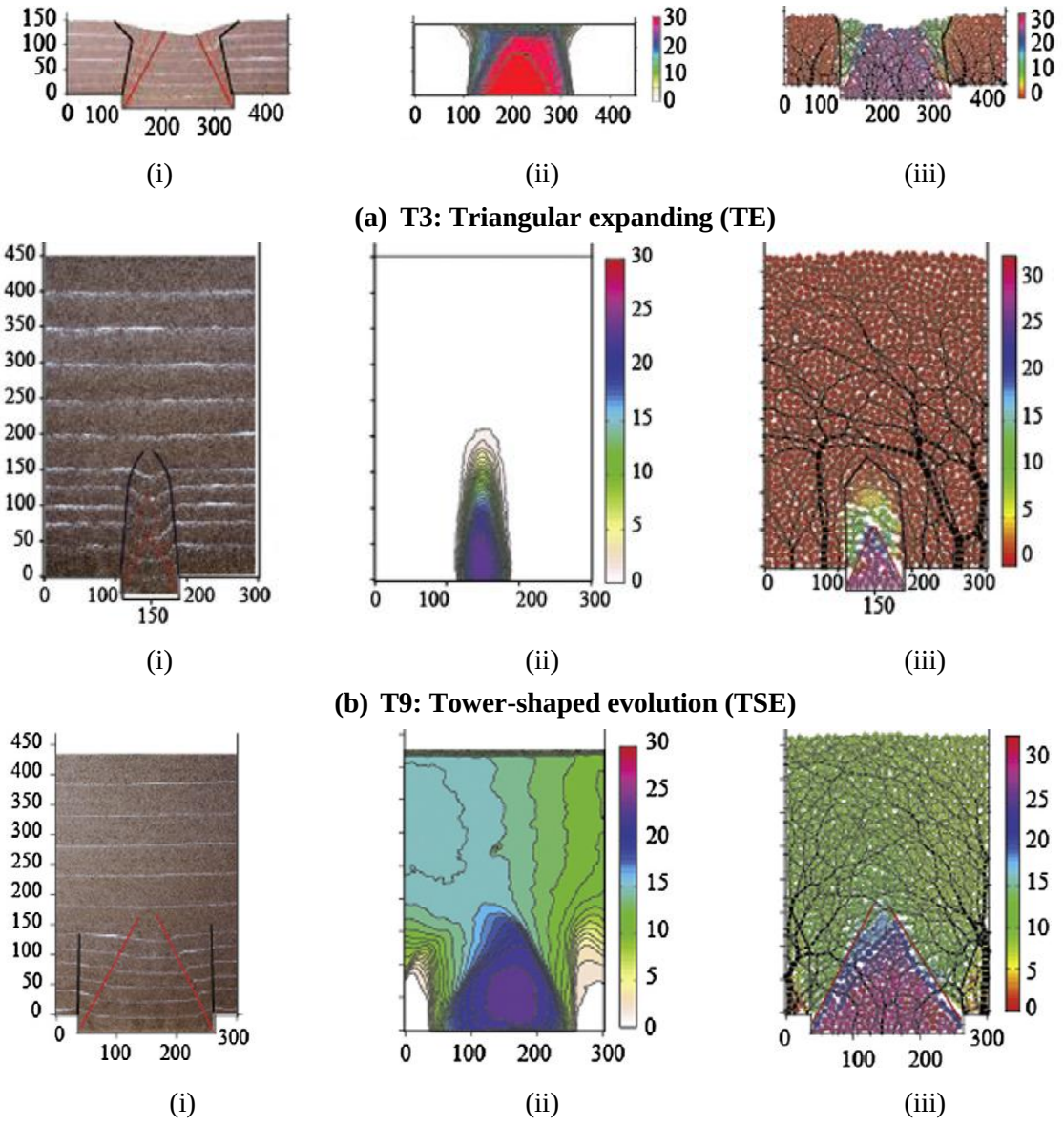

Figure 2-40: Comparison of physical experimental and DEM soil arching patterns for multi-trapdoor systems illustrated by: (i) physical experiment photographs, (ii) physical experiment PIV results and (iii) DEM simulations (30 mm trapdoor displacement) (Rui et al., 2016-b)

The authors found that the DEM simulations verify the conclusion, drawn from the physical experiment results, that three soil arching evolution patterns exist. Figure 2-41 summarises the geometric application conditions of the three arching evolution patterns. The points denoted by "T-" present the results of the DEM simulations conducted by Rui et al. (2016-b). The points emphasised by the red markers represent the test results shown in Figure 2-40 above. These results support the consensus that shallow and deep trapdoors are distinguished by an H/B ratio of two.

From the DEM simulation results, it was further concluded that a strong force chain network encompasses the triangular expanding and tower-shaped evolution patterns, while a weaker force chain in the deforming region supports the outer force chain (Rui et al., 2016-b).

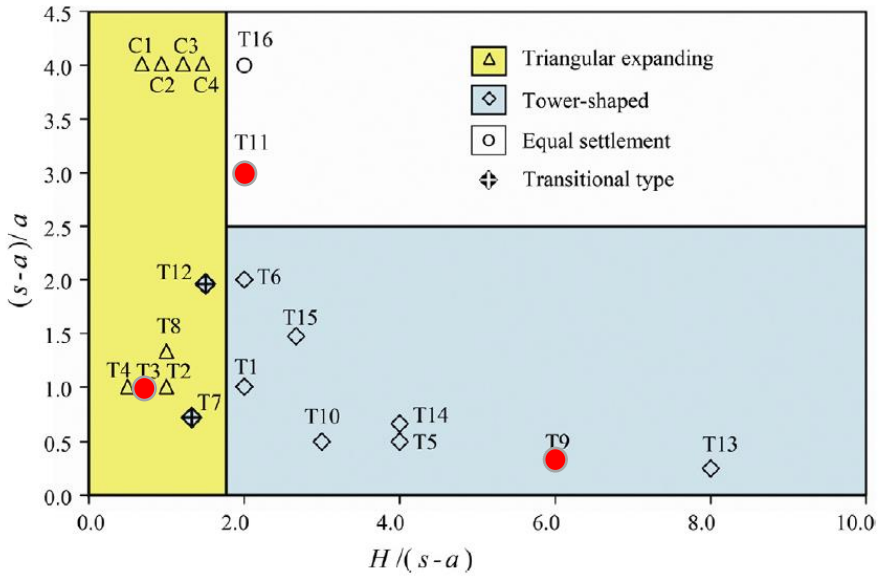

Figure 2-41: Geometric conditions applicable to each of the three arching evolution patterns (Rui et al., 2016-b)

2.6.1.3 Bym et al. (2013)

Bym et al. (2013) used a 2D DEM simulation, with 135 000 disk-shaped particles, to investigate the deformation mechanisms associated with staged excavation during tunnel construction. To simulate the staged excavation, a point sink system was created at the tunnel axis. During each excavation stage the ten particles closest to the tunnel axis (point sink) were deleted.

The nodal displacement vectors, after the excavation of 900 particles, are displayed in Figure 2-42 (a). From the vector plot, it is evident that the maximum vertical displacement occurs at the point sink and decreases with an increase in elevation. In contrast, the magnitude of horizontal deformation increases with increasing elevation above the tunnel axis. The deviatoric strain contours, presented in Figure 2-42 (b), were calculated by applying Delaunay triangulation to the particle centroids and using a linear displacement gradient (shape function) in each of the triangles. The strain contours show the formation of two outward-inclined zones with high deviatoric strain. These bands appear to be symmetrical about the vertical axis of the tunnel and bend upwards, towards the surface, higher up in the ground profile.

The authors conclude that the point-sink DEM model is a useful tool to provide insight into the mechanisms associated with the complex system of tunnel excavation.

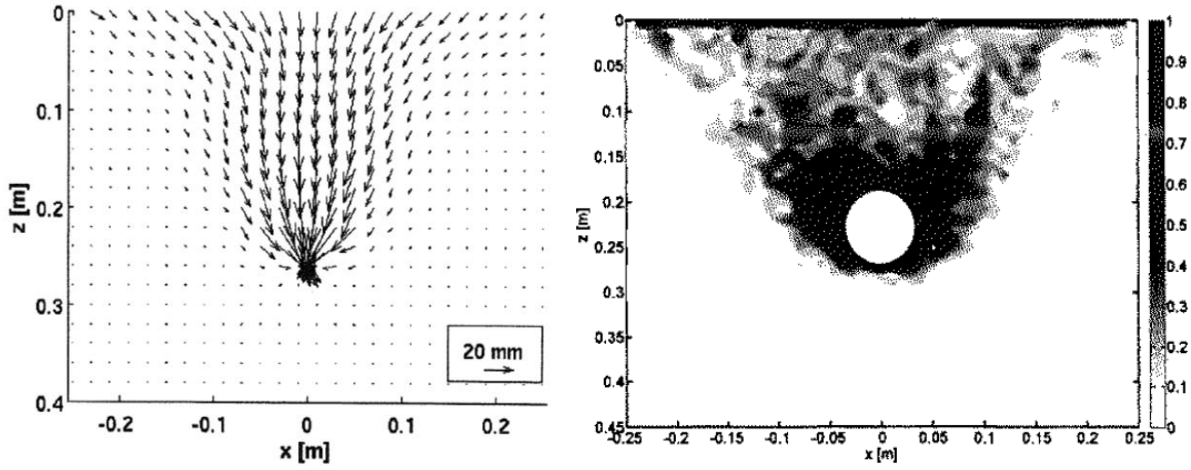

(a) (b)

Figure 2-42: (a) Displacement vector plot and (b) Deviatoric strain contour plot (Bym et al., 2013)

2.6.2 Foreword for DEM-based constitutive models

With the evolution of the DEM in recent years, inhomogeneities at particle level, such as complex networks of force chains, have shown that microscopic features of dense granular materials do not necessarily conform to the generally accepted continuum description of granular materials. This has brought into question the accuracy and applicability of employing continuum mechanics in the study of granular rheology. Based on this observation, Rycroft et al. (2009) assessed the deterministic relationships inherent to continuum mechanics and found that granular deformation or failure is dependent on both strain-rate and total strain. Their findings further confirmed several postulates which are characteristic of plastic flow theory, such as co-axiality, but disproved others, such as the assumption of an incipient Mohr-Coulomb (M.C.) yield criterion, proposing that the M.C. may not be the most applicable yield criterion to model failure of granular assemblies. Evidence was also found that co-directional flow may not be inherent to plastic behaviour of granular materials.

Based on the findings presented by Rycroft et al. (2009), Kamrin (2010) proposed a general 3D constitutive model for granular deformation during dense granular flow, with specific application to moderate shear, as expected in flowing chutes and hoppers. He used a granular elasticity model, proposed by Jiang et al. (2003), with a Drucker-Prager yield criterion (not Mohr-Coulomb), and combined it with a constitutive model proposed by Jop et al. (2006), which accounts for the plastic deformation of the granular material.

A comparison of Kamrin's (2010) non-linear elasto-plastic constitutive model for dense granular flow with the corresponding DEM solution for a flat-bottomed silo (based on numerical model results of Rycroft et al., 2009), is presented in Figure 2-43. The contours depict the plastic shearing rate of the material and the same colour scale is used in both plots. Good agreement is observed between the two models with the primary differences being attributed to box-averaging of the DEM model (a), causing

blurry output results. The elasto-plastic solution (b) presents intricate shear bands between the two primary shearing arms which fall inward, one-by-one, as time passes.

It is of interest to note that the behaviour of Kamrin's (2010) elasto-plastic material resembles the "onion-peeling" effect of cavity propagation proposed by Jennings et al. (1965). Both models further verify the material behaviour reported by Bym et al. (2013) which showed that two primary shearing arms extend from the edges of the orifice/point sink and bend towards the surface higher up in the soil profile.

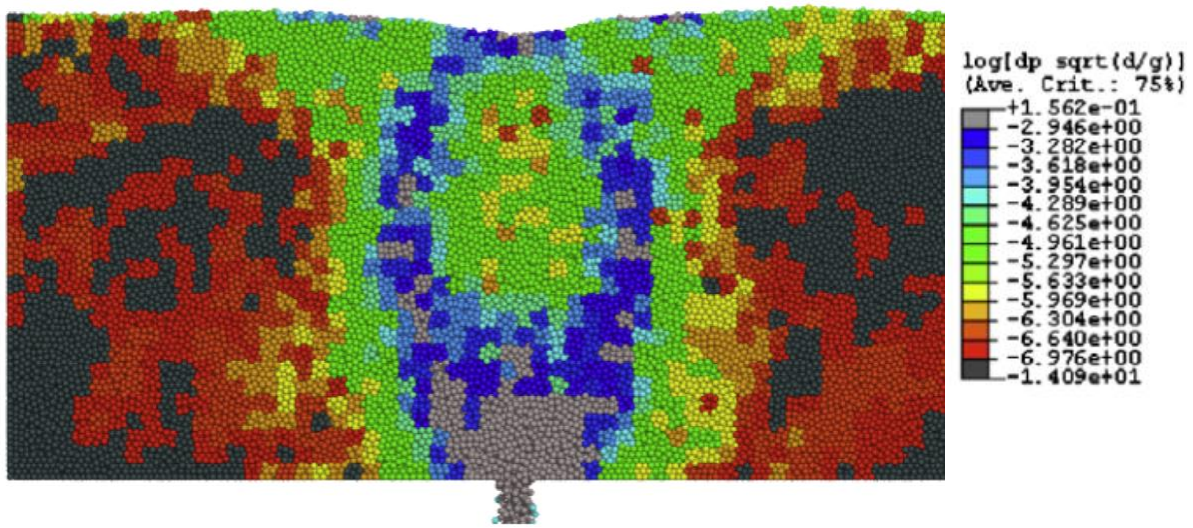

(a)

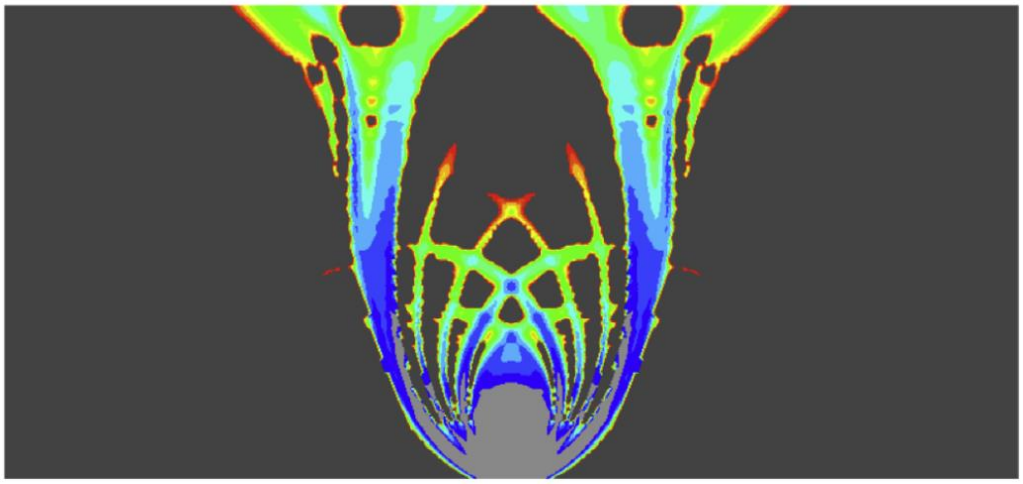

(b)

Figure 2-43: Flat bottomed silo, plastic shearing rate results for (a) DEM solution (b) Non-linear elasto-plastic solution (Kamrin, 2010)

2.7. SUMMARY OF LITERATURE REVIEW

The aim of the literature review is to present relevant background information and show the significance of the study in relation to current or recent studies. An overview of cavity propagation in dolomitic ground conditions is presented and it was shown that current methods used to predict the size of sinkholes is overly conservative, resulting in undeveloped land as designs catering for large sinkholes are economically unfeasible.

The trapdoor experiment is widely accepted as a suitable means to investigating soil arching and the associated soil deformation mechanisms. It is evident that research related to deformation mechanisms in soils overlying deep trapdoors (H/B >> 2) are limited in terms of both physical as well as numerical trapdoor experiments.

The DEM was shown to be the ideal tool to investigate significant shearing or dilation of granular materials due to its discontinuous nature. However, due to the significant computational costs associated with simulating granular materials using DEM, the following methods are commonly employed to reduce computational effort:

1. Particle size scaling
2. Reduction in particle normal contact stiffness
3. Simulating spherical particles in-lieu of angular/polyhedral particles

Recent advancements in DEM, in which the parallel processing power of the GPU is utilised, allows for greater computing power and a model which can represent reality with greater accuracy. Given the advanced computational capacity of Blaze-DEM, numerical modelling of trapdoor experiments without particle size scaling or an artificial reduction in particle contact stiffness and with the application of non-spherical particle shapes is possible. As the shear strength of a soil is directly related to its resistance to deformation/shearing, particle interlock, attributed to particle shape and angularity, plays a significant role in the bulk shear strength of soil. An important advantage of DEM is that the effect of individual particle parameters on soil deformation mechanisms, such as the particle shape, can be isolated.

It is clear that studies which were previously considered to be computationally unfeasible are now possible. In this study both physical and numerical (DEM) deep trapdoor experiments were therefore undertaken to investigate the effect of soil shear strength on shear band formation during a trapdoor lowering simulation.

From the summary the following hypothesis was formulated and investigated:

"A relationship exists between soil shear strength and the cavity propagation mechanism which leads to eventual sinkhole formation."

3. CENTRIFUGE TRAPDOOR EXPERIMENTS

3.1. INTRODUCTION

The study was undertaken to investigate the mechanisms associated with cavity propagation during sinkhole formation by performing deep trapdoor experiments in a centrifuge facility. Centrifuge modelling is based on the similarity of stresses and strains within both the model and prototype continuums. It provided a means by which the material properties and applied stresses could be regulated so that the material behaviour associated with cavity propagation mechanisms, and the extent of the area of influence, could be investigated.

The chapter opens with a brief overview of centrifuge modelling, followed by a detailed description of the strongbox and trapdoor lowering apparatus employed in the experiments. The instrumentation devices used to measure the mechanisms related to cavity propagation are described, this includes a detailed description of the Particle Image Velocimetry (PIV) analysis technique. A geotechnical and physical description of the materials used in the investigation is presented in addition to the model preparation procedure. The chapter concludes with a description of the trapdoor test procedure and test schedule summary.

3.2. CENTRIFUGE MODELLING

It is well known that the behaviour of geomaterials is strongly linked to the stress level. This stress-dependency poses a challenge to researchers when physical modelling is undertaken to investigate the failure mechanisms of soil at depth, such as with the collapse of a subsurface cavity. A large-scale model required to replicate the field stresses associated with sinkhole propagation may not be economically feasible to construct and thus centrifuge modelling was considered to be the best means by which representative stress levels can be replicated during the physical modelling of geomaterials. In order to achieve equal stresses at geometrically corresponding points in the full-scale prototype and small-scale model, the self-weight of the soil in the model is increased by means of centripetal acceleration in a centrifuge facility. The model spins around a fixed axis, inducing an artificial gravitational field, which in turn increases the self-weight of the soil. When the soil model, with dimensions scaled to 1/N of the full-scale prototype, is spun at a centripetal acceleration that results in N-times the earth's gravitational acceleration on the centrifuge, equivalent soil behaviour is achieved (Einstein et al., 1990).

Scaling laws are applied in centrifuge modelling to ensure similitude of stress conditions at geometrically similar points in the centrifuge model, which is accelerated to N-gravities, and a prototype model constructed to scale N (Taylor, 1995). Table 3-1 shows the centrifuge scaling laws applicable to this study, derived from Wood (2004). To convert the full-scale parameter prototype to the scaled

centrifuge model dimensions, the parameter listed in the first column is divided by the Prototype/Model Factor listed in the last column. As shown in the table, if the parameters are scaled accordingly, stress, stiffness, strain and density have a scaling factor of one.

Table 3-1: Applicable centrifuge scaling laws (adapted from Wood, 2004)

Parameter	Units	Prototype/Model Factor
Length	m	N
Area	m^2	N^2
Volume	m^3	N^3
Density	kg/m^3	1
Force	N	N^2
Stress	N/m^2	1
Strain	%	1
Stiffness	N/m^2	1
Force/unit length	N/m	N
Velocity	m/s	1

The trapdoor experiments were undertaken in the geotechnical beam centrifuge at the University of Pretoria, a photograph of which is shown in Figure 3-1. The C67-4 geotechnical centrifuge was manufactured by the French company Actidyn, and has the ability to accelerate a one-ton model to its maximum acceleration of 150g (Jacobsz et al., 2014). The centrifuge has an arm length (i.e. radius) of 3m and the model platform is positioned at the end of the centrifuge arm. A counterweight, on the opposite side of the axis of rotation, is adjusted automatically during spin-up at approximately 4g. The soil model is placed on the platform and swings upwards during spin-up. The hinged connection, which allows free rotation of the model, ensures that the primary gravitational force always acts perpendicularly to the material model.

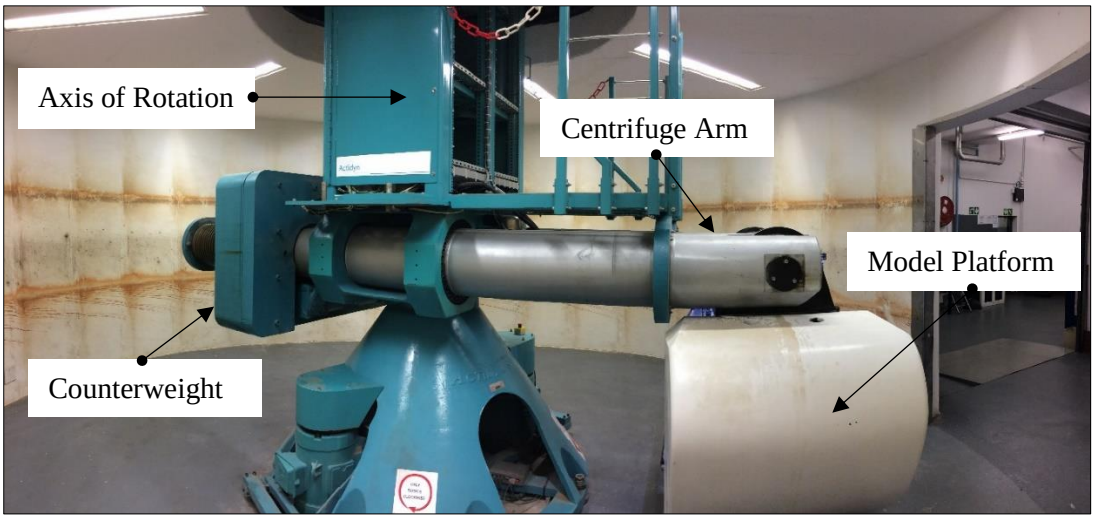

Figure 3-1: Centrifuge facility at the University of Pretoria

3.3. CENTRIFUGE TEST PACKAGE

3.3.1 Trapdoor apparatus

The primary component of the centrifuge test package was the trapdoor apparatus which consisted of a rectangular strongbox with a translating trapdoor in the centre of the container base. The geomaterials were placed in the trapdoor apparatus which was in turn placed on the model platform for testing in the centrifuge. The stiffest members of the strong box frame were the side columns, comprising three back-to-back aluminium channel sections. These members formed support columns to the container and were bolted to a 100 mm deep steel base on which the entire trapdoor apparatus was placed. The back wall of the container was a 10 mm thick aluminium plate supported by the channel sections at either end by means of bolts.

The front wall of the container was a 20 mm thick tempered glass window which was glued to an angle-iron U-frame along the bottom and sides of the glass window. The U-frame was in turn fixed to the support columns of the trapdoor apparatus using four bolts, two on either side. Silicone sealant was used to ensure that there were no gaps between the glass window and trapdoor apparatus through which a sand leak could occur. Furthermore, the glass panel and back plate of the trapdoor apparatus extended below the lowest displaced position of the trapdoor, thereby ensuring that no material could escape during trapdoor lowering in the centrifuge.

The trapdoor mechanism at the centre of the container base was placed between two inverted aluminium channel sections which acted as the false floor to the container. The false floor was supported by a stop block, bolted to the back plate, at the outer end of the inverted channel section and by a slender aluminium panel at the inner end, adjacent to the trapdoor mechanism. The trapdoor, with a width of 50 mm, was free to displace vertically between the two slender aluminium plates (Oberholzer, 2017). The strongbox had an internal length of 630 mm, width of 76.5 mm and maximum height of 360 mm. Given the narrow width of the strongbox in comparison to its internal length, plane strain conditions were assumed for the investigation of soil deformation during trapdoor lowering.

A gravitational acceleration of 50g was selected for the trapdoor experiments undertaken in the centrifuge. This acceleration was selected based on the resulting prototype dimensions, corresponding to those of the model, and a review of relevant literature which showed that several researchers applied between 40 and 50g's during their trapdoor experiments (Costa et al., 2009; Iglesia et al., 2014, and Da Silva, 2018). At the selected gravitational acceleration, the 50 mm trapdoor width results in a sinkhole diameter of 2.5m. Given the inconsistent nature of dolomitic bedrock profiles, sinkhole widths may vary distinctly. The selected width of 2.5 m was therefore considered to be a representative estimation. The height of material placed in the trapdoor apparatus was dictated by the reach of the surface settlement Linear Variable Differential Transformers (LVDTs) placed on the surface of the material.

This restriction resulted in an average material height of 350 mm and a corresponding H/B ratio of approximately 7.0 (i.e. deep trapdoor experiment). The effective overburden depth therefore equated to 17.5 m at peak acceleration. As previously indicated, dolomite is known for its variability in terms of both depth and the extent of the subsurface tunnels that have formed over time. The selected configuration is therefore representative of a possible sinkhole configuration. For the purpose of this study, maintaining the standard dimensions and scale was of greater significance than the specific model or prototype size. A photograph of the trapdoor apparatus, with the translating trapdoor, and a schematic of the primary elements and dimensions of the trapdoor apparatus are displayed in Figure 3-2 (a) and (b), respectively.

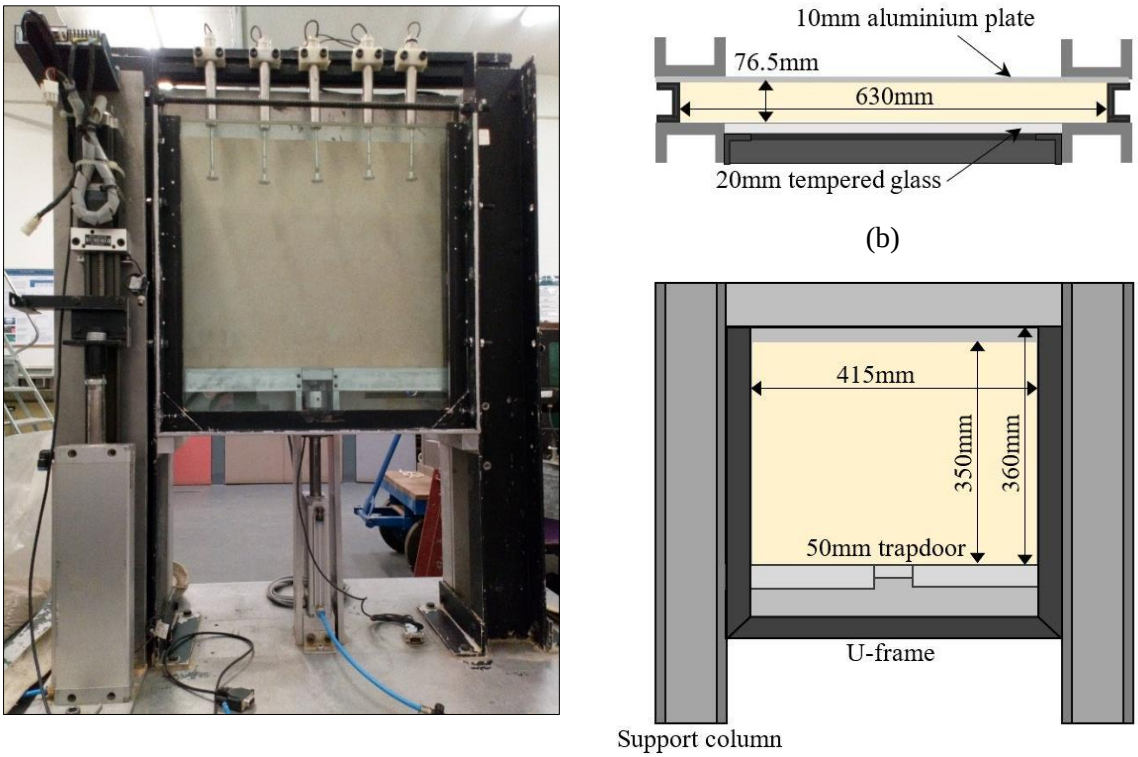

Figure 3-2: (a) Photograph as well as (b) top view and (c) elevation view schematic of the trapdoor apparatus used in the centrifuge trapdoor experiments

3.3.2 Trapdoor lowering system

The trapdoor lowering mechanism was controlled by means of a hydraulic system, in which two cylinders were connected to one another, as well as to a stepper motor. Da Silva (2018) describes both the advantages and disadvantages of employing a hydraulic system for displacement control of the trapdoor system, with the most notable advantages considered to be the ease of setup and the known capacity of hydraulic systems to operate acceptably at increased acceleration. The greatest disadvantage is the precision with which displacement can be controlled in comparison to mechanical gearing systems. The precision discrepancies in trapdoor displacement control were not considered to be critical

in this research study and high precision displacement monitoring systems were used to quantify the discrepancies.

The configuration of the hydraulic system is detailed in Figure 3-3. The piston rod of Cylinder A was attached to a one-dimensional linear actuator with a stepper motor, whereas the trapdoor and load cell were mounted onto the piston rod of the second cylinder, Cylinder B. The top compartment of Cylinder A was connected to the bottom compartment of Cylinder B, forming a closed hydraulic circuit between the two pistons. Both compartments and the connecting Festo tubes were filled with a mixture of anti-freeze and water, in a one-to-one ratio. Although Festo tubes are designed for air systems, a liquid medium was chosen due to its relative incompressibility in comparison to air. The anti-freeze was added to the water to preserve the seals in the pistons. The top compartment of Cylinder B was connected to an external source of water pressure in case the trapdoor became stuck and additional pressure was required to overcome the resistance so that trapdoor lowering could resume. The external water source was isolated by means of a solenoid valve as shown in the trapdoor configuration figure. The bottom compartment of Cylinder A was open to atmospheric pressure. A pressure transducer was connected to the closed hydraulic circuit so that pressure could be monitored during centrifuge spin-up and trapdoor lowering. If, for some reason, the pressure build-up in the system was excessive, a second solenoid valve leading to a discharge container could be opened to relieve pressure in the system. As the piston in Cylinder A was lowered, a reduction in pressure in the top compartment of the cylinder resulted in suction of the liquid medium from the bottom compartment of Cylinder B to the top compartment of Cylinder A, which in turn caused the trapdoor to lower.

The system was de-aired prior to testing to minimise compressibility of the liquid solution in the hydraulic system. A control valve was used to isolate sections of the hydraulic circuit during the de-airing process and is depicted in the setup diagram.

The trapdoor was lowered continuously during testing as previous researchers had noted a spike in load measurement readings when the trapdoor was stopped during staged lowering (Da Silva, 2018). Calibration of the stepper motor velocity and trapdoor velocity was undertaken to control the trapdoor displacement rate and correlate the magnitude of displacement to the corresponding inflight photograph. Photographs of the soil model were taken to analyse the soil deformation mechanisms during trapdoor lowering. The inflight photographs and analysis technique are discussed in Section 3.3.4. The calibration procedure showed that the trapdoor velocity was approximately 80% of the set motor velocity.

The chosen rate of trapdoor displacement was dictated by the maximum frame rate of the digital camera used to take inflight photographs, in this case, a maximum rate of 0.167 Hz (i.e. one photograph every six seconds). The trapdoor velocity was selected as 0.025 mm/s, resulting in a photo being taken every 0.15 mm of trapdoor displacement, comparable to the diameter of the sand grains used. The selected

rate was considered to be slow enough to capture small movements of the material during trapdoor lowering. This rate is further comparable to rates employed by other researchers in the field. Trapdoor velocities of 0.01, 0.18 and 0.033 mm/s were used by Dewoolkar et al. (2007), Iglesia et al. (2014) and Da Silva (2018), respectively. It was found that the trapdoor displacement rate varied for each of the trapdoor experiment tests, despite the fixed motor velocity. The variances, though small and within the range of values listed above, were recorded and considered in the analyses of the results.

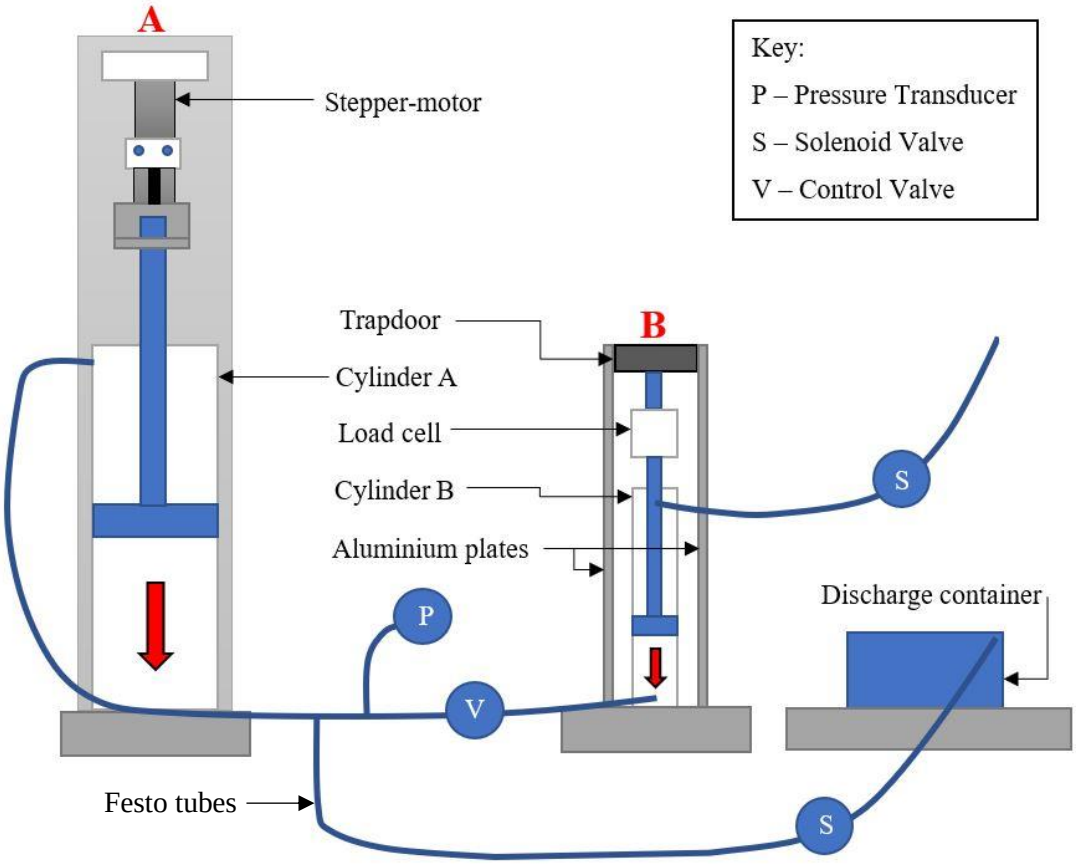

Figure 3-3: Trapdoor mechanism configuration

3.3.3 Instrumentation

The trapdoor displacement was measured using a single LVDT with a range of 100 mm. The body of the LVDT was fastened to the back plate of the trapdoor apparatus using clamps and the extendable portion was placed on an aluminium plate fixed to the top of piston rod of Cylinder B.

The load cell was used to monitor load variation due to stress redistribution or arching in the model material during trapdoor lowering. A perspective view of the trapdoor and load cell configuration is presented in Figure 3-4. As indicated in the figure, the load cell was positioned between the trapdoor and LVDT resting plate. Both the trapdoor displacement and load cell readings were recorded and analysed using HBM's QuantumX data acquisition system and Catman software.

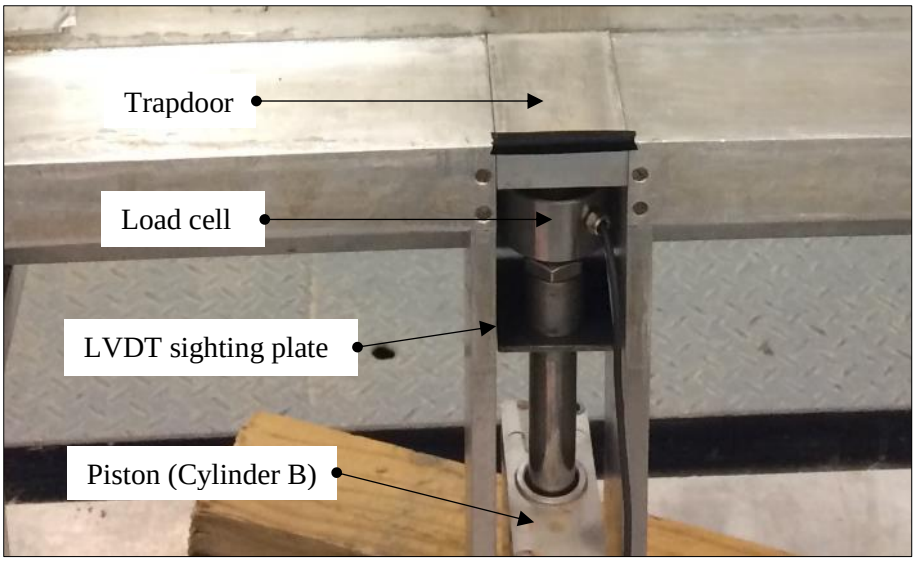

Figure 3-4: Perspective view of the load cell / trapdoor configuration

Five LVDTs were placed on the surface of the model material to monitor surface settlement of the material during trapdoor lowering at the elevated gravitational acceleration. The centre LVDT was placed in line with the centreline of the trapdoor, at a distance of 250 mm form the inner edge of the U-frame, with two LVDTs placed approximately symmetrically on either side of the centre one, as depicted in Figure 3-5. The surface settlement LVDTs were clamped to an aluminium beam which was in turn bolted at either end to the support columns of the model frame. The LVDTs were positioned at 55 mm, 140 mm, 250 mm (centreline of trapdoor), 360 mm and 460 mm from the inner edge of the U-frame. The range of these LVDTs is limited to 30 mm, which consequently restricted the minimum height of the material in the container to 330 mm. The output readings from both the surface settlement LVDTs and the pressure transducer, described in the previous section, were recorded by means of the DigiDAQ data acquisition system.

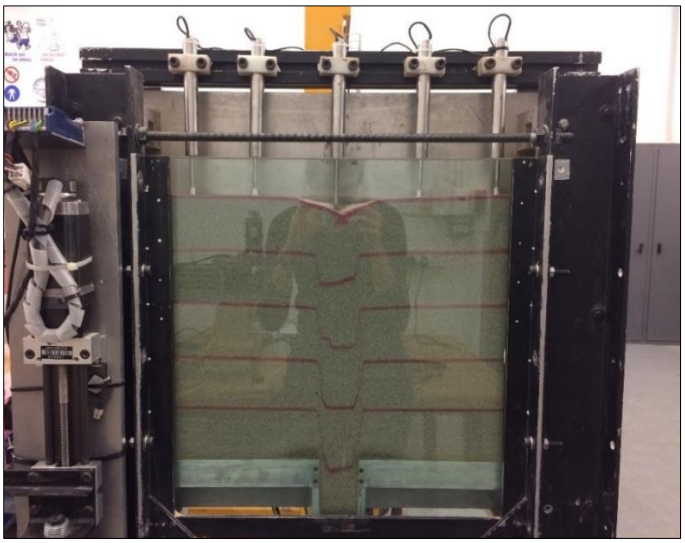

Figure 3-5: Surface settlement LVDTs

3.3.4 Particle Image Velocimetry (GeoPIV)

Particle Image Velocimetry (PIV), also known as Digital Image Correlation (DIC), is a velocity measuring technique used to visualise the flow of materials and calculate related displacement and velocity fields. Material deformations are inferred from these fields. The GeoPIV-RG software (Stanier et al., 2015), which is an update of the GeoPIV program described by White et al. (2003), was used to analyse the deformation mechanisms of the geomaterials during trapdoor lowering. A general overview of the computational approach is discussed below, including inherent errors of GeoPIV and improvements using the updated Reliability Guided (RG) version.

The application of PIV to geotechnical testing involves taking consecutive, digital photographs of the soil model during deformation. The photographs, or images, are divided into a grid of subsets, also referred to as patches, based on the user-defined subset size and spacing. Subset displacements, from the 'reference image' (usually initial photograph), to subsequent 'target images', are calculated using one of the methods described in Figure 3-6. White et al. (2003) ascribe the performance of a measurement system to high quality accuracy, precision and resolution. Both accuracy and resolution are independent of the user-defined input parameters when using the GeoPIV system. The system accuracy is dependent on the calibration process used to convert measured coordinates from image (pixel) to object (mm) space whereas the resolution is camera dependent. The precision with which PIV is applied is related to the selected test subset size, the intensity of the soil texture (variation) and the extent of particle displacement between subsequent photos. White et al. (2003) describe a conflict between subset size selection and precision. It has been demonstrated that a larger subset size (i.e. 50 px) improves precision due to greater variation in soil texture captured within a subset, however, smaller subsets are particularly advantageous in areas with high strain gradients due to the increased grid density or measuring points. For this study, a side length of 48 px was selected for the square subsets, at a subset spacing of 16 px. Based on deep trapdoor experiments undertaken by Oberholzer (2017), a comparatively long side length of 48 px for the square subsets in Geo-PIV, overlapping at a subset centroid spacing of 16 px, adequately captured high strain gradients in the shearing zone of soil during trapdoor lowering. The selected subset dimensions and spacing therefore deemed sufficient for this study. Similarly, the subset spacing was deemed small enough to ensure subset overlap resulting a larger number of subsets and therefore greater precision. The trapdoor lowering rate was selected to ensure that soil particle movements between photos was minimal thereby aiding the precision of the system.

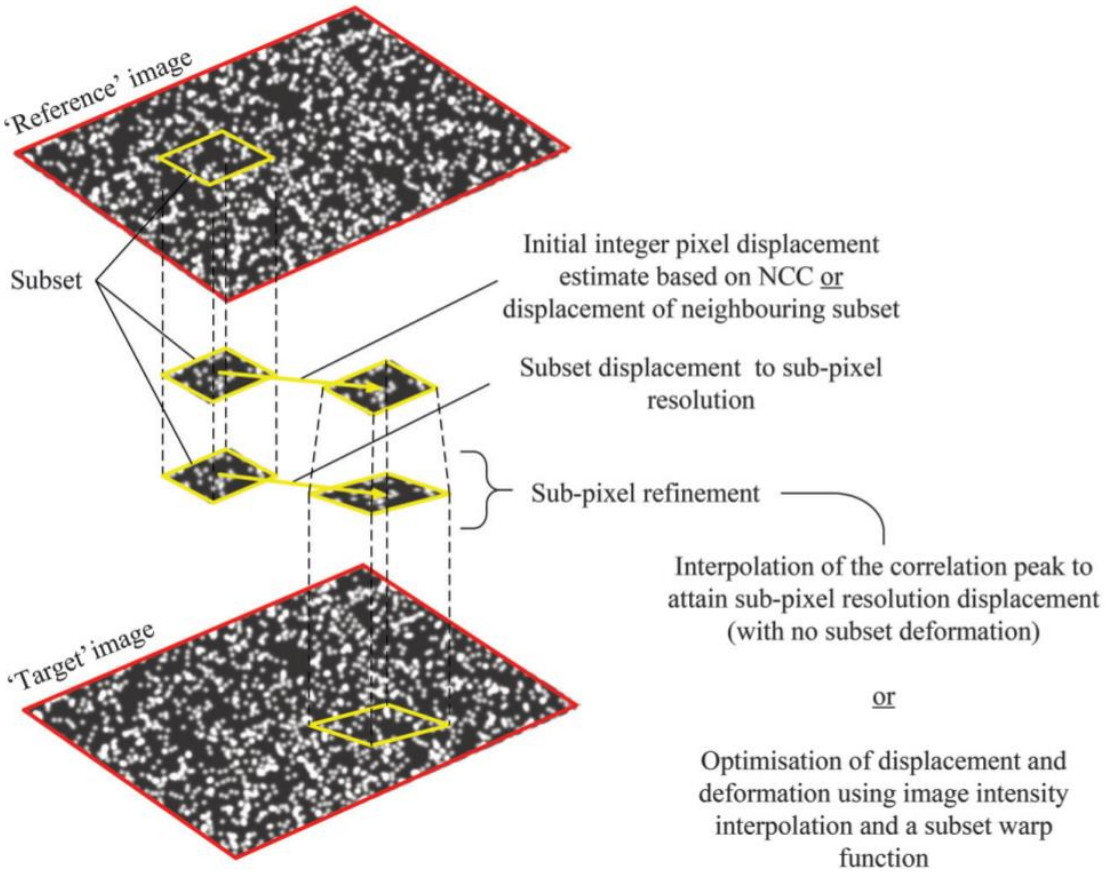

Figure 3-6: General overview of the PIV/DIC method (Stanier et al., 2015)

In the GeoPIV-RG method (Stanier et al., 2015), the seed or starting subset is selected in the initial reference image after which the initial displacement vector of the seed subset, from the reference to the target image, is estimated using the Normalised Correlation Coefficient (NCC). Interpolation of the subset pixel intensities is then used to adjust the deformation parameters to optimise the correlation between the reference and target subset. The degree of match between the reference and target subsets is called the Zero-Normalised Cross-Correlation Correlation Coefficient (CC_{ZNCC}). Interpolation ceases once the maximum error between the reference and target subset ($|\Delta p|_{max}$) is smaller than the user-specified value or if the maximum number of iterations has been exceeded. For this study the recommended values of 10E-06 and 50 were chosen as the starting values for $|\Delta p|_{max}$ and the maximum number of iterations, respectively (Stanier et al., 2015). The seed computation is deemed successful if the CC_{ZNCC} is greater than the user-defined limit and within the deformation optimisation limits described above.

Once the seed computation has been completed, the correlation coefficient of the four subsets neighbouring the seed is estimated using the seed's deformation and displacement parameters. Subsets are queued and processed according to the magnitude of their estimated CC_{ZNCC} values and once a subset has been calculated, it is removed from the queue. As with the seed computation, the CC_{ZNCC} is

optimised by adjusting the displacement and deformation parameters using image intensity interpolation. Due to the broad range and types of deformation experienced by soils, the reference image is set to update automatically when the CC_{ZNCC} of a particular subset is less than the user-defined minimum tolerance. Once all the images have been analysed, the analysis output results in an array of subset coordinates corresponding to each consecutive photo. Subset displacements and strains can then be calculated based on the final coordinate data.

The primary advantage of the GeoPIV-RG system (Stanier et al., 2015) over the GeoPIV (White et al., 2003) system is that it applies a Reliability Guided (RG) method in which each subset is allowed to deform according to a displacement or linear displacement gradient shape function which describes the first-order deformation of the subset. The correlation between reference and target images is improved by applying these first-order subset shape functions in combination with image intensity interpolation techniques as derived by White et al. (2003).

The images for the PIV analyses were captured by mounting a camera in front of the trapdoor apparatus on the model platform in the centrifuge facility. A Canon EOS 100D camera with an EF 40 mm f/2.8 STM lens was used to capture the GeoPIV photographs. It was focused manually as it could not focus automatically at high gravitational accelerations, such as those imposed on the camera in the centrifuge.

3.4. GEOMATERIAL CLASSIFICATION

3.4.1 Dolomitic soil profile

Figure 3-7 (a) presents a typical dolomitic soil profile from Wagener & Day (1986). As illustrated in the figure, WAD (Weathered Altered Dolomite), a soft and compressible residue of dolomite, typically lies above the initial void throat (see Figure 2-1 for corresponding labels). Due to its low shear strength WAD generally cannot span the required distance over the void and therefore mobilises into the receptacle first. The material that typically arches across the receptacle throat during a loss of subsurface support is the cohesionless dolomitic residuum, comprising chert bands and sand. These materials arch by transferring load to the neighbouring dolomitic bedrock pinnacles, as shown in Figure 3-7 (b), while the void migrates to the surface during sinkhole formation. Cohesionless material in the form of chert gravel, manganocrete nodules and sand comprise the remainder of the soil profile overlying cavities (Wagener & Day, 1986). Cohesionless materials were therefore selected in the investigation of arching and shear band propagation.

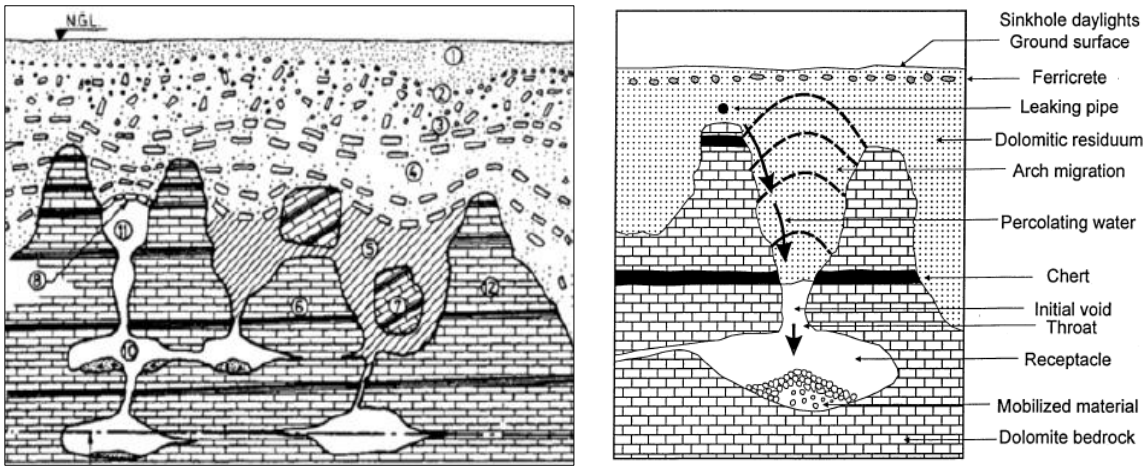

(a) (b)

Figure 3-7: (a) Dolomitic profile (Wagener & Day, 1986) and (b) Arching of dolomitic residuum during cavity propagation (Buttrick & Van Schalkwyk, 1998)

3.4.2 Description of materials

Three cohesionless materials were used during the undertaking of trapdoor experiments in the centrifuge facility, namely coarse-grained Consol sand, fine-grained Afrimat sand and 2 mm glass beads or ballotini, shown in Figure 3-8 (a) to (c), respectively. The Consol sand is greyish in colour with rounded particles and the Afrimat sand has a golden-orange appearance with greater angularity. Both materials were sourced commercially from their namesakes. The appearance of the 2 mm glass beads, purchased from Lasec, varied between translucent and a light blue-opaque colour. These materials are referred to collectively as geomaterials for the purpose of the study. The particle size for which half of the material is finer by mass (i.e. the average particle size, by mass) is denoted by D_{50}. The Consol and Afrimat sands have D_{50} values of 0.737 mm and 0.307 mm, respectively. According to the AASHTO definition of grain size, coarse sands have an average particle size exceeding 0.425 mm, whereas sands with an average particle size smaller than 0.425 mm are classified as fine-grained sands. The Consol sand is therefore also referred to as the coarse-grained sand and the Afrimat sand as the fine-grained sand.

(a) (b) (c)

Figure 3-8: Materials tested in the centrifuge: (a) coarse-grained sand (Consol), (b) fine-grained sand (Afrimat) and (c) glass beads

3.4.3 Particle size distribution

The particle size distribution or gradation of a soil describes the percentage of particles by mass which fall within a specific size range. Uniformly or poorly graded materials will not compact and settle as readily as well-graded materials during centrifuge spin-up and are therefore preferable during centrifuge testing. In a well-graded soil, smaller particles move into the interstitial voids between larger particles thereby increasing the bulk density of the material. As the particles of a uniformly graded material are of comparable size, the material does not contain particles small enough to migrate into the spaces of the particle lattice. Greater control over the material density can therefore be exercised when a uniformly graded material is used in centrifuge testing (Archer, 2014).

The particle densities of the fine- and coarse-grained sands were determined using gas pycnometry. The Consol sand yielded an average specific gravity of 2.654 g/cm^3 with the Afrimat sand yielding a similar value of 2.675 g/cm^3. The supplier's technical data sheet for the glass beads shows an average specific gravity of 2.5 g/cm^3. This material was not measured using gas pycnometry as the size of the container was too small to house the glass beads for testing.

The particle size distributions of the coarse- and fine-grained sands were determined using the Malvern Mastersizer 2000, an apparatus which uses laser diffraction to calculate particle size distribution by volume. The specific gravity of the material was then used to convert the results to a particle size distribution by mass. Figure 3-9 shows the particle size distributions for the coarse- and fine-grained sands based on the Malvern Mastersizer 2000 results. The third graph presents the particle size distribution of the Afrimat sand from the supplier data sheet.

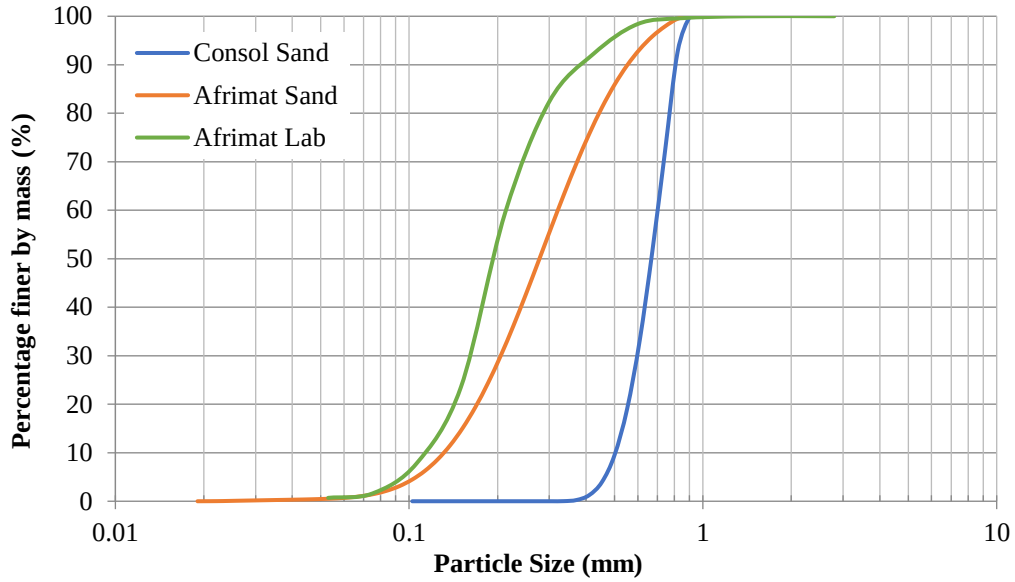

Figure 3-9: Particle size distribution of the geomaterials used in testing

The coefficient of uniformity (C_U) and the coefficient of curvature (C_Z) are shape parameters used to describe the slope and shape of particle size distribution curves, respectively. Both parameters tend towards unity as the material grading approaches complete uniformity (Craig, 2004). The C_U and C_Z values for the glass beads will be approximately one due to the single particle size of the material. A sand is described as well-graded if the C_U value is greater than 6, indicating a wide range of particle sizes, and if the C_Z value lies between 1 and 3 (National Highway Institute, 2006). The equations for the uniformity and curvature coefficients are presented in Equation 3-1 and Equation 3-2 below:

$$C_U = \frac{D_{60}}{D_{10}} \qquad \text{Equation 3-1}$$

$$C_Z = \frac{{D_{30}}^2}{D_{10}D_{60}} \qquad \text{Equation 3-2}$$

Where:

D_{10} = Particle size for which 10% of the soil sample is finer by mass

D_{30} = Particle size for which 30% of the soil sample is finer by mass

D_{60} = Particle size for which 60% of the soil sample is finer by mass

Characteristic particle sizes, derived from the particle size distribution curves and recorded in millimetres, as well as the coefficients of curvature and uniformity are listed in Table 3-2. Both

materials can be classified as uniformly graded, with the fine-grained sand having a slightly broader particle size range. According to the Unified Soil Classification System (ASTM D2487, 2011 (2006)), both the Consol sand and glass beads are classified as poorly-graded sands, whereas the finer Afrimat sand is classified as a poorly-graded sand with silt.

Table 3-2: Particle size distribution characteristic and specific gravity of the natural sands

Material	D_{10}	D_{30}	D_{60}	C_U	C_Z	G_s (g/cm^3)
Coarse-grained Sand	0.556	0.597	0.702	1.263	0.913	2.654
Fine-grained Sand	0.145	0.205	0.321	2.215	0.902	2.675

3.4.4 Particle shape analysis

Material properties that influence the shear strength of a soil are the average particle size, the soil's grading distribution and the angularity of the individual grains, amongst others. The Zeiss Stereo Microscope allows for a three-dimensional (3D) visualisation of individual grains and provides a means of investigating some of the particle properties contributing to the shear strength of the soil.

The Zeiss Stereo Microscope was used to capture the images presented in Figure 3-10 and Figure 3-11, which show magnified images of a small sample of the Consol and Afrimat sand grains, respectively. Figure 3-10 shows that even in the uniformly graded sample with coarse, rounded sand grains (Consol sand), small angular particles are present which would contribute to the shear strength of the material. The photograph of the fine, angular sand (Afrimat sand) displayed in Figure 3-11, emphasises the vast array of particle shapes and sizes present in this granular material. Its high shear strength is attributed to the distinct angularity of the particles and wide-spread particle size distribution. This observation emphasises that is physically impossible to replicate each aspect of the individual grains numerically. An attempt is therefore made later on in the study to predict the bulk material behaviour by adjusting particle shape.

Figure 3-10: Zeiss Stereo Microscope photograph of a sample of Consol sand grains

Figure 3-11: Zeiss Stereo Microscope photograph of a sample of Afrimat sand grains

The Scanning Electron Microscope (SEM) has a significantly greater magnification than the Zeiss Stereo Microscope and it was therefore used to investigate the surface texture of the geomaterials. The SEM scans the surface of a sample using a focused electron beam. The electrons in the beam interact with the surface of the sample and then return various signals from which information about the sample's surface topography and composition can be obtained (Nanoscience Instruments , 2018). The surface of the sample material, or object under investigation, is often coated with a conductive metal, such as carbon, by placing a carbon rod between two high-current electrical terminals in a vacuum and passing an electric current through the rod. When the carbon rod reaches its evaporation temperature it deposits a fine stream of carbon onto the sample below. Carbon-coating is undertaken to reduce thermal damage, prevent charging of the material and to improve transmission of the second electron signals which are required for topographical information of the sample surface (Leica Microsystems, 2013). Samples of each of the three materials were prepared for the SEM, as shown in Figure 3-12 (a). Figure 3-12 (b) presents the sample plate after carbon-coating had been undertaken.

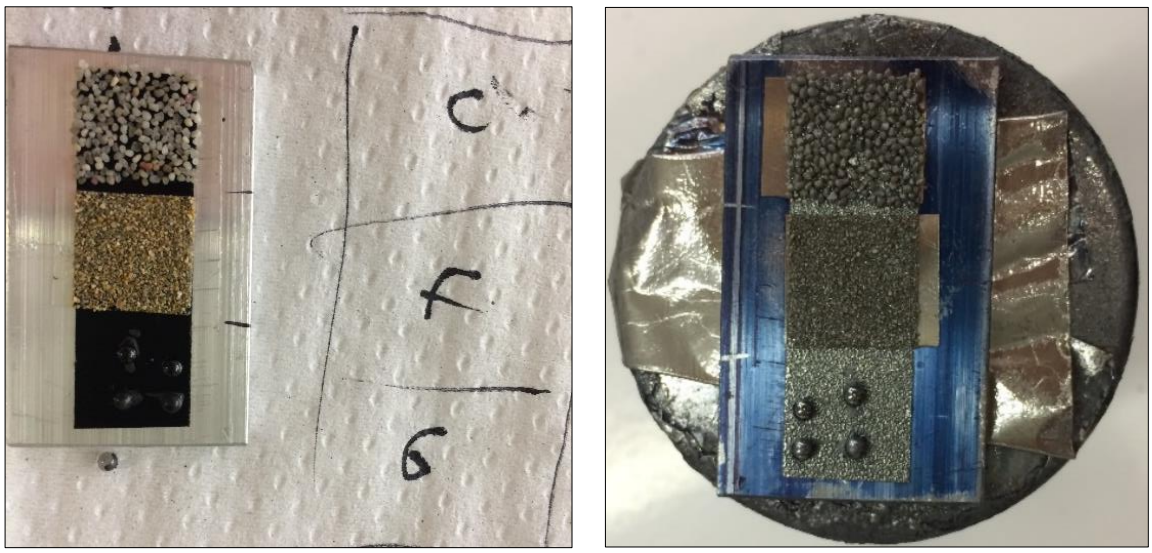

(a) (b)

Figure 3-12: SEM sample preparation (a) prior to and (b) post carbon-coating

The size of Consol sand grains and glass beads proved to be too large to be effectively examined using the SEM, consequently only the Afrimat sand was investigated. Figure 3-13 presents an image of the surface topography of the Afrimat sand sample, created by the SEM. From this image the varying particle roughness is apparent. The bottom right particle is essentially smooth with two jagged ridges whereas the top left particle has an intricate and rough surface. The variation in surface texture adds to the shear resistance of the soil thereby increasing its shear strength.

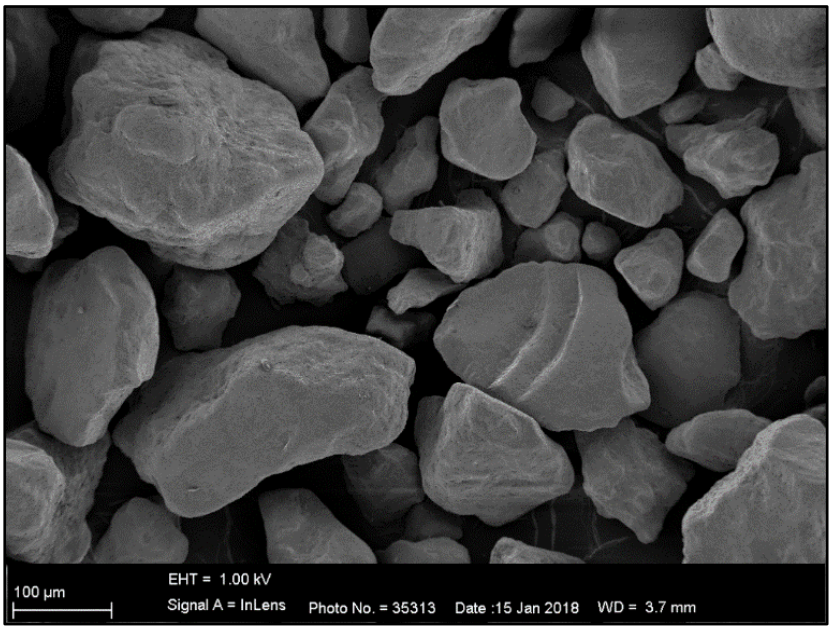

Figure 3-13: SEM image of a sample of Afrimat fine-grained sand particles

3.4.5 Relative density

The angle of dilation and resulting shear band formation of a cohesionless soil is highly dependent on the confined stress level and density of the soil (Bolton, 1986), indicating the importance of soil density when investigating deformation mechanisms during trapdoor lowering. Relative density is a measure of the degree of compactness of a soil and is defined by Equation 3-3 as follows (ASTM D4253-93, 1996):

$$Relative\ Density\ (\%) = \frac{e_{max} - e}{e_{max} - e_{min}} \times 100 \qquad \text{Equation 3-3}$$

Where:

e_{max} = Reference void ratio of soil at minimum index density

e_{min} = Reference void ratio of soil at maximum index density

e = Void ratio of sample material

The Standard Test Methods for maximum and minimum index density were used to calculate the respective densest and loosest state of compactness of the coarse- and fine-grained sands. It is important to note that the standard test procedure to determine the maximum material density does not yield the absolute maximum density, but rather the densest state that a cohesionless soil that can attain using standard laboratory compaction procedures and limiting particle breakdown (ASTM D4253-93, 1996). Similarly, the minimum index density is a reference density for the loosest state of compactness of the material (ASTM D4254-93, 1996). Three maximum and minimum index density tests were undertaken for the coarse and fine sands. The relative density of the glass beads was not determined using the standard testing methods due to the destructive nature of the testing procedure. Table 3-3 presents a summary of the range of dry densities and void ratios for the natural sands.

Table 3-3: Summary of dry density and void ratio ranges for the natural sands

Material	Specific Gravity (g/cm^3)	ρ_{dmax} (kg/m^3)	ρ_{dmin} (kg/m^3)	e_{min}	e_{max}
Coarse-grained Sand	2.654	1773	1590	0.50	0.67
Fine-grained Sand	2.678	1709	1502	0.56	0.77

Dullen (1992) describes the packing arrangement of uniform spheres as either regular, where particles are placed in an ordered array, or random, where the particles placed in a disordered or irregular fashion. The coordination number of a particle describes the number of contact points, or neighbours, of each sphere and therefore gives a good indication of the packing density. The loosest regular packing state

is a cubic lattice and the densest is the rhombohedral, with respective coordination numbers of 6 and 12. These are considered to be the absolute maximum and minimum packing densities of the material.

The packing density of a material is an empirical parameter which represents the volume fraction of solids in a sample and is the complementary number to the porosity parameter in soils. It is multiplied by the specific gravity of the material to determine the corresponding material density. The minimum packing density of irregularly packed uniform spheres is 0.56. This state is achieved when particles are slowly settled into position and is referred to as "very loose random packing". Contrarily, "close random packing" describes a dense state of packing obtained when, for example, a vibrating bed is used to compact the sample (Haughey & Beveridge, 1969). The maximum and minimum densities and void ratios for a regular and random packing of spheres is summarised in Table 3-4.

Table 3-4: Summary of dry density and void ratio ranges for uniformly distributed spherical particles

Packing Arrangement	Specific Gravity (g/cm^3)	ρ_{dmax} (kg/m^3)	ρ_{dmin} (kg/m^3)	e_{min}	e_{max}
Regular Packing	2.5	1851	1309	0.35	0.91
Random Packing	2.5	1603	1400	0.56	0.79

Quantifying the relative density of the centrifuge test models before spin-up was considered essential for the replication of the trapdoor experiment in the discrete element model, described in Chapter 6. The test models were prepared by pluviation to achieve a high relative density, representative of what would be found in *in-situ* conditions.

3.4.6 Shear strength results

Two drained triaxial tests were conducted using the fine-grained Afrimat sand, and the 2 mm glass beads. The triaxial tests comprised of only the shearing stage and the materials were tested in a dry state to replicate the material conditions applied in the centrifuge. Dense samples were prepared by placing the materials in the individual moulds, using a trowel, and tamping the material after each layer had been placed. The fine-grained sand and glass bead samples had relative densities of 90.2% and 87.8% (for a random packing arrangement), respectively. An effective stress of 200 kPa was applied to the samples and they were sheared at 0.1 mm/minute. The triaxial test setup used for both materials is shown in the photograph displayed in Figure 3-14.

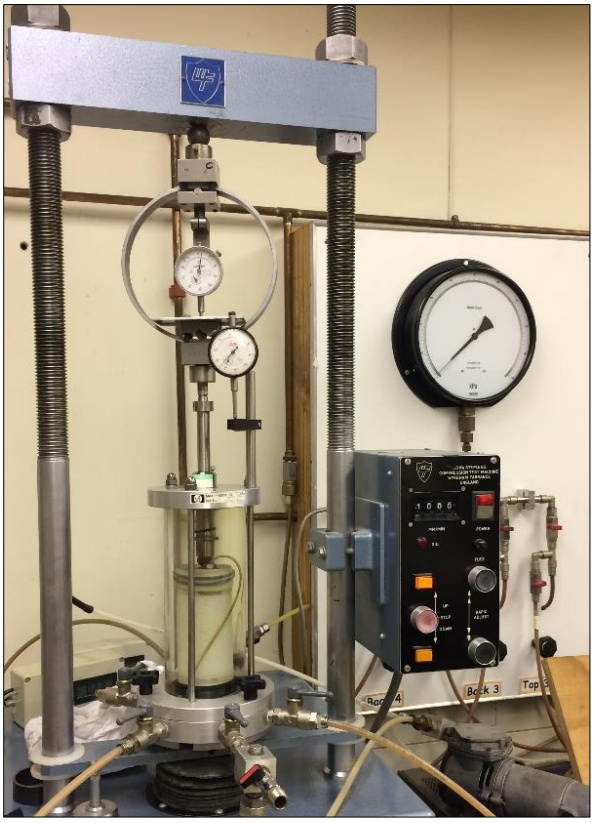

Figure 3-14: Triaxial test setup for fine-grained sand and glass beads

The stress paths for both samples were plotted in s': t' space, where s' and t' represent the maximum normal and shear stresses, respectively. Drained stress paths of both the Afrimat sand and glass beads, in s': t' space, is presented in Figure 3-15. Tangent lines depicting both the critical state and peak failure lines are illustrated in the same figure. These tangent lines were fitted to pass through the origin of the graph as both materials were considered to be cohesionless. The peak and critical state friction angles are a function of the angle of the tangent line with the horizontal and were calculated by applying Equation 3-4.

$$tan\theta = sin\phi \qquad \text{Equation 3-4}$$

Where:

θ = Angle between the tangent line and the horizontal in s': t' space

ϕ = Friction angle of the material

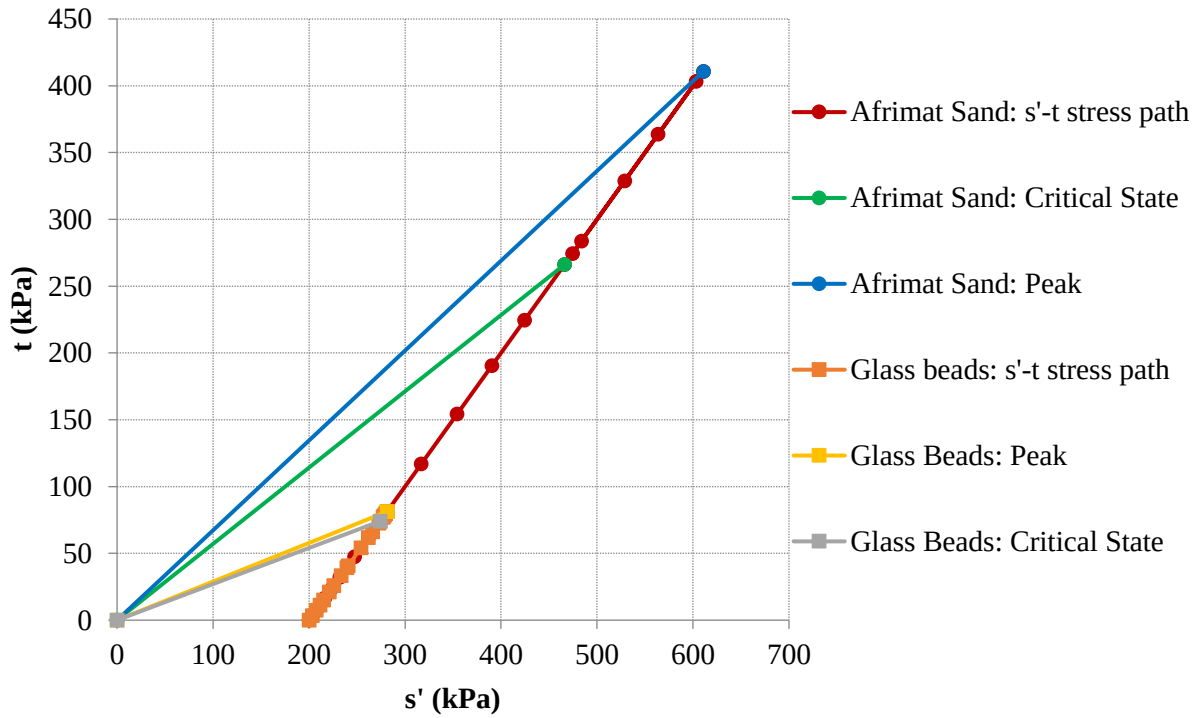

Figure 3-15: Afrimat (fine-grained) sand and glass beads triaxial test stress path in s':t' space at 200 kPa effective stress

The sample failure modes for the triaxial tests of the fine-grained Afrimat sand and glass beads are shown in Figure 3-16 (a) and (b), respectively. Although a diagonal failure plane appears to be evident in both images, it is strongly defined in the Afrimat sand sample shown in Figure 3-16 (a).

(a) (b)

Figure 3-16: Photographs of the (a) Afrimat sand and (b) glass beads triaxial test samples after sample failure

Table 3-5 presents the friction angles derived from the results of the two triaxial tests, as well as those determined by Archer (2014) for the Consol sand. The Consol sand friction angles were obtained for a relative density of 80%.

Table 3-5: Summary of the peak and critical state friction angles of the three geomaterials

	Consol Sand (Coarse-grained)	Afrimat Sand (Fine-grained)	2 mm Glass Beads
Peak Friction Angle (°)	39.0	42.3	16.8
Critical State Friction Angle (°)	32.0	34.8	15.7

The difference in shear strength between the fine-grained sand and glass beads is demonstrated in Figure 3-17 which depicts the deviatoric stress versus axial strain relationships for both materials, based on their respective triaxial test results. In addition to having a much greater strength than the glass beads, the fine-grained material exhibits a distinct difference (35.2%) between its peak and critical state (or residual) strength characteristics. Whereas a negligible reduction in strength is observed in the post-peak behaviour of the glass beads. The difference in peak and critical state friction angles listed in Table 3-5 further illustrates this behaviour.

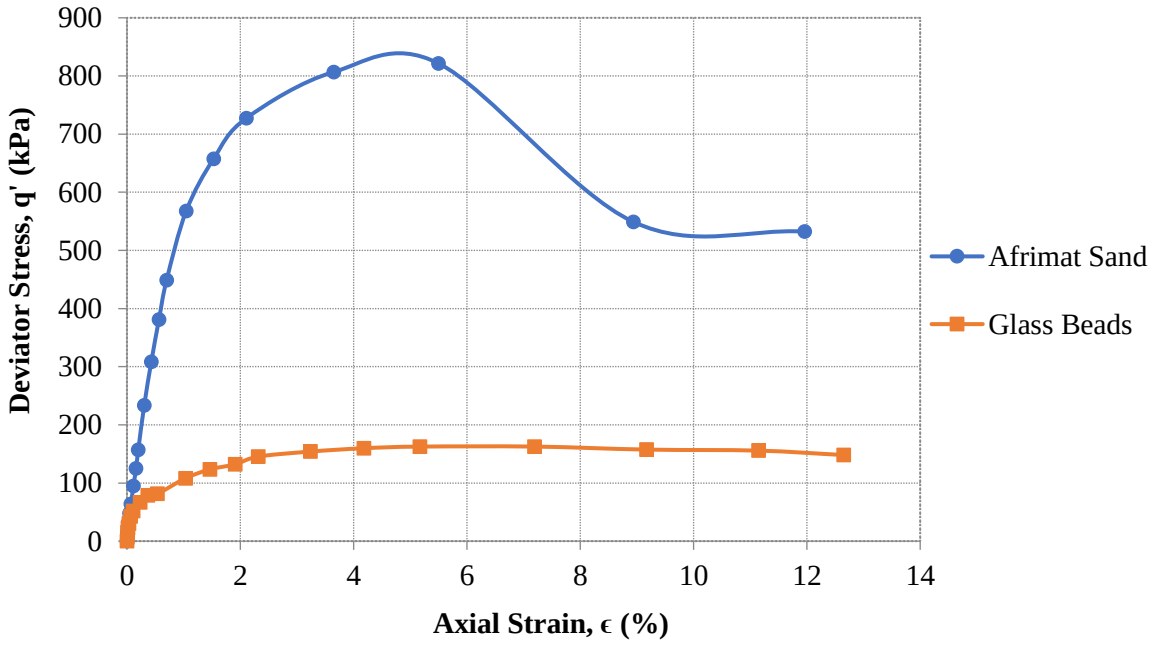

Figure 3-17: Deviatoric stress versus axial strain relationships of the Afrimat sand and glass beads

3.4.7 Particle size effects

Iglesia et al. (2011) investigated the validity of soil system centrifuge modelling by means of a trapdoor experiment. A "modelling-of-models" exercise was undertaken to determine whether particle-size

scaling was required to achieve model-prototype similitude. The structure-to-average grain size ratio was used as the primary variable in the investigation.

The validity of soil system centrifuge testing is often questioned as the overall system dimensions are scaled but the soil grain sizes are not (i.e. the soil type corresponding to the prototype is used in the scale model). Taylor (1995) observed that particle size scaling would be a concern when, for example, a coarse gravel was used in a small-scale model at high gravitational acceleration, as the stress-strain behaviour of the soil in the model would not correspond to that of the prototype. Local effects of the soil particles would prevent the soil from appearing to behave as a continuum. He therefore recommended that a critical ratio, between the major dimension of the model and the average grain diameter, be established to prevent particle-size effects in centrifuge modelling.

In their "modelling-of-models" investigation of the trapdoor experiment, Iglesia et al. (2011) found that with a structure-to-grain size ratio (or B/D_{50}) of at least 20, particle size effects appeared to be negligible and particle size scaling was therefore deemed to be redundant for some geotechnical applications. They concluded that the various trapdoor experiment models with a B/D_{50} ratio greater than 20 behaved similarly up to the point of maximum arching after which particle size effects tended to play a more significant role in the post-peak deformation mechanisms.

Given that the trapdoor in this study had a width of 50 mm and that Iglesia et al. (2011) recommend a minimum structure-to-grain size ratio of at least 20 for a trapdoor experiment, the maximum particle diameter that could be used in the model, with negligible particle size effects, was 2.5 mm. Glass beads of 2 mm diameter were therefore selected to replicate the trapdoor experiment conducted using both the Afrimat and Consol sands. The advantage of modelling the trapdoor experiment with glass beads is that there is minimal variation in the material properties, and it is therefore the ideal tool for a parametric study (Iglesia et al., 2011).

3.5. MODEL PREPARATION

The first step of the model preparation procedure was to ensure that the trapdoor lowering system was fully de-aired. This was done to minimise any trapdoor lowering during spin-up of the centrifuge. Frictionless translation of the trapdoor was attempted by placing Scotch Magic Tape, with a lip, along the front and back edges of the trapdoor. The lip created a container effect which prevented any sand grains from falling in the gaps between the trapdoor and neighbouring surfaces. All four side faces of the trapdoor were sprayed with a lubricant oil (Q20), to assist with smooth displacement of the trapdoor. Furthermore, the slight gaps between the trapdoor and adjacent model bases and backplate were filled with petroleum jelly (Vaseline). This measure was implemented to prevent fine sand particles from entering the gaps and jamming the door, as well as to assist with a smooth trapdoor translation. Before

the front glass panel was fixed to the trapdoor apparatus, it was cleaned with alcohol to assist with subset identification during PIV analysis and to reduce friction effects between the geomaterial and glass. The glass panel was then fixed in place and silicon was used to seal any gaps between the glass and model frame. Finally, for both the Consol and Afrimat sand models, a small sample of sand with a moisture content of 5%, was placed directly over the trapdoor, and the adjacent interfaces with the model base, to add some cohesion to the materials and prevent any fines from being pushed into the gaps at elevated gravitational acceleration.

Once the model had been sufficiently sealed, pluviation of the granular materials could commence. A 1.3m long flexible hose with a 50 mm diameter was connected to a hopper above the model, as shown in Figure 3-18 (a). A 300 mm ruler was fixed to the end of the pipe and it was used to maintain a near-constant drop height, with a variance of approximately 50 mm, to ensure a uniform bulk material model. In addition to the consistent drop height, the pipe was angled to be near vertical and the material flow rate through the pipe was low enough to ensure that the resulting model material was dense, uniform and layered horizontally. A high-density model was chosen as this is believed to best represent the *in-situ* conditions for cohesionless dolomitic residuum. Coloured sand (pink and blue) was placed manually at approximately 70 mm height intervals to highlight the shear band formation during trapdoor lowering. Figure 3-18 (b) presents a photograph of a Consol sand model with evenly spaced coloured bands during pluviation.

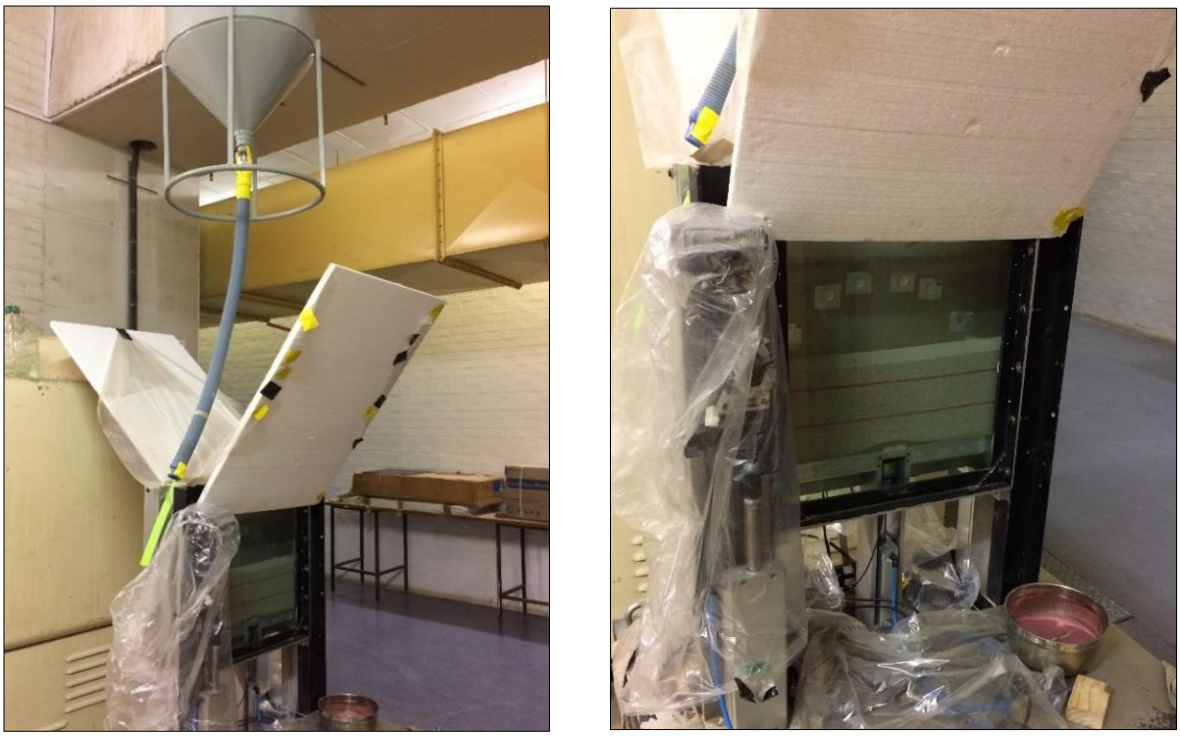

(a) (b)

Figure 3-18: (a) Trapdoor apparatus pluviation system (b) Consol sand model during the pluviation process

Once the model had been filled to the required height, five LVDTs were placed on the material surface and the model was transferred to the centrifuge where the remaining instrumentation devices were placed and connected to the various data acquisition ports. Figure 3-19 (a) shows a photograph of an Afrimat sand model just before it was placed on the centrifuge model platform. The second photograph, in Figure 3-19 (b), depicts the glass beads model once it had been successfully placed on the platform.

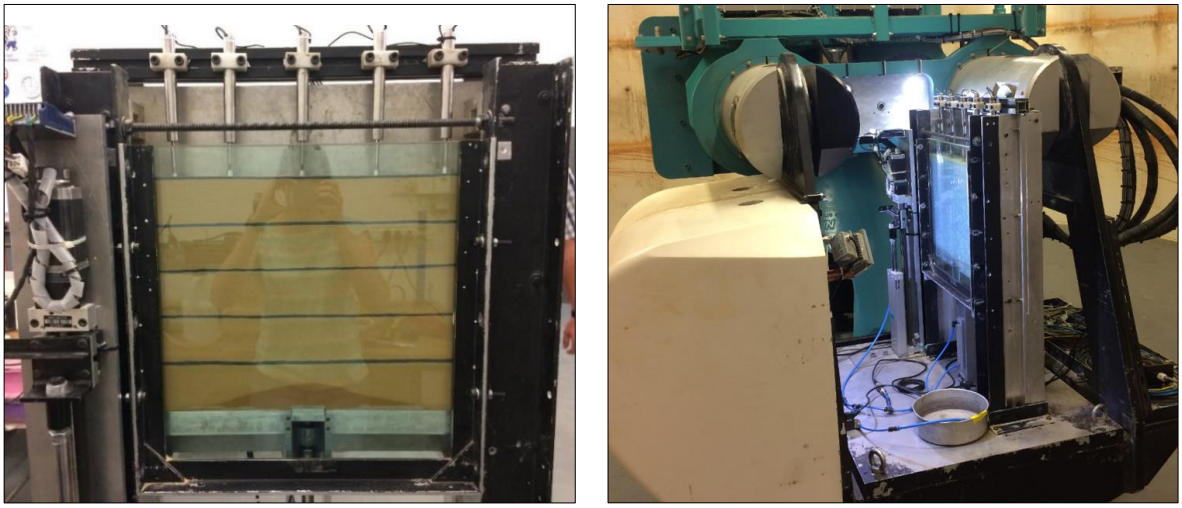

(a) (b)

Figure 3-19: (a) Afrimat sand trapdoor experiment model, (b) trapdoor apparatus positioned on the centrifuge model platform

3.6. TEST PROCEDURE

A single test procedure was employed for all three materials. Once the model had been placed and carefully positioned on the centrifuge model platform, the electronic connections for the stepper motor, solenoid valves, LVDTs, load cell and pressure transducer were secured. Instruments whose readings were measured using the DigiDAQ system (i.e. the surface settlement LVDTs and pressure transducer readings) were calibrated before centrifuge spin-up could commence. The camera was placed in the centrifuge basket, adjacent to the model platform, and angled upwards towards the front glass pane of the model. Photographs were taken at a set rate, starting just before trapdoor lowering commenced. Centrifuge spin-up was initiated once the response of each of the measuring instruments, including the camera, had been tested and verified. The centrifuge spin-up was paused at an acceleration of approximately 4g for the counterweight to be adjusted automatically, based on the weight and centre of mass of the model.

Premature separation of the trapdoor during spin-up is a well-known obstacle for trapdoor experiments conducted in a centrifuge facility. Relative differential settlement of the trapdoor and adjacent base

occurs during centrifuge spin-up as a result of the different stiffnesses of these two elements. The relative displacement results in the activation of the arching effect in the overlying soil and as a result, the load measured on the trapdoor is not consistent with the theoretical geostatic load (Dewoolkar et al., 2007). The trapdoor of the experimental model used by Iglesia et al. (2014) had a greater stiffness than the adjacent base, resulting in relative upward displacement of the trapdoor during spin-up and the activation of passive arching. A compensatory "pre-lowering" of the trapdoor was applied incrementally during the spin-up to obtain geostatic load conditions at the onset of trapdoor lowering. Iglesia et al. (2014) report that although the "pre-lowering" partially prohibited relative displacement, the measured load on the trapdoor was still 20% greater than the theoretical overburden stress. Dewoolkar et al. (2007) used a trapdoor experiment model where the trapdoor had a smaller stiffness than the adjacent base. To prevent premature trapdoor lowering during centrifuge spin-up, an elaborate pre-compression assembly was developed and implemented. Using the pre-compression assembly, a predetermined compressive force was applied gradually during spin-up. The trapdoor setup used in the investigation of cavity propagation in this study was similar to the model used by Dewoolkar et al. (2007), as the base adjacent to the trapdoor had a greater stiffness than the trapdoor itself. In an attempt to prevent premature trapdoor settlement without a pre-compression mechanism the stepper motor was programmed to initiate an upward trapdoor displacement at approximately 30g. The trapdoor did not translate upward, but upward pressure below the trapdoor increased significantly to counter the effect of increased gravitational acceleration on the stiffness differential of the model floor. This technique was found to reduce the initial downward displacement of the trapdoor, however, it was not sufficient to ensure geostatic load cell readings at the initiation of trapdoor lowering.

Once the centrifuge had reached the required acceleration of 50g, and the various LVDT, load cell and pressure transducer readings had stabilised at the constant gravitational acceleration, the trapdoor was lowered continuously at the predetermined rate. The trapdoor was lowered to the maximum stroke of the trapdoor piston, i.e. 100 mm. Where tests included the load cell, the stroke length was restricted to approximately 85 mm. Instrumentation readings from the load cell, LVDTs and pressure transducer were taken from the start of the centrifuge spin-up, continuously during trapdoor displacement, until the centrifuge was stopped.

3.7. TEST SCHEDULE

Five successful trapdoor experiments were undertaken using the three materials described in Section 3.4. The test schedule in Table 3-6 summarises the details of each of the successful tests. The pre-compression pressure describes the maximum pressure applied to the trapdoor, to limit premature trapdoor settlement, as measured by the pressure transducer at the point before trapdoor lowering was initiated.

As shown in Table 3-6, the relative densities of the models indicate that all five test model materials were classified as 'very dense'. Of significance is that the calculated relative densities of both coarse-grained material models were greater than 100%. For his master's dissertation, Oberholzer (2017) had also used the Consol sand to prepare a trapdoor experiment model with dense coarse-grained sand. Based on the minimum and maximum index densities he acquired by undertaking standard index density tests using the coarse-grained sand, he achieved relative densities of 134.3% and 128.7% for his trapdoor experiment models (Oberholzer, 2018). Samples of the Consol sand were subsequently sent to an accredited laboratory by him to conduct maximum and minimum standard density index tests for the material. The results of the laboratory tests, however, yielded even greater relative densities of the trapdoor models. Given the information provided by Oberholzer (2018) the relative densities presented in Table 3-6 were deemed to be acceptable for the purposes of this study. It is proposed that the reason for the significantly high relative densities is that the particle size distribution of the Consol sand is highly uniform (Figure 3-9) and the sand grains are well-rounded. The greater volume of the trapdoor apparatus, in comparison to the container used to determine the maximum and minimum index densities, allowed for a denser packing arrangement of the uniformly graded material.

Table 3-6: Test schedule for the trapdoor experiments undertaken in the centrifuge

Test ID	Soil Type	Bulk Density (kg/m^3)	Relative Density (%)	Load Cell	Pre-compression Pressure (kPa)
CF01	Fine	1693	93	No	555
CF02	Fine	1696	94	Yes	500
CC11	Coarse	1855	139	No	450
CC12	Coarse	1812	119	Yes	577
CG01	Glass beads	1684	76 -Regular*	Yes	437
			133 -Random*		

*Based on the regular or random packing arrangement of spheres detailed in Section 3.4.5, as described by Dullen (1992)

4. DISCUSSION OF RESULTS: CENTRIFUGE EXPERIMENTS

4.1. INTRODUCTION

This chapter presents a discussion of results of the physical deep trapdoor experiments undertaken in the centrifuge laboratory using fine-grained sand, coarse-grained sand and glass beads. Five experiments were undertaken according to the test schedule detailed in Table 3-6. Geomaterial behaviour corresponding to the initial, intermediate and final stages of the trapdoor experiments was investigated using the (1) trapdoor load-displacement results, (2) the deformation mechanisms derived from PIV image analyses, as well as (3) the surface settlement results.

The chapter commences with a presentation and discussion of the trapdoor load-displacement relationships and includes an analysis of the load and trapdoor displacement corresponding to point of maximum arching. The trapdoor load-displacement results are followed by the presentation, discussion and analysis of the deformation mechanisms and shear band formation associated with the various stages of trapdoor displacement. This section includes a critical analysis and theoretical comparison of the angle at which the initial shear bands propagate from the trapdoor edges. The surface settlement results are then presented and discussed in relation to the PIV shear strain plots. Finally, a collective analysis and correlation of all three sources of information, describing the geomaterial behaviour during trapdoor lowering, is undertaken as conclusion to the chapter. The trapdoor load-displacement, shear deformation and surface settlement results are discussed and analysed to gain better understanding of arching and the role of material properties, with specific reference to the material shear strength, in soil arching during sinkhole propagation.

4.2. TRAPDOOR LOAD-DISPLACEMENT BEHAVIOUR

4.2.1 Rate of trapdoor displacement

As detailed in Section 3.7, five trapdoor experiments were undertaken. A load cell was fixed to the bottom of the trapdoor in three of the experiments to measure the variation of load on the trapdoor during trapdoor displacement. Each of the three tests was undertaken using a different material, namely fine-grained sand (CF02), coarse-grained sand (CC12) and 2 mm diameter glass beads (CG01). As noted in Section 3.3.2, the rate of trapdoor displacement was found to vary somewhat despite fixing the motor velocity to yield the desired trapdoor displacement of 0.025 mm/s. The graphs depicting the linear relationship of the trapdoor displacement with time are shown in Figure 4-1 in addition to the trapdoor displacement rates for the three tests (i.e. the gradients of the graphs). The maximum difference of 6% between the trapdoor displacement rates of the three tests was deemed to be negligible.

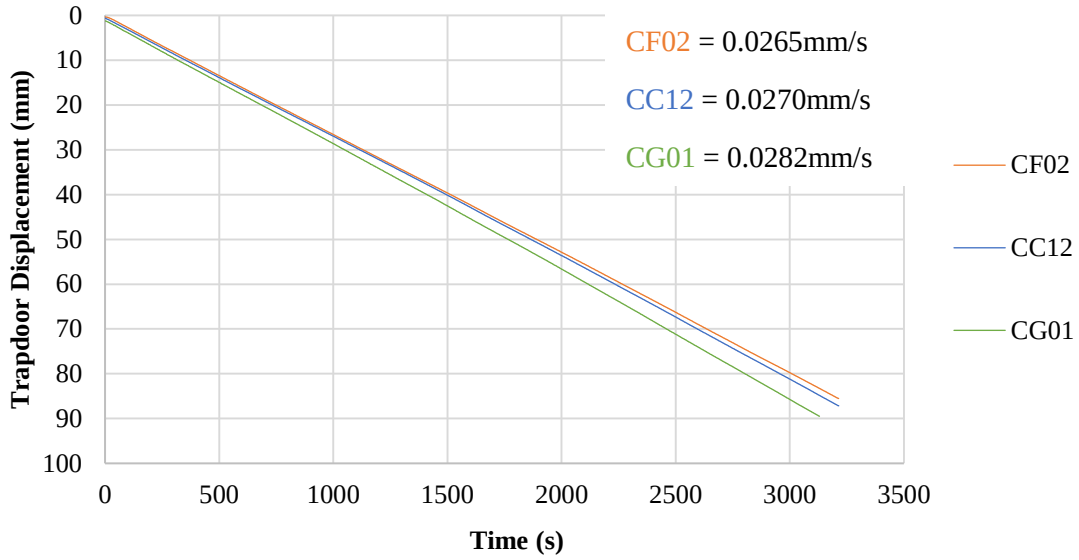

Figure 4-1: Rate of trapdoor displacement for tests CF02, CC12 and CG01

Although not distinctly visible, the three graphs depicted in Figure 4-1 do not initiate at the origin of the two axes as a result of premature separation of the trapdoor, from the strongbox base, during centrifuge spin-up (Section 3.6). Despite attempts to counter the effects of the stiffness differential between the trapdoor and adjacent base by using the motor to apply an upward pressure on the trapdoor, some controlled premature trapdoor displacement and associated load redistribution (arching) in the soil occurred before trapdoor lowering was initiated. The slight downward displacement of the trapdoor, detected during centrifuge spin-up, resulted in the initiation of soil arching prior to the centrifuge reaching its pre-determined test acceleration of 50g. Table 4-1 presents a summary of the trapdoor displacement rates, premature trapdoor displacement and theoretical geostatic load on the trapdoor at 50g.

Table 4-1: Trapdoor displacement rates and premature displacements (for tests CF02, CC12 and CG01)

Test	Trapdoor displacement rate (mm/s)	Premature trapdoor displacement (mm)	Theoretical geostatic load, p_0 (kN)
CF02	0.0265	0.29	1.143
CC12	0.0270	0.63	1.211
CG01	0.0282	1.26	1.045

4.2.2 Overview of trapdoor load-displacement results

Figure 4-2 presents the normalised load versus displacements graphs for CF02 (fine-grained), CC12 (coarse-grained) and CG01 (glass beads) trapdoor tests, with an applied moving average to minimise noise. It is common practice to present these results with normalised units for both the measured load and trapdoor displacement (Iglesia et al., 2014). In Figure 4-2, the units on the y-axis were normalised

by the theoretical geostatic load on the trapdoor (p_0) to ensure comparable results of the three materials with varying densities. The x-axis units (trapdoor displacement), however, were not normalised as the same ratio of trapdoor displacement to trapdoor width (50 mm) was used for all three tests.

The overall trapdoor load-displacement behaviour observed in the tests is comparable to that reported in literature (Terzaghi, 1936, Dewoolkar et al., 2007 and Iglesia et al., 2014). A near-instantaneous reduction in load is recorded at the onset of trapdoor displacement as a result of the induced boundary discontinuity at the edges of the trapdoor. The load reduces until the point of maximum arching is achieved (p_{min}), after which load recovery is observed with increasing trapdoor displacement. During load recovery the material at the edges of the trapdoor adjusts kinematically along these discontinuities, resulting in the propagation of new shear bands and an increase in the load measured with the additional volume of geomaterial contributing to the load on the trapdoor (Dewoolkar et al., 2007). Finally, the ultimate load (p_{ult}) is achieved when the normalised load displays asymptotic behaviour and no longer increases with an increase in trapdoor displacement (see Figure 2-13 (a) in the Literature Review). Although the overall behaviour is comparable to that described in literature, some variation of this typical trapdoor load-displacement behaviour was observed in all three tests. These variations are discussed below, as well as in the collective analysis of results in Section 4.5.

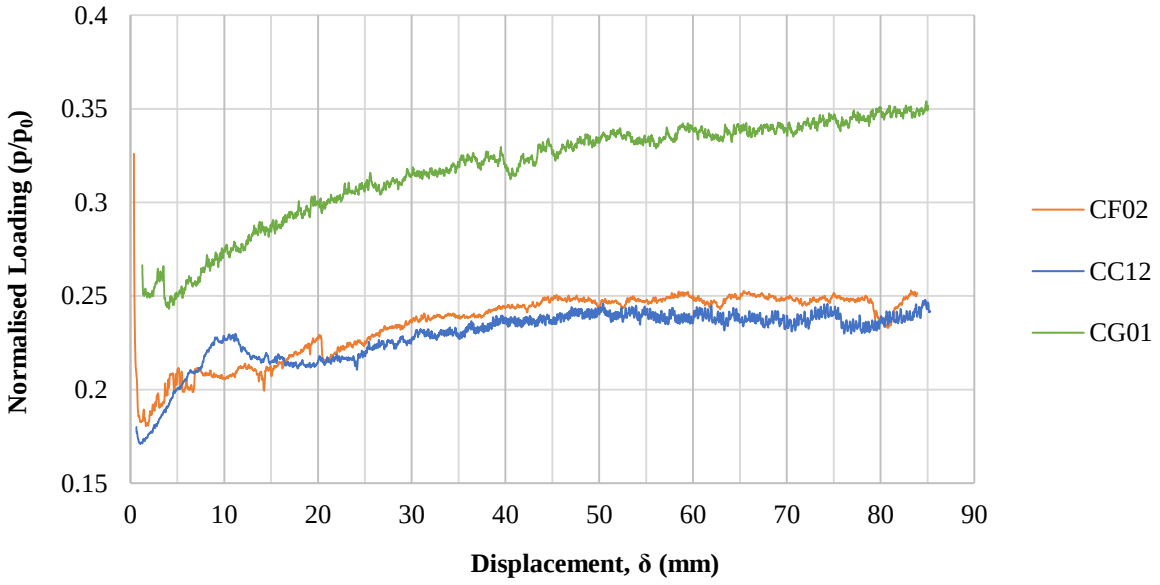

Figure 4-2: Normalised load versus trapdoor displacement

Upon closer inspection of the data presented in Figure 4-2 all three datasets exhibited some irregular behaviour at some point during trapdoor displacement. Although the general trend of the trapdoor load-displacement curves appears to follow the characteristic shape from literature (see Figure 2-8 and Figure 2-13 in Chapter 2), the missing load information at the start of some of the tests and the noisy nature of the data suggest that factors such as friction affected the load measurements taken for all three tests

during trapdoor lowering. These factors include side-wall friction of the cohesionless materials against the glass pane, as well as friction between the lowering trapdoor and its interfaces. Theoretically the starting value for the three graphs should have been a normalised load value of 1.0. Both CF02 and CG01 demonstrate an initial characteristic decline in load, but as a result of premature lowering of the trapdoor during centrifuge spin-up the normalised load drops from a maximum of approximately 0.33 instead of 1.0. The minimum load, presented as P_{min} in Dewoolkar et al.'s (2007) quantitative load-displacement curve (Figure 2-13 (a)), represents the point of maximum arching. This point is depicted clearly in the results for CC12, however, the full geostatic load for this test appears not to have been transferred to the trapdoor during centrifuge spin-up.

Furthermore, some irregularities in the gradients of the graphs exist. For both CC12 and CF02 the most notable irregularities in the load-displacement graphs occur between approximate trapdoor displacements of 6 mm and 21 mm. These deviations from characteristic trapdoor load-displacement behaviour may be attributed to friction between each of the sides of the rectangular trapdoor and the respective adjacent surface, namely the backplate of the strongbox, the sides of the model base plates or the glass panel at the front of the strongbox. It is likely that grains of sand (both coarse and fine) became wedged in the small slits along the edges of the trapdoor, giving rise to additional friction during trapdoor lowering. The induced friction would lessen the measured load on the trapdoor after which an instantaneous increase in load would be measured once the particle(s) had crushed or displaced with the trapdoor, allowing the full load of the soil to be measured by the load cell. An irregular increase in load may be attributed to the instantaneous termination of one shear band and the initiation of the next, at which point additional load would be measured on the trapdoor (as presented in Section 4.3.3).

4.2.3 Point of maximum arching

Figure 4-3 presents the trapdoor load-displacement results for the initial portion of the trapdoor experiments where conditions of maximum arching, corresponding to minimum load measured on the trapdoor, was observed for all three tests. The dotted lines present idealised trapdoor load-displacement behaviour of the materials based on typical trapdoor load-displacement curves from literature and the solid lines the actual measured data. Table 4-2 presents the maximum arching characteristics of the three tests. Both natural sands appear to arch at trapdoor displacements which correspond to typical values specified in literature. Iglesia et al. (2014), who undertook trapdoor experiments using both natural sands as well as glass beads, state that the minimum load typically occurs at a normalised displacement of between 2% and 6%, whereas Dewoolkar et al. (2007) observed that the point of maximum arching occurs at 1% to 2% of the normalised trapdoor displacement in their experiments with only natural sands. Based on the measured data for the glass beads, and as indicated in the table, the point of maximum arching does not fall within the typical range of normalised displacements. However, based on the idealised curve the point of maximum arching would occur at an approximate normalised displacement of 5%.

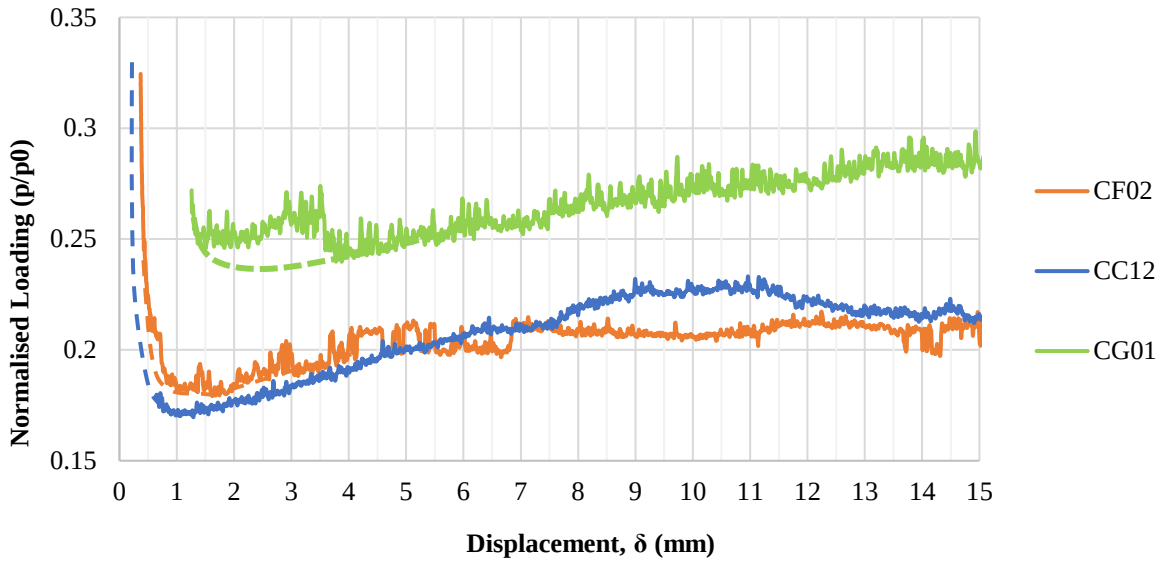

Figure 4-3: Normalised trapdoor load-displacement graphs for 15 mm displacement of the trapdoor

Table 4-2: Trapdoor displacement at the point of maximum arching

	CF02	CC12	CG01	CG01 (idealised)
Trapdoor Displacement (mm)	1.62	1.29	3.88	2.50
Relative Trapdoor Displacement, δ/B (%)	3.2	2.6	7.8	5.0

4.3. DEFORMATION MECHANISMS DURING TRAPDOOR DISPLACEMENT

4.3.1 Soil deformation images

Coloured horizontal bands of fine- and coarse-grained sand were placed in the models in tests CF02 and CC12 during the pluviation procedure. These bands were placed at intervals of approximately 70 mm and were included to visualise the formation and propagation of shear bands during continuous trapdoor lowering in the centrifuge facility in addition to PIV. Table 4-3 presents inflight photographs of (a) CF02 and (b) CC12 at various stages of trapdoor displacement. The discontinuities in the coloured bands represent the locations at which shear bands, propagating from the trapdoor edges, intercepted the coloured bands. The photographs in Table 4-3 (a)(i) - (iii) show that the shear bands for CF02 propagated fairly symmetrically for the first 20 mm displacement of the trapdoor. The results presented below further demonstrate that for natural sands with a high relative density the shear bands tended to propagate vertically from the edges of the trapdoor.

It was further observed that at 20 mm trapdoor displacement, the shear bands of CF02 (Table 4-3 (a)(iii)) had intercepted, and therefore propagated beyond the second coloured band. Conversely, no discontinuities are noticeable in the second coloured band of test CC12 after 20 mm displacement of the trapdoor (Table 4-3 (b)(iii)). Although some settlement of the band had taken place, the shear bands

had not propagated beyond the height of the second coloured band. Based on these results, as well as the PIV results presented in Section 4.3.3, it can be postulated that the propagation of shear bands occurs at a greater rate in the fine-grained materials than in the coarse-grained materials; indicating that the rate of shear band propagation is influenced by the ratio between the mean particle size and trapdoor width.

Table 4-3: Inflight photographs depicting the shear band formations of (a) CF02 and (b) CC12 at trapdoor displacements of (i) 5 mm, (ii) 10 mm, (iii) 20 mm, (iv) 40 mm and (v) 80 mm (Note: Sand was moistened above the trapdoor to prevent sand leaks during testing.)

(a) CF02	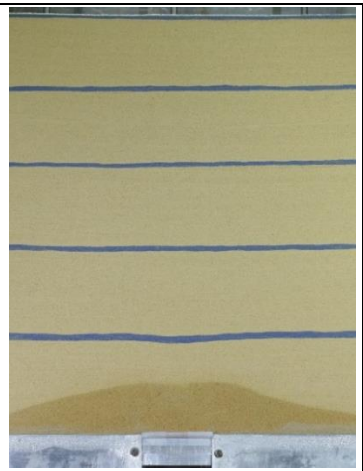	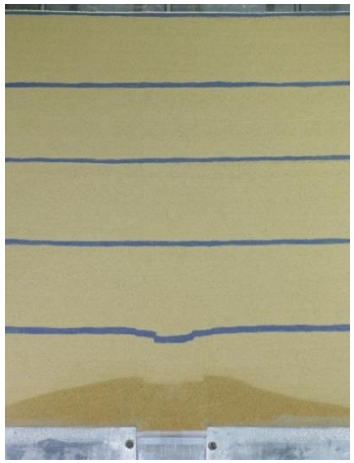	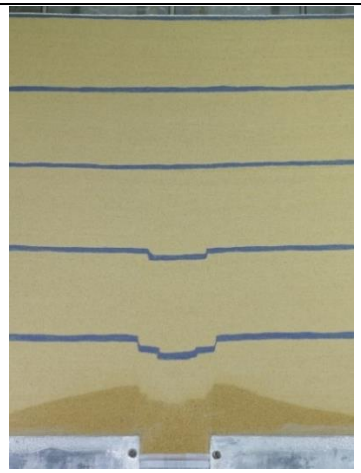	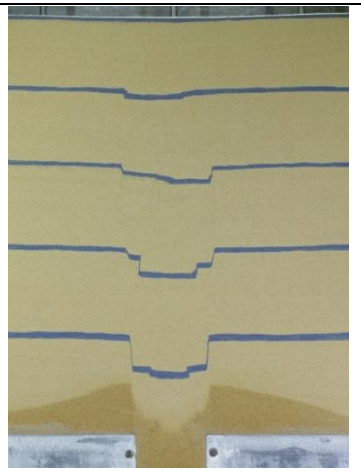	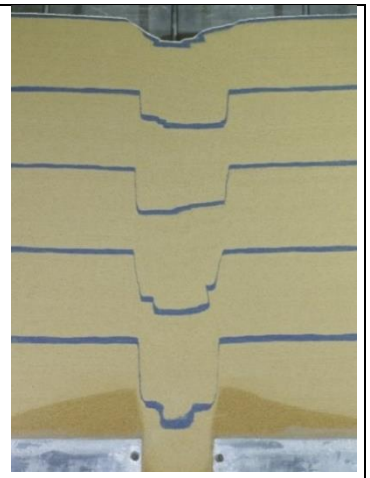
	(i) 5 mm	(ii) 10 mm	(iii) 20 mm	(iv) 40 mm	(v) 80 mm
(b) CC12	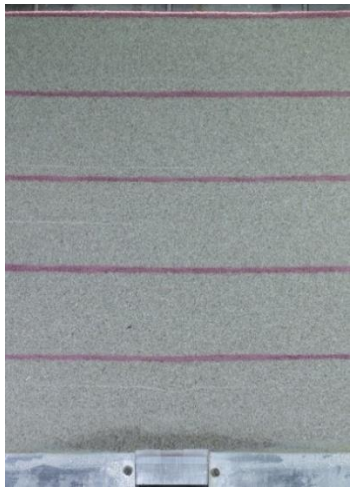	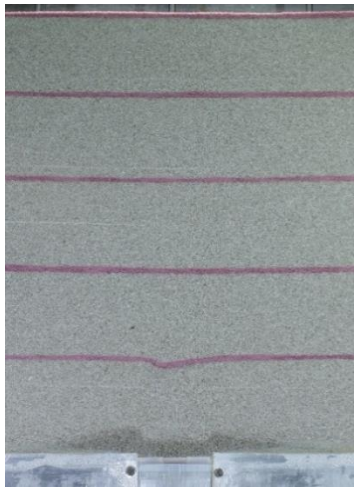	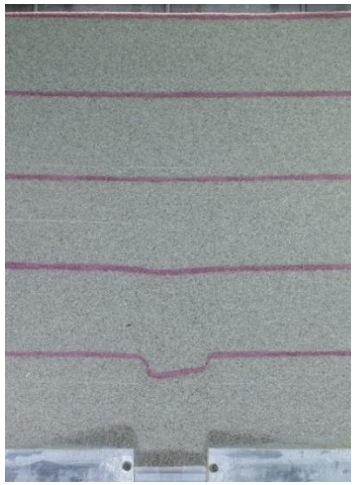	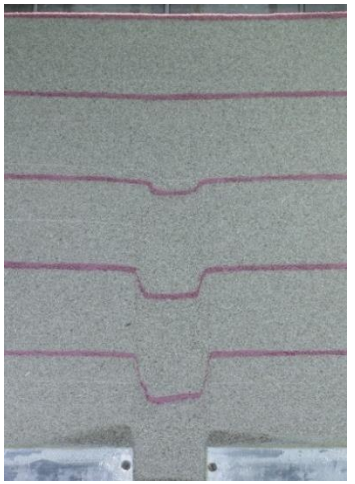	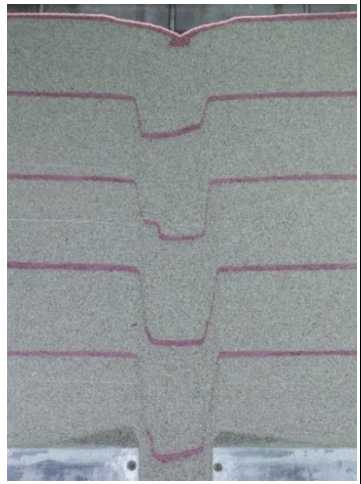
	(i) 5 mm	(ii) 10 mm	(iii) 20 mm	(iv) 40 mm	(v) 80 mm

4.3.2 Initial mechanisms of deformation

Five trapdoor experiments were undertaken during centrifuge testing, however, only three of the tests included a load cell below the trapdoor. Only the results of these three tests were therefore discussed in the preceding section. The total shear strain results, presented in the following sections, were compiled using PIV image analysis and present the total (cumulative) shear strain plots for each of the five tests at specific trapdoor displacements. These results give insight into the deformation mechanisms associated with arching and cavity propagation during trapdoor lowering.

At maximum arching conditions a shear strain band with an arch-like shape is known to form across the width of the trapdoor (Iglesia et al., 2014; Dewoolkar et al., 2017, and others). Actual arching involves stress redistribution of the material in a zone well above the apex of the arch. Stress redistribution (arching) allows for a large portion of the load on the trapdoor to be transferred to the base of the strongbox, adjacent to the edges of the trapdoor, with minimal trapdoor displacement (see stress redistribution schematic for active arching in Figure 2-7 (a)). As detailed in Section 4.2.2, the smallest load (p_{min}) is measured on the trapdoor at the point of maximum arching, as only the material directly above the trapdoor (below the arch-like shear band) contributes to the load.

The total shear strain plots depicting the material deformations associated with the point of maximum arching and a trapdoor displacement of 5 mm ($\delta/B = 0.1$) are presented in Table 4-4 (a) and (b), respectively. As the trapdoor load-displacement results were used to determine the point of maximum arching condition for tests CF02, CC12 and CG01, it was assumed that maximum arching conditions during CF01 and CC11 (no load cell used during testing) occurred at displacements corresponding to that of CF02 and CC12, respectively. The results in Table 4-4 (a) are presented at the same shear strain magnitude, except for Table 4-4 (a)(v) which displays the shear strain results for the glass beads. The point of maximum arching for the three materials tested occurred at different trapdoor displacements as shown in Table 4-2. This is the reason for the distinct difference in shear strain magnitude recorded for the results in Table 4-4 (a). The coarse-grained material reached the point of maximum arching at the smallest trapdoor displacement, and the smallest mobilised shear strains are therefore associated with this material at maximum arching conditions. Greater shear strains (dark red) are recorded for the fine-grained materials and finally, the strains recorded for the glass beads would be too large to compare accurately and are therefore presented at a different scale.

A shear strain band with an arch-like shape, spanning the width of the trapdoor, formed at maximum arching conditions during both coarse-grained sand experiments. However, the fine-grained sand samples did not establish a clearly defined closed shear strain arch. Although a shear strain band resembling that of an arch formed in the fine-grained material models, an open shear band can be seen at the apex of the arch at conditions of maximum arching (Table 4-4 (a)(i) and (ii)). Rui et al. (2016-b) only recorded full shear arch developments in tests with very large H/B ratios ($H/B \geq 6$) and

comparatively narrow trapdoor widths. Trapdoors with a comparatively greater width (B) resulted in initial triangular shear band formations, not curved arches. The reason that the fine-grained material did not yield a complete curved arch deformation pattern during trapdoor lowering is attributed to its lower D_{50} to B ratio, in comparison to that of the coarse-grained sand. Although the trapdoor width was constant for all the tests undertaken in the centrifuge, the ratio of the materials' average grain size to trapdoor width was not. An arch-like region of high shear strain is observed for the glass beads experiment too. The low correlation coefficients employed in the PIV analyses for the glass beads trapdoor experiment (required for reasons of convergence), as well as the large particle size, resulted in indistinct shear strain band formation. The difference between an arch-like and triangular shape shear band is therefore not distinguishable for the glass beads material.

The second stage of the deformation process, according to Iglesia et al. (2014), involves the formation of shear bands in the shape of a triangle above the trapdoor. Findings by Rui et al. (2016-b) support this, as straight slip planes (forming triangular deformation patterns) were observed for most of their tests, regardless of the H/B or D_{50} to B ratios. This triangular shaped mechanism was observed in all four natural sand models. At 5 mm trapdoor displacement, complete triangles were formed in both fine-grained sand models, whereas triangles with a slight curve at the peak were formed in the coarse-grained material models, as shown in Table 4-4 (b). For the glass beads model, the same triangular shape remained fairly constant during the initial stages of trapdoor displacement.

To relate the deformation mechanisms observed in Table 4-4 to the trapdoor load-displacement results recorded in Table 4-2, it is of significance to note that the greater the density of the material, and corresponding greater mobilised friction angle and dilatancy, the smaller the size of the arch-like shear band above the trapdoor required to initiate conditions of maximum arching. Consequently, the smaller the arch, the smaller the relative trapdoor displacement required to reach maximum arching conditions (Dewoolkar et al., 2007). It is therefore expected that for materials with a comparatively lower shear strength, the minimum load will be measured at greater displacements of the trapdoor. This is evident in the results listed in Table 4-2. The difference in the recorded trapdoor displacements at which the point of maximum arching occurred for the three materials is therefore in accordance with their shear strength, which is dependent on their relative densities and friction angles. The results therefore compare well to those in literature, as illustrated in Figure 2-8 (Terzaghi, 1936; revised by Evans, 1983).

Iglesia et al. (2014) found that regardless of the overburden material height, the actual load measured on the trapdoor at the point of maximum arching was the same for all tests performed with the same material, at the same density. This was attributed to the constant volume of material under the arch-like shear band directly above the trapdoor. Based on the trapdoor load-displacement results presented in Figure 4-3, it was found that the actual loads in CF02 and CC12 at the point of maximum arching were 204.9 N and 205.4 N respectively. The negligible difference in the actual minimum load measured

between the two materials, at maximum arching conditions, is considered to be attributable to the similar strength properties and relative densities of these two material models.

Table 4-4: Total shear strain plots (from PIV) corresponding to conditions of (a) maximum arching and (b) 5 mm trapdoor displacement for centrifuge tests (i) CF01, (ii) CF02, (iii) CC11, (iv) CC12 and (v) CG01 (units in percentage)

(a) Maximum arching	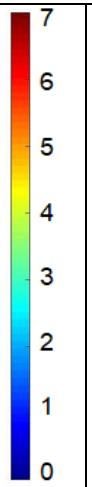	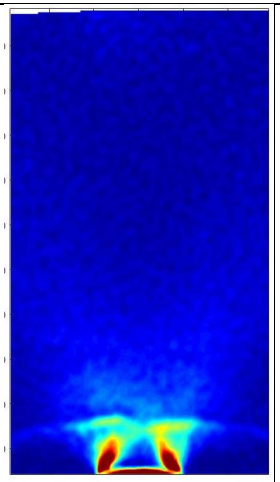	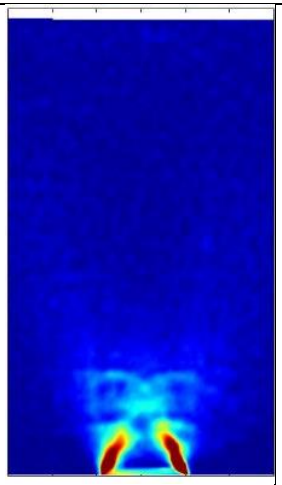	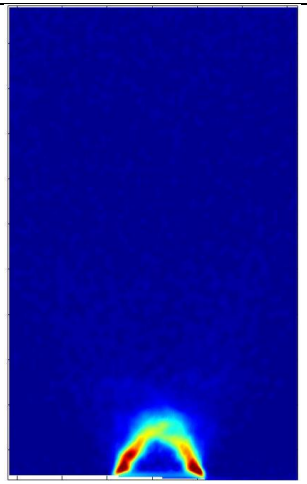	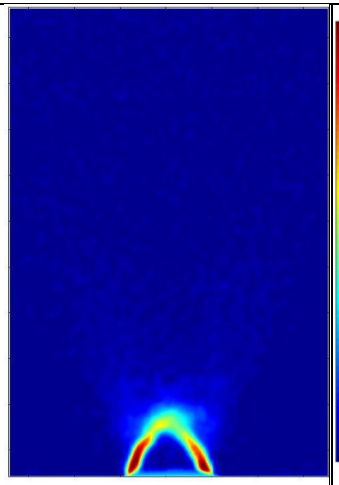	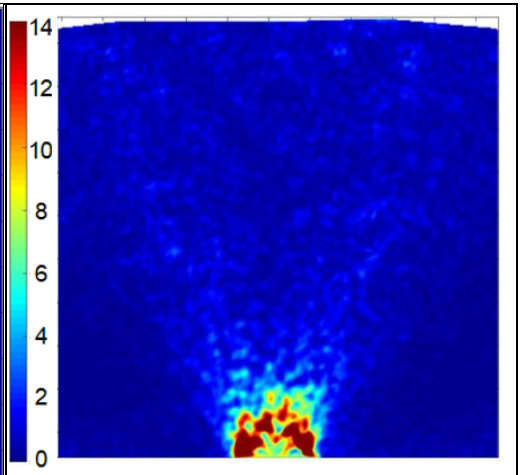
		(i) CF01	(ii) CF02	(iii) CC11	(iv) CC12	(v) CG01
(b) 5 mm Trapdoor displacement	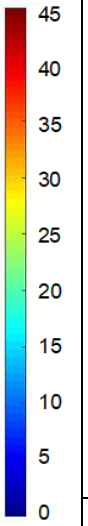	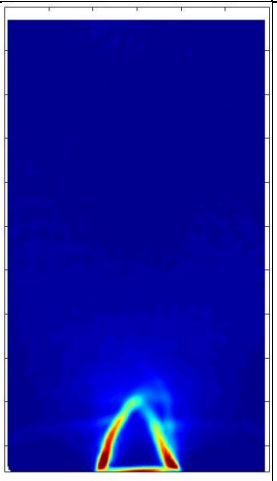	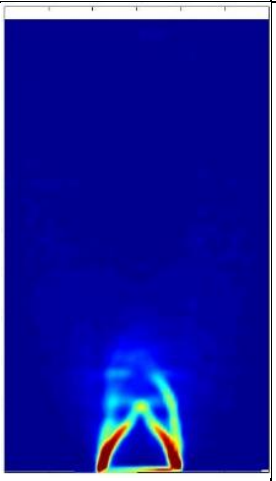	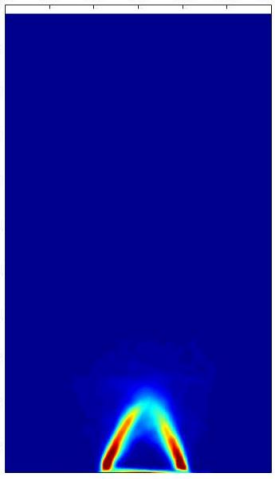	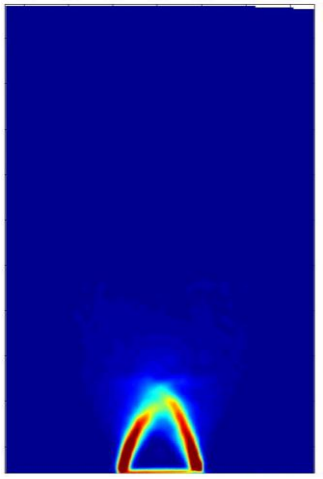	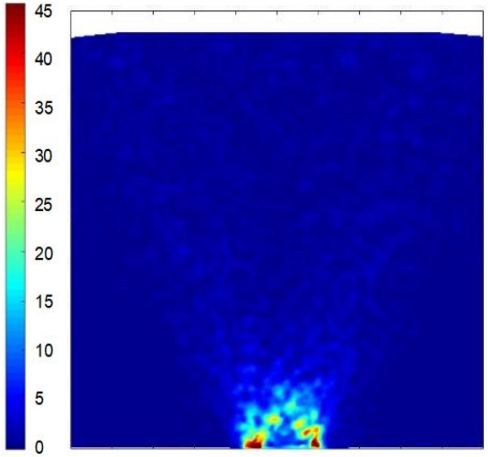
		(i) CF01	(ii) CF02	(iii) CC11	(iv) CC12	(v) CG01

4.3.2.1 Comparative theoretical analysis of initial shear band formation

As discussed in Section 2.3.3, many researchers have investigated the deformation mechanisms associated with deep trapdoor experiments. Evans (1983), Dewoolkar et al. (2007), Stone & Wood (1992) and several others proposed that the angle of the shear band to the vertical is dictated by the dilation angle of the material. Stone & Wood (1992) found that the direction of the shear band, propagating from the trapdoor edge, was constrained due to the dilation angle mobilised within the shear zone. This finding was founded on Bolton's (1986) theory of suppressed dilation at high confined stresses. Dewoolkar et al. (2007) further applied Bolton's (1986) relative density index (I_R) to calculate the stress-related maximum angle of dilation of the material. The relative density index is defined in Equation 4-1 and the corresponding angle of dilation is calculated by applying Equation 4-3 (Bolton, 1986). To determine the mean effective stress level (p') at the trapdoor depth, Dewoolkar et al. (2007) assumed a lateral earth pressure coefficient of K_0 (i.e. earth pressure coefficient at rest). The relative density index was therefore derived using the horizontal stress corresponding to the maximum vertical stress at the base of the trapdoor model at K_0. By applying Equation 4-3 they obtained results comparable to those recorded during their trapdoor experiments conducted at 1g and at 75g. In addition to the above, Dewoolkar et al. (2007) list Equation 4-2 as part of Bolton's (1986) general expressions for relating the peak angle of dilation and peak friction angle to the relative density index:

$$I_R = I_D(10 - \ln p') - 1 \qquad \text{Equation 4-1}$$

$$\varphi'_{max} - \varphi'_{cs} = 0.8\,\Psi_{max} \qquad \text{Equation 4-2}$$

$$0.8\,\Psi_{max} = 5I_R \qquad \text{Equation 4-3}$$

Where:

I_R = Relative density index

I_D = Relative density

p' = Mean effective stress level (kPa)

φ'_{max} = Peak friction angle (°)

φ'_{cs} = Critical state friction angle (°)

Ψ_{max} = Peak angle of dilation (°)

Evans (1983) was the first to assign the angle of dilation to the angle between the shear band and the vertical as shown in Figure 2-11 (b). Dewoolkar et al. (2007) employed this approach by using the peak

angle of dilation calculated from Equation 4-3 in their trapdoor analyses. As displayed in Figure 2-12 (c), the angle of dilation is known to decrease with an increase in strain, until it reaches zero at the critical state.

Both Iglesia et al. (2014) and Rui et al. (2016-a) relate the initial angle of shear band propagation to the friction angle of the material (Section 2.3.3). Iglesia et al. (2014) found that the angle at which both the arch-like and triangular deformation patterns initiate from the trapdoor edge to the vertical is equal to friction angle of the material (Figure 2-17). Although they did not specify whether the peak or critical state friction angle was used in this finding, only the peak friction angle is referred to in their discussion. Rui et al. (2016-a) assumed that the initial triangular surface planes are active rupture planes at an angle of 45° + φ'/2 to the horizontal and achieved greater correlation and repeatability when applying the critical state friction angle in their postulate. Equation 4-4 therefore presents the angle of the shear band to the vertical (θ) according to Rui et al. (2016-a):

$$\theta = 45° - \frac{\varphi'}{2} \qquad \text{Equation 4-4}$$

Table 4-5 presents the average angle of the left-hand and right-hand shear bands, measured to the vertical, for trapdoor displacements related to the point of maximum arching, as well as at 5 mm trapdoor displacement.

Table 4-5: Average measured angles of the shear bands to the vertical for the natural sand tests

	CF01	CF02	CC11	CC12
Point of maximum arching (°)	39.5	38.5	39.7	35.0
5 mm Trapdoor displacement (°)	26.0	30.3	25.9	24.3

Based on the above discussion, Figure 4-4 presents a comparison of the various methods used to predict the angle at which the shear bands propagate from edges of the trapdoor. The measured angles presented in Table 4-5 are used as an indicator of the applicability of the various methods. Findings by Iglesia et al. (2014) and Rui et al. (2016-a) based on the friction angle were investigated, as well as the widely accepted postulate that the shear bands propagate at the angle of dilation to the vertical (Evans, 1983; Dewoolkar et al., 2007; and others). A summary of the measurements and calculations used to determine the initial angles of shear band propagation is attached as Appendix A.

The initial angle of the shear bands, measured to the vertical and associated with conditions of maximum arching, was found to correspond best to Iglesia et al.'s (2014) proposal for the peak friction angle. However, they further propose that the triangular deformation pattern, which forms after the initial arch – following additional displacement of the trapdoor – does so at the same angle (i.e. at the friction angle

to the vertical). Based on the results from both Table 4-5 and Figure 4-4, this is not the case. The angle at which the triangular deformation pattern occurs, does so at a significantly smaller angle to the vertical. This corresponds to the reduction in dilation angle with increase strain and reduction in stress level during lowering of the trapdoor. It is possible that the first triangular deformation pattern formed before a trapdoor displacement of 5 mm. However, a review of the PIV shear strain plots at 1 mm intervals for the first 5 mm of trapdoor displacement showed that even during formation of the triangular deformation patterns, these initiated at a smaller angle to the vertical than the initial curved arch. It is of significance to note that the angle of dilation, calculated using Equation 4-3, also presented highly comparable results for the coarse-grained sand at maximum arching conditions.

For the triangular deformation patterns measured at a trapdoor displacement of 5 mm, Rui et al.'s (2016-a) solution, using the critical state and peak friction angles, were found to best replicate the results for the fine-grained and coarse-grained sands, respectively.

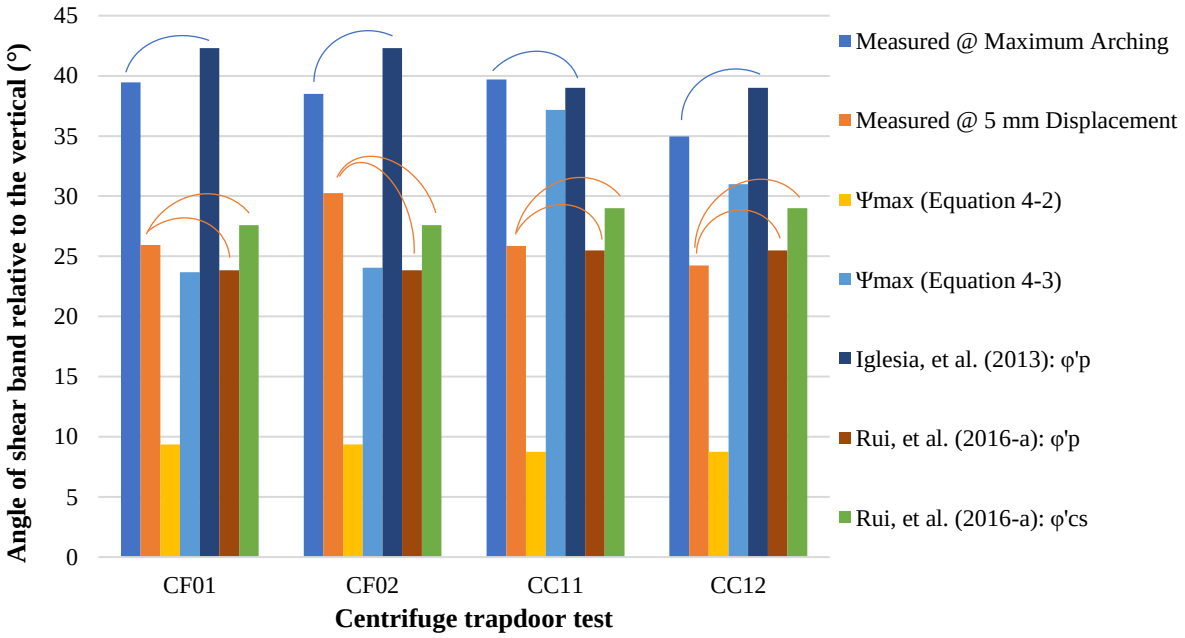

Figure 4-4: Comparison of methods used to calculate the initial angle of shear band propagation

Although not distinctly evident in Figure 4-4, a relationship between the measured angles at the point of maximum arching and the angle of dilation, calculated using the density index formulated by Bolton (1986) and applied by Dewoolkar et al. (2007), was found to exist. The reason that the relationship is seemingly apparent at this point, but not at greater trapdoor displacement, is because the density used in the calculation is applicable at maximum arching conditions. However, for greater displacement of the trapdoor (i.e. greater shearing) the density will reduce, thereby affecting the calculated angle of dilation. Similarly, stress conditions within the model are largely unknown and those assumed in this exercise are based on Dewoolkar et al.'s (2007) assumption that the maximum horizontal stress,

corresponding to an earth pressure coefficient at rest (K_0), should apply. As continuous stress redistribution occurs during trapdoor lowering, this assumption may not be applicable at greater trapdoor displacements. The angles between the shear band and the vertical for each of the natural sand test results, as well as the calculated angle of dilation at maximum arching conditions, is presented in Table 4-6. This data strengthens the conjecture that a relationship exists between the initial angle of dilation and the shear band orientation at maximum arching conditions. However, the variation in percentage difference between the two materials indicates that this relationship may be material dependent.

Table 4-6: Angles (in degrees) between the shear band and the vertical at conditions of maximum arching

	CF01	CF02	CC11	CC12
Point of maximum arching	39.5	38.5	39.7	35.0
Dilation angle (Equation 4-3)	23.7	24.0	37.2	31.0
Difference	15.8	14.5	2.5	4.0
% Difference	40.0	37.7	6.3	11.4

The results in Figure 4-4 show that a single method that can be used to calculate the angle of shear band propagation for all material types does not currently exist. Different prediction methods were found to yield best-fit results, depending on the material density, degree of strain (related to the trapdoor displacement) and material type. Equation 4-3, used to calculate the angle of dilation based on the density index, is the only method which showed some consistency in the relationship between the predicted angle and the measured angle for all four tests. It is also the only method which takes into account the density and stress level of the material.

Stone & Wood (1992) state that dilation, and the corresponding failure surface patterns, are greatly dependent on stress confinement, density and particle size. The particle size is not considered in Bolton's (1986) density index formulation for the angle of dilation. The stress confinement in the coarse- and fine-grained tests were very similar. The soil density and average particle size, however, varied somewhat. The apparent change in relationship between the angle of dilation of the fine-grained material and coarse-grained material, respectively, is therefore attributed to the variation in average particle size as well as soil density.

4.3.3 Intermediate and final state deformation mechanisms

Table 4-7 (a) and (b) present the shear strain bands for all five models at 40 mm and 80 mm trapdoor displacement, respectively. The onion-peeling effect of cavity propagation during sinkhole formation, postulated by Jennings et al. (1965), is observed in the shear strain results of the tests undertaken with natural sands, as shear bands propagating from the left- and right-hand edges of the trapdoor tend to alternate until they reach the surface. The deformation mechanisms observed for the natural sands may further be likened to the tower-shape mode attributed to deep trapdoor experiments by Rui et al. (2016-a,b). As shown in Figure 2-18, the tower-shape pattern involves vertical bands propagating from the edges of the trapdoor, which form advancing triangular peaks between the two vertical shear bands as they propagate towards the surface. As initially predicted by Terzaghi (1936), and later confirmed by several researchers, once the alternating shear bands reach the surface, vertical shear bands propagating from the edges of the trapdoor are the primary regions of shear strain as the trapdoor lowers to its final displacement.

Dewoolkar et al.'s (2007) qualitative description of a trapdoor experiment undertaken in a centrifuge facility, presented and discussed in Section 2.3.3, corresponds to the results of the four natural sand tests displayed in Table 4-7. As observed in the shear strain plots presented in Table 4-4, the secondary set of shear bands, corresponding to a trapdoor displacement of 5 mm, initiate at a smaller angle to the vertical than those corresponding to the trapdoor displacement at maximum arching conditions. Similarly, from the results in Table 4-7, it is evident that the angle of the shear bands with the vertical decrease with an increase in trapdoor displacement. This observation is most noticeable in the shear strain plots of CF02 and CC12 (Table 4-7 (b)(ii) and (iv)). As discussed previously, several researchers, including Costa et al. (2009), Stone & Wood (1992), Santichainaint (2002), Evans (1983) and Dewoolkar et al. (2007) relate the angle formed between the shear band and the vertical to the soil's dilatancy angle. The results in Table 4-7 support this supposition. As the trapdoor lowers, the soil's dilatancy decreases due to shearing of the material at the edges of the trapdoor and further along the vertical shear bands at greater trapdoor displacement. The angle of dilation will decrease until the material has been sheared to its critical state, at which point the angle of dilation is zero and vertical shear bands propagate to the surface, as observed in Table 4-7 (b)(i) to (iv).

The stress level profiles of tests undertaken in the centrifuge vary considerably. The shear strain plots in Table 4-7 show that dilation of the soil is suppressed at high stresses lower down in the soil profile, as per Bolton's (1986) theory. As the shear bands propagate towards the surface, moving towards zones of lower confined stress, the shear bands tend to curve towards the centreline of the trapdoor at a greater angle than that at which they originally propagated. The shear strain plots in Table 4-7 (a)(ii) and (iv) clearly demonstrate that, as a single shear band propagates upwards to zones of lower stress, the shear band curves towards the centreline of the trapdoor.

Table 4-7: Total shear strain plots (PIV) corresponding to (a) 40 mm and (b) 80 mm trapdoor displacement for centrifuge tests (i) CF01, (ii) CF02, (iii) CC11, (iv) CC12 and (v) CG01 (units in percentage)

(a) 40 mm Trapdoor displacement	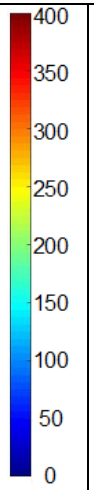	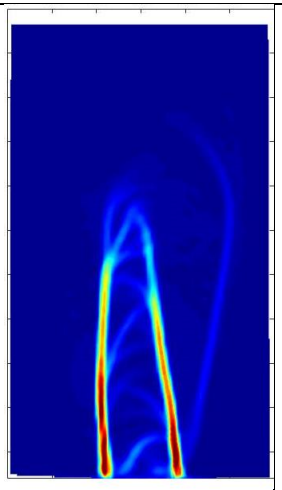	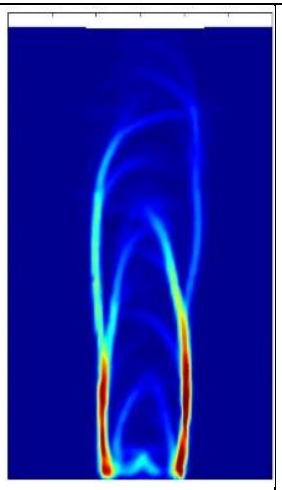	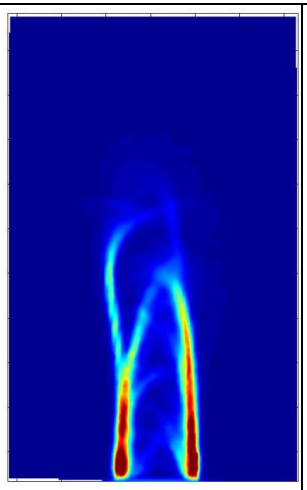	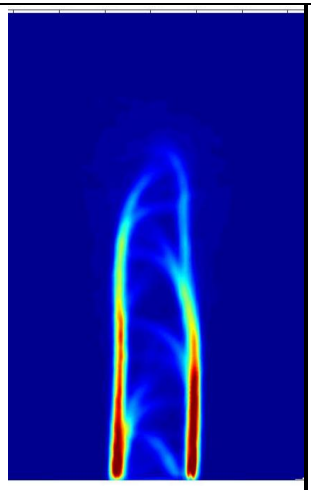	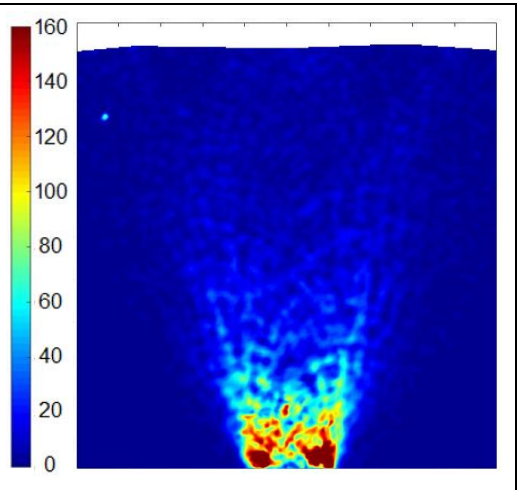
		(i) CF01	(ii) CF02	(iii) CC11	(iv) CC12	(v) CG01 – Glass beads
(b) 80 mm Trapdoor displacement	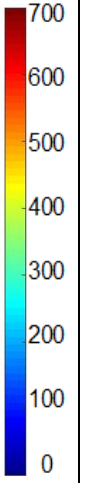	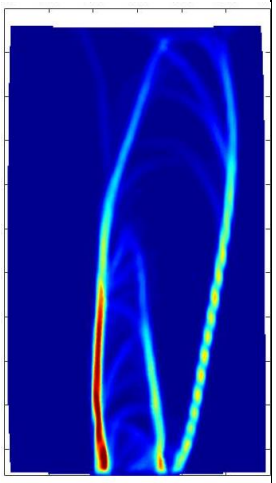	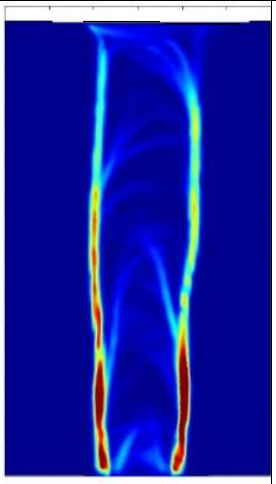	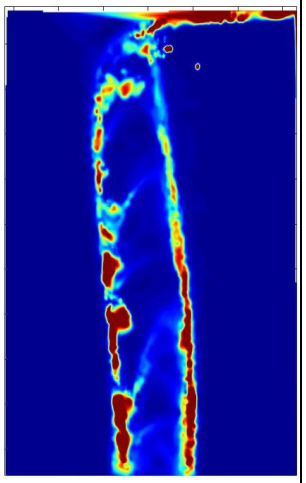	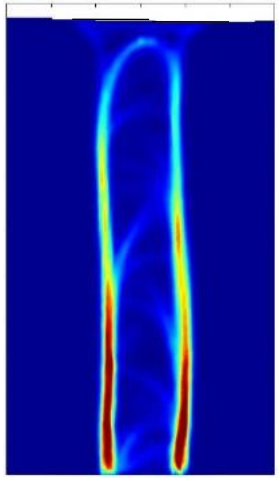	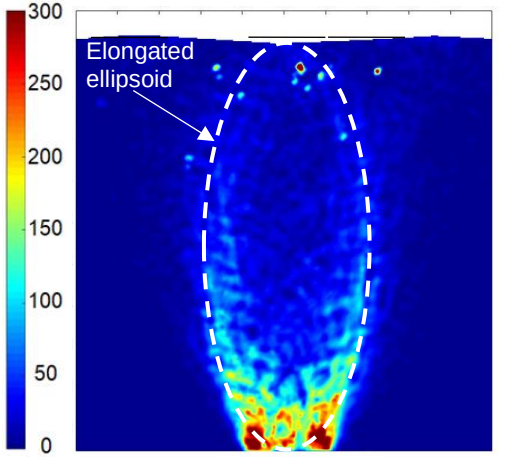
		(i) CF01	(ii) CF02	(iii) CC11	(iv) CC12	(v) CG01 – Glass beads

4.3.3.1 Discussion on glass beads

The shear strain plots for the trapdoor experiment undertaken with glass beads are presented in Table 4-7 (a)(v) and (b)(v) for 40 mm and 80 mm displacement of the trapdoor, respectively. These figures indicate that a significantly greater zone of extent/influence exists in the glass beads model resulting from trapdoor displacement (i.e. loss of subsurface support) compared to the natural sands at the same trapdoor displacement. The wider zone of influence is attributed to the comparatively lower shear strength of the material. Costa et al. (2009) conducted a series of deep trapdoor experiments at varying densities, stresses and relative trapdoor displacements. They found that external failure surfaces (referring to shear bands that propagate in an outward direction, away from the centreline of the trapdoor) develop at large relative trapdoor displacements ($\delta/B = 57\%$) of the trapdoor, as shown in Figure 2-15, and that the distance of between the trapdoor edge and the horizontal projection of the outermost failure surface increases in loose material with a comparatively lower shear strength. The results in Table 4-7 (b)(v) are consistent with the findings of Costa et al. (2009), as the shear bands in glass beads, with a significantly lower shear strength than the natural sands, extend beyond the vertical projection of the trapdoor edges, forming an ellipsoidal failure pattern.

It is well-known that the shear band width is a function of the average particle size. The shear strain deformations for fine-grained sand, coarse-grained sand and glass beads in Table 4-7 (b)(ii), (iv) and (v), respectively demonstrate a distinct increase in the width of the shear bands with increasing particle size.

4.3.3.2 Comparison of fine- and coarse-grained sands

Distinct differences were observed in the deformation mechanisms that formed during trapdoor lowering in the fine- and coarse-grained sands. As observed in the shear strain results displayed in Table 4-7 (a)(ii) to (iv), it is apparent that the shear bands in the fine-grained sand models propagated towards the surface at a faster rate with trapdoor movement than those in coarse-grained sand. This may be attributed to the comparatively lower relative density of the fine-grained sand models to that of their coarse-grained counterparts. The denser coarse-grained material models appear to exhibit greater shear resistance to the lowering of the trapdoor and therefore slower propagation of shear bands to the surface.

For comparative purposes, the failure deformations of CF02 and CC12 at 40 mm trapdoor displacement are shown in Figure 4-5. The total shear strain plots reveal that a greater number of individual shear bands form in the fine-grained sand model than in the coarse-grained model. Furthermore, greater curvature of the shear bands in the fine-grained model is observed, specifically at lower stresses higher up in the model where dilation has not been suppressed. As a result of the smaller average particle size of the fine-grained model and the resulting smaller shear band width, there are a greater number of available paths along which the shear bands can propagate, while maintaining the geometry dictated by

the soil's dilation. The number of paths available for shear band propagation in the coarse-grained model is restricted due to the larger average particle size and subsequent increased shear band width.

Similarly, it is proposed that the greater curvature exhibited by the shear bands in the fine-grained model are due to the material's smaller average particle size. As discussed, a high confined stress suppresses the dilation between sand particles within the shear band. As the shear band propagates from the trapdoor edge to regions of lower stress, the shear band in the fine-grained model has a greater opportunity to recover the suppressed dilation over a given distance as there are more particles and voids in the fine-grained model over this specific distance than in the coarse-grained model. The coarse-grained material therefore needs a greater distance over which to recover the same suppressed dilation. The difference in rate of shear band curvature between the fine- and coarse-grained material models may also be attributed to the varying dilation angle of the two materials. A distinct difference in the dilation angle was recorded in the dilation angle calculations for the materials based on their respective relative densities and stress levels. The angle may further vary as a result of the different average particle size of the two materials.

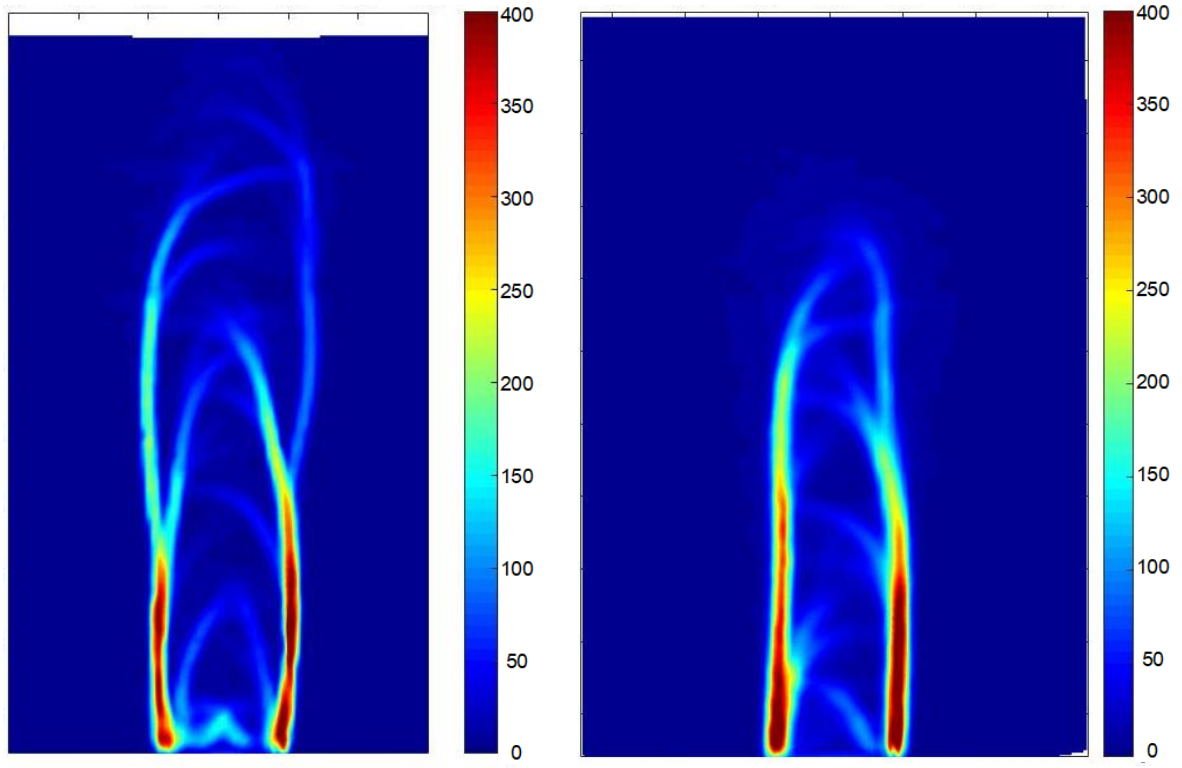

(a) (b)

Figure 4-5: Comparison of the deformation mechanisms corresponding to (a) CF02 and (b) CC12 at 40 mm trapdoor displacement (maximum shear strain, units in percentage)

4.3.3.3 Uncharacteristic soil deformation behaviour

The characteristic vertical shear bands observed at the final stage of deep trapdoor experiments reported in the literature were not observed in the final shear strain results for CF01 or CC11 (see Table 4-7 (b)(i) and (iii) respectively). The primary shear bands of CC11 did not propagate vertically from the trapdoor edges, but at a slight angle. The two bands, separated by a distance equal to that of the trapdoor width, remained parallel for the duration of the test and the associated deformation mechanism was therefore considered to be fairly characteristic. The deformation mechanism progression of CF01 was, however, considered to be somewhat uncharacteristic as shown in Table 4-7 (b)(i). As the initial shear band at the right-hand edge of the trapdoor of CF01 did not propagate vertically, an additional shear band, propagating outwards, formed later on in the test, at approximately 40 mm trapdoor displacement. The uncharacteristic deformation mechanisms observed in these two tests, with specific reference to CF01, may be attributed to slight variations in the manner in which the model material was pluviated which could in turn have resulted in areas of varying density and preferential failure planes.

Both CF02 and CC12 present results which correspond to the general deformation mechanisms for deep trapdoor experiments from literature. Based on the final shear strain results presented in Table 4-7 (b), it is of interest to note that two additional shear bands propagated outwards towards the surface from the primary vertical shear arms in tests CF02 and CC12, as well as in CG01. This may be likened to the numerical model deformation mechanisms shown in Figure 2-43.

4.3.4 Incremental shear strain

Incremental shear strain plots were created using PIV image analysis. Figure 4-6 (a) to (d) present the incremental shear strain plots for all four natural sand tests at 80 mm displacement of the trapdoor. These plots show the instantaneous shear band formation and shear strain over a set displacement of approximately 0.8 mm for both CF02 and CC12 (0.795 mm and 0.81 mm, respectively). As the plots show only the accumulated shear strain over a set increment of trapdoor displacement, no “noise” caused by shear bands that had developed previously contributes to the instantaneous shear strain plots. This contrasts with total shear strain plots which aid the investigation of the progression of deformation mechanisms in the soil body as they provide cumulative shear strain plots from zero displacement to the required degree of trapdoor displacement.

The incremental shear strain plots for all four natural sand trapdoor experiments yielded vertical shear bands, as predicted, once the shear bands had propagated to the surface, with the exception of the right-hand shearing arm of CF01. In addition to the vertical shearing arms, each of the four tests showed an additional ‘steady-state’ triangular shear strain pattern above the trapdoor during lowering, but at a significantly lower shear strain magnitude. The steady-state arching triangles, or triangular shear bands, initiated after approximately 30 mm of trapdoor displacement for the two coarse-grained materials and after 12 mm displacement for the fine-grained materials. The incremental shear strain triangles subsided

slowly with increasing displacement of the trapdoor, only to be replaced with a new set of triangular shear bands. These steady state triangles were not detected in the total shear strain plots due to the cumulative nature of strain surface plotting and associated shear strain scale. This would have rendered these bands of relatively low strain intensity invisible.

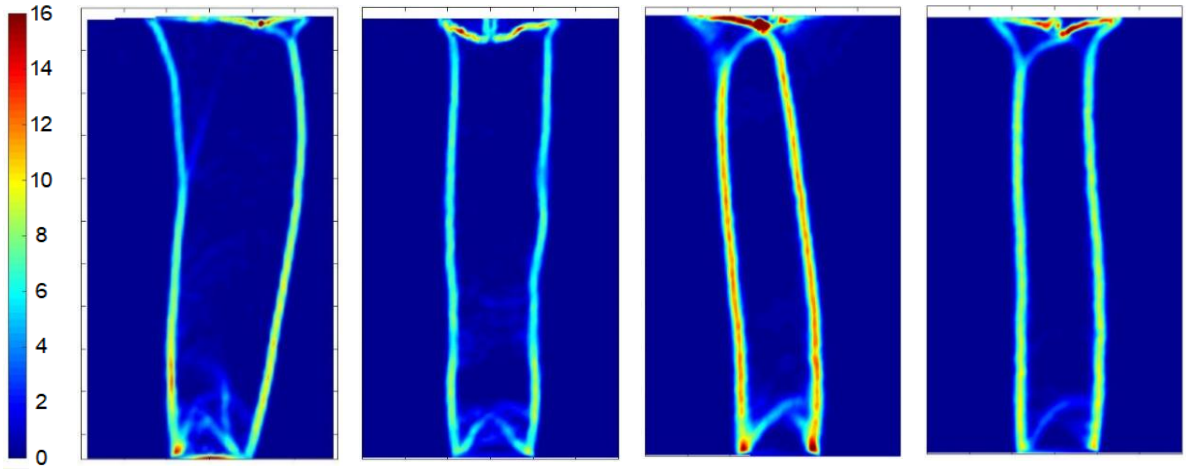

(a) (b) (c) (d)

Figure 4-6: Incremental shear strain plots of (a) CF01, (b) CF02, (c) CC11 and (d) CC12 at 80 mm trapdoor displacement (units in percentage)

The steady-state shear strain pattern observed above the trapdoor is analogous to that observed by Bransby & Blair-fish (1975) in their investigation of the deformations near rupture surfaces in flowing sand in an angled hopper. Figure 4-7 (a) and (b) show the rupture surfaces, or shear bands, which formed at the transition point between the vertical bin walls and angled hopper section. As the dense sand flowed downwards through the orifice, the first two shear bands moved down with the material. Subsequently, a second pair of shear bands formed at the transition point in the hopper. This shear band formation and subsidence continued for the duration of their test; not dissimilar to the formation and subsidence of the triangular deformation patterns in the natural sand trapdoor experiments.

In order to understand the mechanisms associated with the continuous triangular deformations observed above the trapdoor in the natural sand experiments at large trapdoor displacements, Evans' (1983) application of plasticity theory to trapdoor experiments was investigated. The observed dilation of the soil during trapdoor lowering is associated with non-recoverable plastic deformations. According to Evans (1983) the behaviour of granular materials is generally independent of rate, as instantaneous reactions to changes in boundary conditions are observed for these materials. However, as this assumption does not hold within classical plasticity theory, the terms "velocity" and "strain rate" are therefore used in discussion in respect of "displacement" and "strain".

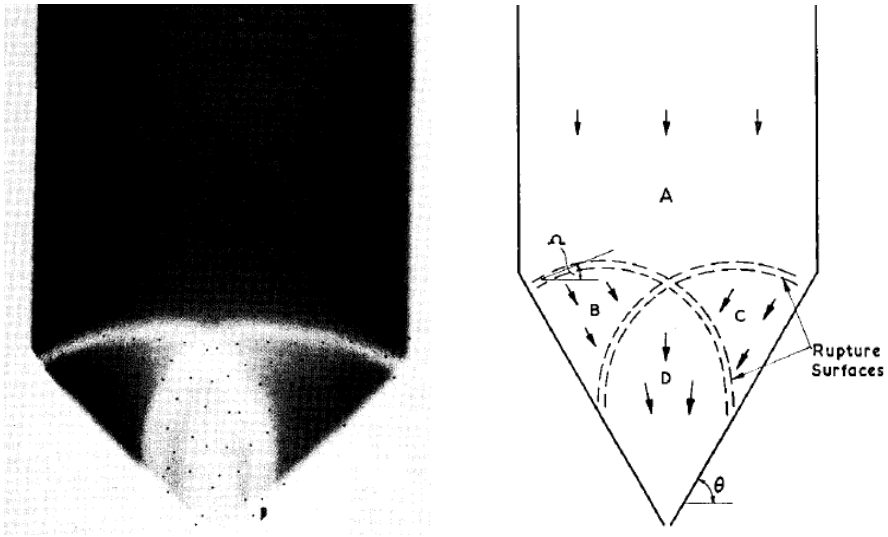

(a) (b)

Figure 4-7: (a) Radiograph image and (b) illustration of the shear band formation during dense sand hopper flow (Bransby & Blair-Fish, 1975)

A velocity (or displacement) characteristic is a curve along which there is no extension during plastic flow (Bransby & Blair-fish, 1975, and Evans, 1983). They are located at $\pm(45° - \Psi/2)$ to the direction of the major principal strain (rate) and are therefore a function of the plastic flow rule. Given the assumption that the major principal strain rate direction is coincident with that of the major principal stress direction, the velocity and stress characteristics coincide when the friction and dilation angles are equal ($\Psi = \varphi'$). However, they will be perpendicular to one another and at a 45° angle to the principal stress direction when the angle of dilation is 0° (Evans, 1983).

During shear deformation of a material, discontinuities develop within the velocity field of the material across which there is a change in velocity. Evans (1983) states that this discontinuity is referred to as a velocity discontinuity (or slip plane) and that it must coincide with a velocity characteristic. He further states that the direction of the change in velocity of the material across this discontinuity occurs at the dilation angle relative to the velocity discontinuity (Davis, 1968, Bransby & Blair-fish, 1975 and Evans, 1983).

The steady state triangular deformation patterns observed in the PIV results in the trapdoor experiments with natural sands formed after vertical shear bands had propagated from the trapdoor edges. At some point during trapdoor lowering the material at the trapdoor edges was sheared to its critical state so that the mobilised angle of dilation was zero. Figure 4-8 presents the velocity characteristics and discontinuities associated with a trapdoor experiment for a dilation angle of zero. The mechanisms shown in the figure correspond to the material behaviour of test CF02, CC11 and CC12. Due to the continuous displacement of the trapdoor, the full arches are intercepted by the vertical shear bands and

therefore only the central portion of the mechanism is present, as indicated by the orange lines in the figure below.

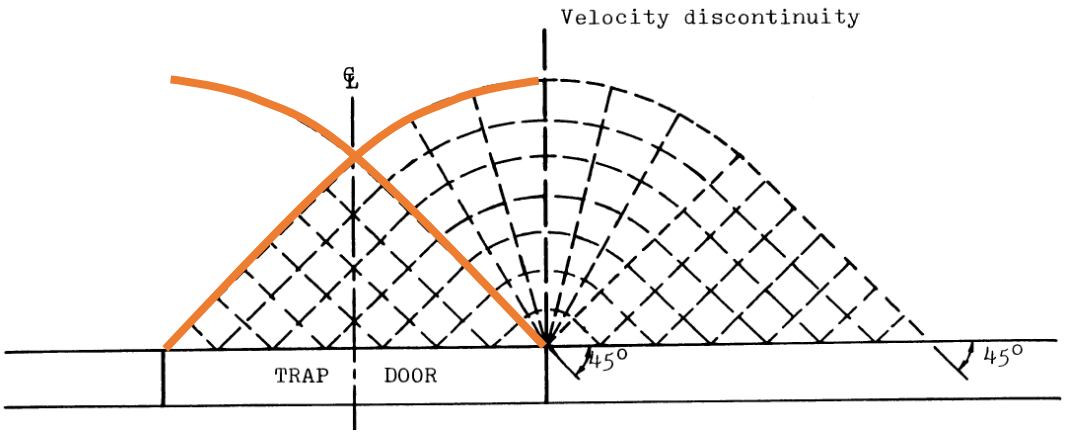

Figure 4-8: Velocity characteristics and discontinuities for material sheared to critical state, Ψ = 0° (adapted from Evans, 1983)

The steady-state shear strain patterns which formed in the trapdoor experiments with natural sands shown in Figure 4-6 resemble the pattern of Bransby & Blair-fish (1975) (Figure 4-7). The rupture surfaces correspond to the velocity characteristics. They resemble the velocity discontinuities associated with a dilation angle of zero in Figure 4-8 presented by Evans (1983), indicating that the sand above the lowering trapdoor appears to be at or near the critical state.

4.4. SURFACE SETTLEMENT RESULTS

Figure 4-9 presents the relationship between the maximum surface settlement of the material model, directly above the trapdoor (S_{max}), and the trapdoor displacement for all five trapdoor experiments undertaken in the centrifuge. As per Dewoolkar et al.'s (2007) findings illustrated in Figure 2-13 (b), and as portrayed by the maximum surface settlement curves of CF02, CC11 and CC12 in Figure 4-13, the characteristic settlement versus displacement plot yields two distinct gradients. The first graph gradient relates to the portion of the trapdoor experiment when the shear bands are still developing and propagating upwards towards the material surface, whereas the second corresponds to the latter portion of the test where the shear bands have reached the surface and the material continues to shear along the vertical bands propagating from the edges of the trapdoor. Dewoolkar et al. (2007) reported that the point at which the two gradients intercept, demonstrated by the blue ring for CC12 in the figure below, corresponds to the point of minimum arching (p_{ult}) which occurs when the shear bands reach the surface of the material and a constant load is measured on the trapdoor. The maximum surface settlement versus trapdoor displacement results for the tests undertaken with a load cell, namely CF02, CC12 and CG01, are discussed and analysed in greater detail in the following Section 4.5.

Based on the maximum surface settlement versus trapdoor displacement relationships in the figure below, the comparable curves of CC11 and CC12 indicate that there is a high degree of similarity between the deformation mechanisms of the two coarse-grained material tests. This is confirmed by the PIV shear strain plots for the two materials (Table 4-7). Of greater interest is the surface settlement graph of CF01 which has a gradient equivalent to that of CF02 for the first half of the test, but for the second half of the test the graph tends to run parallel to that of CG01. This behaviour coincides with the uncharacteristic propagation of a shear band which formed at an angle to the vertical from the right-hand edge of the trapdoor as seen in Table 4-7 (a)(i) and (b)(i).

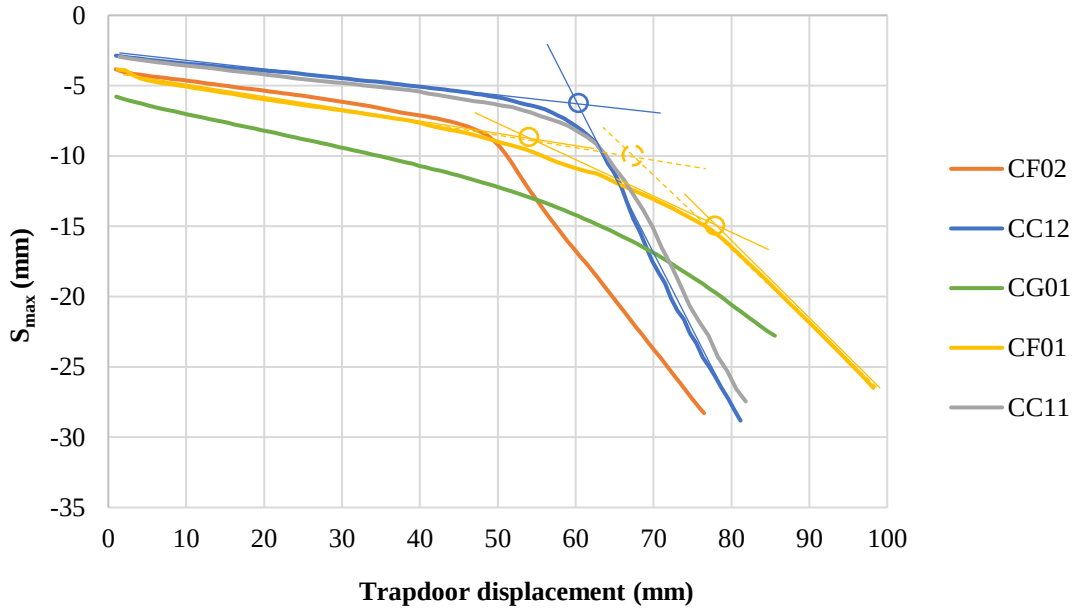

Figure 4-9: Maximum surface settlement versus trapdoor displacement curves

Dewoolkar et al.'s (2007) method of identifying the point of slope change from the two gradients formed by the settlement versus trapdoor displacement plot indicated that the shear bands for CF01 would reach the surface at a trapdoor displacement of 68 mm (see yellow dash line in Figure 4-9). However, based on the incremental PIV shear strain plots for CF01, this was not the case. The surface settlement curve for CF01 was therefore divided into three sections with three different gradients, resulting in two corresponding slope changes, indicated by the two solid yellow rings in Figure 4-9. The first change in gradient, recorded at a trapdoor displacement of 53 mm, corresponds to the displacement at which the first shear band reached the surface, as demonstrated in the corresponding incremental shear strain plot presented in Figure 4-10 (a). The second change in gradient corresponds to the trapdoor displacement at which the left-hand shear band widened towards the surface, resulting in a broader zone of influence at the surface and subsequent change in the gradient of the surface settlement curve. This occurred at a trapdoor displacement of 78 mm and the corresponding incremental shear strain plot is illustrated in Figure 4-10 (b).

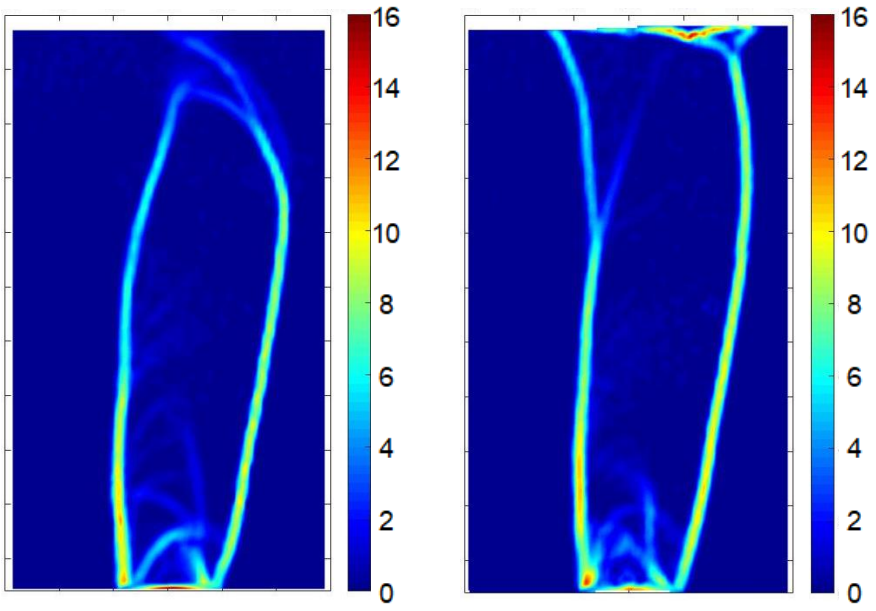

(a) (b)

Figure 4-10: Incremental shear strain plots for CF01 at (a) 53 mm and (b) 78 mm trapdoor displacement (units in percentage)

Based on the incremental shear strain plots for CF01, the right-hand shear band initiated at a trapdoor displacement of 26 mm. Figure 4-11 presents the surface settlement measurements, recorded by the LVDTs positioned on the surface for each of the five centrifuge tests, at 25 mm trapdoor displacement (i.e. just before the propagation of the uncharacteristic shear band of CF01). The centreline of the trapdoor corresponds to the position of the central LVDT at an x-axis coordinate of 250 mm (as described in Section 3.3.3). There is a clear correlation between the surface settlement graphs of the two fine-grained sand tests, as well as the two coarse-grained tests in this figure. As indicated by the PIV shear strain results, as well as the graph of CG01 in the figure below, the surface zone of the influence for the glass beads test extends some distance beyond the edges of the trapdoor.

Similarly, Figure 4-12 presents the surface settlement measurements for all five tests at the final trapdoor displacement of 85 mm. From this graph it is evident that CF01 has a wider zone of influence at the surface than the remaining three natural sand tests, for which the surface settlement results are highly comparable at final trapdoor displacement. The results for the natural sand tests illustrate that cavity propagation is concentrated in a vertical direction and that the surface zone of influence is generally limited to a region in close proximity to the centreline of the trapdoor. The glass beads tests yielded settlement results which show that the zone of influence at the surface is significantly greater when material with low shear strength acts as overburden to the underlying cavity. The greater surface settlement recorded in the experiment with glass beads may also be attributed to lower friction between the glass beads and the glass pane of the strongbox in comparison to that of the natural sands and the

glass pane. As a result of the low "side-friction" the glass beads displace downwards with less resistance resulting in a larger depression in the material at the surface.

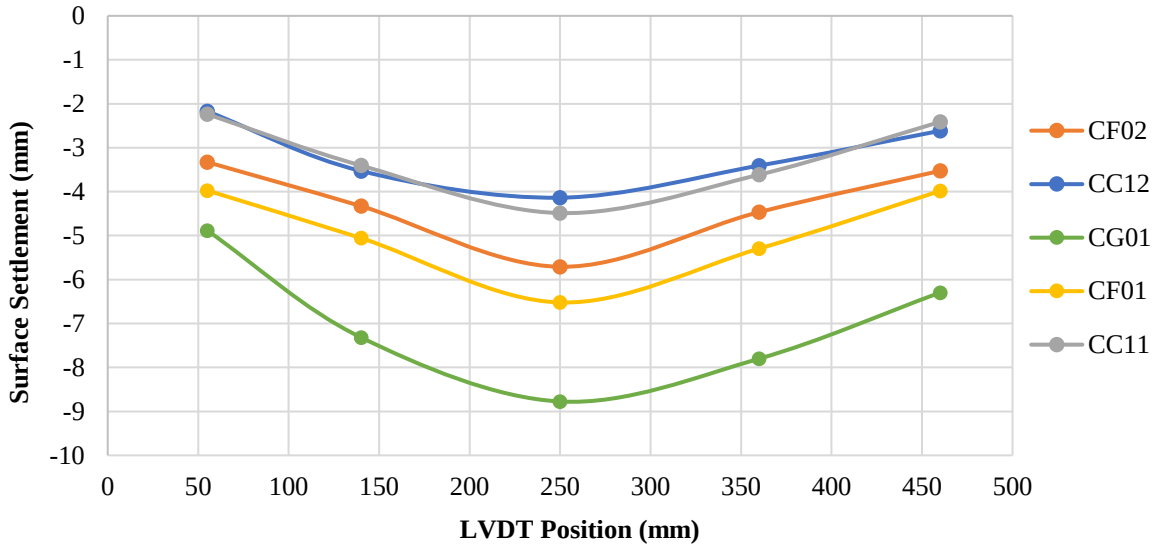

Figure 4-11: Surface settlement LVDT readings at 25 mm trapdoor displacement

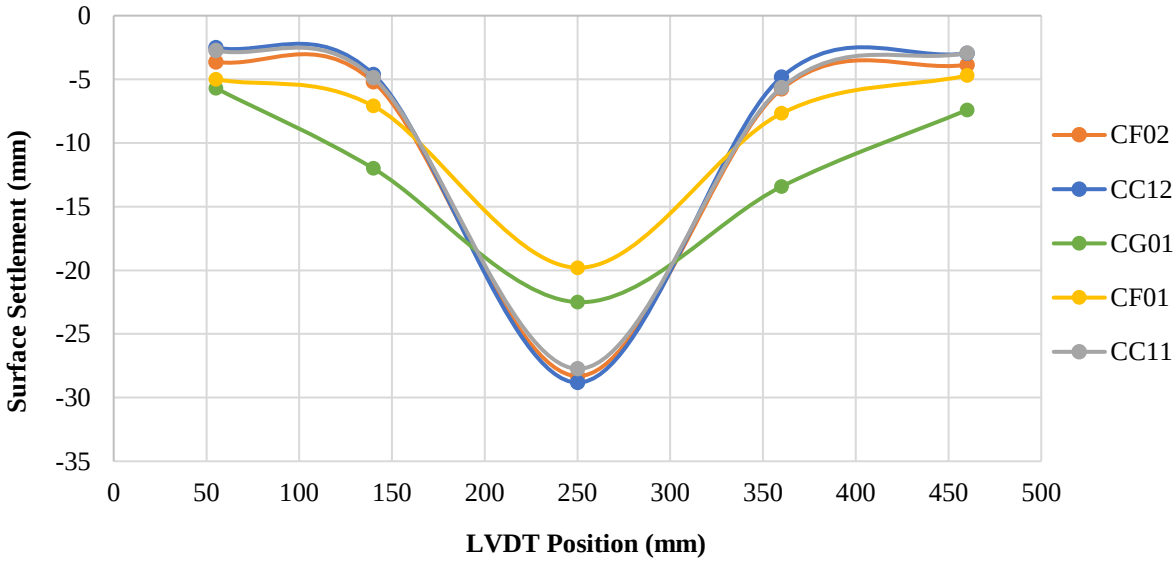

Figure 4-12: Surface settlement LVDT readings at 85 mm trapdoor displacement

4.5. COLLECTIVE ANALYSIS OF RESULTS

4.5.1 Deformation mechanisms, trapdoor load-displacement and surface settlement behaviour

Figure 4-13 presents the maximum surface settlement versus trapdoor displacement relationships for each of the centrifuge tests undertaken with a load cell. The two gradients as well as point of slope change described in Section 4.4 are indicated in the figure. The points of minimum arching (point of

slope change) occur at approximately 48 mm, 60 mm and 62 mm for CF02, CC12 and CG01, respectively.

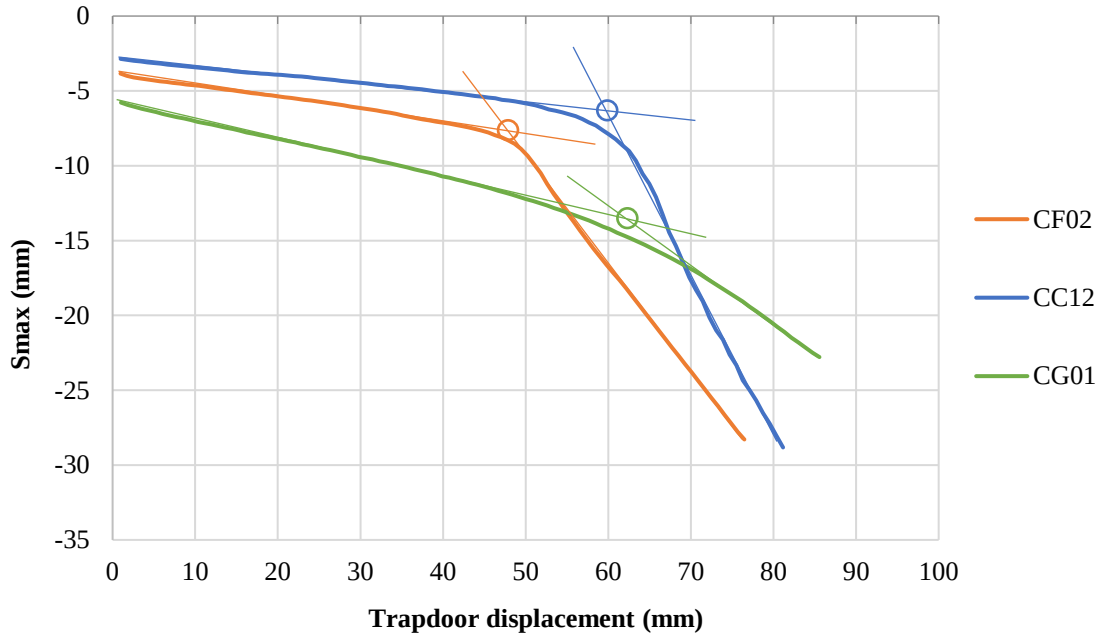

Figure 4-13: Maximum surface settlement versus trapdoor displacement curves for CF02, CC12 and CG01

To determine whether the graphs in Figure 4-13 accurately depict the trapdoor displacement at which the shear bands reach the surface, the instantaneous incremental shear strain plots (cumulative shear strain over 0.8 mm intervals) were carefully scrutinised. Figure 4-14 (a) and (b) display the incremental shear strain plots at which the first shear bands reach the soil surface for CF02 and CC12, respectively. These plots correspond to the incremental shear strain accumulated between trapdoor displacements of 47.9 mm and 48.7 mm for CF02, and between 57.7 mm and 58.5 mm for CC12, showing good agreement with the results in Figure 4-13 above. For both natural sands distinct slope change points are exhibited in Figure 4-13. However, this was not the case for the test undertaken with the glass beads. The exact trapdoor displacement at which the shear bands reached the surface for the glass beads test could not be determined with accuracy. Figure 4-14 (c) therefore presents the incremental shear strain plot between trapdoor displacements of 61.9 mm and 62.7 mm, corresponding to the point of slope change for CG01 in Figure 4-13.

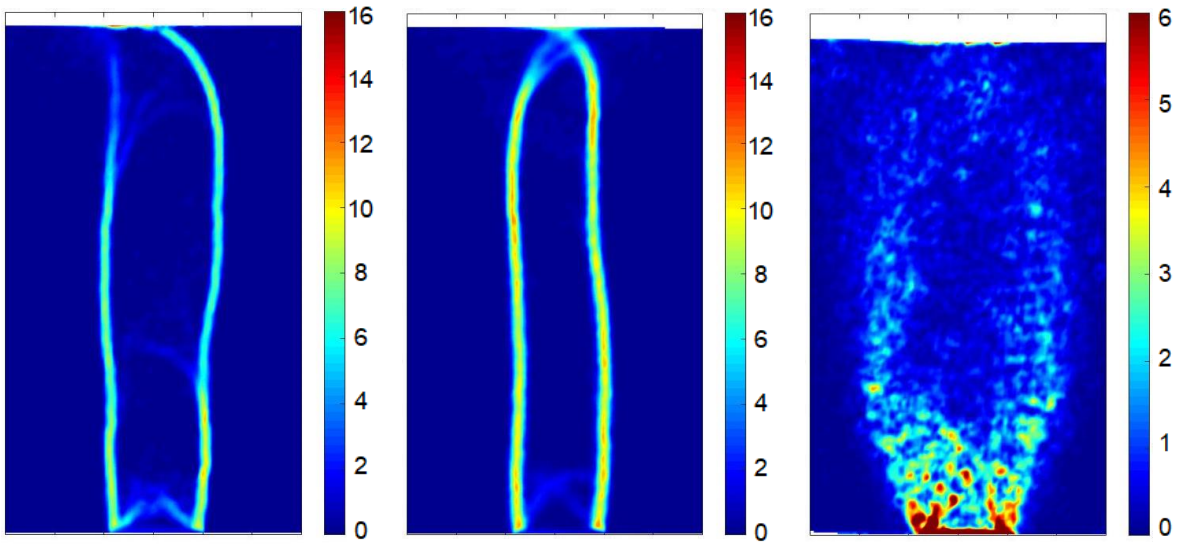

(a) (b) (c)

Figure 4-14: Incremental shear strain plots corresponding to the slope change points of (a) CF02, (b) CC12 and (c) CG01 (units in percentage)

The trapdoor displacements corresponding to the points of slope change in Figure 4-13 were further compared to the p_{ult} loads in the trapdoor load-displacement graphs shown in Figure 4-15. The shaded circles in this figure represent the trapdoor displacement corresponding to the slope change points identified in Figure 4-13. The trapdoor displacement at which the load for CF02 becomes constant (p_{ult}) coincides with the slope change point and incremental shear strain plots in Figure 4-13 and Figure 4-14 (a), respectively. Good agreement therefore exists between the surface settlement, trapdoor load-displacement and PIV shear strain results for the fine-grained sand trapdoor experiment. This, however, was not the case with the coarse-grained sand (CC12). A constant load was measured from approximately 50 mm displacement of the trapdoor for CC12, which does not coincide with the surface settlement or PIV shear strain results for this test. Significant deviation/noise in the trapdoor load-displacement curve of CC12 was recorded after a trapdoor displacement of approximately 50 mm. Based on the irregular deviation of the trapdoor load-displacement curve and the related discussion in Section 4.2.2, the load-displacement data for CC12 was considered not to be entirely representative of the deformation mechanisms associated with CC12 and greater reliability is therefore assigned to the PIV shear strain plots and surface settlement readings.

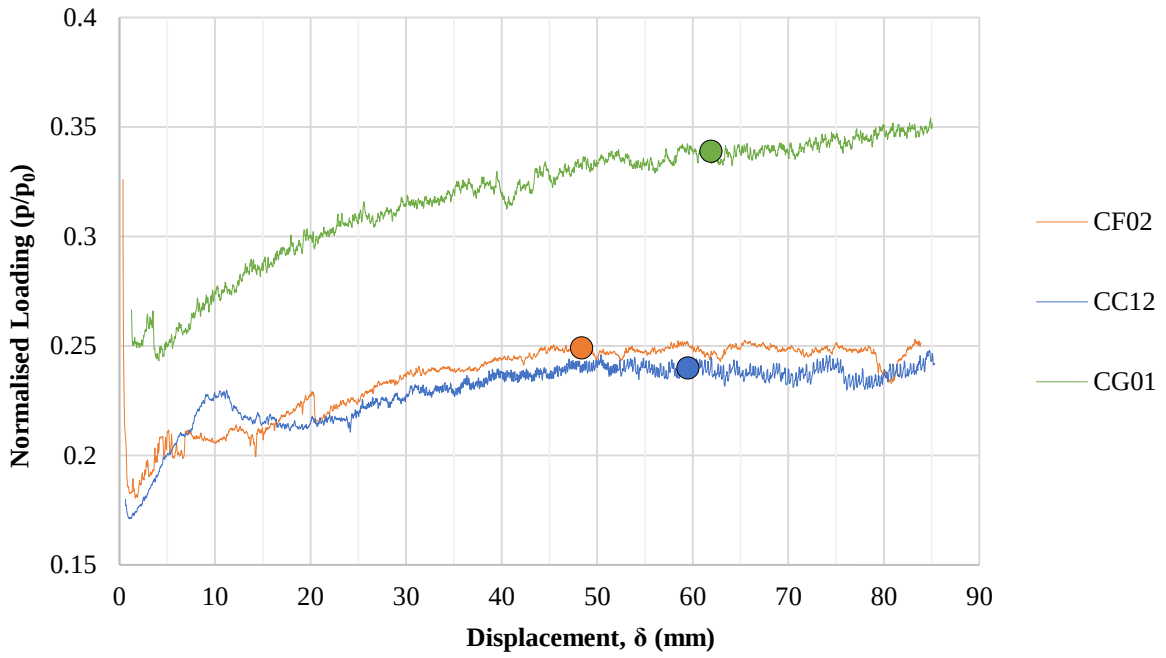

Figure 4-15: Trapdoor load-displacement graph and corresponding to the slope change points of (a) CF02, (b) CC12 and (c) CG01 in Figure 4-13

The trapdoor load-displacement behaviour of the glass beads test (CG01) did not adhere to the qualitative trend proposed by Dewoolkar et al. (2007) as the graph does not plateau at p_{ult} (or at the point at which the shear bands presumably reach the material model surface), but rather continues to recover load for the duration of the test, as the deformation mechanism widens and material mobilisation occurs progressively. The incremental shear strain progression plots presented in Figure 4-16 demonstrate that the deformation mechanism for the glass beads differs to that of the natural sands, giving rise to the variation in trapdoor load-displacement behaviour. Figure 4-16 (a) does not show distinctive bands of concentrated shear strain, but rather a mass of mobilised material in the form of a wedge, participating in the arching process. A significant volume of material in the model is affected by the displacement of the trapdoor, as a relatively greater volume of material is required to support the material overlying the trapdoor during stress redistribution (arching) due to the low shear strength of the material. Based on the slope change point in Figure 4-13 and the incremental shear strain plot presented in Figure 4-14 (c), the predicted trapdoor displacement at which the primary shear bands reach the surface appear to correspond fairly well to the postulate by Dewoolkar et al. (2007) despite the difference in trapdoor load-displacement behaviour between the glass beads and natural sands.

The increase in load in CG01 between trapdoor displacements of 62 mm and 85 mm (i.e. between p_{ult} and the end of the test), corresponding to the incremental shear strain plots in Figure 4-16 (b) and (c) respectively, is attributed primarily to the addition of material load as the primary shear bands widen towards the surface (Figure 4-16 (c)). As the trapdoor displaces, more material contributes to the load

on the trapdoor as the shear bands tend to widen towards the surface of the overburden material thereby including a significant amount of material within the deformation mechanism. Furthermore, as the trapdoor continues its downward trajectory, the zone of influence tends to narrow from the wide inverted triangular wedge towards the centreline of the trapdoor (not considering the portion where the bands widen towards the surface). Simultaneously, the primary shear bands tend towards the vertical, resulting in a reduction of the distance (length) over which the shear resistance of the material is applied. Less shear resistance along the primary shear bands results in a greater load measured on the trapdoor (Terzaghi, 1936). The comparatively larger normalised load measured on the trapdoor for the glass beads test may be attributed to the lower shear strength of the material, resulting in the ellipsoidal deformation pattern with a significantly larger volume of material contained within the two primary shear bands than in the natural sand tests.

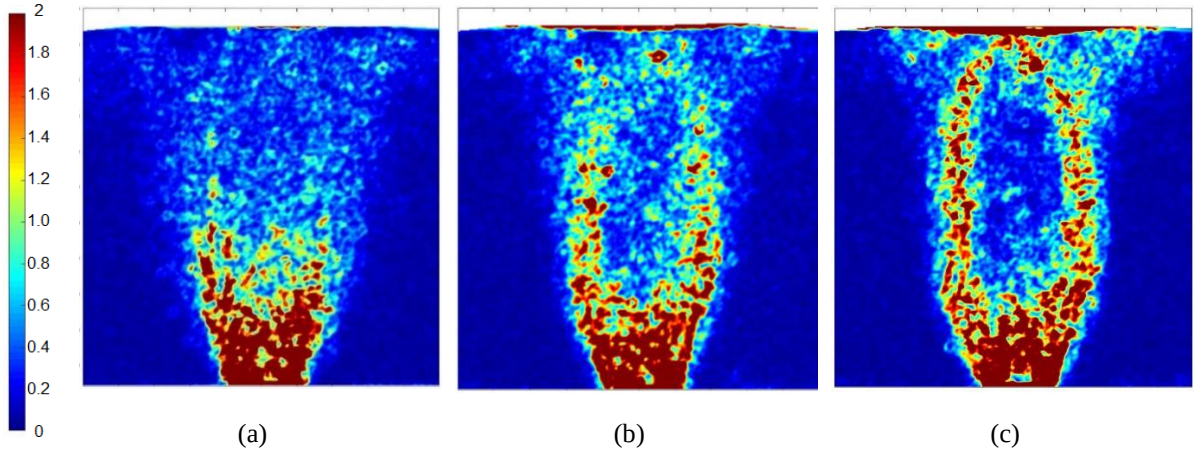

Figure 4-16: Incremental shear strain plots for CG01 at (a) 35 mm, (b) 62 mm and (c) 85 mm trapdoor displacement (units in percentage)

4.5.2 Curved arch to triangular deformation pattern analysis

The trapdoor load-displacement results presented in Figure 4-15 show four distinct gradients in the trapdoor load-displacement relationships for both the fine- and coarse-grained sands. Despite the irregular readings observed between trapdoor displacements of approximately 6 mm and 21 mm in both CF02 and CC12, the general trend for the trapdoor load-displacement relationship of the natural sands was interpreted as follows:

1. The initial gradient corresponds to the distinct reduction in load between the onset of trapdoor lowering and the displacement at which the state of maximum arching occurs as a result of stress redistribution within the material. A shear band arching over the trapdoor is characteristic of maximum arching conditions.
2. The trapdoor load-displacement test results for both CF02 and CC12 show that a comparatively large load is added between the point of maximum arching and a trapdoor displacement of

approximately 5 mm as observed in Figure 4-15 (i.e. steep incline in load is observed between these two trapdoor displacements).

3. Beyond the irregularities in load readings between 6 mm and 21 mm, a gradual increase in load was observed between a trapdoor displacement of 21 mm and approximately 50 mm for both tests. This corresponds to the alternating shear bands propagating towards the surface, observed in the PIV shear strain plots.
4. Finally, a constant load was recorded for both materials corresponding to the lines of zero gradient beyond 50 mm trapdoor displacement. The point at which the load becomes constant corresponds to p_{ult} for CF02, but not for CC12, as discussed in the preceding section.

Discussion points 1, 3 and 4, above, correspond to the general trapdoor load-displacement trends discussed in literature. In order to evaluate the sharp load increase observed between maximum arching conditions and 5 mm trapdoor displacement (Point 2), the shear strain plots corresponding to the start and end points of the steep gradient section were investigated. It was found that the steep incline in load may be attributed to the additional volume of sand included within the failure surfaces between the curved arch-like deformation pattern at the point of maximum arching and the triangular deformation pattern at 5 mm trapdoor displacement. This is illustrated in the corresponding PIV shear strain plots for CF02 and CC12 in Figure 4-17 (visual comparison of shear bands, the shear strain scale was therefore excluded from the plots).

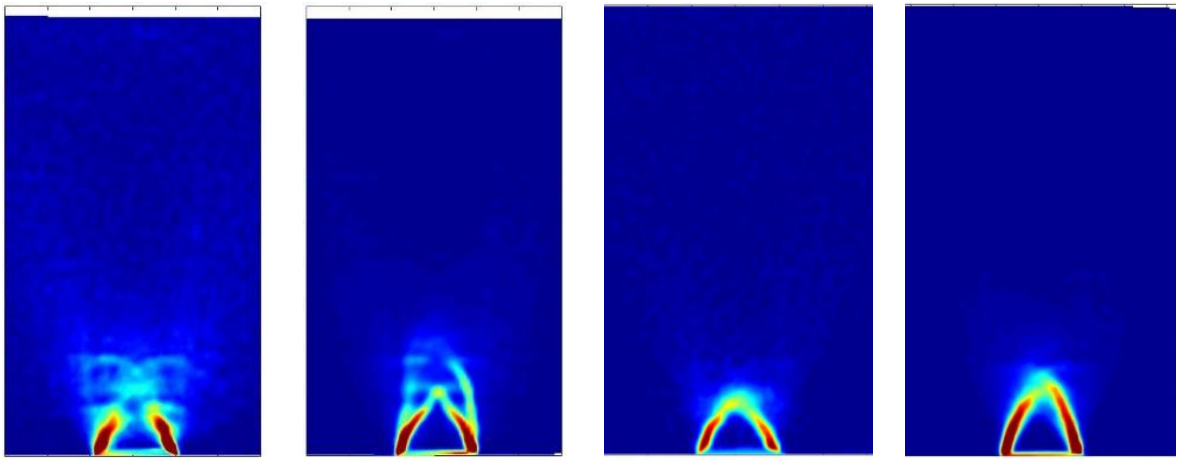

(a) CF02: Maximum arching (b) CF02: 5 mm (c) CC12: Maximum arching (d) CC12: 5 mm

Figure 4-17: Comparison of total shear strain plots of CF02 and CC12 at (a), (c) point of maximum arching and (b), (d) 5 mm trapdoor displacement, respectively (note: magnitude of shear strain varies)

The deformation progression with increasing displacement of the trapdoor is illustrated in Figure 4-18 against a typical trapdoor load-displacement curve from Dewoolkar et al. (2007). The condition of maximum arching corresponds to a single arch-shaped shear band spanning the trapdoor width (1). This

is followed by an increase in the load as the arch-like shear band grows in height to include more material directly above the arch, thereby forming a triangular shear strain mechanism (2). As the shear bands alternately propagate towards the surface, more material contributes to the load applied to the trapdoor and a steady increase in load is therefore recorded with increasing trapdoor displacement (3). Once the shear bands have reached the surface, the entire column of material between the vertical shear bands contributes to the load on the trapdoor and the load therefore remains constant as the trapdoor displaces further (4).

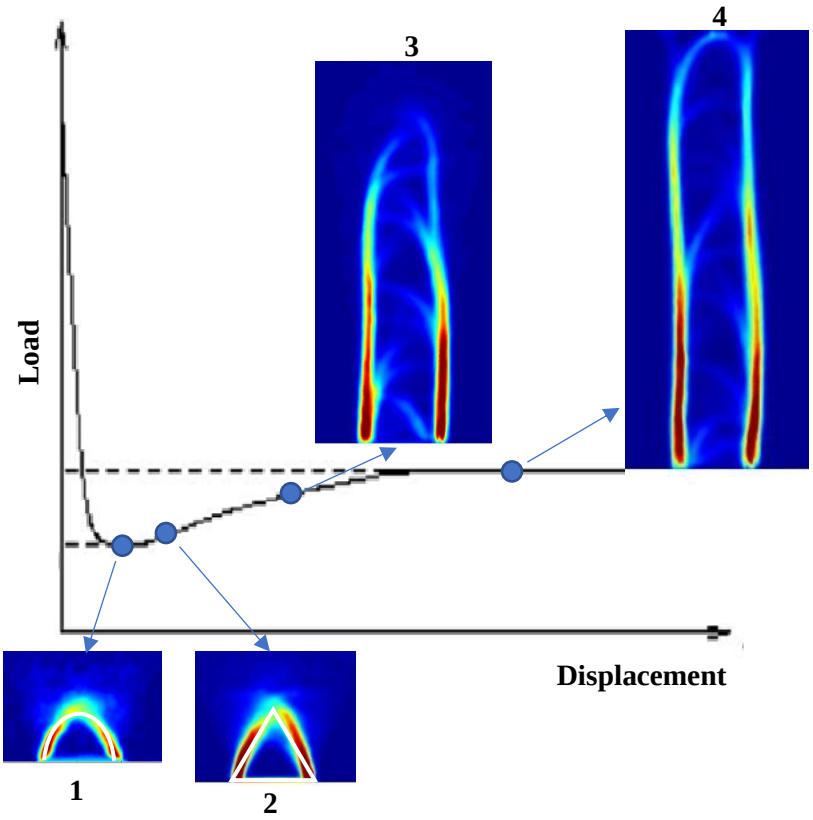

Figure 4-18: Schematic of trapdoor load-displacement progression and associated shear band formation (note: magnitude of shear strain in plots varies)

5. NUMERICAL TRAPDOOR EXPERIMENTS

5.1. INTRODUCTION

This chapter presents the methodology followed to investigate the effect of material shear strength on shear band propagation during the loss of subsurface support using the Discrete Element Method (DEM). This study intended to investigate only the effect of simulated particle shape effects on the deformation mechanisms of granular material during sinkhole formation. This was undertaken by replicating the centrifuge trapdoor experiments using discrete element simulations. A DEM trapdoor experiment simulation with spherical particles was calibrated to match the displacement and shear strain results of the centrifuge trapdoor experiment undertaken with spherical glass beads. The calibrated parameters and an equivalent modelling procedure were used to simulate the trapdoor experiment with varying particle shapes in the form of convex polyhedral particles, thereby isolating the material shear strength as a function of particle shape as the only variable. As a result of a numerical constraint inherent to the DEM code used in the research project (Blaze-DEM), a trapdoor experiment with polyhedral particles could not be simulated. The same approach was therefore adopted to investigate the simulated particle shape effects on the deformation mechanisms of the sphere model by applying a rolling resistance coefficient to the DEM particles.

The chapter opens with a description of the software used for the DEM simulations and the advantages of a GPU-based code are highlighted. The selected trapdoor container geometry is discussed in terms of the increased gravitational acceleration, selected contact model and critical time step, and the simulated modelling procedure is defined in detail. Initial particle parameters for the sphere model are described and their selection is explained based on a review of relevant literature.

The methodology used to perform a sensitivity study of the DEM parameters is discussed in line with the calibration procedure adopted to replicate the trapdoor experiment with glass beads. Furthermore, displacement contours, individual particle displacement trajectories and shear strain plots, as methods for calibration, are described. Lastly, the application and importance of particle shape effects in the DEM models is discussed. The selection of the polyhedral particles and corresponding modelling approach are explained, as well as the application of rolling resistance as an additional means to simulate particle shape effects.

5.2. BLAZE-DEM GPU CODE

Blaze-DEM is a three-dimensional research Discrete Element Method (DEM) code based on Graphical Processing Unit (GPU) computing architecture. The GPU-based code offers parallel processing capabilities which allows for the simulation of realistic models, as a greater number of particles with varying shapes can be modelled within in a reasonable time frame (Govender et al., 2016). For the

GPU-based code to surpass the performance of the traditional Central Processing Unit (CPU)-based DEM codes, the Blaze-DEM algorithm assumes a decoupled system in which the motion of the individual particles is modelled independently. The GPU-based architecture is then able to apply the same set of instructions to each data set or particle and access the extensive number of threads available for task processing by the GPU (Govender et al., 2015).

Four Gigabyte GeForce GTX 1080 G1 Graphical Processing Units were used to run the discrete element simulations. These GPUs each have 20 Streaming Multiprocessors (SM) with 2048 threads per SM, resulting in 40 960 threads available for task processing. Typically, CPUs have 8 to 16 cores and each core has the capacity to launch 2 threads. The parallel computational efficiency offered by the GPU-based code is attributed to the considerable number of threads available for processing, in comparison to the significantly smaller number of threads available on CPUs.

5.3. BLAZE-DEM TRAPDOOR MODEL

5.3.1 Trapdoor container geometry

The size of the physical trapdoor experiment strongbox was reduced in the Blaze-DEM numerical model to aid the computational efficiency of the model. The length and depth of the strongbox (dimensions in x- and z-directions) were reduced to dimensions at which boundary effects, influencing the results of the trapdoor lowering experiment, would be negligible. Care was taken to replicate the fill height of the model (y-dimension) to ensure corresponding stress states in the numerical and experimental soil models. Figure 5-1 demonstrates the difference in size between the centrifuge trapdoor experiment strongbox (green) and the scaled version used in Blaze-DEM (orange). The blue frame is a scaled representation of the glass panel through which the material behaviour was monitored during centrifuge testing.

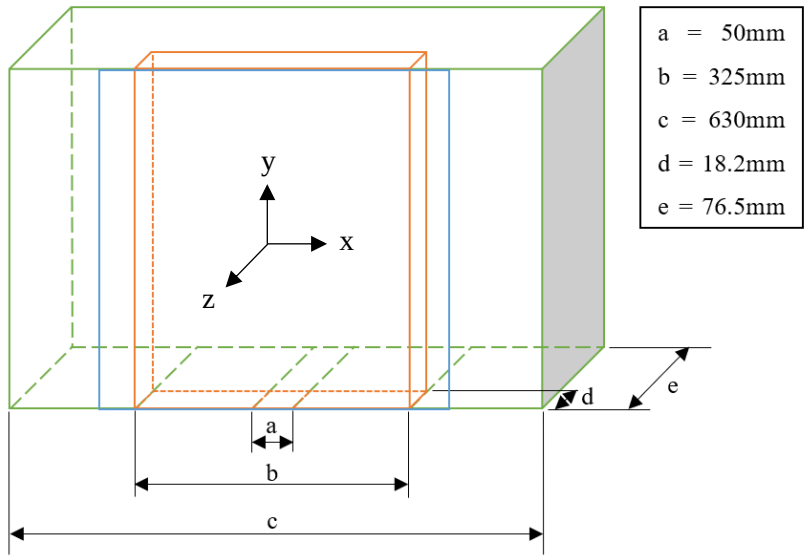

Figure 5-1: Blaze-DEM scaled dimensions of strongbox

5.3.2 Contact model and critical time step

An important consideration when using the DEM is the time step between iterations. The critical time step is defined in terms of the Rayleigh wave speed, as detailed in Section 2.4.6 of the Literature Review. Several researchers recommend using a DEM time of step of between 10 and 20% of the critical time step (Δt_c) (Santos et al., 2016, Ai et al., 2011 and Yan et al., 2015). From Thornton & Randall (1988), the critical time step is defined in Equation 5-1 and the corresponding relationship between the normal and shear stiffness of a material is described in Equation 5-2.

$$\Delta t_c = \frac{\pi R \sqrt{\frac{\rho}{G}}}{0.01631\nu + 0.8766} \qquad \text{Equation 5-1}$$

Where:

$$G = \frac{E}{2(1+\nu)} \qquad \text{Equation 5-2}$$

And:

Δt_c = Critical time step (s)

R = Particle radius (m)

p = Particle density (kg/m^3)

G = Shear modulus (N/m^2)

ν = Poisson's Ratio

E = Young's modulus (N/m^2)

As established from Equation 5-1 and Equation 5-2, the critical time step scales linearly with the particle radius – a greater particle size results in a greater critical time step. Thakur et al. (2016) further report that the normal contact stiffness (k_n) of a particle scales linearly with the particle radius. It is important to note that these relationships only apply when a linear spring-dashpot contact model is applied. The particle stiffness is scale invariant when the Hertz-Mindlin contact model is applied in three-dimensional simulations (Feng et al., 2007). The Blaze-DEM trapdoor model was optimised by taking advantage of the above relationships. It was decided to scale the DEM model to prototype dimensions and normal gravitational acceleration (9.81 m/s^2) so that the large particle radius would allow for a greater and more realistic stiffness to be modelled within a reasonable time step. The linear spring-dashpot contact model was therefore chosen as the force-displacement model. Particle upscaling, to increase particle mass and the related critical time step, is a well-known and often applied method used to ease computing burden (Cheng et al., 2017).

5.4. BLAZE-DEM PARAMETERS

The initial DEM parameters were selected based on a literature study of particle properties for simulations in which glass beads had been modelled. A bulk calibration approach was then employed to finalise the particle parameters for the corresponding trapdoor experiment undertaken in the centrifuge. Where possible, directly measured particle parameters were assigned to the spherical particles.

5.4.1 Directly measured particle properties

The DEM trapdoor simulations were modelled by assigning specific material parameters to the particles and container. A density of 2500 kg/m^3 was assigned to the spherical particles, as per the manufacturer's technical data sheet (Preciosa Ornela, 2011), and the particle radius (1 mm) was scaled up by a factor of 50 to 0.05 m according to the prototype dimensions at normal gravitational acceleration.

5.4.2 Particle contact stiffness

Thakur et al. (2016) describe several solutions proposed by researchers, relating contact normal stiffness (k_n) to the material modulus of elasticity (E) and particle radius (R). Equation 5-3 and Equation 5-4 are two of the listed solutions proposed by Potyondy & Cundall (2004).

$$k_n = 2E \times R \qquad \text{Equation 5-3}$$

$$k_n = \frac{\pi R_{avg} E}{2} \qquad \text{Equation 5-4}$$

As per the technical data sheet for the 2 mm glass beads, the Modulus of Elasticity ranges between 78 and 85 GPa. Considering the scaling factors of 1 and 1/50 for the Young's Modulus and particle radius respectively, initial values for normal contact stiffness were therefore estimated to range from 6.0E+09 to 8.5E+09 N/m for the up-scaled DEM model. Due to the additional computational effort required for greater stiffnesses, Yousefi & Ng (2017) record the reduction in contact stiffness as a well-known approach to reducing simulation runtime. The assigned particle stiffness was reduced during the filling process of the container, as detailed in Section 5.5.1, and calibrated to match the experimental results for the trapdoor lowering simulation.

It is important to note that the tangential particle contact stiffness is not required as an input parameter to the Blaze-DEM simulation. It is assigned a value corresponding to half the magnitude of the normal contact stiffness within the Blaze-DEM code. The tangential contact stiffness was therefore not calibrated.

5.4.3 Rolling resistance coefficient

Particle shape is computationally expensive to model in DEM simulations and, as a result, spherical particles are a popular substitute. Spherical particles require significantly less computational effort due to an efficient contact detection algorithm and the insignificance of particle orientation, as opposed to other particle shapes. When investigating soil deformation mechanisms, spherical particles cannot realistically model the shear strength of natural sands. Consequently, researchers often apply rolling resistance in an attempt to model the effect of particle shape on the shear strength of soil (Wensrich & Katterfeld, 2012). As detailed in Section 2.5.4, the rolling resistance coefficient (μ_r or η) is used to apply a rolling resistant moment or torque to particles in contact which opposes the direction of relative rotation between two particles. This rolling resistant moment (M_r) is included as an additional term in Newton's second law of motion for rotational motion (Equation 2-10). Initially, a near-zero magnitude of the rolling resistance coefficient of 0.001 was selected to ensure that particle rotations were not restricted. A value of 0.001 was also used by Thakur et al. (2016) to model free rotation of the particles.

5.4.4 Coefficients of friction and restitution

The coefficient of restitution is defined as the ratio of relative velocity of a particle before a collision to its relative velocity after the collision. It ranges from zero, for an inelastic collision, to unity, for a perfectly elastic collision (Lorenz et al., 1997). Both the normal (c_n) and tangential (c_t) damping coefficients are important parameters in the contact model framework (Section 2.4.4). These damping coefficients are a function of the coefficient of restitution, as detailed for the normal damping coefficient in Equation 5-5 below (Govender, 2015). Blaze-DEM requires only the coefficient of restitution as input, as the corresponding damping coefficients are then calculated within the code.

$$c_n = \frac{2\ln(e)\sqrt{k_n m_{eff}}}{\sqrt{\ln(e)^2 + \pi^2}} \qquad \text{Equation 5-5}$$

Where:

e = Coefficient of restitution

m_{eff} = Effective mass of the particles

The coefficients of friction describe the ratio between the frictional resistance and the normal reaction force as a result of interaction between two bodies. The static friction coefficient applies when neither object is sliding against the other, as opposed to the kinetic friction coefficient which applies when two objects are sliding against each other. Several researchers have undertaken DEM studies with glass beads of varying size. The initial particle parameter values chosen for the coefficients of friction and restitution were approximated from values used by Chung (2006), Hartl & Ooi (2011) and Lorenz et al.

(1997), amongst others. Similarly, the corresponding parameters for interaction with the container were estimated from the publications of the researchers listed above, as well as from Gonzalez et al. (2011).

5.4.5 Summary of input parameters

The initial material parameters selected for the DEM trapdoor simulations are listed in Table 5-1 below. These were verified or adjusted during the calibration procedure described in Section 5.6.

Table 5-1: Initial DEM input parameters

Material Parameters	Symbols	Values
Particle density (kg/m^3)	ρ	2500
Particle radius (m)*	R	0.05
Particle-Particle Interactions		
Coefficient of restitution	e or COR	0.95
Normal Contact Stiffness (N/m)	k_n	Varied
Static friction coefficient	μ_s	0.18
Kinetic friction coefficient	μ_k	0.18
Rolling Resistance	μ_r	0.001
Particle-Wall Interactions		
Coefficient of restitution	e	0.8
Normal Contact Stiffness (N/m)	k_n	5.0E+06
Static friction coefficient	μ_s	0.3
Kinetic friction coefficient	μ_k	0.3

* Scaled up
** Units dimensionless unless indicated otherwise

5.5. MODELLING PROCEDURE

5.5.1 Filling of container

Stone & Wood (1992) report that the angle of dilation is the primary factor that influences the direction of localisations during shearing of soil. It is also known that the measured angle of dilation in a shear test reduces with increasing stress level (Bolton, 1986). An accurate representation of the DEM model fill height and density was therefore crucial to ensure that the DEM and centrifuge models correspond and that that results would be comparable. For the filling of the DEM model, the particles were placed by means of pluviation from an equivalent height of 1.3 m and at a gravitational acceleration of 1/50g or 0.196 m/s^2 due to the scaled dimensions of the DEM model. This filling procedure attempted to replicate the actual filling conditions of the centrifuge test models at 1g.

The number of particles required to achieve the same fill height was approximated by scaling down the volume and corresponding number of particles from the centrifuge model to the DEM model. This value

was then used as the initial number of particles. The particle stiffness was reduced during the filling process to allow for a greater time step and subsequent time-saving during the iterative exercise. The bulk density of the model was calculated from an equivalent height of 15 mm below the Y-coordinate of the top particle's centroid; this approach was adopted to account for the uneven model surface caused by the raining down of particles. Using a Python subroutine, the particles within the confined volume, with known volume and specific gravity, were then counted and the resulting bulk density of the model determined. The number of particles and particle stiffness were varied during the iterative process until a corresponding fill height and bulk density were obtained. Appendix B.1 lists the simulation details used in the iterative process. Two initial fill experiments, detailing each particle's centre of mass coordinates and velocity vectors, were obtained with satisfactory results.

5.5.2 Spin-up simulation

The initial fill experiments were used as the starting files for the spin-up simulations, which were in turn used to simulate the acceleration of the model to 50g. The gravitational acceleration of these experiments (prototype dimensions) was adjusted to 9.81 m/s^2 so that the system would be representative of the glass beads experiment in the centrifuge at 50 times gravitational acceleration. The particle stiffness was also increased during the spin-up process to better represent the actual glass bead stiffness values. The bulk density and resulting fill height were monitored with stiffness increase to ensure that they were comparatively similar to the initial values. The application of the increased particle normal contact stiffness resulted in particles trying push each other away, to reduce the particle-particle overlap distance as a result of the increased particle stiffness, while the increased gravitational acceleration forced the particles together. This resulted in an applied disturbance to each particle yielding increased particle accelerations and velocities. Consequently, the spin-up simulations were allowed to run for approximately 48 hours to ensure that the particle velocities had decreased sufficiently before lowering of the trapdoor commenced. The spin-up procedure was applied to both accepted fill experiments. A log of the spin-up experiments is attached as Appendix B.2.

5.5.3 Trapdoor displacement simulation

The resultant "spin-up" system state files, containing each particle's positional and velocity data, were used as the starting files for the trapdoor displacement simulations. These simulations were used to calibrate the DEM spherical model to the centrifuge glass beads model by varying several of the DEM model input parameters.

5.6. CALIBRATION PROCEDURE

Coetzee (2017) defines the bulk calibration approach, used in DEM, as follows: "*Field or laboratory experiments are performed to measure specific bulk properties of the material. The experiments are then repeated numerically, following the same setup and procedures as closely as possible, while the*

model parameters are iteratively changed until the measured bulk behaviour is matched to a certain degree of accuracy."

Several bulk calibration approaches are used universally to calibrate DEM parameters for granular flow. Coetzee (2017) and Marigo & Stitt (2015) emphasise the importance of calibrating DEM parameter values at stress levels corresponding to those used in the physical laboratory experiments, due to the stress-dependency of various parameters. Given the high stresses in the centrifuge model, standard calibration tests such the angle of repose and hopper discharge test could not be used to calibrate the model parameters accurately. Simulations of biaxial and triaxial tests are often used to calibrate models at higher stresses, however, Blaze-DEM does not have the capability to simulate the particles at a steady stress state while translating the surfaces bounding the particles. It was therefore decided to use the PIV displacement and shear strain results from the glass beads centrifuge test to calibrate the spherical DEM model. Appendix B.3 presents a comprehensive log of the calibration and analyses simulations undertaken using Blaze-DEM.

5.6.1 Displacement contours: Sensitivity analysis

Particle displacements were calculated by converting the DEM simulation output files to a positional centre of mass array, detailing each particle ID and its Cartesian coordinates. Only the two-dimensional displacements of particles in the XY-domain and in contact with the equivalent glass panel of the DEM container were considered. This was achieved by using a Python subroutine to search for particles whose centroid lay within a distance slightly greater than the particle radius width from the equivalent DEM glass panel. This approach was followed as an attempt to replicate the procedure used in PIV to plot displacement contours (i.e. only the displacements of soil grains adjacent to the glass pane are captured using PIV). The displacement vector magnitudes were assigned to the initial particle positions to create a displacement contour plot. The displacement plots, used for calibration, were calculated at a trapdoor displacement of 10 mm (prototype equivalent of 0.5 m) for time saving purposes during the iterative calibration process. This was deemed sufficient as more than 10% of the total trapdoor displacement would have taken place at this point. The DEM results were post-processed using Python. Copies of the code used to analyse the results are attached as Appendix C.

A sensitivity analysis, using full colour displacement contours for 10 mm displacement of the trapdoor, was undertaken to evaluate the effect of:

- Trapdoor velocity
- Selected time step
- Container properties
- Contact (force-displacement) law

Modelling the actual trapdoor velocity of 0.025 mm/s was not deemed to be realistic at typical DEM time steps of 10E-06 seconds and a total trapdoor displacement of 80 mm. As discussed in Chapter 3, the experimental trapdoor velocity was dictated by the maximum rate at which photographs could be taken for PIV analysis purposes; this was not a constraint for the DEM analyses. The trapdoor velocity for the DEM simulation was therefore reduced until no dynamic effects were recorded. The selected time step was evaluated in the same manner and the time step, as a fraction of the critical time step, was varied until no effect of the change in time step was evident in the resulting displacement contours of the material.

The material properties for the container, namely the stiffness, coefficient of restitution and friction coefficients, were obtained from literature and varied to match those of the glass beads to determine whether a change in the numerical container properties affected the bulk material behaviour of spherical particles. Similarly, the sensitivity of the simulation to contact model selection was tested to ensure that there was no significant difference between the results of the linear spring-dashpot and Hertz-Mindlin contact models.

5.6.2 Displacement contours: Calibration with experimental results

The PIV displacement contours for 10 mm trapdoor displacement were recorded in image space with pixels as the units of subset displacement. In order to calibrate the DEM particle parameters based on 10 mm displacement contours of the physical trapdoor experiment undertaken with glass beads, the units of the centrifuge experiment and DEM simulation results were scaled to be compatible.

From the photographs used for the PIV analyses, the pixel-mm calibration factor was determined by recording the number of pixels for a known dimension in the corresponding photo. However, due to the upward angled direction of the camera and the position of the camera at the base of the centrifuge model, an error of parallax was evident in the photos. The calibration factor therefore varied with the height of the model (in the y-direction). The trapdoor width and length of the glass panel were the known dimensions used to calibrate the image space PIV, with resulting calibration factors of 7.03 and 6.28 pixels/mm for the bottom and surface of the material, respectively. However, applying a number of calibration factors to the global displacement or shear strain analyses created artefacts at the calibration factor transitions, thereby distorting the results. A single scale factor of 6.7 pixels/mm was therefore selected to scale the entire image and it was ensured that the use of a single calibration factor had a negligible effect on the contour plot results.

Once the PIV subset coordinates had been converted to millimetres, they were multiplied by factor of 5 to account for unit conversion to centimetres at 50 times gravitational acceleration. The subset centres were then translated to correspond to the DEM model dimensions with the trapdoor centre at an x-coordinate of 1555 cm. It should be noted that the Blaze-DEM geometric setup uses centimetres as the input unit for length.

The scaled displacement contour plots were used to evaluate the effect of varying input parameters such as particle stiffness, coefficient of restitution and the particle friction coefficients. They were also used to calibrate these particle parameters.

5.6.3 Displacement trajectories

The displacement contours were used to calibrate the bulk material properties of the spherical glass beads. Validation of the calibrated DEM parameters was undertaken at particle level by tracking the displacement trajectories of individual discrete particles at strategically selected locations, as shown in Figure 5-2, during trapdoor lowering in the DEM simulation. Corresponding PIV subset displacement paths were mapped to compare the particle trajectories of the two experiments. Using PIV to track soil element trajectories was first used by White & Bolton (2004) to investigate soil behaviour during pile installation in sand.

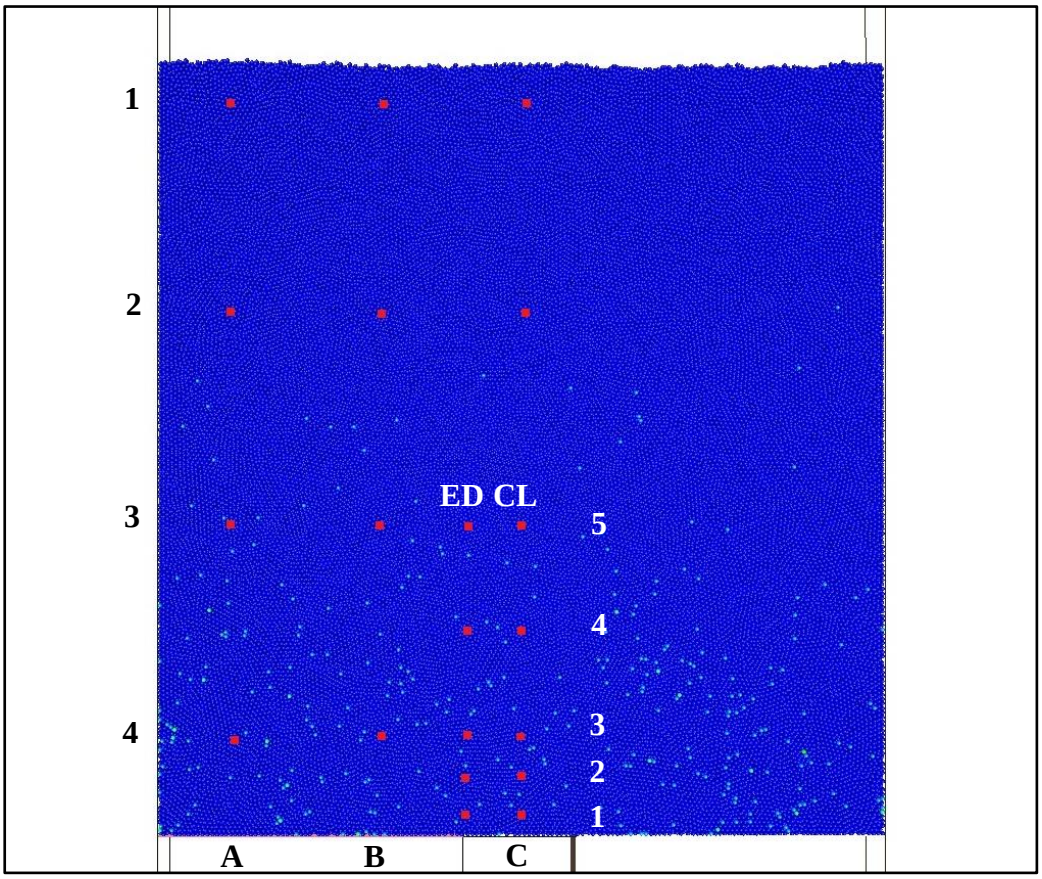

Figure 5-2: DEM sphere coordinates for displacement trajectory monitoring

The predetermined grid of analytical points was compiled to investigate representative particle behaviour across the entire model, focussing specifically on the material behaviour above the edge and centre of the trapdoor. It was assumed that the material would behave symmetrically about the centreline of the trapdoor and therefore only one half of the model was investigated. Search areas were coded in Python to identify particles within the predetermined grid area. The centroid coordinates of the

representative particles (at prototype scale) were converted to millimetres (at model scale) by multiplying the centimetre coordinates by a factor of 0.2. As discussed in the previous section, the pixel-millimetre calibration factor of the PIV results is dependent on the y-coordinate or height of the subset. The distances between particle centroids in the scaled grid were converted to pixel distances by applying the corresponding calibration factors. Distances in the x-direction were scaled directly according to the interpolated calibration factor, whereas distances in the y-direction were calibrated using an average of the calibration factors corresponding to the respective particle heights. The centroids of the PIV subsets (pixels) were scaled from a reference point 2 mm above the centre of the trapdoor. The red squares in Figure 5-3 represent the calibrated subset locations as well as actual subset sizes. Subset side lengths of 35 px were chosen for the PIV analyses. A smaller subset size would better represent the displacement path of single particle, however, a subset side length of 27 pixels yielded questionable results for some of the subsets. To ensure that slight camera movement during centrifuge rotation did not affect the PIV results, the displacement of a subset on the frame of the model was tracked, recorded and subtracted from the PIV results.

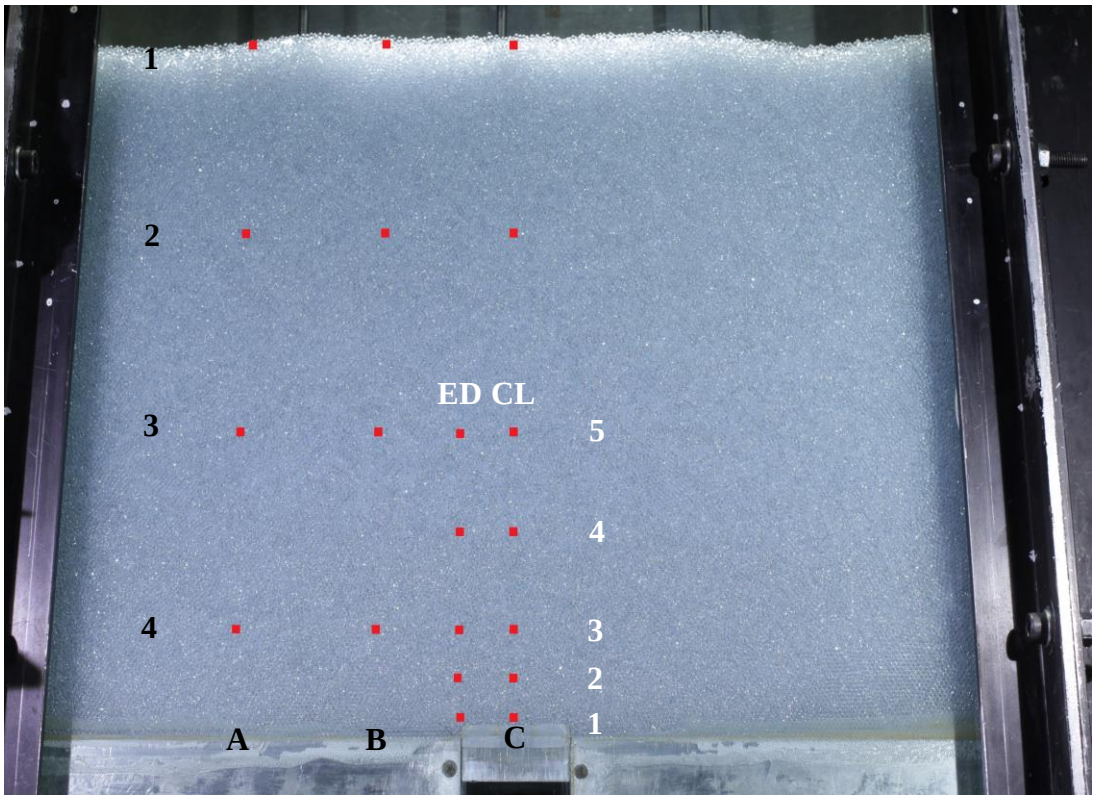

Figure 5-3: PIV subset coordinates for displacement trajectory monitoring

5.6.4 Maximum shear strain plots

Stone & Wood (1992) state that a maximum shear strain plot is the best tool to represent shear band formation and development in deforming sand. The calculation of shear strains for the DEM simulations was therefore essential to the investigation of shear band propagation during trapdoor lowering and as a final assessment of the selected particle parameters. The rigorous shear strain calculation procedure described by White & Bolton (2004) was applied to the DEM particles to ensure comparable strain results.

The finite element method uses shape functions to interpolate the displacements at points inside an element in terms of the element nodal displacements (Chandrupatla & Belegundu, 2002). The constant strain triangle (CST) is an element often used in finite element analysis "to provide an approximate solution in a 2D domain to the exact solution of given differential equation" and applies linear shape functions over an element. As revealed by the name, strain within the constant strain triangle element is constant. Delaunay triangulation was applied to the particle centroids of the DEM simulations to create a network of triangular, CST elements. Figure 5-4 describes the notation used for the nodes and nodal displacement vectors.

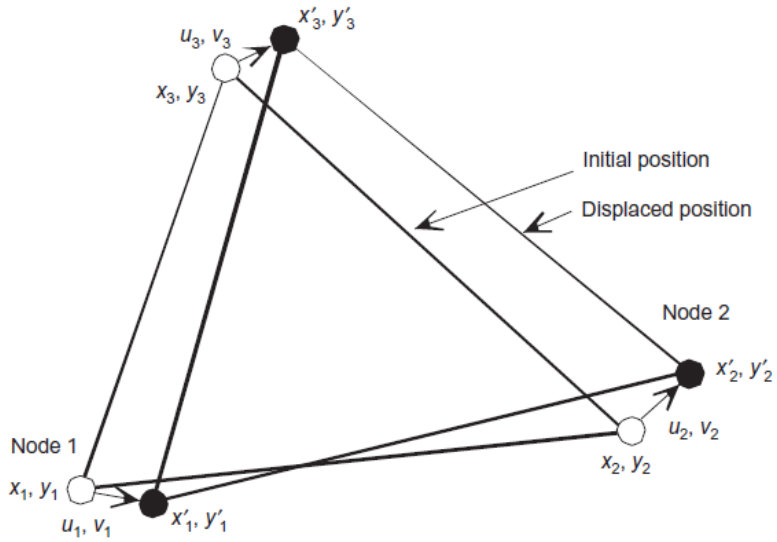

Figure 5-4: Constant strain triangle notation for strain calculations

The displacement matrix (q), strain-displacement matrix (B) and strain matrix (ϵ) formulations are described below. For the strain-displacement notations, y_{ij} represents the displacement between the y-coordinates of nodes i and j (i.e. $y_{23} = y_2 - y_3$).

The displacement matrix is presented in Equation 5-6 below:

$$q = \begin{Bmatrix} u_1 \\ v_1 \\ u_2 \\ v_2 \\ u_3 \\ v_3 \end{Bmatrix}$$ Equation 5-6

Equation 5-7 presents the strain-displacement matrix:

$$B = \frac{1}{\det(J)} \begin{bmatrix} y_{23} & 0 & y_{31} & 0 & y_{12} & 0 \\ 0 & x_{32} & 0 & x_{13} & 0 & x_{21} \\ x_{32} & y_{23} & x_{13} & y_{31} & x_{21} & y_{12} \end{bmatrix}$$ Equation 5-7

Where J is defined as shown in Equation 5-8:

$$J = \begin{bmatrix} x_{13} & y_{13} \\ x_{23} & y_{23} \end{bmatrix}$$ Equation 5-8

Finally, the strain matrix is displayed as Equation 5-9:

$$\epsilon = Bq = \begin{Bmatrix} \dfrac{\partial u}{\partial x} \\ \dfrac{\partial v}{\partial y} \\ \dfrac{\partial u}{\partial y} + \dfrac{\partial v}{\partial x} \end{Bmatrix}$$ Equation 5-9

The CST strain matrix of each element was converted to a 2x2 matrix to resemble the displacement gradient matrix (L) used by White & Bolton (2004) in their engineering strain calculation procedure, where L is defined as shown in Equation 5-10:

$$L = \begin{bmatrix} \dfrac{\partial u}{\partial x} & \dfrac{\partial u}{\partial y} \\ \dfrac{\partial v}{\partial x} & \dfrac{\partial v}{\partial y} \end{bmatrix}$$ Equation 5-10

The matrix operations presented as Equation 5-11, Equation 5-12 and Equation 5-13 were used to convert the displacement gradient matrix to the Biot strain matrix, from which the engineering strains could be derived:

$$F = L + I$$ Equation 5-11

$$U = (F^T F)^{1/2}$$ Equation 5-12

$$E^{Biot} = U - I$$ Equation 5-13

Where:

F = Deformation matrix

I = Identity matrix

U = Stretch matrix (U^2 is the Cauchy-Green strain matrix)

E^{Biot} = Biot strain matrix

The principal engineering strains ($\varepsilon_{eng,I}, \varepsilon_{eng,II}$) are equal to the eigenvalues of the Biot strain matrix. The engineering linear and shear strains can therefore be derived from the Biot matrix by applying Equation 5-14, Equation 5-15 and Equation 5-16, as follows:

$$\varepsilon_{eng,xx} = E_{11}^{Biot}$$ Equation 5-14

$$\varepsilon_{eng,yy} = E_{22}^{Biot}$$ Equation 5-15

$$\gamma_{xy} = E_{12}^{Biot} + E_{21}^{Biot}$$ Equation 5-16

The engineering principal strains were converted to the natural principal strains ($\varepsilon_{log,I}, \varepsilon_{log,II}$) by applying Equation 5-17 and Equation 5-18:

$$\varepsilon_{log,I} = log_e(1 + \varepsilon_{eng,I})$$ Equation 5-17

$$\varepsilon_{log,II} = log_e(1 + \varepsilon_{eng,II})$$ Equation 5-18

Finally, the maximum natural shear strain ($\gamma_{log,max}$) was defined as the difference between the natural principal strains as demonstrated in Equation 5-19:

$$\gamma_{log,max} = \varepsilon_{log,I} - \varepsilon_{log,II}$$ Equation 5-19

The algorithms above were incorporated into a Python subroutine to generate surface plots of the maximum natural shear strains which were compared to those obtained from the PIV results for validation of the calibrated parameters (see Appendix C).

5.7. PARTICLE SHAPE EFFECTS

In discrete element modelling, the shear strength of bulk material can be increased by either using non-spherical particles to simulate particle interlock or by assigning a rolling resistant moment which directly restricts the particle rotation (Coetzee, 2017). Rolling resistance is typically used to model shape effects in DEM, as it is computationally inexpensive in comparison to physical shape modelling. Several researchers have, however, reported distinct differences in the localisation behaviour of materials when comparing the two methods of particle shape modelling in DEM (Zhou et al., 2013). Given the advantage of parallelism of the Blaze-DEM architecture, it was considered the ideal tool to investigate shear band propagation, by modelling various particle shapes.

The importance of particle shape as an input parameter was emphasised by Höhner et al. (2012) after undertaking hopper discharge tests with polyhedral particle shapes and clumped particles.

5.7.1 Polyhedral particles

In order to investigate the influence of varying particle shape on the propagation of shear bands and cavity propagation mechanisms during trapdoor lowering, isolation of particle shape effects on the simulation was essential. The DEM experimental setup used for the spherical simulations, as well as the calibrated particle parameters, was therefore replicated for the tests undertaken with the polyhedral particles.

The selected particle shapes, namely a dodecahedron and tetrahedron, are shown in Figure 5-5 and were chosen due to the distinct differences in the acuteness of their interior angles (degree of angularity) and sphericity.

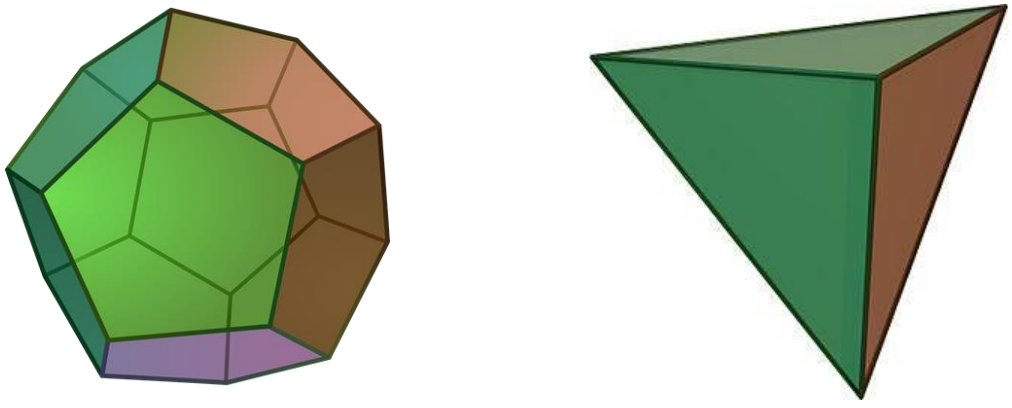

(a) (b)

Figure 5-5: Polyhedral particle shapes (a) Dodecahedron: 12 Faces and 20 Vertices and (b) Tetrahedron: 4 Faces and 4 Vertices (Wikipedia, 2018)

Zhou et al. (2018) describe sphericity of a given particle as the ratio of the surface area of a sphere, with the same volume as that of the particle, to the particle's surface area. The resultant formulation is described by Equation 5-20, below.

$$S = \frac{\sqrt[3]{36\pi V^2}}{SA} \qquad \text{Equation 5-20}$$

Where:

S = Sphericity

V = Particle volume

SA = Particle surface area

The pattern of discontinuities formed during the lowering of the trapdoor is governed by the dilation of the soil and is a function of the particle size. Stone & Wood (1992) further report that the same pattern of discontinuities would be observed if the stress level and ratio of boundary movement to particle size was the same. By virtue of changing the particle shape, the particle size and resulting packing density and fill height of the model would change. In an attempt to isolate particle shape effects, two simulations were run with each particle shape. Given the time constraints associated with determining the number of particles needed to attain the required fill height, the number of particles was standardised to match the number of particles in the simulation with spheres (i.e. 300 000 particles were used).

In the first of the two simulation types, termed the "Equal Volume" (EV) simulation, polyhedral particles with the same volume and density as that of the spheres were used to replicate the stress profile of the original model. This resulted in particles being larger than the equivalent-volume spheres, particularly in the case of the tetrahedrons, which in turn affected the ratio between the particle size and trapdoor. A second simulation, termed the "Equal Bounding Perimeter" (EBP) simulation, scaled the polyhedral particles so that the maximum circumscribed sphere bounding the particles was equal in volume to that of the spheres in the original simulation. The ratio of particle size to boundary movement was therefore kept constant in this simulation, but it yielded smaller particles, resulting in a reduced fill height for the same number of particles. To model equivalent stress levels, the particle densities were increased according to the volume ratio between the individual polyhedral and spherical particles. Although the stress profile would not be the same throughout the fill height, the EBP simulation would allow for a comparison of the initial orientation of shear bands to be investigated. Table 5-2 lists the equivalent particle properties at 50 times gravitational acceleration.

Table 5-2: Particle properties for the polyhedral particle DEM simulations

	Volume (m^3)	Circumscribed Sphere		Sphericity	Density (kg/m^3)
		Radius (m)	Volume (m^3)		
Sphere	0.524E-03	0.05	0.524E-03	1	2500
Doc_EBP	0.348E-03	0.05	0.524E-03	0.910	3760
Doc_EV	0.524E-03	0.0573	0.787E-03		2500
Tet_EBP	64.2E-06	0.05	0.524E-03	0.671	20405
Tet_EV	0.524E-03	0.1007	4.27E-03		2500

*Doc – Dodecahedron simulations
*Tet – Tetrahedron simulations

5.7.2 Model preparation

The polyhedral particle simulations were prepared in the same manner as the sphere simulations. The models were scaled to prototype (life) size as results would therefore be directly comparable to those of the sphere simulations.

Filling of the container was undertaken by means of pluviation, analogous to that of the spheres. The particle stiffness was reduced to 0.1E+09 N/m (as per the selected filling experiment for the sphere simulation, detailed in Section 6.3.2 and Table 6-1) during the filling process to allow for a greater time step and reduction in computational time. During the 'spin-up' simulation and application of gravitational acceleration, the calibrated particle stiffness of 45.0E+09 N/m was applied, and the corresponding bulk density and fill height recorded.

After several attempts at various model scales, particle stiffnesses and time steps, it was not possible to run stable polyhedral particle simulations. This was attributed to the Blaze-DEM's single precision computing capability and is discussed in detail in Section 7.2. Figure 5-6 shows the filling of the container with dodecahedrons of equal bounding perimeter (same particle-boundary size ratio) at a reduced particle contact stiffness of 0.13E+06 N/m. Once the particles had settled, the stiffness was increased to 78.0E+06 N/m to simulate the stiffness of the glass beads while allowing for a large enough time step to be applied and the trapdoor was lowered. As per the linear force-displacement law for the normal direction in Equation 2-11, particle contact stiffness and particle-particle overlap are inversely proportional to one another. Therefore, a decrease in particle stiffness results in "softer" particles with greater overlap volume. This may result in particles pushing through one another and the artificial strongbox with high force application. A decrease in particle stiffness, however, allows for a significantly larger time step as per the critical time step formulation in Equation 5-1 and Equation 5-2.

Although there were indications of initial stability, it was found that at the selected particle stiffness of 78.0E+06 N/m, the particles were too soft (i.e. large particle-particle overlap as a result of the low

particle contact stiffness) and they soon pushed through the walls of the strongbox, resulting in an unstable simulation.

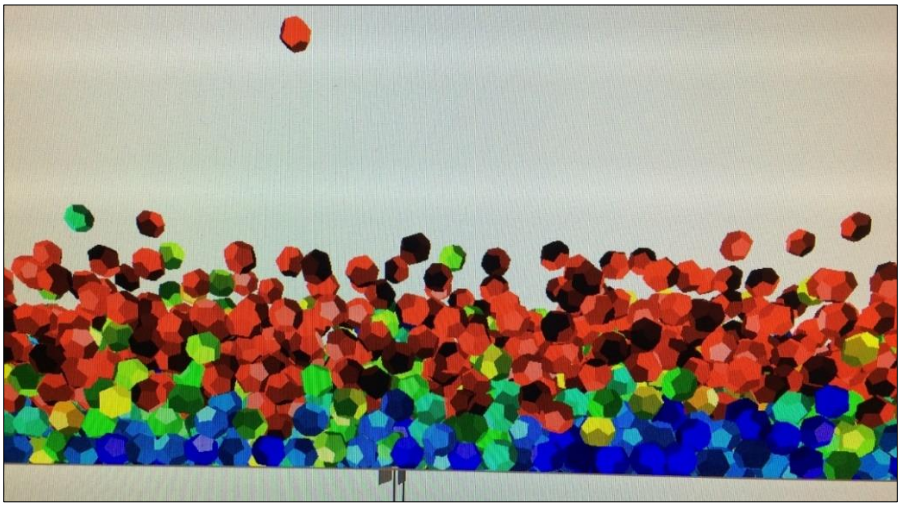

Figure 5-6: Dodecahedron DEM filling simulation (Doc_EBP)

5.7.3 Rolling resistance application

Given the unsuccessful trapdoor simulations with the polyhedral particles, an alternative investigation was initiated to determine particle shape effects on shear band propagation during trapdoor lowering. This was done by applying a rolling resistance coefficient to the particles of the calibrated spherical model.

Yan et al. (2015) showed that the effect of increasing the rolling resistance coefficient is negligible when the friction coefficient is low (<0.05). This conclusion confirms that the friction and rolling resistance coefficients work together to introduce shape-like effects, as inferred by Wensrich & Katterfeld (2012). They demonstrated this statement by simulating the angle of repose of spherical particles with varying particle-particle friction coefficients (μ or μ_p) and rolling resistance coefficients (μ_r), as shown in Figure 5-7.

From Figure 5-7, three combinations of rolling resistance and friction coefficient values were selected to investigate the development of discontinuities at various imposed angles of repose. With the exception of the rolling resistance and friction coefficients, the particle properties selected for this investigation differ to those applied by Wensrich & Katterfeld (2012). The angle of repose contours presented in Figure 5-7 were therefore used solely as a guideline to determine the range of applicable friction and rolling resistance coefficients required to determine the effect of simulated particle interlock on soil deformation mechanisms during cavity propagation.

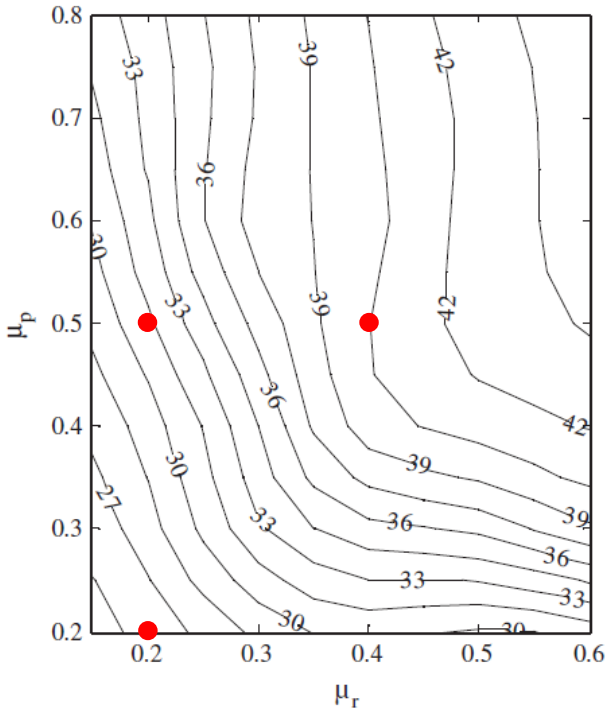

Figure 5-7: Angle of repose contours for spheres with varying μ_r and μ (Wensrich & Katterfeld, 2012)

For this investigation, the value of the particle-particle friction coefficient (μ) in Figure 5-7 was assigned to both the kinetic and static friction coefficients in Blaze-DEM. Table 5-3 summarises the variable input parameters for the simulations; the calibrated parameters were assigned to the remaining particle parameters (see Table 6-3 for calibrated particle parameters) .

Table 5-3: Particle properties for the rolling resistance DEM simulations

Simulation Name	Rolling Resistance Coefficient (μ_r)	Friction Coefficient (μ)	Angle of Repose (°)
Rolling Friction 1 (RF1)	0.2	0.2	25.5
Rolling Friction 2 (RF2)	0.2	0.5	31
Rolling Friction 3 (RF3)	0.4	0.5	40.5

For the purpose of investigating the effect of material shear strength on deformation propagation mechanisms, a comparison of the shear deformation experienced by the material in each of the three simulations was undertaken by means of maximum shear strain plots. These were plotted at the physical experiment equivalent of 80 mm trapdoor displacement (4 m trapdoor displacement at prototype scale) and are presented in Chapter 7.

6. CALIBRATION OF NUMERICAL TRAPDOOR EXPERIMENT

6.1. INTRODUCTION

Chapter 6 details the procedure employed to calibrate the DEM trapdoor experiment parameters, using spherical particles, against the centrifuge test undertaken with glass beads.

Blaze-DEM was used to conduct a twofold sensitivity analysis, in which material displacement contours for an equivalent trapdoor displacement of 10 mm were used to investigate the sensitivity of various parameters. The chapter opens with a comparison of the two numerical experiments used in the first portion of the sensitivity study, after which the results of the sensitivity study are presented and discussed. The first portion of the sensitivity analysis illustrates the effect of the time step, particle stiffness, container properties, contact model and trapdoor velocity on the material behaviour and numerical stability of the model during trapdoor lowering. The second portion focuses on the influence of the individual particle parameters on the bulk material behaviour and establishes a feasible range of values for the calibration of each parameter.

Calibration of the DEM model was then based on the results of the second phase of the sensitivity analysis. The total displacement contours of the physical model, plotted using GeoPIV, were used as the benchmark for the calibration of each of the numerical particle parameters. The particle stiffness was found to be the crux of the calibration procedure and its results are therefore presented first, followed by those of the COR and friction coefficients.

Following the calibration of the numerical model, using equivalent displacement contours, validation of the selected model parameters was undertaken at particle level by means of particle displacement trajectories. For the validation process three numerical models with varying input parameters were investigated, including the calibrated model. Graphs of the displacement trajectories, at an equivalent trapdoor displacement of 20 mm, are plotted and presented for the numerical models, as well as for the corresponding subset positions of the physical model. Further numerical model validation is then presented in the form of maximum shear strain plots and are discussed in the preceding section. The plots present the maximum shear strains for all three numerical models at an equivalent trapdoor displacement of 80 mm.

The chapter concludes with a visual comparison of the maximum shear strain plots of the calibrated numerical model and the corresponding GeoPIV plots of the physical trapdoor experiment with glass beads, at various magnitudes of trapdoor displacement. A discussion of the numerical model calibration and validation results concludes that the calibrated model replicates the physical model material behaviour sufficiently for the purposes of this study.

6.2. NUMERICAL MODEL PREPARATION: PLUVIATION AND SPIN-UP

As detailed in Section 5.3.2, the Blaze-DEM trapdoor experiment was modelled to prototype dimensions (i.e. the model strongbox and particle dimensions were scaled to correspond to the centrifuge trapdoor dimensions at 50 times gravitational acceleration). Numerical modelling of the trapdoor experiment at these life-size dimensions allowed for a reduction in the computational effort required.

The initial DEM simulation experiments were created by raining the spherical particles into the prototype-sized container at 1/50g. The initial particle parameters listed in Table 5-1 were assigned to the particles, however, the particle stiffness and number of particles were varied until a resultant fill height and bulk density, corresponding to the experimental setup, were obtained. Two representative initial trapdoor simulation experiments were created which represented the model material state after pluviation and centrifuge spin-up. These two experiments were used as the initial experiments (files) for the sensitivity analyses presented later in the chapter.

The primary difference between the two initial experiments was the normal contact stiffness assigned to the particles during the pluviation phase, as detailed in Table 6-1. Two different particle stiffnesses were assigned in the two initial experiments to investigate the effect of a comparatively low and high particle stiffness on the bulk material model after pluviation. As discussed in Section 5.5.1, the particle stiffness was reduced during the pluviation stage to allow for a greater time step (as per Equation 5-1) which ultimately reduces the run-time and computational cost of the simulation. The particle stiffness was then increased during the spin-up simulations to values approximating the particle normal contact stiffness for glass beads as defined by Equation 5-3. The remaining particle parameters for both pluviation and spin-up experiments were similar and are included in Appendix B.1 and Appendix B.2, respectively.

Table 6-1: Pluviation and spin-up experiment properties

	Pluviation		**Spin-up**	
Experiment Names	TD_Initial16	TD_Initial25	TD_SU04	TD_I26
Initial Experiment	-	-	TD_Initial16	TD_Initial25
Gravity (m/s^2)	-0.196	-0.196	-9.8	-9.8
Particle normal stiffness, k_n (N/m)	9.00E+06	0.10E+09	55.0E+09	12.3E+09
Resultant fill height (mm) (model dimensions)	331	331	348	346
Resultant bulk density (kg/m^3)	1692	1688	1671	1677

Once the model container had been filled with the required number of particles, at the lower particle contact stiffness, the spin-up simulations were initiated. During spin-up simulations both the particle

stiffness and gravitational acceleration were increased to correspond to the centrifuge experiment. The first experiment (TD_Initial16) had a much lower initial particle contact stiffness which resulted in greater particle overlap and higher bulk density of the material. According to the linear force-displacement law described in Equation 2-11, the particle stiffness and particle-particle overlap distance are inversely proportional to one another. A low contact stiffness will therefore result in a larger particle overlap and greater bulk density as more material is confined within a set space. The second pluviation experiment (TD_Initial25), with greater particle stiffness, had a lower material bulk density due to the smaller particle overlap. During the spin-up simulation, the particle contact stiffnesses were increased, causing the particles to push each other away to reduce the particle overlap according to the force-displacement law applied by the DEM code. However, the gravitational acceleration was increased simultaneously, resulting in higher inter-particle forces which in turn caused the particles to push into each other. The effect of these two counteracting phenomena on the bulk density of the material is dependent on the magnitude of stiffness increase. A relatively small difference in bulk density was observed for the second starting experiment, however, a notable decrease in bulk density was observed for TD_Initial16, for which the particle stiffness increase was significant. Both resulting fill heights were slightly greater than the desired equivalent height of 331 mm (physical model dimensions), but height differences of 5.0% and 4.6% for TD_SU04 and TD_I26, respectively, were deemed to be inconsequential to the study of the global material behaviour. The spin-up simulations were terminated after a set period (approximately 48 hours). The average particle velocities for TD_SU04 and TD_I26 at simulation termination were 8.2E-03 m/s and 0.8E-03 m/s, respectively.

6.3. SENSITIVITY ANALYSIS: DISPLACEMENT CONTOURS

6.3.1 Overview of the sensitivity analysis

A twofold numerical sensitivity analysis was undertaken by comparing the displacement contour plots of the material at a model trapdoor displacement of 10 mm, or the prototype equivalent of 0.5 m. The first part of the sensitivity analysis targeted the parameters which would affect the numerical stability of the model, as well as ensure a realistic representation of the physical model within a reasonable time frame and resulting time step, such as the trapdoor velocity and critical time step. The second facet of the sensitivity analysis entailed investigating the influence of the individual particle input parameters on the bulk response of the material and their significance when using the DEM to model sinkhole propagation. Displacement contours were used to undertake the sensitivity analysis as changes to model parameters significant to this study would be visually discernible. They could further be compared to the GeoPIV displacement contour results from the centrifuge modelling. Finally, displacement contour plots were selected as the tool to complete the sensitivity study as they are less computationally expensive than shear strain plots.

As discussed in Chapter 5, the dimensions of the numerical model were scaled up by a factor of 50 to match the stress conditions of the physical model. The dimensions in the following figures therefore reflect the numerical model or prototype dimensions (units in metres). Unless specifically stated otherwise, the parameters listed in Table 6-2 are the benchmark parameters from which the sensitivity analysis followed. With the exception of the particle normal contact stiffness, which was calibrated to obtain realistic results, these benchmark values for glass beads were obtained or derived from literature (see Section 5.4.5). A trapdoor velocity of 0.02 m/s (20 mm/s) was selected as the standard trapdoor velocity for the numerical model (prototype dimensions).

Table 6-2: Benchmark parameters for sensitivity analysis

COR	$k_n\ (N/m)$	μ_s	μ_k	μ_r
0.9	55.0E+09	0.18	0.18	0.001

Figure 6-1 presents the total displacement contours (resultant particle displacement in the x- and y-directions) for the centrifuge experiment with glass beads at 10 mm displacement of the trapdoor. This figure is presented to indicate the magnitude and shape of the total displacement contours for comparison and calibration purposes. Model dimensions and particle displacements were upscaled to prototype dimensions (i.e. at 50g). It should be noted that the units in the figure are centimetres (see Section 5.6.2 for clarification of selected units).

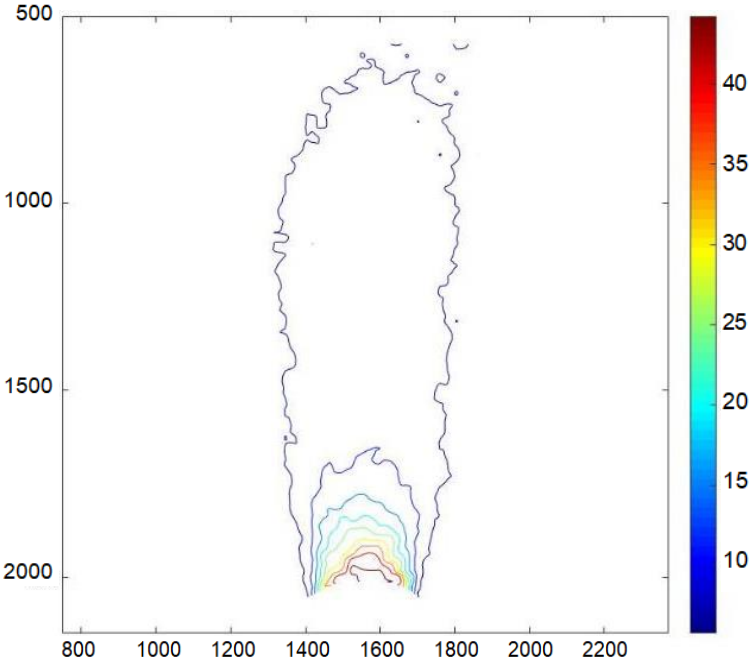

Figure 6-1: Total displacement contours at 50 cm trapdoor displacement (prototype dimensions), corresponding to 10 mm trapdoor displacement of the centrifuge experiment undertaken with glass beads (units in centimetres)

6.3.2 Selection of the spin-up experiment

The spin-up (initial) experiments listed in Table 6-1 were the starting files for the numerical trapdoor displacement simulations using Blaze-DEM. The material stress state and model configuration in these files correspond to that of the physical centrifuge model at the instant before trapdoor lowering is initiated. The TD_SU04 initial experiment was used in addition to the TD_I26 initial experiment to investigate the appropriate time step and trapdoor velocity for the numerical model. However, the remainder of the sensitivity study was completed by using only TD_I26 as the starting experiment. A review of the displacement contours from the time step and trapdoor velocity sensitivity analyses showed that the displacement contours which use TD_I26 as the starting experiment better represented the centrifuge model material behaviour. This was attributed to the near-zero average particle velocity of TD_I26 and the fact that its average particle velocity was an order of a magnitude smaller than that of TD_SU04.

6.3.3 Sensitivity analysis: Time step

Time step selection is crucial to the numerical stability of the simulation and a fraction of 10% to 20% of the critical time step is often recommended for the time step magnitude (Yan et al., 2015). A sensitivity analysis of the time step was undertaken for both initial experiments, the results of which are presented in Figure 6-2 and Figure 6-3, for TD_SU04 and TD_I26, respectively. A stark difference is noted between the contours of Figure 6-2 (b) and (c) alluding to a greater instability of the simulation at a time step greater than 25% of the critical time step. Although slightly wider contours exist between (a) and (b) of the same figure, the difference is negligible. The behaviour of the geomaterial at a time step of 17% and 25% of the critical time step is therefore considered to be analogous.

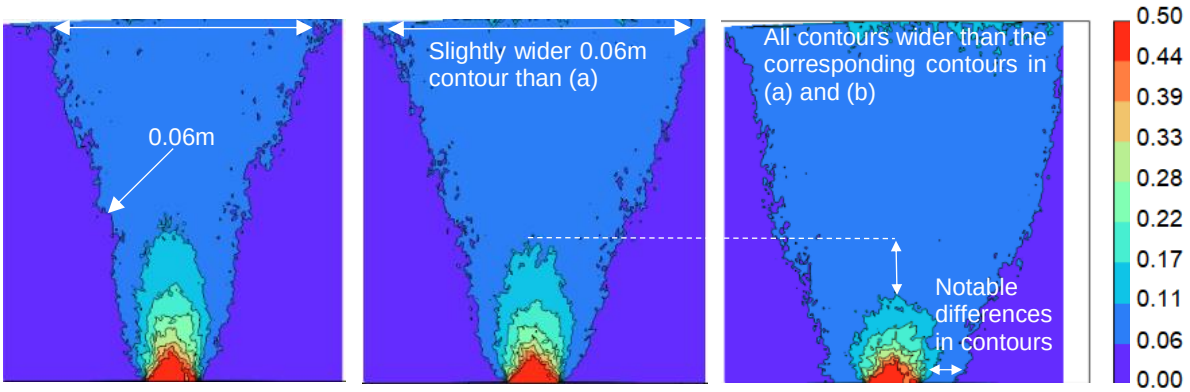

Figure 6-2: Total displacement contours for TD_SU04 at a time step of (a) 17% (b) 25% and (c) 34% of the critical time step, at 0.5 m displacement of the trapdoor (units in metres)

A comparison of Figure 6-3 (b) and (c) serves as confirmation of the above conclusion and recommended time step from literature. The wider contours are attributed to particles travelling too far within a single time step (i.e. the particles travel further than what the force-displacement law allows

for a given particle stiffness, thereby creating a wider zone of influence). Wider contours are evident in the figure depicting a time step fraction of 30% than in the figures depicting fractions of 10% and 20%. A time step of 20% of the critical time step was deemed acceptable for the simulation as an insignificant difference is again noted between Figure 6-3 (a) and (b). Furthermore, selection of a value of 20% instead of 10% would contribute to obtaining realistic results within a reasonable time frame.

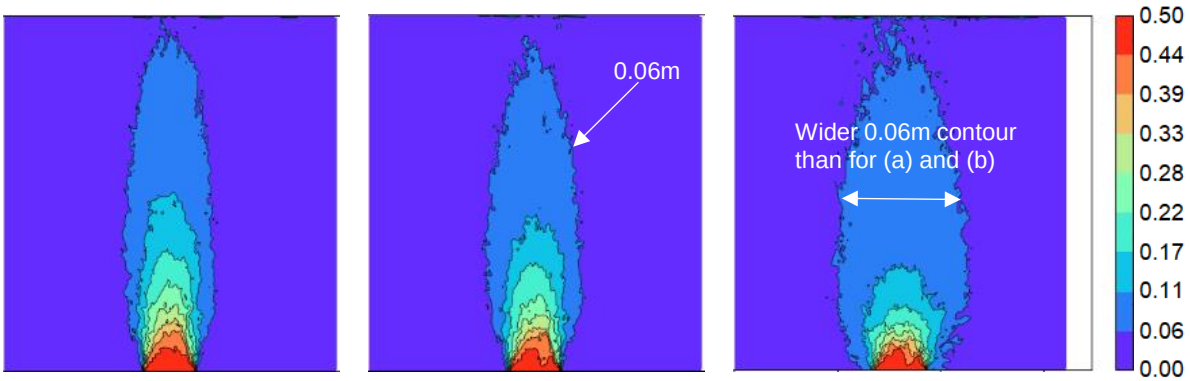

(a) (b) (c)

Figure 6-3: Total displacement contours for TD_I26 at a time step of (a) 10% (b) 20% and (c) 30% of the critical time step, at 0.5 m displacement of the trapdoor (units in metres)

6.3.4 Sensitivity analysis: Trapdoor velocity

The primary objectives of the sensitivity analysis for the trapdoor velocity were to minimise the required computational time and effort, as well as to ensure a realistic representation of the physical model. It was not feasible to replicate the centrifuge model trapdoor velocity of 0.025 mm/s (normalised equivalent of 1.25 mm/s at prototype dimensions) and a comparison of the material displacement contours was undertaken to determine at what velocity the dynamic effects of trapdoor lowering were negligible. From Figure 6-4, which showcases the variations in displacement contours resulting from a change in trapdoor velocity for TD_SU04, virtually no difference exists between trapdoor velocities of 0.01 and 0.02 m/s shown in Figure 6-4 (a) and (b), respectively. As shown in Figure 6-4 (c), the displacement contours for a trapdoor velocity of 0.03 m/s tend towards verticality. It is conjectured that at the faster rate of trapdoor lowering, the time allowed for the disturbance to propagate through the material is limited and the zone of influence therefore extends primarily in the direction of movement (i.e. vertically). From Figure 6-4 it is evident that dynamic effects are introduced at trapdoor velocities equal to or greater than 0.03 m/s (at prototype dimensions).

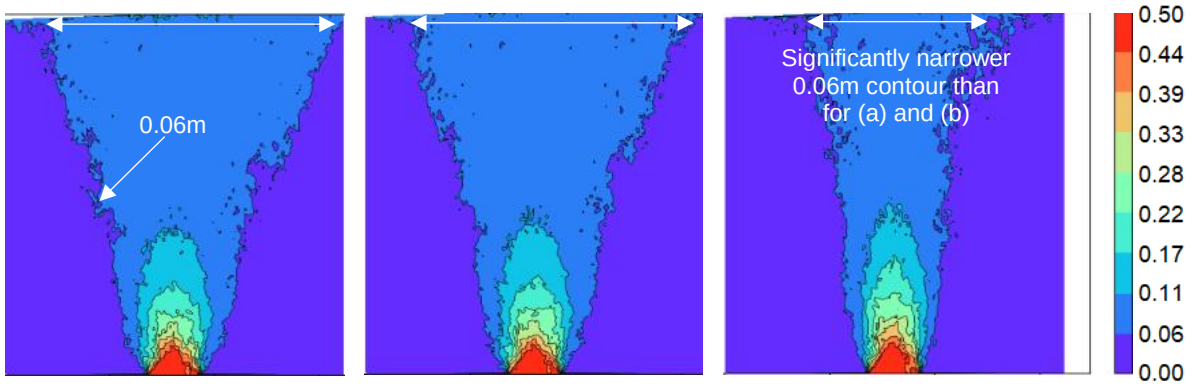

(a) (b) (c)

Figure 6-4: Total displacement contours for TD_SU04 at trapdoor velocities of (a) 0.01 m/s (b) 0.02 m/s and (c) 0.03 m/s, at 0.5 m displacement of the trapdoor (units in metres)

Figure 6-5 displays the equivalent trapdoor velocity comparison for the TD_I26 initial experiment. These results are not entirely consistent with those presented in Figure 6-4, as virtually no difference is observed between the displacement contours for a trapdoor velocity of 0.02 m/s and 0.03 m/s, shown in Figure 6-5 (b) and (c), respectively. A greater zone of influence is noted in Figure 6-5 (a), which presents the trapdoor displacement contours for a trapdoor velocity of 0.01 m/s, indicating that dynamic effects may influence the results for trapdoor velocities greater than 0.01 m/s. The difference between the results for a trapdoor displacement of 0.01 m/s (a) and 0.02 m/s (b) was, however, deemed to be sufficiently small and a trapdoor velocity of 0.02 m/s (20 mm/s) was therefore selected. Additionally, the trapdoor velocity selection of 0.02 m/s instead of 0.01 m/s halved the required computational time for the numerical trapdoor experiments.

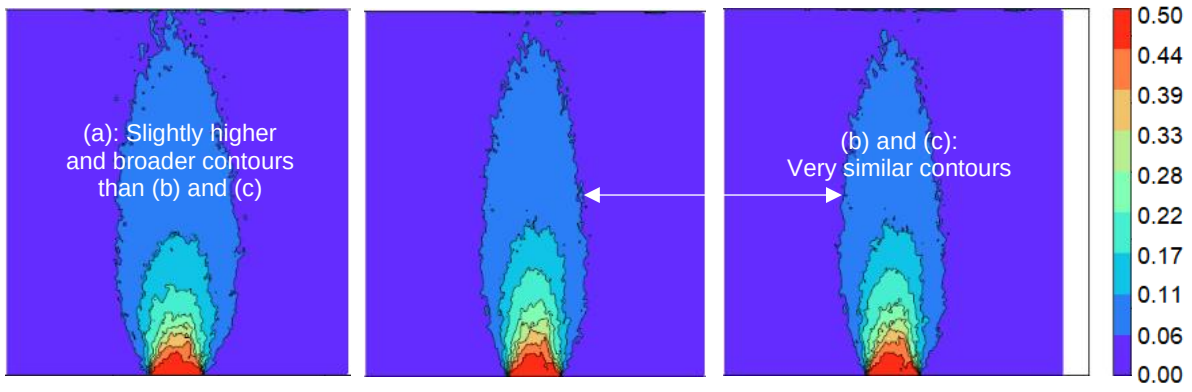

(a) (b) (c)

Figure 6-5: Total displacement contours for TD_I26 at trapdoor velocities of (a) 0.01 m/s (b) 0.02 m/s and (c) 0.03 m/s, at 0.5 m displacement of the trapdoor (units in metres)

6.3.5 Sensitivity analysis: Force-displacement contact law

A force-displacement contact law comparison was undertaken to validate the application of the linear-spring dashpot model instead of the non-linear Hertz-Mindlin (H-M) contact model. A slightly smaller

particle stiffness of 45.0E+09 N/m was used in this comparison and the time step was reduced to approximately 10% of the critical time step, for both contact models. The time step was reduced as the particle stiffness, and therefore required time step, is scale invariant when the H-M contact model is used in 3D simulations (Feng et al., 2007). Figure 6-6 (a) and (b) present the total displacement contours for the linear-spring dashpot and H-M contact models, respectively. Figure 6-6 (c) presents the difference in displacement between the two plots in (a) and (b). The recorded difference in displacement between the displacement contours for the two contact models is considered to be negligible (note the colour bar scale difference of (c) in comparison to that of (a) and (b)). This validates the application of the linear-spring dashpot contact model for the DEM trapdoor experiment.

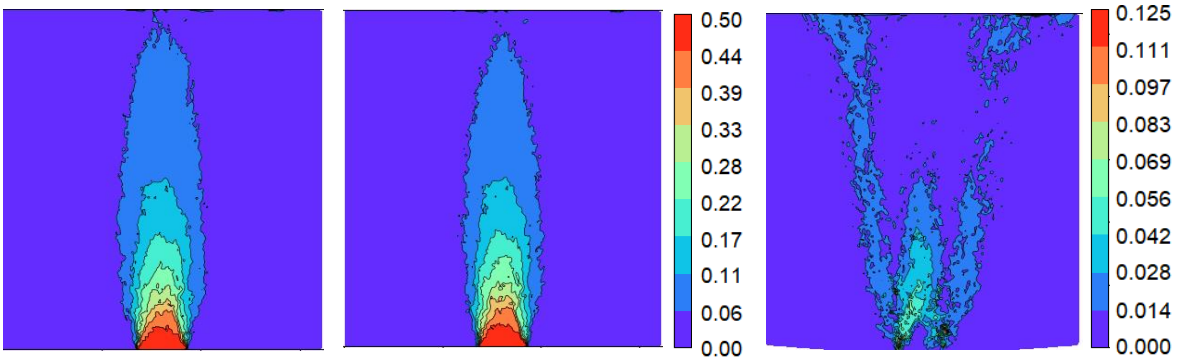

(a) (b) (c)

Figure 6-6: Total displacement contours for the (a) linear-spring dashpot and (b) non-linear Hertz-Mindlin force-displacement contact models as well as the (c) difference in displacement for the two contact models, at 0.5 m displacement of the trapdoor (units in metres)

6.3.6 Sensitivity analysis: Model container properties

The displacement contours represent the displacements of the glass beads in contact with the glass panel of the material container or strongbox. A sensitivity analysis was therefore undertaken to determine what effect the properties of the numerical 'glass panel' would have on the bulk material behaviour during trapdoor lowering. To investigate this effect, the COR, friction coefficients and normal contact stiffness of the container were adjusted to match those of the glass beads. Figure 6-7 (a) shows the displacement contours for initial container COR of 0.7, friction coefficient values of 0.3, and normal contact stiffness of 5.0E+06 N/m (see Table 5-1). For the displacement contours shown in Figure 6-7 (b), respective COR and friction coefficient values of 0.9 and 0.18 were assigned to the container and the normal contact stiffness was increased to 55.0E+09 N/m. From the difference plot (Figure 6-7 (c)), it is evident that the material parameters assigned to the container have very little to no effect on the bulk material behaviour during trapdoor lowering. The initial parameter values for the COR, friction coefficients and normal contact stiffness were therefore retained for the remainder of the calibration and investigative simulations.

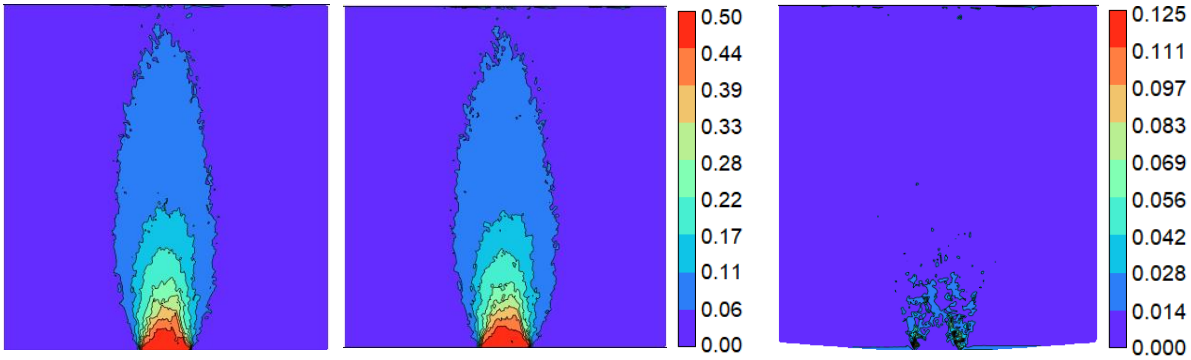

(a) (b) (c)

Figure 6-7: Total displacement contours for the (a) initial and (b) adjusted model container material properties as well as the (c) difference in displacement of the two contour plots, at 0.5 m displacement of the trapdoor (units in metres)

6.3.7 Sensitivity analysis: Particle normal contact stiffness

It is well-known that for spherical, elastic particles the normal contact stiffness, also referred to as the particle stiffness (expressed in units of N/m), is directly related to the Young's Modulus of the material by means of the particle radius (Thakur et al., 2016). When investigating the effect of the particle stiffness on the material behaviour, numerical instability of the system was observed at lower contact stiffness values. According to Equation 5-3, for a particle radius of 0.05 m and Young's Modulus of 78 GPa (glass beads material) the estimated particle normal contact stiffness is 7.8E+09 N/m. The particle stiffness assigned to the models for which the total displacement contour plots are presented in Figure 6-8 increases by two orders of magnitude between consecutive displacement contour plots in the figure. The calculated value of 7.8E+09 N/m was used as the baseline value (Figure 6-8 (b)). As described in Section 2.4.2, and from the linear force-displacement law for the normal direction (Equation 6-1), the particle stiffness is directly related to the extent of particle-particle overlap. Particle overlap, in addition to the damping coefficient, is used to simulate particle deformation during a collision. The greater the particle stiffness, the smaller the amount of particle overlap and allowed particle deformation (Cundall & Strack, 1979).

$$F_n = -k_n.\Delta n_n + c_n.v_n \qquad \text{Equation 6-1}$$

Where:

F_n = Particle-particle contact force

k_n = Particle normal contact stiffness

Δn_n = Particle-particle overlap

c_n = Normal damping coefficient

v_n = Normal inter-particle relative velocity

Given that the experiment was undertaken at 50g and that the maximum stress within the material was approximately 300 kPa, the inter particle forces were significantly greater than what would be encountered at normal gravitational acceleration. From Equation 6-1 and assuming a constant stiffness, the inter particle contact force is directly proportional to the overlap distance. It is proposed that at higher stress levels induced by the centrifuge or equivalent scaling the particle overlap may become too large, resulting in numerical instability as the particles are pushed into one another. This confirms the findings presented by Li et al. (2015) which state that particle contact stiffness increases with an increase in confining pressure. Figure 6-8 (a) indicates that at a lower stiffness, particles penetrate each other with an overlap distance so great that the maximum resultant particle displacement exceeds 1.2 m, with a trapdoor displacement of only 0.5 m. This means that the simulation is neither stable nor representative.

The sensitivity analysis presented in Figure 6-8 was used to determine an approximate range within which the particle stiffness would yield a numerically stable and representative model, within a reasonable time frame. A comparison of the results indicated that the calibrated particle stiffness value would lie between 7.8E+09 N/m and 0.78E+12 N/m. The displacement contours for the lower and upper extremes of this range are shown in Figure 6-8 (b) and (c), respectively.

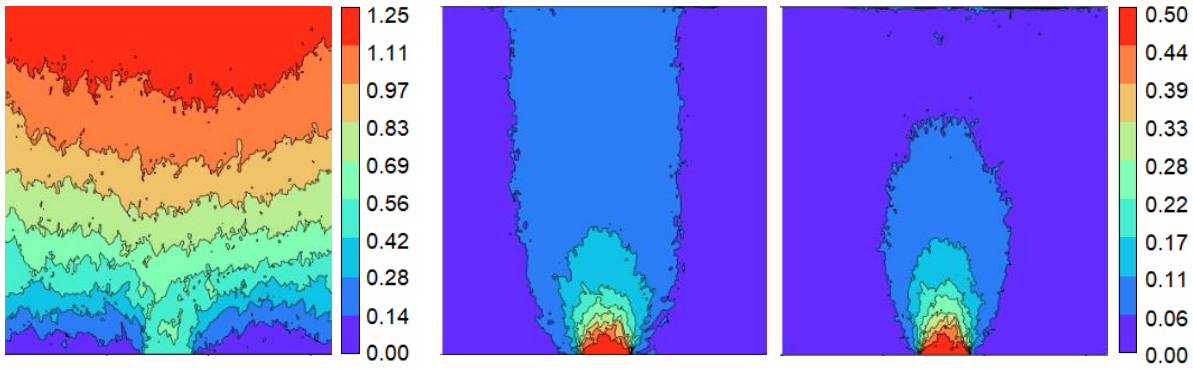

(a) (b) (c)

Figure 6-8: Total displacement contours for a particle normal contact stiffness of (a) 78.0E+06 N/m (b) 7.8E+09 N/m and (c) 0.78E+12 N/m at 0.5 m displacement of the trapdoor (units in metres)

The second aim of the stiffness sensitivity analysis was to investigate the difference in displacement contours within a smaller range of values. Figure 6-9 presents the displacement contours for stiffness values within the range described above. A greater zone of influence is observed for lower particle stiffnesses, resulting in a comparatively greater particle overlap. This means that more particles will be affected, and the 'disturbance' initiated by the lowering of the trapdoor will propagate further. Conversely, where a greater stiffness is applied, the particles are rigid and little overlap is allowed. The greater stiffness value therefore limits the propagation of the disturbance, yielding a stiff bulk material response as shown in Figure 6-9 (c) and (d).

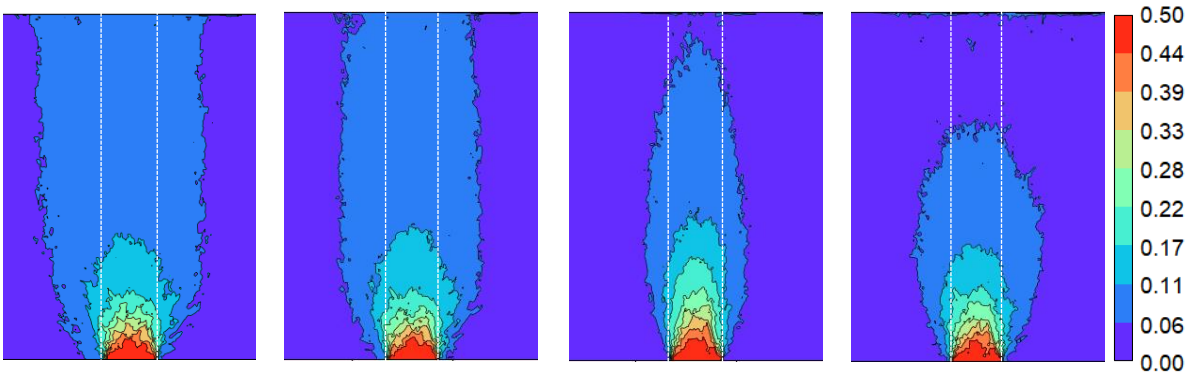

(a) (b) (c) (d)

Figure 6-9: Total displacement contours for a particle normal contact stiffness of (a) 7.8E+09 N/m (b) 12.0E+09 N/m (c) 55.0E+09 N/m and (d) 0.78E+12 N/m at 0.5 m displacement of the trapdoor (units in metres)

6.3.8 Sensitivity analysis: Particle coefficient of restitution (COR)

As discussed in Section 5.4.4, the Coefficient of Restitution (COR) can be described as a measure of the elasticity of a collision between two particles (Lorenz et al., 1997). An inelastic collision, represented by a COR value of zero, represents complete energy dissipation during the collision, whereas an elastic collision, COR value of 1, describes a collision in which there is total energy conservation and as such the final velocities of the particles will be equal to their respective initial velocities.

Figure 6-10 (a) – (d) presents the total displacement contours of the specimen during trapdoor lowering, with increasing COR values (see Table 6-2 for benchmark particle properties). Very little difference is observed in the successive tests which may be attributed to the quasi-static nature of the simulation. As the particles are in contact with each other and slide over one another during trapdoor lowering, their velocities are very small in comparison to dynamic DEM simulations, such as a ball mill simulation. The COR fraction essentially represents the damping coefficient in Equation 6-1 and describes the amount of energy dissipated during a particle-particle collision. If there is very little energy in the collision to begin with, as with particle interactions in a quasi-static system, then the selected fraction of energy conserved will have very little effect on the bulk material behaviour. This observation is supplemented by Cheng et al. (2017) who state that the effects of damping can be neglected for a quasi-static simulation. As a result, they selected a constant COR value of 0.9 in the DEM calibration procedure of Fujian quartz sand modelling triaxial tests.

The slight variation in displacement contours observed in Figure 6-10 shows that as the COR value is increased (decrease in energy dissipation), the zone of influence widens in the horizontal direction, and reduces in the vertical direction. For the displacement contour plots with lower COR values, such as those displayed in Figure 6-10 (a) and (b), the contours plots extend almost exclusively in the vertical direction. At low COR values the vertical translation of the trapdoor is directly transferred to the

particles, but any additional energy is dissipated resulting in a vertical propagation of the disturbance. The zone of influence for a higher COR value increases in the horizontal direction, due to the conservation and transfer of energy during particle-particle collisions.

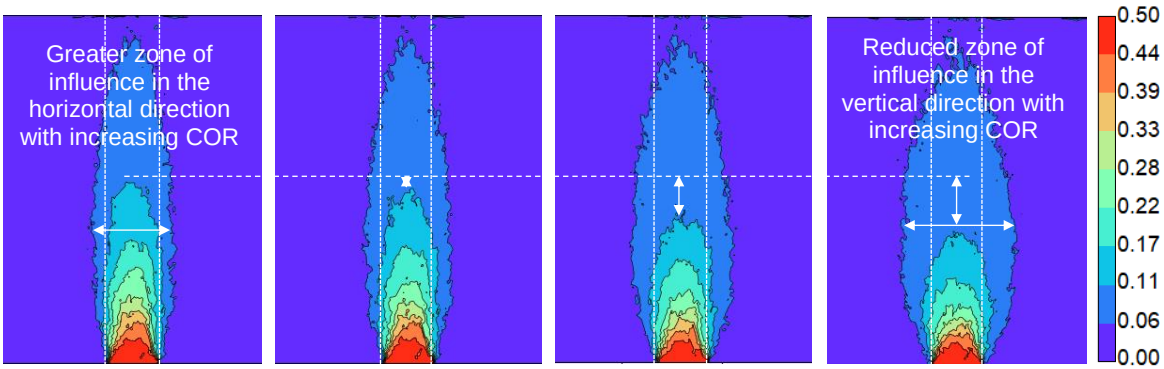

(a) (b) (c) (d)

Figure 6-10: Total displacement contours for particles with a COR of (a) 0.3 (b) 0.6 (c) 0.9 and (d) 0.96 at 0.5 m displacement of the trapdoor (units in metres)

6.3.9 Sensitivity analysis: Particle friction coefficients

During the calibration of the DEM trapdoor model, the particle parameters were considered to be independent numerical entities. Physical limitations between some parameters were therefore not necessarily strictly enforced, e.g. kinetic friction coefficients between particles were allowed to exceed the static friction coefficient. This was done to assess whether this consideration might improve the correlation between the physical and numerical models.

The displacement contours in the following section present an investigation of the effect of friction coefficient variation. Where not specifically stated, the particle parameters are equal to those listed as the benchmark values in Table 6-2. The static and kinetic friction coefficients are important parameters in the simulation of a quasi-static system in which particles push and slide slowly against each other. The displacement contour plots for static friction coefficients ranging from 0.09 to 0.8 are shown in Figure 6-11 (a) to (d) (kinetic friction coefficient remained constant at 0.18). A similar plume shape is observed for all four contour plots. A slight reduction in the zone of influence is observed in the horizontal direction with an increase in the static friction coefficient. With reference to the extent of influence in the vertical direction, the 0.06 m contour diminishes in height as the static friction coefficient increases. However, with the exception of the 0.06 m contour, the vertical contours appear largely unaffected by the change in static friction coefficient. These observations are attributed to the fact that the static friction coefficient resists initial displacement. Once the particle or discrete element has a velocity component, the kinetic friction coefficient will govern material behaviour.

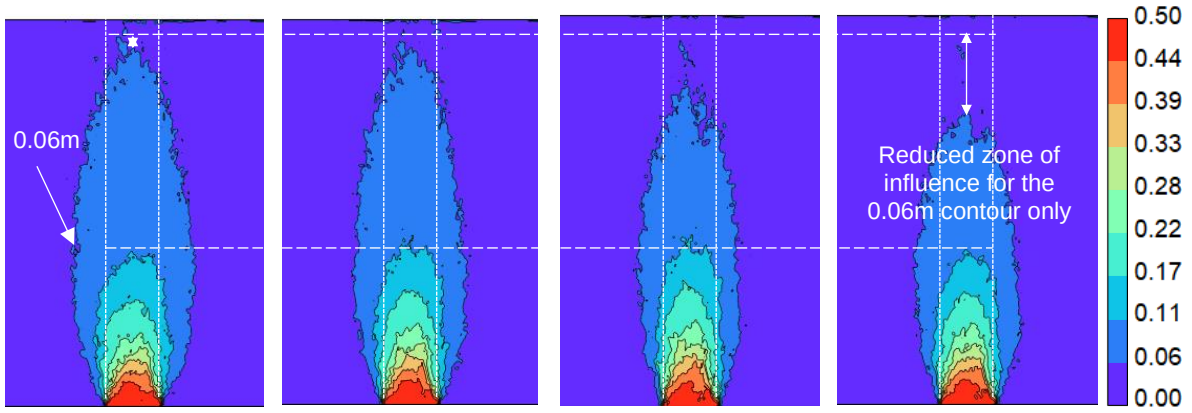

(a) (b) (c) (d)

Figure 6-11: Total displacement contours for particles with a static friction coefficient of (a) 0.09 (b) 0.18 (c) 0.4 and (d) 0.8 at 0.5 m displacement of the trapdoor (units in metres and μ_k = 0.18)

Equivalent displacement contour plots for the same range of kinetic friction coefficient values are displayed in Figure 6-12 (a) to (d) (static friction coefficient remained constant at 0.18). Downward translation of the trapdoor induces sliding between the particles as the material above the trapdoor follows the downward displacement of the trapdoor. In contrast to the displacement contour plots in Figure 6-11, the vertical zone of influence in the displacement contour plots presented in Figure 6-12 reduces for all contour intervals with an increase in the kinetic friction coefficient. Once particle displacement has been initiated, the kinetic friction coefficient is the governing friction parameter and therefore influences all magnitudes of trapdoor displacement. During contact, the static friction coefficient resists particle movement whereas the kinetic friction coefficient specifically resists the movement of particles which are already sliding against one another. The short and wide zone of influence visible in Figure 6-12 (d) (simulation with a kinetic friction coefficient of 0.8) is indicative of the intense vertical sliding resistance as more shear force is transferred to the adjacent material, thereby widening the horizontal zone of influence while limiting the vertical zone of influence.

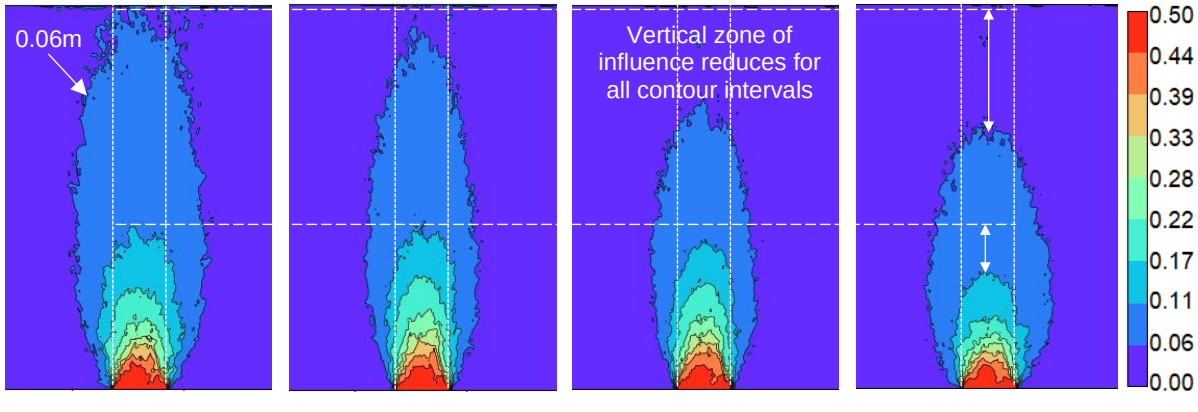

(a) (b) (c) (d)

Figure 6-12: Total displacement contours for particles with a kinetic friction coefficient of (a) 0.09 (b) 0.18 (c) 0.4 and (d) 0.8 at 0.5 m displacement of the trapdoor (units in metres and μ_s = 0.18)

From Figure 6-12, the resistance to particle sliding imposed by the kinetic friction coefficient appears to increase incrementally regardless of whether the kinetic friction coefficient was greater or smaller than the corresponding static friction coefficient. The displacement contour plots in Figure 6-11 and Figure 6-12 show that the static and kinetic friction coefficients in Blaze-DEM can be manipulated numerically to obtain the desired bulk material behaviour or reaction to trapdoor displacement.

6.4. CALIBRATION: TOTAL DISPLACEMENT CONTOURS

Total (resultant) displacement contours for 10 mm displacement of the centrifuge model trapdoor were used as a benchmark against which the particle contact parameters of the spherical particles in the numerical Blaze-DEM model were calibrated to replicate the material behaviour of the physical experiment, in which glass beads were used. Cheng et al. (2017) noted that the macroscopic behaviour of a specimen is directly dependent on the particle contact parameters.

The displacements of the glass beads in the centrifuge experiment were tracked and analysed using GeoPIV, as described in Section 5.6.2. Figure 6-13 presents the total displacement contour plot of the glass beads centrifuge experiment at a trapdoor displacement of 10 mm. The units of displacement and the model configuration were converted from image-space pixels to centimetres so that the results could be compared to those obtained from the numerical model which was scaled to the prototype dimensions (i.e. dimensions corresponding to an acceleration of 50g). The physical trapdoor displacement of 10 mm is therefore equivalent to a trapdoor displacement of 50 cm at prototype dimensions.

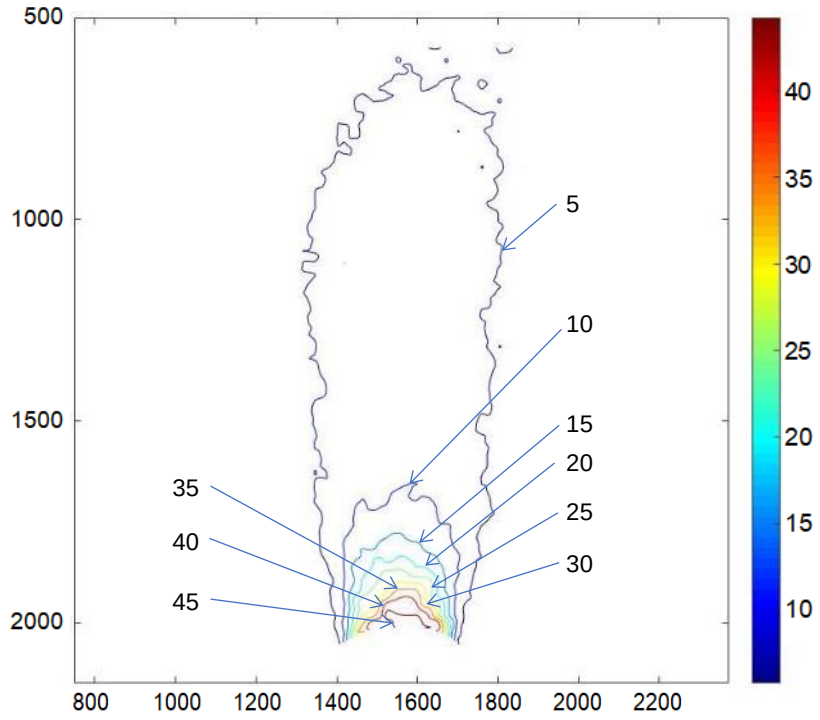

Figure 6-13: Total displacement contours at 50 cm trapdoor displacement (prototype dimensions), corresponding to 10 mm trapdoor displacement of the centrifuge experiment undertaken with glass beads (units in centimetres)

Calibration of the DEM simulation with the physical glass beads experiment was undertaken so that the effect of material shear strength, as a result of simulated particle shape, on the formation of shear bands during trapdoor lowering could be isolated and therefore investigated. The results of the sensitivity analysis in Section 6.3 were used as indicators of the permissible range of values for each of the particle parameters in the calibration procedure. It is noted that these ranges were restricted due to the initial values chosen for each parameter from literature.

6.4.1 Calibration overview: Sensitivity analysis results and trial-and-error calibration

The sensitivity analysis of the particle input parameters presented in Section 6.3 showed that the particle normal contact stiffness and friction coefficients can be used to control the extent of the zone of influence, or propagation of the disturbance, during trapdoor lowering. The bulk material behaviour was found to be most sensitive to variations in the particle contact stiffness, whereas changes to the COR appeared to have the smallest effect on the displacement contour plots of the particle parameters investigated. A trial-and-error approach, based on the results of the sensitivity analysis, is used in the following section to calibrate the numerical model against the total displacement contour plot from the centrifuge experiment undertaken with glass beads (Figure 6-13). The benchmark parameters listed in Table 6-2 hold true for this calibration procedure.

6.4.2 Particle normal contact stiffness calibration

Particle contact stiffness is often reduced in DEM simulations to decrease the required computational effort (Yousefi & Ng, 2017). However, from the sensitivity analysis undertaken in Section 6.3 it is evident that a reduction of the particle stiffness to more commonly assigned stiffness values (as per Equation 5-3 and Equation 5-4) yields unstable or unrealistic results for this experiment. The significance of the stiffness parameter is attributed to the higher stresses simulated in the numerical model as a result of the increased gravitational acceleration (and resulting scaled up dimensions). Given the basic formulation of the linear force-displacement contact law, forces generated in the model cause the particles push into one another and therefore a greater stiffness is required to limit the amount of particle overlap at 50g than would be required for a trapdoor experiment at 1g.

From Figure 6-9 in the sensitivity analysis, it was deduced that the minimum particle stiffness needed to yield representative numerical model results was approximately 12.0E+09 N/m. The required particle contact stiffness was found to be greater than the values predicted using the derivations recommended by Potyondy & Cundall (2004) listed in Section 5.4.2. Figure 6-14 (a) shows the total displacement contour plot for a particle stiffness derived using Equation 5-3 whereas Figure 6-14 (b) represents the displacement plots with a final calibrated particle contact stiffness of 45.0E+09 N/m. See Figure 6-13 for discrete contour interval magnitudes. The trapdoor experiment is classically used to investigate arching and the associated increase in horizontal stress within the material mass during trapdoor lowering. The greater horizontal zone of influence recorded in Figure 6-14 (a) is indicative of horizontal propagation of the disturbance (i.e. trapdoor displacement) as stress redistribution results in an increase in horizontal stress and decrease in vertical stress. The "softer" particles with a comparatively low contact stiffness allow greater particle-particle overlap resulting in a greater zone of influence in the horizontal direction, and less effective arching. Where particles were assigned a comparatively greater stiffness (Figure 6-14 (b)), particle overlap is limited thereby restricting the horizontal zone of influence.

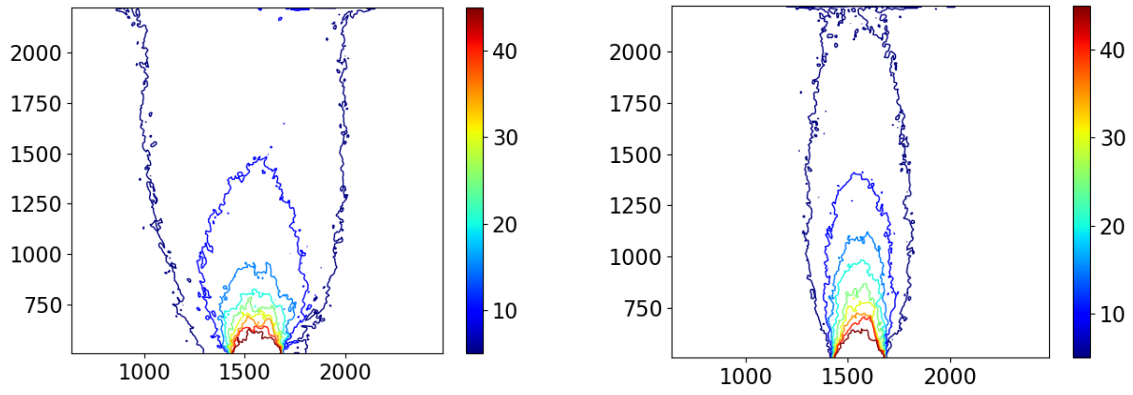

Figure 6-14: Calibration total displacement contours for normal particle contact stiffness values of (a) 7.8E+09 N/m and (b) 45.0E+09 N/m at 50 cm displacement of the trapdoor (prototype dimensions and units in centimetres)

Based on the sensitivity analysis presented in Section 6.3.9, the friction coefficients can also be used to limit the extent of the disturbance propagation. The total displacement contour plots in Figure 6-15 were mapped to determine whether an increase in both friction coefficients could be used to reduce the zone of influence (due to trapdoor displacement) in the bulk material, in the same manner that an increase in particle contact stiffness did as shown in Figure 6-14. Applying greater friction coefficients to reduce the zone of influence instead of the application of a greater particle stiffness would aid in reducing the computational effort required for the simulation. A particle contact stiffness of 7.8E+09 N/m (from Equation 5-3) was assigned to the models presented in both Figure 6-15 (a) and (b) (note the similarity to Figure 6-14 (a)). The particles corresponding to Figure 6-15 (a) were assigned static and kinetic friction coefficients of 0.18 whereas for the numerical model presented in Figure 6-15 (b) both the static and kinetic friction coefficients were increased to 0.4. A comparison of the displacement contour plots in Figure 6-15 shows that the contour plots are virtually identical, however, particle displacement is restricted slightly at the surface of the plot with greater friction. As a result of the similarity between the contour plots, it can be concluded that an increase in the friction coefficient values cannot be used to artificially impose shear strength or restrict particle displacement when the particle contact stiffness value is too low. It appears that a minimum particle stiffness value is required before the friction coefficients can be used to dictate the zone of influence during trapdoor lowering. Figure 6-15 again highlights the importance of the particle stiffness parameter and adds confidence to the chosen value of 45.0E+09 N/m for the calibrated model.

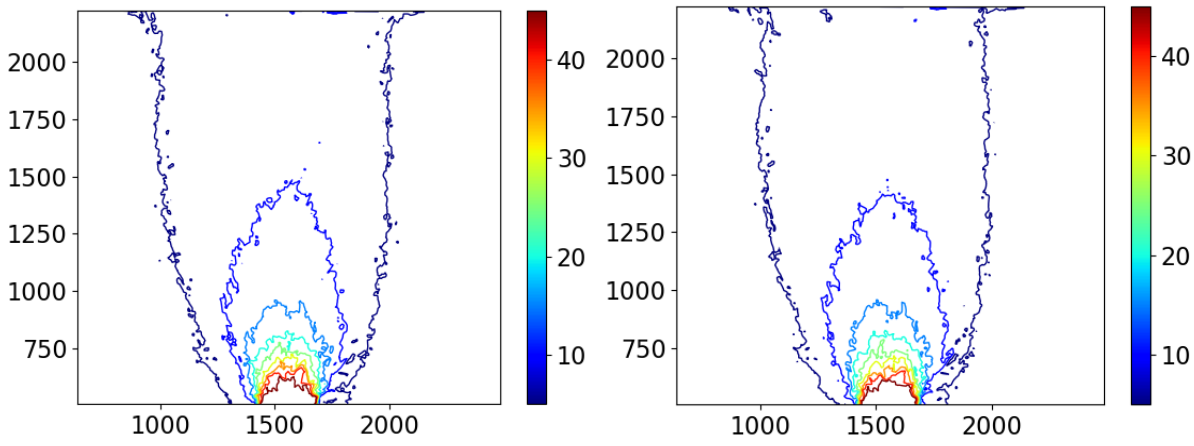

Figure 6-15: Calibration total displacement contours for static and kinetic friction coefficients of (a) 0.18 and (b) 0.4 at 50 cm displacement of the trapdoor (prototype dimensions and units in centimetres)

6.4.3 Calibration of the coefficient of restitution

The COR of the DEM particles was calibrated after the stiffness parameter. However, it was found to have a minor effect on the bulk material behaviour due to the quasi-static nature of the test. Based on the COR sensitivity analysis results presented in Figure 6-10, with initial parameter values described in

the previous section, a COR value of 0.6 or greater results in total displacement contours resembling those of the physical glass beads model at the corresponding trapdoor displacement. From the contour plots in Figure 6-10 it appears that a COR value of 0.6 or smaller results in the zone of influence being restricted, especially in the horizontal direction. Particle displacement is limited as a result of the greater damping effect caused by a lower COR value. Total displacement contours for COR values of 0.7 and 0.96 are displayed in Figure 6-16 (a) and (b), respectively. The contours corresponding to particle displacements of 10 to 25 cm propagate much higher for the lower COR value of 0.7. The displacement contours corresponding to a COR of 0.96 (Figure 6-16 (b)) widen slightly and show varying displacements at the surface of the model. This does not correspond to the physical experiment displacement contours in Figure 6-13 and is attributed to the fact that virtually no damping is applied at a COR of 0.96. For the remaining calibration simulations, the COR values were varied between 0.9 and 0.92. Both yielded realistic results with negligible differences and a final value of 0.9 was therefore chosen for the calibrated DEM trapdoor model.

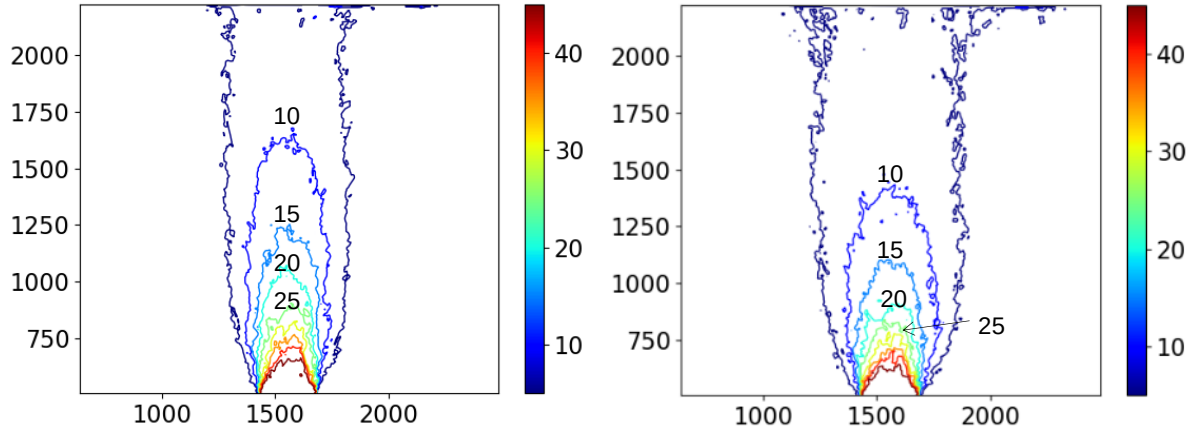

Figure 6-16: Calibration total displacement contours for COR values of (a) 0.7 and (b) 0.96 at 50 cm displacement of the trapdoor (prototype dimensions and units in centimetres)

6.4.4 Calibration of the coefficients of friction

Having established the particle contact stiffness and COR, the static and kinetic friction coefficients were calibrated next. From the friction coefficient sensitivity analysis results presented in Section 6.3.9, it was observed that where static and kinetic friction coefficients of 0.4 magnitude or greater were applied, the zone of influence did not propagate high enough to be comparable to the glass beads physical experiment displacement contours shown in Figure 6-13. Therefore, various combinations of friction coefficient values of between 0.09 and 0.4 were applied during the DEM trapdoor simulation calibration investigation. As noted in Section 6.3.9, the static and kinetic friction coefficients were assumed to be independent numerical entities during this calibration exercise.

Figure 6-17 shows total displacement contour plots for varying static and kinetic friction coefficient combinations. As detailed in Appendix B.3 (Calibration and Analyses Log) several DEM simulations were used to investigate the effect of the friction coefficients on the zone of influence resulting from the trapdoor displacement. Figure 6-17 (a) and (b) demonstrate that very similar material behaviour can be simulated in Blaze-DEM regardless of the relationship between the static and kinetic friction coefficients. They further illustrate that friction coefficients of 0.12 and 0.15 are too low to represent the behaviour of glass beads accurately. Figure 6-17 (c) demonstrates that a friction coefficient value of 0.4 restricts particle displacement to such an extent that it does not accurately simulate the inter-particle sliding behaviour of glass beads.

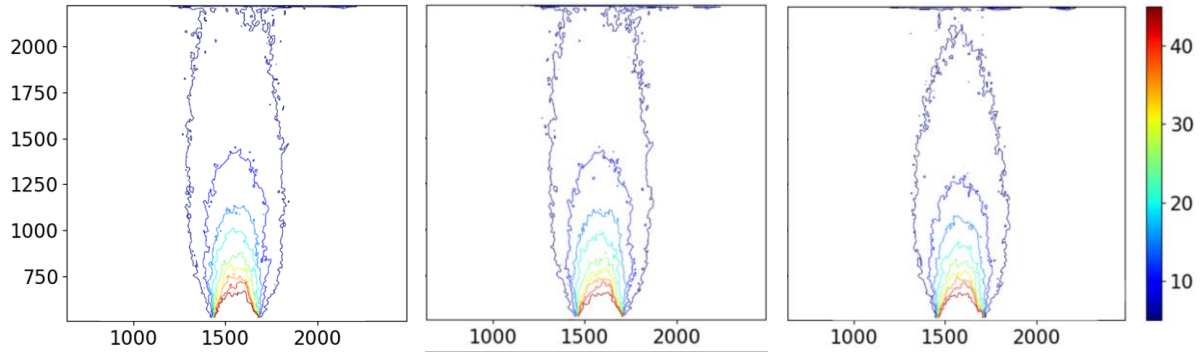

(a) (b) (c)

Figure 6-17: Calibration total displacement contours for static and kinetic friction coefficient values of (a) μ_s = 0.18 & μ_k = 0.15 (b) μ_s = 0.12 & μ_k = 0.15 and (c) μ_s = 0.18 & μ_k = 0.4 at 50 cm displacement of the trapdoor (prototype dimensions and units in centimetres)

From Figure 3-17 in Chapter 3, the triaxial test results for the 2 mm glass beads show that virtually no peak is exhibited in the deviatoric stress versus axial strain relationship. The flat "plateau" of this graph may be indicative of a material with an equal or similar peak and critical state friction angle. Given this relationship as well as the observations from Figure 6-17, a single value of 0.18 was chosen for both the static and kinetic friction coefficients.

6.4.5 Calibrated numerical model

Figure 6-18 shows a comparison of the displacement contours corresponding to 10 mm translation of the trapdoor in the centrifuge test using GeoPIV (a) and the corresponding plot for the final calibrated DEM model (b), at prototype dimensions (units in centimetres for both plots). The plots were deemed to be comparable, however two distinct differences were observed. The first is the absence of the 'arching triangle' at the base of the GeoPIV displacement plot. This may be attributed to the removal of GeoPIV subsets once they leave the 'Region of Interest', i.e. when the subsets of pixels in the region just above the trapdoor displace beyond the base of the container. Their movement is no longer tracked, and their final displacements are therefore not recorded. The second noticeable difference is that the second contour line of the calibrated model (10 cm displacement contour) propagates significantly

higher than the corresponding contour line in the PIV plot. This difference is discussed in detail in Section 6.7. Both differences were deemed to be inconsequential and the final calibrated DEM model was therefore used for the particle shape effects investigation.

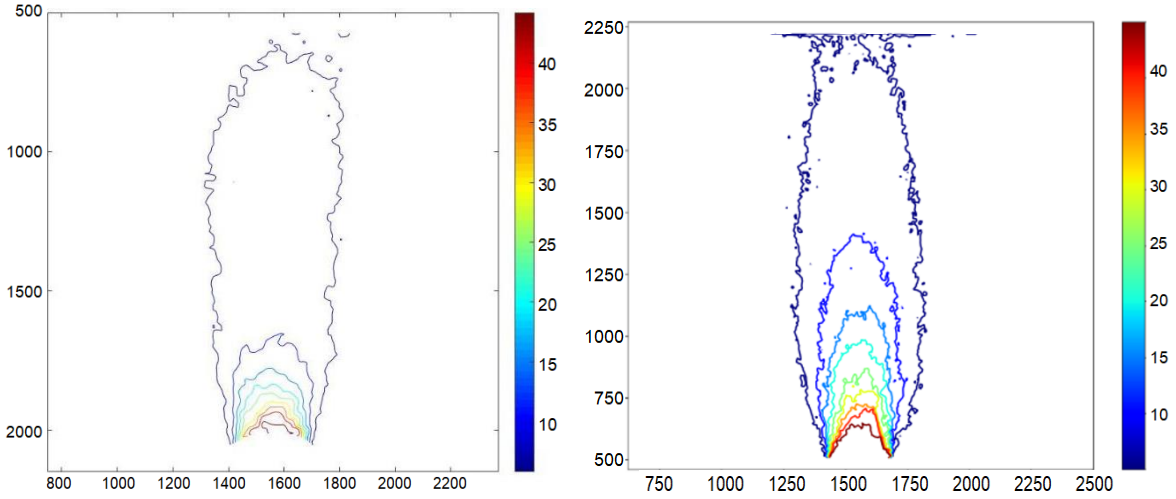

(a) (b)

Figure 6-18: Comparison of the total displacement contour plots of the (a) glass beads physical centrifuge model and the (b) calibrated DEM model at 50 cm displacement of the trapdoor (prototype dimensions and units in centimetres)

A summary of the final calibrated particle parameters is presented in Table 6-3 below. These parameters correspond to the trapdoor displacement simulation TD_C72 (Appendix B.3) and yielded the calibrated displacement contours presented in Figure 6-18 (b).

Table 6-3: Calibrated particle parameters for the numerical model with spherical particles

COR	$k_n\ (N/m)$	μ_s	μ_k	μ_r
0.9	45.0E+09	0.18	0.18	0.001

6.5. VALIDATION: DISPLACEMENT TRAJECTORIES

From the calibration procedure three DEM trapdoor displacement simulation configurations with varying sets of particle parameters were chosen to investigate the individual particle displacement trajectories, in terms of both direction and magnitude, during lowering of the trapdoor. The three configurations were chosen based on their displacement contour plots for 10 mm displacement of the trapdoor (displacement of 50 cm in prototype dimensions) as all three contour plots showed fairly good agreement with the corresponding GeoPIV displacement contour plot. The simulations were numbered according the Calibration and Analyses Log in Appendix B.3. 'TD' refers to trapdoor, 'C' indicates that the simulation is part of the calibration exercise and the final number represents of the simulation sequence number. The first of the three configurations (TD_C54) resulted in a displacement contour

plot in which particle displacement appeared to be restricted to a slightly smaller region within the overburden material than the calibrated model. Contrary to the first configuration, the second simulation (TD_C60) yielded a contour plot with greater (broader and higher) displacement contours than that of the calibrated model. The final displacement contour plot (TD_C72) was the calibrated configuration described previously. The 50 cm total displacement contour plots for TD_C54, TD_C60 and TD_C72 (calibrated model) are shown in Figure 6-19 (a), (b) and (c), respectively.

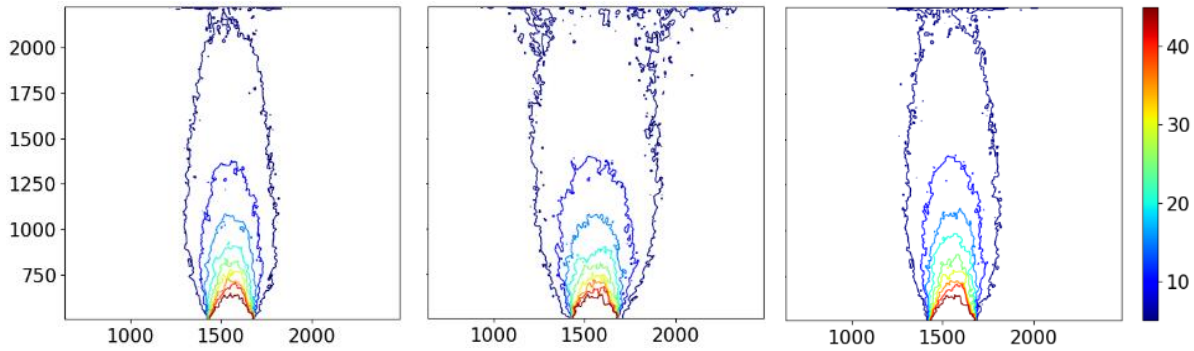

(a) (b) (c)

Figure 6-19: Total displacement contour plots for DEM calibration simulations (a) TD_C54 (b) TD_C60 and (c) TD_C72 at 50 cm displacement of the trapdoor (prototype dimensions and units in centimetres)

The particle parameters assigned to the above described DEM configurations are listed in Table 6-4. The broader and wider displacement contours associated with TD_C60 is a result of low coefficients of friction of 0.1 and a relatively high COR of 0.92. This contrasts with the narrower displacement contours for TD_C54 caused by a lower COR value of 0.7 and a higher kinetic friction coefficient of 0.4.

Table 6-4: Particle parameter configurations for the displacement trajectory DEM validation

	TD_C54	TD_C60	TD_C72
Coefficient of Restitution (COR)	0.7	0.92	0.9
Particle contact stiffness (k_n)	45.0E+09	85.0E+09	45.0E+09
Static friction coefficient (μ_s)	0.15	0.1	0.18
Kinetic friction coefficient (μ_k)	0.4	0.1	0.18

The displacements of discrete particles from the three numerical models were tracked at a centrifuge model equivalent of 5 mm trapdoor displacement intervals, starting at an initial displacement of 0 mm and ending with a final trapdoor displacement of 20 mm (i.e. five displacement points). The DEM particle coordinates were converted to PIV pixel coordinates and a subset was created which was centred at the corresponding pixel coordinates, using GeoPIV. The subset displacements were then traced, and displacements were recorded for the same trapdoor displacement intervals as for the DEM simulation. The displacement trajectory investigation is described in detail in Section 5.6.3. Figure 6-20

shows a representative layout of the corresponding subset positions and sizes for which displacement trajectories were monitored. From the centrifuge trapdoor experiments, the region above the edge of the trapdoor was observed to be significant as it is the point from which the shear bands propagate. Therefore, a densely populated particle displacement layout was selected in the area above the edge and centre of the trapdoor. For each point mapped in Figure 6-20, the displacement trajectories for the three DEM configurations listed in Table 6-4, as well as the corresponding GeoPIV trajectories, were plotted and compared to validate the selection of the calibrated particle parameters. Six representative positions were selected, and their displacement trajectories are discussed in the following section. All twenty graphs are included as Appendix D.

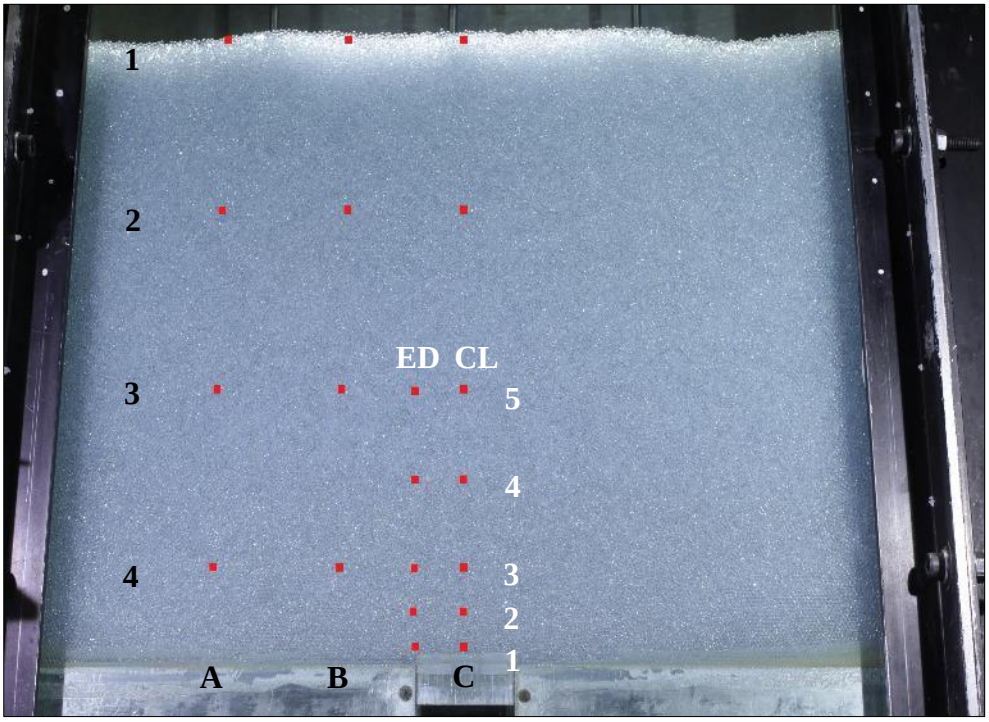

Figure 6-20: Layout of displacement trajectory monitoring points

Figure 6-21 displays the displacement trajectories for the particles and subset at the surface of the material, at the furthest point from the model centreline. As would be expected, very little movement is recorded for the particle and subset displacements. Although the actual subset trajectory (GeoPIV) most resembles the calibrated numerical model (TD_C72) as well as TD_C60, it has a greater horizontal component than both of these particle trajectories. The final positions of the subset and calibrated DEM particle differ by approximately 0.3 and 0.4 mm in the vertical and horizontal directions, respectively. The PIV subset displaced by a resultant magnitude of 0.83 mm (red), whereas the corresponding particle in the calibrated DEM model has a resultant displacement of 0.38 mm (green).

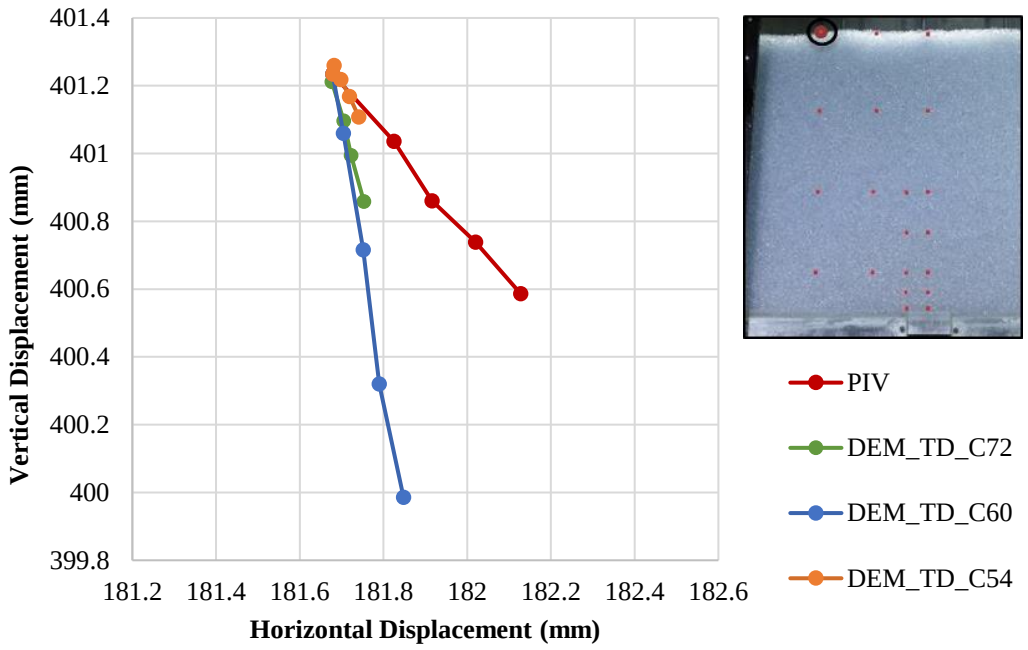

Figure 6-21: Physical and numerical displacement trajectories for position A1

The displacement trajectories in Figure 6-22 show fairly comparable results for all four trajectories, with TD_C60 being the greatest outlier. Contradictory to Figure 6-21 (previous figure), the PIV subset trajectory now has a smaller horizontal component than all three numerical trajectories, resulting in a near vertical path of movement. The final positions of the PIV subset and calibrated configuration differ by approximately 0.5 mm in both the horizontal and vertical directions, with the PIV subset displacing by 1.29 mm and the corresponding particle in the calibrated model by 1.87 mm.

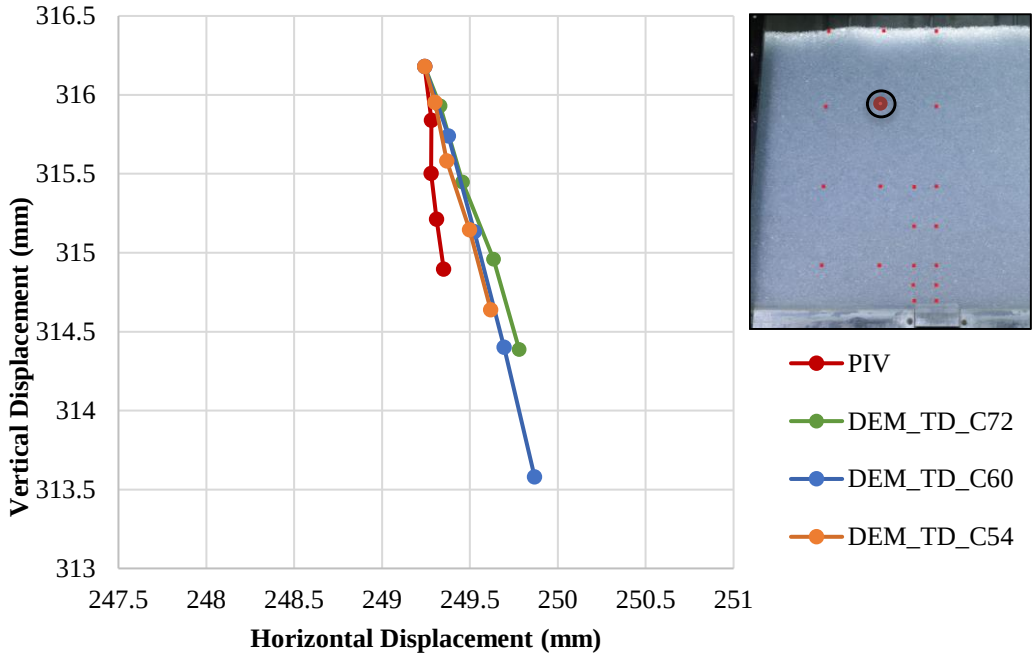

Figure 6-22: Physical and numerical displacement trajectories for position B2

Figure 6-23 shows the displacement trajectories for particle and corresponding subset positions in the middle of the model, above the trapdoor edge (position ED5). The DEM paths are all very similar in terms of displacement magnitude, but a slight variation in the direction of each path is observed. This may be as a result of shear band formation above the edge of the trapdoor. The magnitude of PIV subset displacement is significantly smaller than that of the corresponding numerical model displacements and although the results are not comparable, the greatest resemblance of the PIV trajectory is that of the calibrated model's trajectory.

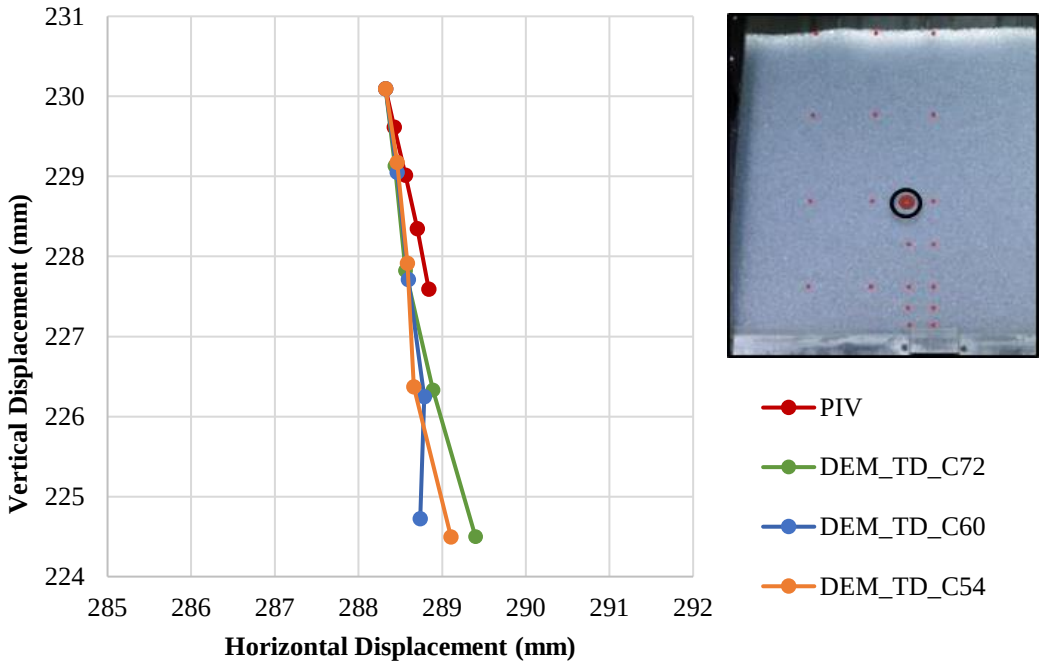

Figure 6-23: Physical and numerical displacement trajectories for position ED5

The magnitudes of the displacement trajectories shown in Figure 6-24, for position B4, vary for each of the trajectories charted. The trajectories generally propagate in the same direction, although a slight direction change is noted for TD_C72. Similar to the results for position ED5, the PIV subset trajectory is the shortest (indicating the least displacement) and it again draws its closest resemblance to the trajectory of TD_C72, the calibrated model. Position B4 lies outside the typical displacement contour zone shown in Figure 6-18 and therefore very little movement is expected and observed at this position. The resultant displacements of the PIV subset and corresponding calibrated particle are 0.17 mm and 0.37 mm, respectively.

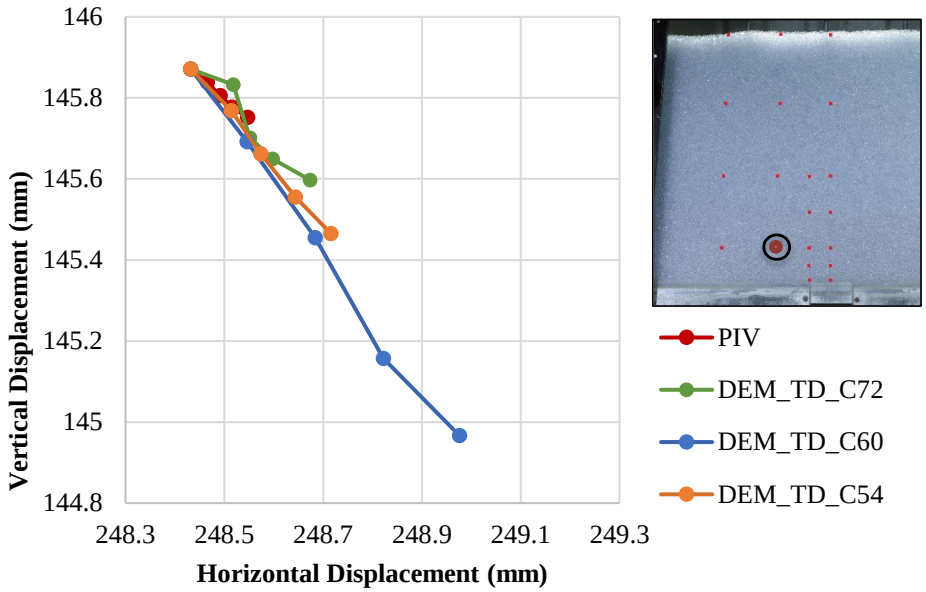

Figure 6-24: Physical and numerical displacement trajectories for position B4

Figure 6-25 presents the displacement trajectories for an initial particle and subset position at ED1. Although these displacement paths differ quite significantly, a direction change is noted for all four trajectories at a trapdoor displacement of approximately 10 mm. The change of direction is attributed to the particle's interference/interception with the shear band propagating from the edge of the trapdoor, forming one side of the triangular localisation pattern observed during trapdoor lowering. This figure emphasises the sensitivity of material behaviour to the formation of shear bands during failure. The resultant displacement of the PIV subset is 8.3 mm, whereas that of the corresponding particle in the calibrated model is 14 mm. The extent of PIV subset displacement is again observed to be significantly smaller than that of the DEM particle displacements.

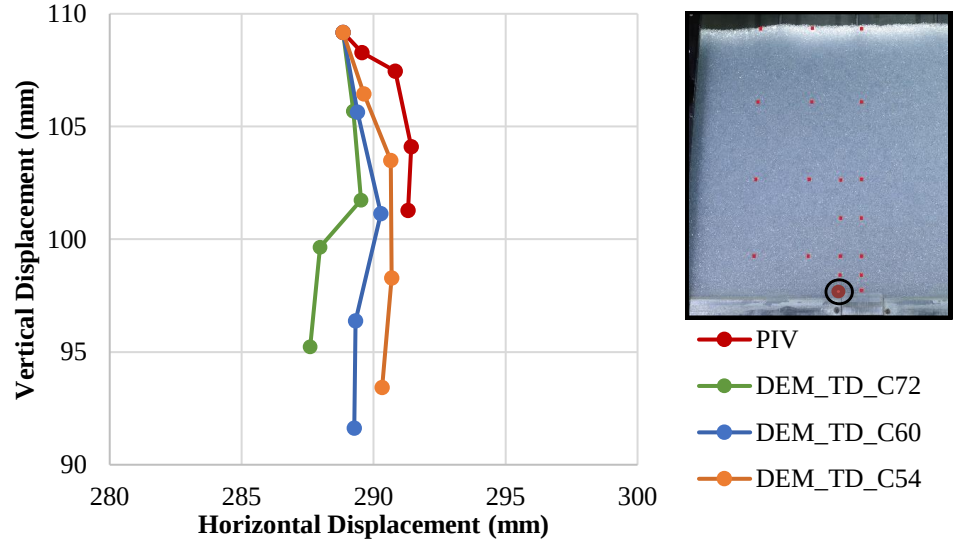

Figure 6-25: Physical and numerical displacement trajectories for position ED1

The displacement trajectories for a particle or subset directly above the centre of the trapdoor are shown in Figure 6-26. The position was selected as the particle would lie within the stable triangular material mass directly above the translating trapdoor and below the overhead "arch". Therefore, individual particle displacements would not be influenced by any interaction with shear bands propagating through the model material. All four trajectories suggest a strong likeness to the trapdoor displacement i.e. explicit downward vertical displacement of 20 mm. As the length of the PIV subset trajectory is approximately 1 mm shorter than that of the calibrated DEM model's trajectory, good agreement is noted between the physical and numerical models for particle behaviour directly above the trapdoor.

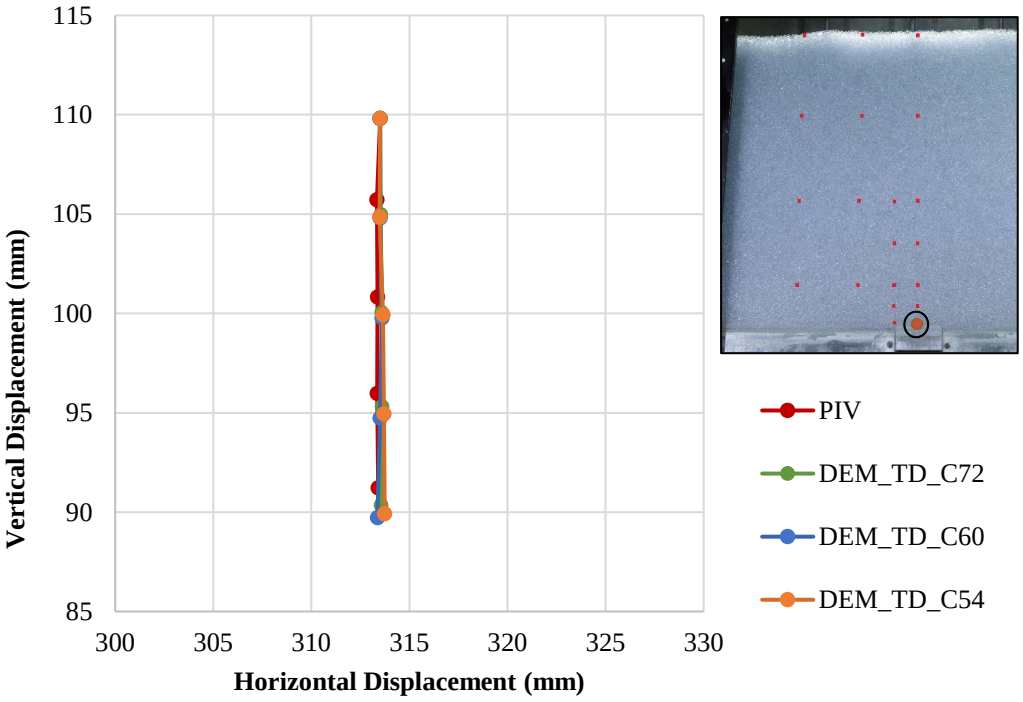

Figure 6-26: Physical and numerical displacement trajectories for position CL1

The particle displacement trajectory investigation yielded varying results. In most cases the PIV subset displacement magnitude was found to be significantly smaller than the corresponding DEM trajectories. Despite the difference in magnitude, the particle trajectories of the calibrated DEM model (TD_C72) consistently showed the closest resemblance to those from the GeoPIV analysis. A discussion on the difference in displacement magnitude recorded for the DEM and PIV subset displacements is presented in Section 6.7.

6.6. VALIDATION: MAXIMUM SHEAR STRAIN PLOTS

Understanding the mode and manner of overburden failure during sinkhole formation is a fundamental point of interest in this study. Validation of the calibrated numerical model was therefore accomplished by comparing the maximum shear strain plots of the three DEM simulations listed in Table 6-4 to the

corresponding GeoPIV maximum shear strain plot at 80 mm displacement of the trapdoor (corresponding to a 4 m trapdoor displacement at prototype dimensions). The formulation of the Python subroutine used to plot the maximum shear strains for the numerical models is described in Section 5.6.4.

The maximum shear strain plots for TD_C54, TD_C60 and TD_C72 at an equivalent physical trapdoor displacement of 80 mm (4 m at prototype dimensions) are shown in Figure 6-27 (a), (b) and (c), respectively. A distinct difference in the zone of influence is observed when comparing the plots. As indicated by the displacement contours in Figure 6-19, TD_C60 has a much broader zone of influence than the other two numerical models. The shear bands propagate at a greater angle to the vertical, resulting in wider and more dispersed regions of strain, with no clear bands forming between the centre and surface of the plot. The shear bands for both TD_C72 and TD_C54 propagate vertically to form a seemingly elongated ellipsoidal deformation mechanism. Although the deformation mechanism in TD_C60 also resembles an ellipsoid, it is much broader, and tends to widen towards the surface. Another notable difference between the shear strain plots is that the dominant (red) shear bands propagating from the edge of the trapdoor are rounded for TD_C60, in comparison to the straight bands shown in Figure 6-27 (a) and (c) for the configurations with greater friction and lower COR values. A substantial difference exists between the shape and area of influence of the shear bands in all three shear strain plots, indicating the sensitivity of the numerical model deformation mechanism to the input parameters. Of the three DEM model maximum shear strain plots presented in Figure 6-27, that of the calibrated model (TD_C72) was found to be the best representation of the deformation mechanism observed for the physical model glass beads at 80 mm displacement of the trapdoor. The maximum shear strain plot at 80 mm trapdoor displacement for the centrifuge experiment undertaken with glass beads is shown in Table 4-7 (v).

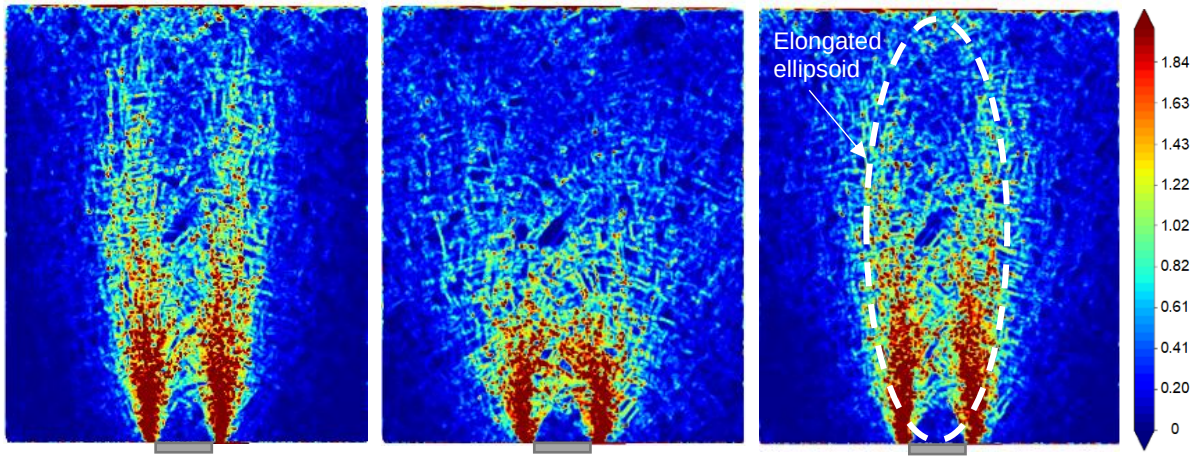

(a) (b) (c)

Figure 6-27: Maximum shear strain plots for DEM simulations (a) TD_C54 (b) TD_C60 and (c) TD_C72 at 80 mm displacement of the trapdoor (unitless strain)

To validate the selection of the calibrated input parameters for the numerical model, the maximum shear strain plots for the physical glass beads tests and calibrated DEM model (TD_C72) were plotted at various trapdoor displacements. These comparison plots are displayed in Table 6-5.

A major difference between the two sets of plots at equivalent trapdoor displacements of 40 mm and 80 mm is the absence of the stable triangular form above the trapdoor of the physical model plots. According to the physical model (PIV) plots, significant shear strain is experienced by the material above the trapdoor. This may be a result of the low threshold correlation coefficient selected to ensure a solution for the GeoPIV analyses of the glass bead experiment due to changing texture of the subsets as the beads rotate during movement. The texture of the glass bead subsets is attributed to shadows cast by the particles, as well as the reflection of light by the glass beads. The rotation of the glass beads results in a change in subset texture as the rotating beads cause light to reflect in a different manner (due to the composition of the glass beads) causing new light and dark areas in the subset. Subset texture therefore varies to a greater extent than it would for a corresponding subset of angular particles, such as the fine and coarse sand samples used in the centrifuge trapdoor experiments, in which particle rotation was partially restricted due to particle interlock. The absence of the stable triangle above the trapdoor may also be due to the pixel subsets directly above the trapdoor leaving the region of interest (RoI) during trapdoor lowering, as discussed earlier in the chapter. The shear strains assigned to these subsets are not mapped in the GeoPIV shear strain plots below. The numerical model plots also have a much finer texture than the physical model plots. The reason for this is that shear strain is calculated between particle centroids for the DEM model, but between subsets for the PIV analyses. The subsets are much larger than the particles, resulting in a coarser shear strain plot.

Good agreement exists between the shear strain plots at 80 mm trapdoor displacement, in terms of the deformation mechanism, shear band width and direction of propagation, as well as shear strain magnitude. Although the shear bands are better defined by the PIV plot, especially towards the material surface, the same ellipsoidal mechanism is observed with the same approximate aspect ratio for both plots. Similarly, a comparison of the shear strain plots at the remaining trapdoor displacement magnitudes shows that the calibrated model yields comparable shear strain results in terms of both shear strain magnitude and zone of influence.

Table 6-5: Comparison of physical (glass beads) and calibrated numerical model (TD_C72) maximum shear strain plots at an equivalent trapdoor displacement of (a) 80 mm (b) 40 mm (c) 10 mm and (d) 5 mm

	(a) 80 mm Trapdoor displacement	(b) 40 mm Trapdoor displacement	(c) 10 mm Trapdoor displacement	(d) 5 mm Trapdoor displacement
GeoPIV (CG01): Units of %	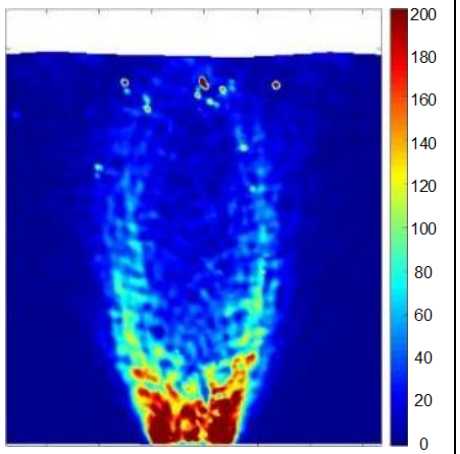	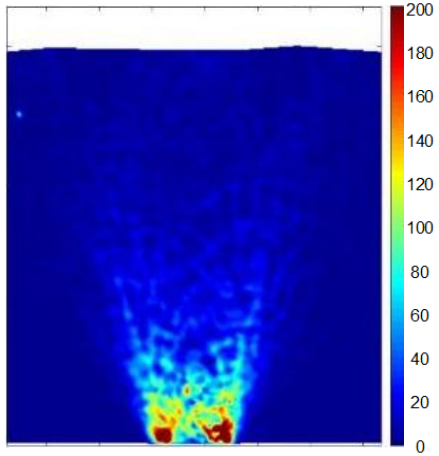	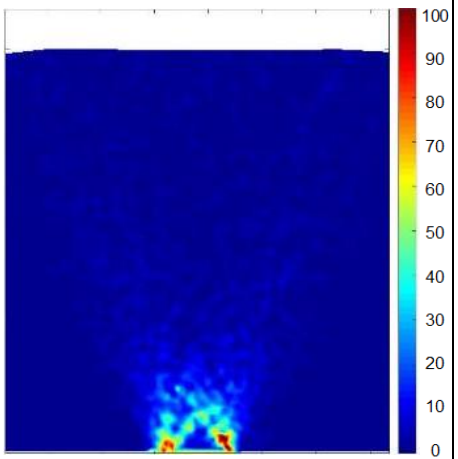	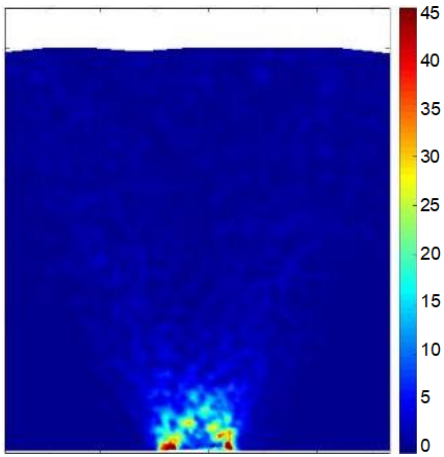
Blaze-DEM (TD_C72): Unitless strain	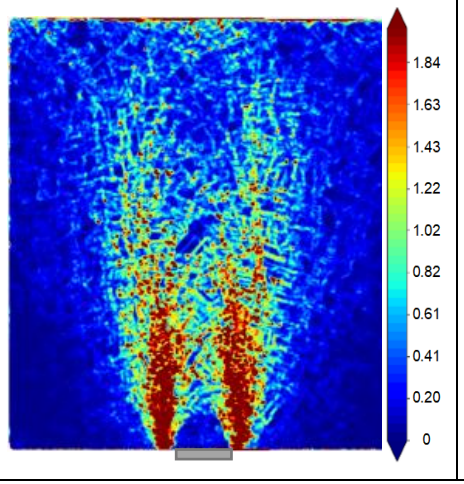	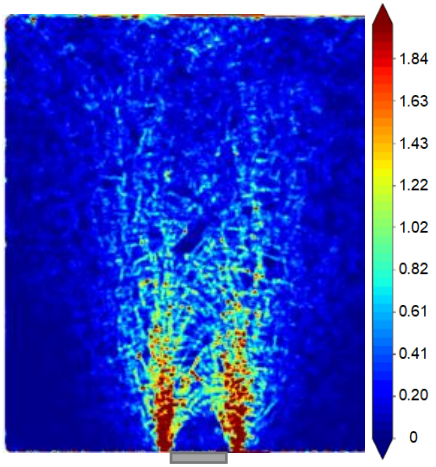	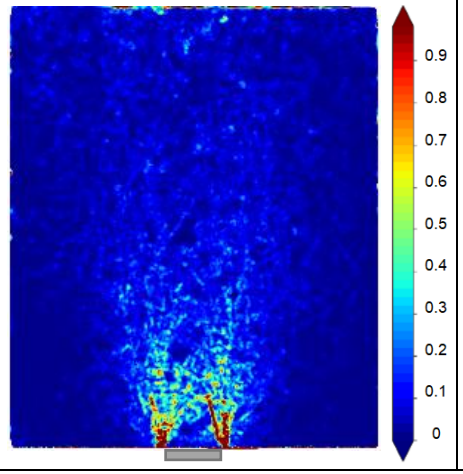	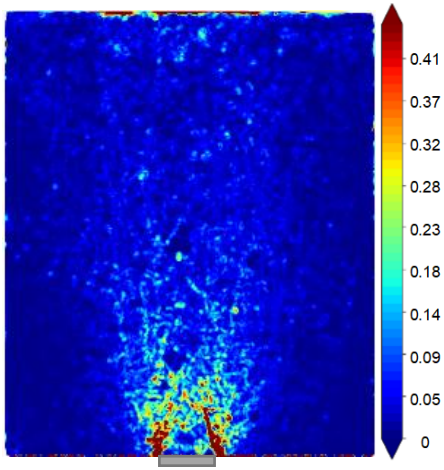

6.7. DISCUSSION OF THE CALIBRATION AND VALIDATION RESULTS

As discussed in the calibration procedure above, the calibrated normal contact stiffness (k_n) of the particles used in the numerical simulation of the trapdoor experiment was found to be significantly greater than the corresponding value determined from literature (almost an entire order of magnitude greater). Based on the calibration and validation results of the displacement contours and displacement trajectories, respectively, it is believed that the greater stiffness was required as a result of the higher rate of trapdoor displacement in the numerical model than in the physical model. From the sensitivity analysis, the rate for trapdoor lowering in the numerical model was selected at 20 mm/s (prototype dimensions) in comparison to the rate of 0.025 mm/s for the physical model. When normalising the numerical and physical trapdoor velocities by the respective trapdoor widths, the DEM trapdoor velocity was found to be 16 times greater than that of the centrifuge model trapdoor velocity. The greater trapdoor displacement rate of 20 mm/s, selected during the sensitivity analysis, was retained to reduce computational cost, specifically during the laborious calibration procedure. Typical Blaze-DEM simulation durations at the calibrated trapdoor velocity were 1 day and 8 days, for respective trapdoor displacements of 10 mm and 80 mm (i.e. trapdoor displacement of 0.5 m and 4 m at prototype dimensions). If these durations are multiplied by a factor of 16, the corresponding simulation durations increase to 16 days for 10 mm trapdoor displacement (calibration simulations) and 128 days for 80 mm trapdoor displacement (maximum shear strain plot comparisons). It was therefore considered unfeasible to simulate a trapdoor velocity corresponding to that of the physical experiments within the timeframe of this study.

Although not distinctly observed in the displacement contours at 10 mm displacement of the trapdoor, it is proposed that the higher rate of trapdoor displacement resulted in the DEM particles having a greater instantaneous acceleration component. According to Newton's second law for translational motion in Equation 2-9 this would result in higher inter-particle forces at a constant particle mass. Based on the linear force-displacement law, the greater inter-particle forces resulting from the greater rate of trapdoor displacement in turn yielded greater particle-particle overlap distances within a single time-step at a constant particle contact stiffness (Equation 6-1). This resulted in a greater zone of influence (propagation of the disturbance) within model fill material. A greater particle contact stiffness was therefore required to reduce the particle-particle overlap according to the force-displacement law. As shown in Figure 6-18, and discussed in the preceding paragraph, the second displacement interval contour of the calibrated numerical model propagated to a much higher level in the model fill than its corresponding contour for the physical model. This suggests that particles in the numerical model had a greater displacement in the region above the trapdoor (bottom half of model) despite being measured at the same trapdoor displacement. It is further conjectured that at a trapdoor displacement rate corresponding to that of the physical model, the particle acceleration and velocity components would

have been lower. This would result in lower particle-particle overlap distances and a limited zone of influence corresponding to that of the physical model.

The results from the particle displacement trajectory investigation show good alignment with the above conjecture. The validation of the calibrated model, using the particle displacement trajectories, showed significant deviation between the displacements of the particles in the calibrated numerical model and the corresponding subset displacements from the physical model. From Figure 6-20 and Appendix D, a holistic view of the particle trajectory results show that as the observer moves from Column A to C (i.e. from the column furthest away from the trapdoor towards its centreline) the magnitude of the calibrated numerical particle displacements increases in comparison to the GeoPIV subset displacements. The elevated stiffness of the particles in the calibrated DEM model appears to limit particle displacement to the column above the trapdoor and limits horizontal propagation of the 'disturbance' caused by trapdoor lowering. Therefore, the numerical particle displacements in Column C (above the trapdoor) are significantly greater than the corresponding GeoPIV subsets. However, further away from the trapdoor (e.g. Column A) the elevated stiffness also restricts particle-particle overlap, but as these are essentially unaffected by the increased rate of the trapdoor displacement the greater stiffness prohibits natural displacements. This therefore yields smaller numerical particle displacements than the corresponding GeoPIV subset displacements. In summary, the closer the particle to the centreline of the model, the greater the numerical particle displacement is in comparison to its GeoPIV subset counterpart. Material horizontally furthest away from the centreline result in greater GeoPIV subset displacements than calibrated numerical particle displacements.

6.8. SUMMARY

The primary conclusions reached in this chapter are summarised in the bullet points below:

- Particle normal contact stiffness (k_n) was found to be the most significant particle parameter when simulating material behaviour in response to trapdoor lowering, followed by the friction coefficients. Material behaviour was observed to be least sensitive to the COR due to the quasi-static nature of the simulation.
- If the normal contact stiffness of the particles is not big enough to accommodate the high inter-particle forces, the effect of the friction coefficients will be negligible regardless of their magnitude.
- Various parameter combinations can be used to obtain the same material behaviour.
- The effect of the DEM input parameters on the material response during trapdoor lowering is summarised as follows:
    - Increase in normal contact stiffness: Significant reduction in the zone of influence in both the horizontal and vertical directions

    - Decrease in normal contact stiffness: Significant increase in the zone of influence in both the horizontal and vertical directions
    - Increase in friction coefficients: Reduction in the vertical zone of influence
    - Decrease in friction coefficients: Increase in the vertical zone of influence
    - Increase in coefficient of restitution: reduction in the vertical zone of influence and increase in the horizontal zone of influence; vice versa for a decrease in the COR.

- The duration of a DEM simulation is dependent on the real-time experiment duration. At the physical trapdoor velocity of 0.025 mm/s and maximum displacement of 80 mm, a single simulation would have run for 128 days. For direct comparison with laboratory experiments, DEM is therefore suited to shorter real-time experiments. In the case of a trapdoor experiment this would translate to smaller trapdoor displacements (i.e. shallow trapdoor experiment), a greater trapdoor velocity or a combination of the two.
- Despite the differences between the calibrated DEM model and the physical glass beads experiment, the calibrated model was deemed sufficient to investigate the effect of material bulk shear strength on the deformation mechanisms associated with trapdoor experiments.

7. ANALYSIS AND DISCUSSION OF RESULTS

7.1. INTRODUCTION

The chapter commences with a brief description of the investigation objective and overview of the Blaze-DEM trapdoor experiments using polyhedral particles. Shortcomings of the simulations with polyhedral particles are detailed followed by a problem-solving methodology for these experiments which were found to be unstable at the calibrated particle parameters and predetermined time step. Based on this approach, it was discovered that the particle normal contact stiffness was a significant parameter in terms of simulation stability, particularly at an elevated model acceleration of 50g. An in-depth investigation was therefore undertaken using the calibrated Blaze-DEM model with spherical particles. The findings of this investigation are presented subsequently.

It was desired to investigate the effect of particle shape on the propagation mechanism above a lowering trapdoor. However, as discussed, the experiments with polyhedral particles proved to be unstable at the calibrated model configuration. To assess the effect of particle shape and interlock on shear band propagation in deep trapdoor experiments, the effects of particle shape were simulated by imposing a rolling resistance coefficient applied incrementally to the calibrated Blaze-DEM model with spherical particles. The findings of the rolling resistance coefficient investigation are followed by a short discussion in which conclusions from the available literature on deformation mechanisms associated with trapdoor experiments using DEM are compared to the findings of this study.

The chapter concludes with a discussion of the potential of using Blaze-DEM to simulate propagation mechanisms in deep trapdoor experiments. The advantages and limitations of the application of Blaze-DEM to model deformation mechanisms associated with sub-surface cavity propagation by means of a deep trapdoor experiment is evaluated and recommendations for further work are presented.

7.2. INVESTIGATION OBJECTIVE

7.2.1 Overview of the study objective

The aim of the investigation was to determine the effect of material shear strength, as a function of particle shape and interlock, on the deformation mechanisms associated with subsurface cavity propagation, ultimately resulting in sinkhole formation. A deep trapdoor experiment with spherical particles was modelled using Blaze-DEM and calibrated to match the corresponding displacement contours of a deep trapdoor experiment undertaken in the centrifuge facility using glass beads. The calibrated model was then adjusted by varying only the particle shape, using polyhedral particles, as well as the corresponding particle density or volume. As detailed in Section 5.7.1, two types of polyhedral particle simulations were modelled, namely the “Equal Volume” (EV) and “Equal Bounding

Perimeter" (EBP) simulations. Further, two polyhedral particle shapes with distinct differences in sphericity and angularity, namely the dodecahedron and tetrahedron, were selected to investigate the effect of particle shape on shear band propagation. The EV and EBP simulations were modelled for both polyhedral particle shapes. A detailed discussion of the polyhedral particle shape selection and the EV and EBP simulation configurations is presented in Section 5.7.1.

7.2.2 Blaze-DEM simulations with polyhedral particles

The application of a force-displacement law is inherent to the fundamental DEM computational process (see Section 2.4.2). The same force-displacement formulation is used for all collisions between spherical particles as the overlap displacement is calculated in the same manner for any possible contact type. However, for polyhedral particles in Blaze-DEM the force-displacement law is substituted by a force-volume law (Govender et al., 2016). The same principal is applied in the force-volume law as is applied in the force-displacement law, but instead of the force being a function of the particle overlap distance (displacement), it becomes a function of the overlap volume of two polyhedral particles in the collision. The adaption of the law is necessary because of the numerous modes of contact that convex polyhedral particles can undergo during a collision in Blaze-DEM. Different contact modes have a different overlap volume depending on the particle type (e.g. cube, dodecahedron) and part of the respective polyhedral particles partaking in the collision (e.g. edge, face). The narrow phase contact detection algorithm employed in Blaze-DEM, which determines the contact type and particle-particle overlap volume, accounts for the majority of the computational effort of a Blaze-DEM simulation with polyhedral particles. The narrow phase contact detection is executed once the broad contact phase, in which potential particle collisions are detected, has been completed (see Section 2.5.2).

7.2.3 Problem solving implementation

In order to investigate the effect of different particle shapes on deformation mechanisms in deep trapdoor experiments, the modelling procedure and calibrated DEM particle parameters listed in Chapter 6 were employed in the EV and EBP numerical experiments for dodecahedron and tetrahedron polyhedral particles. The Blaze-DEM numerical simulations with polyhedral particles did not yield stable simulations despite using the same normal contact stiffness and stable time step determined from the respective calibration and sensitivity analyses defined in Chapter 6. The instability in the numerical model appeared to be a result of the time step being too big for the applicable force-volume law and associated particle stiffness. Dodecahedrons are fairly stable polyhedral particles due to their high degree of sphericity. The overlap volume and depth of penetration of two dodecahedrons during a particle-particle collision are similar to that of monodispersed spheres. However, a considerably greater depth of penetration is required to achieve the same volume of particle overlap when a collision between two tetrahedron particles is modelled. The investigation therefore focussed on achieving a stable model

using dodecahedron particles. By means of trial-and-error, several other solutions were attempted to obtain a stable simulation with results which could be analysed. These included the following:

- Modelling the container and system setup at various scales and adjusting the gravitational acceleration accordingly,
- applying the smallest time step possible within the single precision Blaze-DEM code and
- adjusting the particle contact stiffness and corresponding time step incrementally in pursuit of a stable simulation which would still yield realistic results.

The trial-and-error approach described in the last bullet point was considered to be the last resort to obtaining a stable simulation as the resulting model and associated results would not correspond to the calibrated spherical model. Direct comparisons would therefore not be an accurate assessment of the effect of particle shape on the associated deformation pattern. However, as none of the listed measures attempted to obtain a stable simulation yielded successful results, an incremental adjustment of the particle contact stiffness was unavoidable. A detailed description of the "trial-and-error" approach, in which the particle contact stiffness of the polyhedral particles was adjusted incrementally, is presented in Section 7.3. Several DEM simulations were modelled to find a compromise between particle contact stiffness and realistic output results. It was found that the corresponding time step could not be made small enough, given Blaze-DEM's single precision capability, to accommodate the high normal contact stiffness required to simulate realistic results in a stable model using polyhedral particles.

Using the calibrated Blaze-DEM model based on spherical particles, an investigation into the significance of the normal contact stiffness was therefore undertaken. As discussed in Section 2.5.4, Coetzee (2017) lists the use of polyhedral particles and the application of a rolling resistance coefficient as the two methods by which particle shape effects are commonly simulated in DEM. Given the inability to obtain results using polyhedral particles, a second investigation was undertaken to model the effects of particle shape and interlock by applying a rolling resistance coefficient to the spherical particles.

7.3. SIGNIFICANCE OF NORMAL CONTACT STIFFNESS

7.3.1 Investigation of particle normal contact stiffness and application to polyhedral particle simulations

The significance of the particle normal stiffness (k_n) is highlighted in the linear spring-dashpot force-displacement contact model for the normal direction defined in Equation 2-11, as well as in the description of the DEM computational cycle presented in Section 2.4.2. In addition to the damping coefficient (represented by the COR) the particle-particle overlap distance (Δn) represents the deformation of the particles during contact, whereas the normal contact stiffness parameter acts as the "spring" or elastic contact force during a particle-particle collision.

For the purpose of reducing the computational cost associated with DEM numerical modelling when using large numbers of particles, Thakur et al. (2016) investigated the scaling of discrete element model parameters for both cohesionless and cohesive solids under quasi-static simulation conditions. Based on a literature study, as well as their own findings, Thakur et al. (2016) report that the normal particle contact stiffness in DEM simulations is to be scaled linearly with the particle size (or radius). Two equations defining the normal contact stiffness as a function of both the particle radius (R) and the Young's Modulus (E) are presented in Equation 7-1 and Equation 7-2 below. The third equation (Equation 7-3) defines the normal contact stiffness in terms of the maximum particle velocity (v) in addition to the two parameters mentioned. The original equations include "equivalent" or "average" values for the input variables. However, these are only applicable in cases where particles with varying sizes and material properties are used in the simulation and were therefore not applied in this study. Equation 7-1 and Equation 7-2 were proposed by Potyondy & Cundall (2004) and are presented in Chapter 5 in a discussion of the contact normal stiffness (Section 5.4.2), whereas Equation 7-3 is a solution provided by Maw et al. (1976).

$$k_n = 2E \times R \qquad \text{Equation 7-1}$$

$$k_n = \frac{\pi RE}{2} \qquad \text{Equation 7-2}$$

$$k_n = \frac{16}{15}\sqrt{R}.E\left(\frac{15mv^2}{16E\sqrt{R}}\right)^{\frac{1}{5}} \qquad \text{Equation 7-3}$$

Where:

R = Particle radius (m)

m = mass (kg)

E = Young's Modulus (Pa)

v = typical impact velocity (m/s)

The equations presented above were used to assess the magnitude of the calibrated normal particle contact stiffness for the DEM trapdoor experiment using spherical particles, derived and discussed in Chapter 6. For the DEM trapdoor model at prototype scale, the particle radius and mass were 0.05 m and 1.309 kg, respectively (i.e. mass and radius upscaled to 50g). The Young's Modulus for the glass beads was sourced from the supplier's datasheet (Preciosa Ornela, 2011) and was reported to vary between 78 and 85 GPa. A value of 78 GPa was selected to determine the normal contact stiffness. The maximum particle velocity was assumed to be that of the particles directly above the trapdoor, displacing at a constant velocity of 0.02 m/s, equal to that of the numerical simulation trapdoor velocity.

Table 7-1 lists the normal contact stiffness values calculated using Equations 7-1 to 7-3, as well as the calibrated normal contact stiffness from Chapter 6. The contact stiffness calculated using Equation 7-3 is three orders of magnitude lower than the calibrated stiffness. This is attributed to comparatively low particle velocity used in the calculation due to the pseudo-static nature of this trapdoor experiment. It is proposed that this empirical equation may be better suited to highly dynamic DEM simulations. Although a comparison of the calibrated stiffness and the stiffnesses derived from Equation 7-1 and Equation 7-2 showed good correlation, the calibrated stiffness was still significantly greater than the calculated values. As discussed in Section 6.7, a greater particle contact stiffness needed to be applied in the calibrated model to counter and limit the effects associated with the higher rate of trapdoor displacement applied in the DEM trapdoor experiment.

Table 7-1: DEM trapdoor experiment normal contact stiffness comparison

Source	Normal contact stiffness, k_n (N/m)
Calibrated contact stiffness (Section 6.4.2)	45.0E+09
Equation 7-1	7.8E+09
Equation 7-2	6.1E+09
Equation 7-3	36.0E+06

Based on the results presented in Table 7-1, the normal contact stiffness values applied in both the spherical and polyhedra DEM numerical simulations lie within one order of magnitude of the calculated contact stiffnesses from literature. However, at the calibrated normal contact stiffness, stable trapdoor simulations using polyhedral particles could not be modelled successfully. The time step for the computationally expensive polyhedral particles could not be made small enough to ensure a stable simulation given the single precision framework of Blaze-DEM. A literature search was therefore undertaken to determine the magnitude of normal contact stiffness values applied successfully in similar experiments where soil deformations were studied using both a geotechnical centrifuge and discrete element analysis.

Chang et al. (2013) presented research in which a reverse fault slip was modelled in a centrifuge facility as well as in PFC^{2D}, a 2-dimensional DEM code in which the particles are represented by discs. Quartz sand with a D_{50} value of 0.149 mm was used in the physical model. However, the D_{50} particle size was scaled by a factor of 20 to 2.98 mm for the DEM model. A maximum gravitational acceleration of 80g was applied in the centrifuge. Assuming a Young's Modulus value of 24.1 GPa for quartz sand (Cheng et al., 2017) and by applying Equation 7-1 and Equation 7-2 above, the resulting normal contact stiffness of the particles varied between 4.5E+09 and 5.7E+09 N/m. Chang et al. (2013), however, applied a normal contact stiffness of only 5.0E+06 N/m to the particles in their DEM simulation – three orders of magnitude lower than the values recommended by equations obtained from literature.

A particle normal contact stiffness of 7.8E+06 N/m (i.e. within the same order of magnitude successfully applied by Chang et al. (2013) at 80g) was therefore used in the polyhedra simulations in an attempt to create a stable trapdoor experiment simulation using Blaze-DEM. Visually, the simulation appeared to be more stable at this stiffness. However, particles soon pushed through the container walls during the simulation. This was attributed to the low particle stiffness ("soft" particles) which resulted in a high overlap volume, given the force-volume law. The normal contact stiffness of the particles was then increased in multiples of an order of magnitude, and the time step adjusted accordingly, to find a feasible compromise between the particle stiffness and time step that would yield a stable simulation. As stated in Section 7.2.3, no midway point between an acceptable particle stiffness and stable time step could be obtained.

7.3.2 DEM spherical model contact stiffness analysis

To investigate the instability of the polyhedra simulations at lower contact stiffnesses based on values comparable to those used successfully in literature (Chang et al., 2013), the normal contact stiffness values applied incrementally to the polyhedra simulations were assigned to the particles in the calibrated spherical Blaze-DEM model. This was implemented to investigate the shear strains associated with each of the stiffness magnitudes and to determine whether realistic and comparable results could be obtained for contact stiffnesses lower than the calibrated value of 45.0E+09 N/m. Figure 7-1 (a) to (d) presents the shear strain plots for the Blaze-DEM model with spherical particles at an equivalent physical trapdoor displacement of 80 mm (4 m at prototype dimensions). The contact stiffness of the particles was increased by an order of magnitude for each of the shear strain plots, starting with a value of 7.8E+06 N/m, as was done in the "trial-and-error" approach for the simulations with polyhedral particles.

From the shear strain plots in Figure 7-1 it is evident that at particle normal contact stiffness values lower than 7.8E+09 N/m the shear strain distributions are not realistic in comparison to those from the physical models. The characteristic shear bands and ellipsoidal deformation pattern observed for the physical glass beads experiment appear to be present in Figure 7-1 (d). However, for contact stiffnesses smaller than 7.8E+09 N/m the shear strain deformation patterns are either random or do not correspond to those obtained from physical modelling. The shear strain plot in Figure 7-1 (d) represents the deformation patterns for the DEM model in which the contact stiffness derived from Equation 7-1 was applied. Although similarities between the DEM shear strain plot in Figure 7-1 (d) and the corresponding PIV shear strain plot for the glass beads exist, it is evident that at a gravitational acceleration of 50g this contact stiffness results in particles that are still too soft to adequately represent the physical glass beads and their corresponding deformation mechanisms.

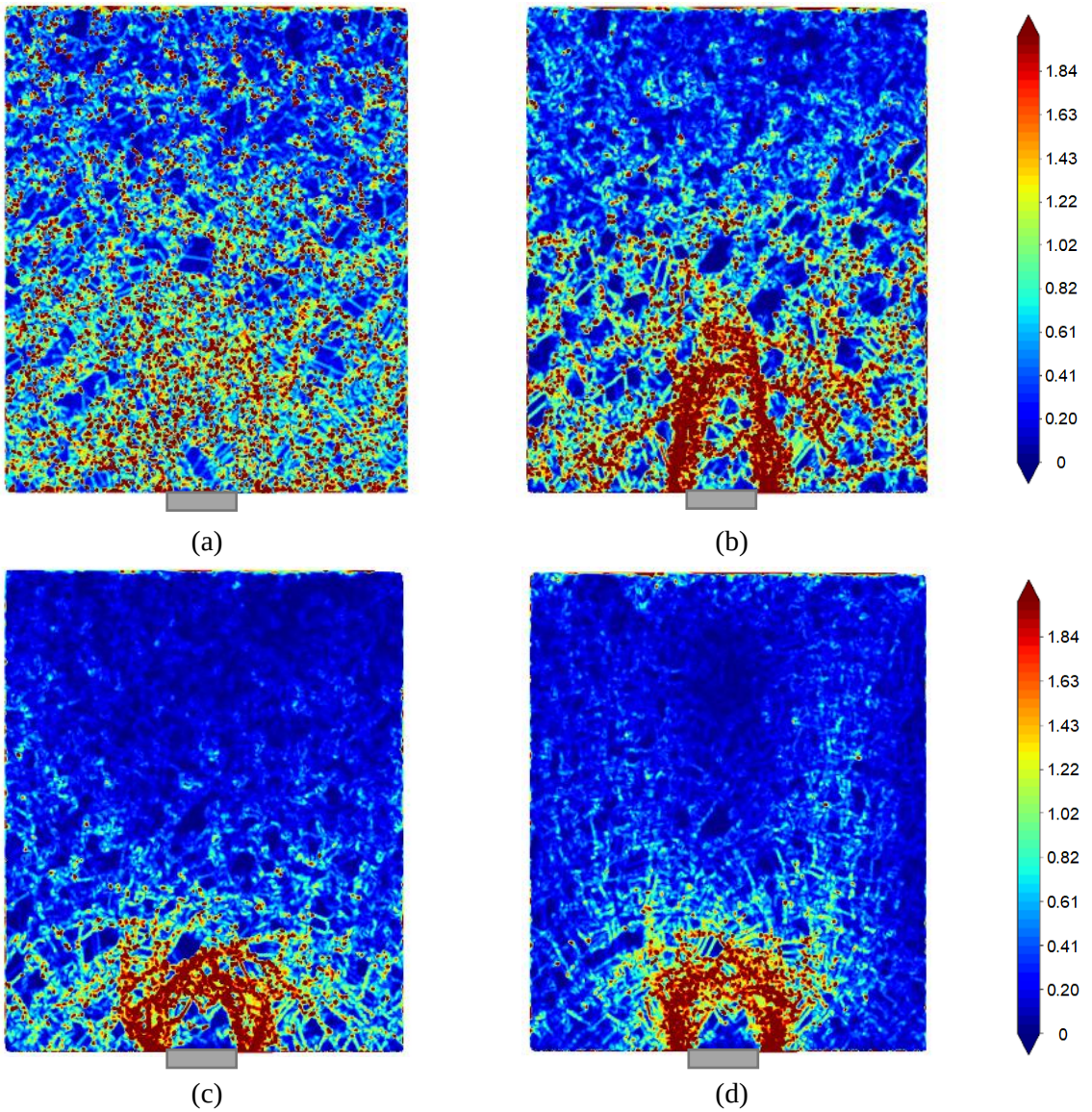

Figure 7-1: Shear strain plots at 80 mm trapdoor displacement for the calibrated DEM model (spherical particles) with a contact stiffness of (a) 7.8E+06 N/m, (b) 78.0E+06 N/m, (c) 0.78E+09 N/m and (d) 7.8E+09 N/m (unitless strain)

The results presented in Figure 7-1 demonstrate the importance of undertaking a thorough investigation of the particle contact stiffness and its effect on the DEM model results, especially when a lower normal contact stiffness is considered to reduce the computational effort of the simulation. As shown in Chapter 6 (Figure 6-15), the static and kinetic friction coefficients alone cannot be used to achieve the effect of particles with a greater stiffness.

7.4. APPLICATION OF ROLLING RESISTANCE COEFFICIENT

7.4.1 Particle shape simulation using DEM friction coefficients

Coetzee (2017) lists two methods of simulating particle shape effects when using DEM. The first method, which entails physically modelling non-spherical particles such as polyhedra, was unsuccessful

as explained in Section 7.2.3. The second method in which a rolling resistance coefficient is applied to the particles was therefore instituted. Wensrich & Katterfeld (2012) showed that rolling resistance is dependent on the friction coefficient assigned to the particles. In similar findings Obermayr et al. (2011) stated that the friction coefficient would need to be greater than 0.05 for the rolling resistance coefficient to have any effect on the model because inter-particle slip would simply occur. Both friction coefficients as well as the rolling resistance coefficient were therefore varied in an attempt to simulate effects resulting from particle shape. Particle shape would affect the shear resistance of the material, which would in turn influence the cavity propagation mechanisms during trapdoor translation.

Three DEM models with spherical particles and the calibrated particle parameters listed in Table 6-3 were used to investigate the effect of the application of a rolling resistance coefficient and friction coefficient in the Blaze-DEM trapdoor experiment. The friction and rolling resistance coefficients applied to each of the three models are listed in Table 7-2. These values were selected based on a study by Wensrich & Katterfeld (2012) in which they related various combinations of the rolling resistance and particle friction coefficients to the angle of repose of the material that was being modelled. See Figure 5-7 for a graphical presentation of the selected particle parameters. As discussed in Section 5.7.3, the particle-particle friction coefficient magnitude was assigned to both the static and kinetic friction coefficients in Blaze-DEM. It should be noted that the angle of repose and corresponding coefficients were used as a guideline, as these are likely to be material, contact model and DEM code specific.

Table 7-2: Particle rolling resistance and friction coefficients used to simulate particle shape effects

Blaze-DEM Model	Friction coefficient (μ)	Rolling resistance coefficient (μ_r)	Angle of repose* (°)
TD_C72 (Calibrated model)	0.18	0.0	N/A (triaxial 24)
Rolling Friction 1 (RF1)	0.2	0.2	25.5
Rolling Friction 2 (RF2)	0.5	0.2	31
Rolling Friction 3 (RF3)	0.5	0.4	40.5

*Wensrich & Katterfeld (2012)

The shear strain plots at an equivalent physical trapdoor displacement of 80 mm (4 m at prototype dimensions) for the simulations listed in Table 7-2 are shown in Figure 7-2 (a) to (d). With an increase in both the friction and rolling resistance coefficient magnitudes, the zone of influence reduces, especially in the horizontal direction, and the shear bands tend to become narrower and more defined. As discussed in Chapter 4, the shear bands of materials with a greater shear strength appear to tend towards verticality, as with the fine- and coarse-grained sand experiments. Curved shear bands with a wide zone of influence formed when glass beads, with a comparatively low friction angle and shear strength, were tested. The increase in the rolling resistance and friction coefficients simulates an increase in the material's shear strength. Similar deformation trends are observed in the shear strain

plots presented in Figure 7-2 (b) to (d) with increasing coefficient values. Finally, at a friction coefficient of 0.5 and a rolling resistance coefficient of 0.4, corresponding to simulation RF3 (Table 7-2) presented in Figure 7-2 (d), the shear bands are well-defined and effectively vertical. This plot is comparable to that of the coarse-grained sand shear strain plot presented in Table 4-7 (b)(iv), with the shear band width being the primary difference between the two plots. The difference in shear band width is attributed to the significant difference between the average particle size (D_{50}) of the coarse-grained sand and glass beads.

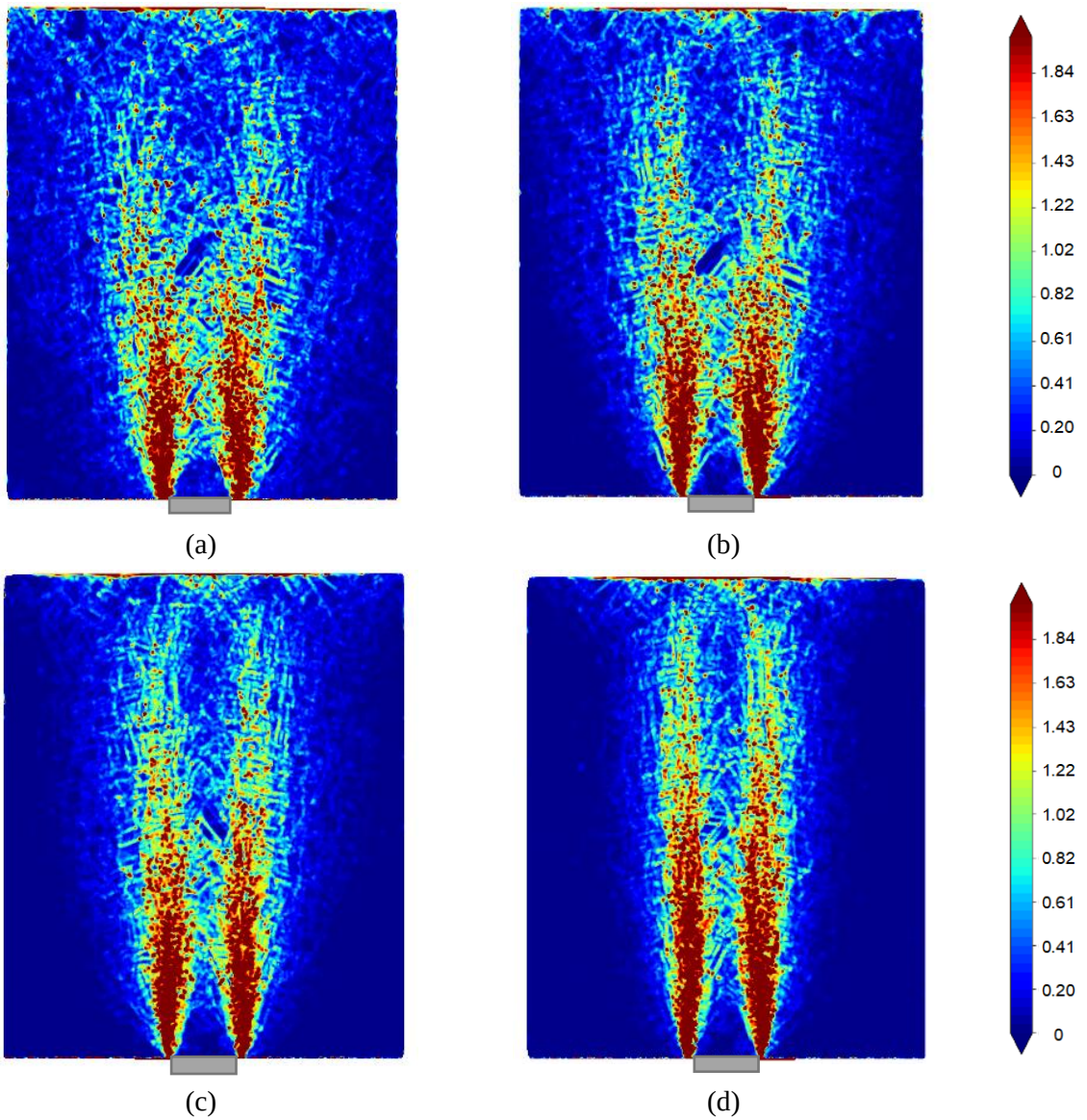

Figure 7-2: Shear strain plots at 80 mm trapdoor displacement for the calibrated DEM model with rolling resistance and friction coefficients as per Table 7-2: (a) Calibrated model (TD_C72), (b) RF 1, (c) RF 2 and (d) RF3 (unitless strain)

All four models presented in Figure 7-2 exhibit the same inherent deformation mechanism illustrated by Kamrin (2010) and Rycroft et al. (2009) in Figure 2-43 (a) and (b) in Section 2.6.2, respectively. Two primary shear bands propagate from the edges of the trapdoor and meet at the surface to form an

elongated ellipsoidal deformation mechanism. Furthermore, two additional bands branch off from the primary shear bands near the top of the soil profile and extend outwards towards the soil surface. Based on the shear strain results of the physical trapdoor experiments discussed in Section 4.3.3, as well as the results presented in Figure 7-2, the width of the ellipse and corresponding zone of influence is governed by the shear strength of the soil. The shear bands of a material with a low shear strength are curved, with the associated deformation ellipsoid mechanism widening with a decrease in strength, whereas a material with a high shear strength generally exhibits a columnar or rectangular deformation shape.

The results presented in Figure 7-2 validate the application of the rolling resistance coefficient, in conjunction with the friction coefficients, in assigning shear strength to a material to model particle shape effects. However, as observed by Wensrich & Katterfeld (2012), there is no physical basis for the rolling resistance parameter selection and the associated increase in material shear resistance can therefore not be quantified. An additional drawback of the rolling resistance coefficient is that micro-mechanical properties may be compromised although realistic bulk material behaviour is produced (Obermayr et al., 2011). For the application of sinkhole propagation investigation, a realistic representation of the bulk material behaviour is deemed sufficient as this would provide detail pertaining to the general deformation mechanism and zone of influence above a propagating cavity.

7.4.2 Material shear strength and contact stiffness comparison

An investigation was undertaken to determine the effect of an increase in material shear strength, applied using the DEM friction and rolling resistance coefficients, on a model with a normal contact stiffness of 7.8E+09 N/m. This stiffness corresponds to the stiffness calculated from Equation 7-1 (i.e. lower than the calibrated stiffness of 45.0E+09 N/m). As this contact stiffness is equal to the value assigned to the model for which the shear strain plot is presented in Figure 7-1 (d), this plot was used as a benchmark for this investigation.

Figure 7-3 (a) presents a shear strain plot of the RF3 simulation at a trapdoor displacement corresponding to 80 mm displacement of the physical trapdoor. As described above, a second DEM analysis was undertaken in which only the particle contact stiffness was reduced from 45.0E+09 N/m to 7.8E+09 N/m; the rolling resistance and friction coefficients were kept constant at 0.4 and 0.5, respectively. The corresponding shear strain plot for the model with the reduced contact stiffness is presented in Figure 7-3 (b). The particle friction and rolling resistance coefficients as well as the normal contact stiffness magnitudes for the shear strain plots in Figure 7-3 are presented in Table 7-3.

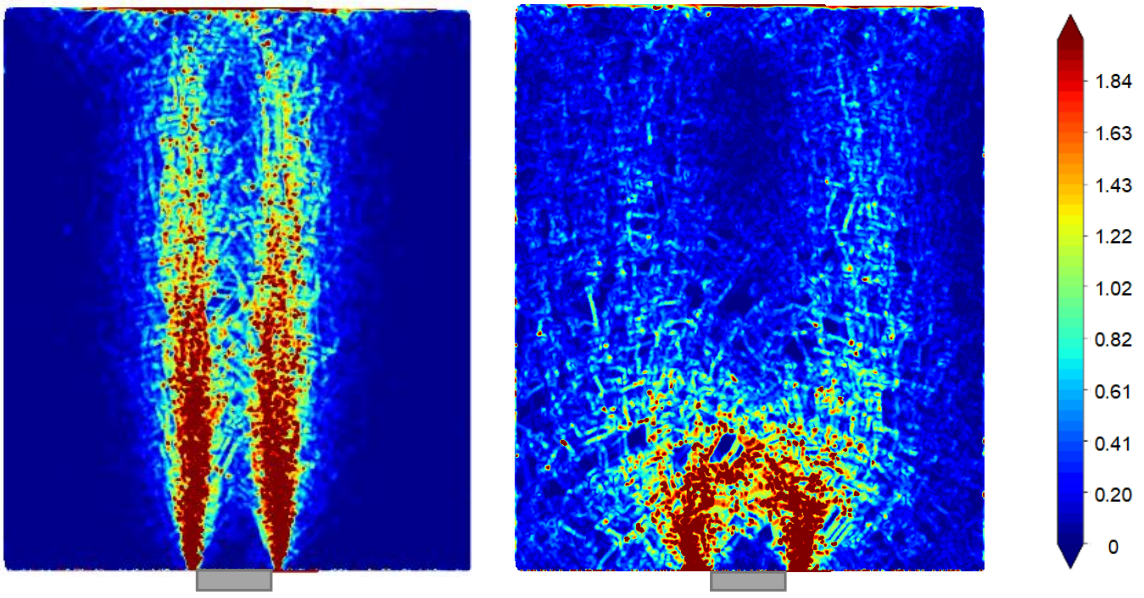

(a) (b)

Figure 7-3: Shear strain plots at 80 mm trapdoor displacement for the RF3 DEM model with a contact stiffness of (a) 45.0E+09 N/m and (b) 7.8E+09 N/m (unitless strain)

Table 7-3: Particle stiffnesses, friction coefficients and rolling resistance coefficients corresponding to shear strain plots in Figure 7-3

Blaze-DEM Model	Friction coefficient (μ)	Rolling resistance coefficient (μ_r)	Particle contact stiffness, k_n (N/m)
RF3 Figure 7-3 (a)	0.5	0.4	45.0E+09
RF3 Figure 7-3 (b)	0.5	0.4	7.8E+09

Based on the shear strain plots in Figure 7-3, it is clear that friction and rolling resistance coefficients cannot be used to dictate material shear strength in DEM analyses when the normal contact stiffness of the material has not been calibrated correctly or when it has been lowered purposefully to reduce computational effort. Furthermore, an inference may be made to the deformation mechanisms associated with cavity propagation in soil. Based on the results in Figure 7-3 it is hypothesized that the shape of the sinkhole or cavity propagation mechanism is not only a function of the shear strength of the soil as determined in Chapter 4, but also of the bulk soil stiffness. Where materials with low particle contact stiffnesses were simulated, deformation patterns resembling those associated with materials of low shear strength were observed, i.e. widening above the trapdoor. Further investigation of this hypothesis is, however, required.

7.5. NUMERICAL MODEL TRAPDOOR EXPERIMENT COMPARISON

An evaluation of the results presented in this chapter was undertaken by comparing the findings to those determined by Chevalier et al. (2012) and Rui et al. (2016-b) who conducted similar studies for shallow

and mixed trapdoor geometries, respectively. Both researchers also used DEM to investigate deformation mechanisms associated with trapdoor experiments. From their study, Chevalier et al. (2012) concluded that the effect of particle shape on the bulk behaviour of the material was evident, specifically with reference to the material's shear strength. However, the effect of particle shape on the deformation mechanisms associated with trapdoor lowering was negligible when the materials had similar shear strength properties (despite different particle shapes). This finding supports the application of the rolling resistance coefficient to simulate particle shape effects, as it demonstrates that it is the simulated shear strength of the material that dictates its behaviour.

Rui et al. (2016-b) found that the deformation mechanism associated with deep trapdoor experiments resembles that of a tower-shaped evolution, as illustrated in Figure 2-39 (b). From Figure 7-3 (a), which presents the shear strain plot for the calibrated glass beads model with friction coefficients corresponding to that of RF3 (Table 7-3), "inner" shear bands between to two primary shear bands are visible. Although these bands are not as distinct as those observed in the PIV shear strain plots for trapdoor experiments undertaken with the natural sands in this study, some correlation between the tower-shaped evolution pattern and the deformation pattern attributed to RF3 is observed. These intermediate shear bands are also a semblance of the "onion-peeling" effect used by Jennings et al. (1965) to describe cavity propagation.

7.6. THE APPLICATION OF BLAZE-DEM TO TRAPDOOR EXPERIMENTS

The potential of using DEM to predict cavity propagation mechanisms associated with the formation of sinkholes was evaluated by modelling deep trapdoor experiments in Blaze-DEM. The shear strain results obtained from the laboratory trapdoor experiments using natural sands were compared to the DEM shear strain results to which a rolling resistance coefficient was applied. Figure 7-4 presents the shear strain plots for centrifuge tests CF02 and CC12, as well as for the DEM simulation "RF3" with friction and rolling resistance coefficients listed in Table 7-2. All three deformation mechanisms displayed in Figure 7-4 show essentially vertical shear bands propagating from the edges of the trapdoor which widen at the surface. This shows that material arches in an "onion-peeling" or progressive manner as the cavity propagates towards the surface, until material can no longer arch at natural ground level. Just below surface level, two shear bands propagate outwards upwards at what is likely to be the angle of repose of the material. This material behaviour was also observed in the deformation mechanisms presented in Figure 7-2 as well as in Figure 2-43, where two shear bands propagate from the sides of the ellipsoidal deformation mechanism near the surface of the overburden material.

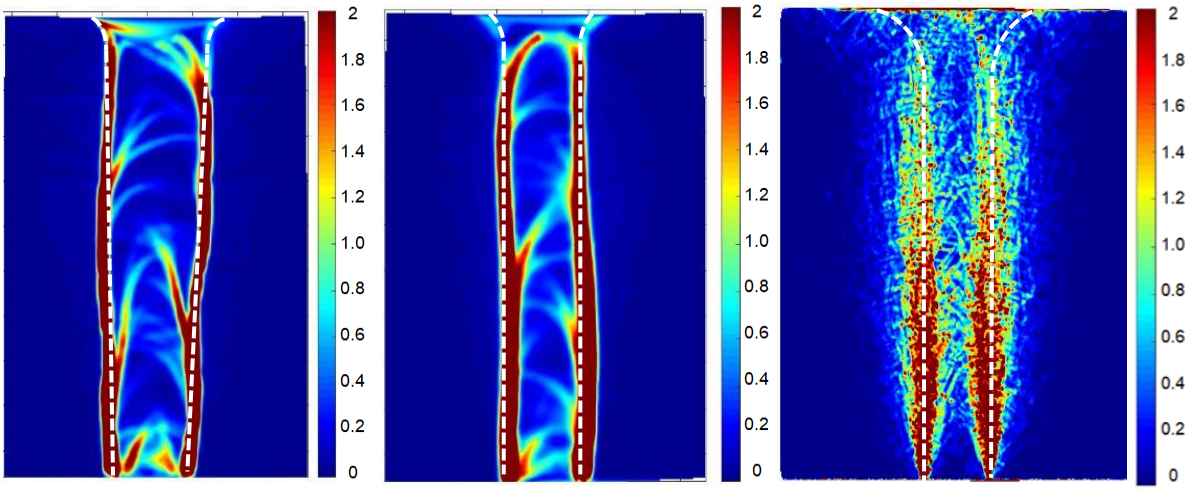

(a) (b) (c)

Figure 7-4: Shear strain plots for the (a) fine-grained sand (CF02), (b) coarse-grained sand (CC12) and (c) RF3 DEM simulation at 80 mm trapdoor displacement (unitless strain)

Based on the maximum shear strain plots presented in Figure 7-4, as well as general conclusions drawn from the results presented in Chapter 7, the potential for using Blaze-DEM to predict deformation mechanisms associated with sinkhole formation is discussed below:

- The global deformation mechanism for the two natural sands (CF02 and CC12 in Figure 7-4 (a) and (b), respectively) and that of the DEM model with simulated particle shape effects (RF3) are highly comparable. Although the bulk material behaviour is replicated fairly accurately using DEM, the results further verify that the micro-mechanical properties, such as individual shear band propagation and dilation, may be compromised (Obermayr et al., 2011).
- A wide range of deformation mechanisms associated with loss of subsurface support can be simulated using DEM. As displayed in Figure 7-2, these deformation mechanisms range from curved shear bands to vertical shear bands depending on the material shear strength and stiffness.
- Deep trapdoor experiments require large trapdoor displacements to evaluate associated deformation mechanisms as they propagate towards the surface of the model material. Due to the computational effort required to simulate this displacement, DEM (and Blaze-DEM) may be better suited to shallow trapdoor experiments, requiring comparatively smaller trapdoor displacements.
- A distinct difference between the shear strain plots from the natural sand centrifuge trapdoor experiments and those undertaken with DEM is the variation in shear band width. The shear band width is a function of the average particle size and, as a result, the DEM shear strain plots with greater particle size will exhibit wider shear bands. Particles with a smaller average diameter would be required to simulate narrower shear bands. This would result in modelling

a significantly larger number of particles, thereby increasing the required computational effort significantly. Despite the slightly wider zone of influence modelled at the surface of the DEM shear strain plot, the difference in shear band width is not deemed to be a major concern. Particle size scaling techniques discussed in Section 2.4.6 may be employed to achieve more comparable results.

- The polyhedral particle trapdoor experiments in Blaze-DEM could not be simulated successfully at the high material stresses corresponding to those of the centrifuge tests. This was attributed to the single precision computing capability of the code. Although Blaze-DEM has remarkable computing power, caution should be exercised when using it to model centrifuge experiments (associated with high stresses), specifically when simulating polyhedral particles.

Recommendations for further work are listed and discussed in the following paragraphs.

- The instability of the Blaze-DEM trapdoor experiments simulated with polyhedral particles was a significant constraint to this study. It is therefore recommended that similar experiments be undertaken at gravitational acceleration (1g) or at low model accelerations of approximately 5g. Due to the comparatively smaller inter-particle forces and corresponding smaller particle contact stiffness required at these accelerations a larger time step can be selected. Numerically stable trapdoor experiments with polyhedral particles may therefore be achievable. As the field of computer power is advancing at an astounding rate, it is envisaged that DEM trapdoor experiments with polyhedral particles at 50g will be viable in the near future.
- This study was focused on cohesionless granular overburden material. However, it is well-known that dolomitic residuum is highly heterogeneous. An investigation into the application of particle-particle cohesion using the DEM should be undertaken to understand the deformation mechanisms associated with cohesive materials during cavity propagation. Chert gravel inclusions of varying size and angularity and chert bands are often found within the residuum overlying a subsurface cavity. Different dolomitic profiles should be investigated to determine the effect of the following on sinkhole formation:
    - layering of granular and cohesive materials,
    - variations in particle size and angularity, and
    - gravel inclusions in a highly cohesive stratum.
- As detailed in Section 7.4.2, it was hypothesised that the shape of a sinkhole or cavity propagation mechanism is not strictly a function of only the shear strength of the soil, but also of the bulk soil stiffness. It is therefore recommended that the effect of bulk material stiffness on cavity propagation mechanisms be investigated using both the DEM and laboratory experiments in a controlled environment.

- It is recommended that manufactured polyhedral particles be used in the centrifuge trapdoor experiments to investigate the effect of particle angularity on shear band propagation in lieu of natural sands. DEM parameters can therefore be directly calibrated with the centrifuge trapdoor experiment PIV results and particle shape uncertainty will be eliminated. Furthermore, this will save calibration time and increase the reliability of the findings.

8. CONCLUSIONS AND RECOMMENDATIONS

This chapter summarises the main conclusions drawn from the research study based on the objectives detailed in Section 1.2. Subsequently, recommendations for the implementation of the findings as well as further research relating to the research topic are presented.

8.1. CONCLUSIONS

The following conclusions are presented:

- The primary objective of this research study was to investigate the relationship between the soil shear strength, controlled by simulated particle shape or interlock, and the associated deformation mechanism during cavity propagation resulting in sinkhole formation. Consolidated-undrained triaxial tests were conducted to determine the shear strength of the natural sands and glass beads used in the centrifuge trapdoor experiments. These results showed that for natural sands, with a comparatively high shear strength (critical state friction angle of between 32° and 35°), the primary shear bands propagated vertically until they reached the soil surface. In contrast, an elongated ellipsoidal deformation mechanism was observed for the experiment undertaken with the glass beads which had a lower shear strength (critical state friction angle of approximately 16°). The ellipsoidal deformation mechanism affected a much greater region within the overburden material than the vertical deformation mechanisms. The general finding, described above, was also observed in the results of the numerical trapdoor experiments conducted using Blaze-DEM. The initial numerical simulation was calibrated to match the material behaviour of the physical trapdoor experiment with glass beads and therefore exhibited an ellipsoidal deformation mechanism with curved shear bands. As the rolling resistance and friction coefficients were increased incrementally, simulating greater particle angularity and interlock (i.e. shear strength), the deformation mechanism tended towards verticality until effectively vertical shear bands were simulated. It was therefore concluded that the greater the shear strength of the overburden material, the greater the tendency of the shear bands to propagate vertically. It was further observed that the deformation mechanisms widened outward, away from the trapdoor centreline, at the surface. This was attributed the fact that the overburden material could no longer arch and redistribute stresses above the apex of the arch, resulting in the formation of a failure mechanism

- A collective analysis of the results of the physical trapdoor experiments showed that material behaviour compared well with the findings described in literature (Dewoolkar et al., 2007, Iglesia et al., 2014 and Costa et al., 2009). Several deviations from the standard qualitative characteristics were observed and these were primarily attributed to the test undertaken with

glass beads for which the material shear strength was significantly lower than common geomaterials. The following conclusions related to material shear strength were drawn from the results of the centrifuge trapdoor experiments:

- Trapdoor load-displacement characteristics: It was observed that the fine- and coarse-grained sands, with a comparatively higher shear strength than the glass beads, reached a state of maximum arching (at which the minimum load is applied to the trapdoor during trapdoor lowering) at a much smaller trapdoor displacement than in the case of the glass beads. Furthermore, a greater reduction in load measured on the trapdoor was recorded for the natural sands. This was attributed to the greater load-transfer capacity and hence arching ability of the materials with the greater shear strength.
- Deformation mechanisms: No significant differences were observed in terms of deformation mechanisms (shear band formation) in the materials tested during the initial stages of the experiment (trapdoor displacements < 5 mm). However, during the intermediate stage of the trapdoor experiment (trapdoor displacements between 10 mm and 40 mm) the glass beads experiment exhibited a wedge-like deformation mechanism in the form of an inverted triangle. The mechanism then evolved into an elongated ellipsoidal failure surface towards the latter part of the experiment (at trapdoor displacements > 60 mm). These deformation mechanisms extended well beyond the vertical projection of the trapdoor edges. This was in contrast to the natural sands, with greater shear strength. As noted above, the shear bands in the natural sands propagated vertically towards the surface.
- Surface settlement: The natural sands, with a comparatively higher shear strength, exhibited settlement behaviour in which the surface settlement was concentrated in the area directly above the trapdoor. Conversely, a wide and shallow zone of influence was recorded for the experiment with glass beads, corresponding to materials with a lower shear strength. Although settlement was observed over a significantly larger width along the surface, the settlement was not as deep as for the materials with greater shear strength.

- From the results of the numerical trapdoor experiments it was concluded that the influence of particle normal contact stiffness was substantial, especially at the large inter-particle forces corresponding to the high stresses occurring in the material at prototype dimensions. Materials to which a low particle normal contact stiffness was assigned generated elongated ellipsoidal deformation mechanisms resembling those associated with low shear strength materials. The influence of friction coefficients was observed to be significant when the particle normal contact stiffness was calibrated to reflect the physical experiment results accurately. If the

normal particle contact stiffness was not set large enough to yield a representative material response, the friction coefficients had virtually no influence. Due to the quasi-static nature of this specific trapdoor experiment (slow rate of trapdoor displacement) the coefficient of restitution was not found to be significant during the simulation of a trapdoor experiment using the DEM.

- Particle normal contact stiffness is commonly lowered to reduce the computational effort required to run DEM simulations. However, this was found to be unsuitable at the high stresses associated with the problem under consideration as the material response with "soft" particles resulted in unrealistic deformation mechanisms. Furthermore, trapdoor experiments with polyhedral particles could not be simulated successfully in Blaze-DEM at the model acceleration corresponding to that of the centrifuge trapdoor experiments (i.e. at 50g). This was attributed to the single precision computing capability of the code. Caution should therefore be exercised when using Blaze-DEM to model centrifuge experiments (associated with high stresses), specifically when simulating polyhedral particles.

- Based on the findings in Chapter 7, it was concluded that the numerical trapdoor experiments with polyhedral particles might have been successful had a lower model acceleration been applied. This would have resulted in smaller inter-particle forces, a lower normal contact stiffness and a greater critical time step.

- Despite Blaze-DEM's limitations, the results of this research study show that Blaze-DEM can be used to model deformation mechanisms associated with cavity propagation in trapdoor experiments when using spherical particles. Once an appropriate model had been created and calibrated, changes to the material properties could be made by varying single or multiple particle properties and rerunning the simulation. Although the overall deformation mechanism could be simulated using Blaze-DEM, the propagation of individual shear bands, in addition to the shear band width, remained the biggest discrepancy between the DEM maximum shear strain plots and the corresponding coarse- and fine-grained sand plots.

8.2. RECOMMENDATIONS

Based on the findings of this research study, the following recommendations should be considered when developing infrastructure on dolomitic land:

- Shear strength characterisation of the materials overlying dolomitic bedrock should be considered an essential component of a geotechnical investigation as it influences the manner in which cavities propagate to the surface.
- Where overburden materials with poor shear strength properties such as WAD are dominant in the profile of a potential site in an area underlain by dolomite, a sinkhole will be expected to widen towards the surface.

Recommendations for future research based on the application of the DEM to investigating cavity propagation by means of deep trapdoor experiments are listed below:

- Investigate the effect of bulk material stiffness on the deformation mechanisms associated with cavity propagation. As materials with a low particle normal contact stiffness yielded deformation mechanisms akin to those with a low shear strength, it is predicted that material bulk stiffness may govern cavity propagation to a certain extent.
- Simulating numerical trapdoor experiments at lower accelerations, corresponding to smaller inter-particle forces, may make the application of polyhedral particles viable. Otherwise, consider the use of double precision computation to allow small enough time steps to be modelled.
- Consider the utilisation of manufactured polyhedral particles for centrifuge testing to ensure a direct correlation of the particle shape used in the physical trapdoor experiments to those applied in the numerical DEM model.
- Dolomitic residuum is highly heterogenous. It is therefore recommended that an investigation of varying residuum profiles be undertaken. The significance of the shear strength of individual blanket layers should also be determined.

9. REFERENCES

Ai, J., Chen, J. F., Rotter, J. M. & Ooi, J. Y., 2011. Assessment of rolling resistance models in discrete element simulations. *Powder Technology,* 206(3), pp. 269-282.

Archer, A., 2014. *Using small-strain stiffness to predict the settlement of shallow foundations on sand.* University of Pretoria: Masters dissertation.

ASTM D2487, 2011 (2006). *Practice for Classification of Soil for Engineering Purposes (Unified Soil Classification System),* s.l.: ASTM.

ASTM D4253-93, 1996. *Standard Test Methods for Maximum Index Density and Unit Weight of Soils Using a Vibratory Table,* s.l.: ASTM.

ASTM D4254-93, 1996. *Standard Test Methods for Minimum Index Density and Unit Weight of Soils and Calculation of Relative Density,* s.l.: ASTM.

Belheine, N. et al., 2009. Numerical simulation of drained triaxial test using 3D discrete element modelling. *Computers and Geotechnics,* 36(1-2), pp. 320-331.

Bolton, M., 1986. The strength and dilatancy of sands. *Geotechnique,* 36(1), pp. 65-78.

Boon, C., Houlsby, S. & Utili, S., 2012. A new algorithm for contact detection between convex polygonal and polyhedral particles in the discrete element method. *Computers and Geotechnics,* Volume 44, pp. 73-82.

Bransby, P. L. & Blair-Fish, P. M., 1975. Deformations near rupture surfaces in flowing sand. *Geotechnique,* 25(2), pp. 384-389.

Buttrick, D. & Van Schalkwyk, A., 1995. The method of scenario supposition for stability evaluation of sites on dolomitic land in South Africa. *Journal of the South African Institution of Civil Engineers,* 37(4).

Buttrick, D. & Van Schalkwyk, A., 1998. Hazard and risk assessment for sinkhole formation on dolomite land in South Africa. *Environmental Geology,* 36(1-2), pp. 170-178.

Bym, T., Marketos, G., Burland, J. B. & O'Sullivan, C., 2013. Use of a two-dimensional discrete-element line-sink model to gain insight into tunnelling-induced deformations. *Geotechnique,* 63(9), p. 791.

Chandrupatla, T. R. & Belegundu, A. D., 2002. *Introduction to Finite Elements in Engineering.* 3rd ed. s.l.:Prentice Hall, Inc Publishers.

Chang, Y. Y. et al., 2013. Use of centrifuge experiments and discrete element analysis to model the reverse fault slip. *International Journal of Civil Engineering,* 11(2), pp. 79-89.

Cheng, K. et al., 2017. Determination of microscopic parameters of quartz sand through tri-axial test using the discrete element method. *Computers and Geotechnics,* Volume 92, pp. 22-40.

Chevalier, B., Combe, G. & Villard, P., 2007. Experimental and numerical studies of load transfers and arching effect in the trap-door problem. *Laboratoire Sols, Solides, Structures-Risques, Grenoble, France.*

Chevalier, B., Combe, G. & Villard, P., 2012. Experimental and discrete element modelling studies of the trapdoor problem: influence of the macro-mechanical frictional parameters. *Acta Geotechnica,* 7(1), pp. 15-39.

Chung, Y. C., 2006. *Discrete element modelling and experimental validation of a granular solid subject to different loading conditions.* Edinburgh: Doctoral Dissertation.

Coetzee, C., 2016. Calibration of the Discrete Element Method and the effect of particle shape. *Powder Technology,* Volume 297, pp. 50-70.

Coetzee, C., 2017. Calibration of the discrete element method. *Powder Technology,* Volume 310, pp. 104-142.

Costa, Y. D., Zornberg, J. G., Benedito, S. B. & Costa, L., 2009. Failure mechanisms in sand over a deep active trapdoor.. *ASCE Journal of Geotechnical and Geoenvironmental Engineering,* 135(11), pp. 1741-1753.

Craig, R., 2004. *Craig's soil mechanics.* s.l.:CRC Press.

Cundall, P., 2001. A discontinuous future for numerical modelling in geomechanics?. *Proceedings of the institution of civil engineers-geotechnical engineering,* 149(1), pp. 41-47.

Cundall, P. A. & Strack, O. D., 1979. A discrete numerical model for granular assemblies. *Geotechnique,* 29(1), pp. 47-65.

Da Silva, T., 2017. *Centrifuge modelling of the behaviour of geosynthetic-reinforced soils over voids.* University of Cambridge: Doctoral Dissertation.

Davis, E. H., 1968. Theories of plasticity and failures of soil masses. *Soil Mechanics, selected topics.,* pp. 341-380.

Department of Water Affairs, 2009. *Dolomite Guideline: A short guide to available documents on procedures for developing dolomitic land,* Pretoria: DWAF.

Dewoolkar, M. M., Santichainaint, K. & Ko, H. Y., 2007. Centirfuge modelling of granular soil response over active circular trapdoors. *Soils and foundations,* 47(5), pp. 931-945.

Donze, F. V., Richefeu, V. & Magnier, S. A., 2009. Advances in discrete element method applied to soil, rock and concrete mechanics. *Electronic Journal of Geotechnical Engineering,* 8(1), p. 44.

Dullen, F. A., 1992. *Porous Media: Fluid Transport and Pore Structure.* San Diego: Academic Press inc.

EDEM Software, 2012. *EDEM Technical Overview,* s.l.: DEM Solutions.

Einstein, H. H. et al., 1990. *Stochastic and centrifuge modelling of jointed rock (No. MIT-CE-R90-22),* s.l.: Massachusetts Inst of Tech Cambridge Dept of Civil Engineering.

Engesser, F., 1882. Ueber den Erdduck gegen innere Stützwande (Tunnelwande). *Deutsche Bauzeitung,* Volume 16, pp. 91-93.

Evans, C., 1983. *An examination of aching in granular soils.* Massachusetts Institute of Technology: Doctoral dissertation.

Feng, Y., Han, K., Owen, D. & Loughran, J., 2007. *Upscaling of discrete element models for particle systems.* Brisbane, Proceedings of the 4th International Conference on Discrete Element Methods.

Goldsmith, W., 1960. *Impact: The theory and physical behaviour of colliding solids,* s.l.: Edward Arnold.

Gonzalez-Montellano, C., Ramirez, A., Gallego, E. & Ayuga, F., 2011. Validation and experimental calibration of 3D discrete element models for the simulation of the discharge flow in silos. *Chemical Engineering Science,* 66(21), pp. 5116-5126.

Govender, N., 2015. *Blaze-DEM: A GPU based large scale 3D discrete element particle transport framework.* University of Pretoria: Doctoral dissertation.

Govender, N., Rajamani, R. K., Kok, S. & Wilke, D. N., 2015. Discrete element simulation of mill charge in 3D using the BLAZE-DEM GPU framework. *Minerals engineering,* Volume 79, pp. 152-168.

Govender, N., Wilke, D. N. & Kok, S., 2016. Blaze-DEMGPU: Modular high-performance DEM framework for the GPU architecture. *Software X,* Volume 5, pp. 62-66.

Govender, N., Wilke, D. N., Kok, S. & Els, R., 2014. Development of a convex polyhedral discrete element simulation framework for NVIDIA Kepler based GPUs. *Journal of Computational and Applied Mathematics,* Volume 270, pp. 386-400.

Handy, R.L., 1985. The arch in soil arching. *Journal of Geotechnical Engineering, 111*(3), pp.302-318.

Härtl, J. & Ooi, J. Y., 2011. Numerical investigation of particle shape and particle friction on limiting bulk friction in direct shear tests and comparison with experiments. *Powder Technology,* 212(1), pp. 231-239.

Haughey, D. P. & Beveridge, G. S., 1969. Structural properties of packed beds - A review. *The Canadian Journal of Chemical Engineering,* 47(2), pp. 101-200.

Hertz, H., 1882. Über die Berührung fester elastischer Körper und über die Härte. *Verhandlung des Vereins zur Beförderung des Gewerbfleißes,* Volume Berlin, p. 449.

Höhner, D., Wirtz, S. & Scherer, V., 2013. Experimental and numerical investigation on the influence of particle shape and shape approximation on hopper discharge using the discrete element method. *Powder Technology,* Volume 235, pp. 614-627.

Iglesia, G., Einstein, H. H. & Whitman, R. V., 1990. *Stochastic and centrifuge modelling of jointed rock,* Cambridge, Massachusetts: MIT Department of Civil Engineering.

Iglesia, G. R., Einstein, H. H. & Whitman, R. V., 2011. Validation of centrifuge model scaling for soil systems via trapdoor tests. *Journal of Geotechnical and Geoenvironmental Engineering,* 137(11), pp. 1075-1089.

Iglesia, G. R., Einstein, H. H. & Whitman, R. V., 2014. Investigation of soil arching with centrifuge tests. *Journal of Geotechnical and Geoenvironmental engineering,* 140(2), p. p.04013005.

Iwashita, K. & Oda, M., 1998. Rolling resistance at contacts in simulation of shear band development by DEM. *Journal of engineering mechanics,* 124(3), pp. 285-292.

Jacobsz, S. W., 2016. Trapdoor experiments studying cavity propagation. *Proceedings of the first Southern African Geotechnical Conference,* pp. 159-165.

Jacobsz, S. W., Kearsley, E. P. & Kock, J. H., 2014. *The geotechnical centrifuge facility of the University of Pretoria.* s.l.:s.n.

Jennings, J. E., Brink, A. B., Louw, A. & Gowan, G. D., 1965. *Sinkholes and subsidences in the Transvaal dolomites of South Africa.* Montreal, In Proceedings of the 6th International Conference on Soil Mechanics and Foundation Engineering.

Jiang, M. J., Yu, H. S. & Harris, D., 2005. A novel discrete model for granular material incorporating rolling resistance. *Computers and Geotechnics,* 32(5), pp. 340-357.

Jiang, M. & Yu, H. S., 2006. Application of discrete element method to geomechanics. *Modern trends in geomechanics,* Volume Springer, Berlin, Heidelberg, pp. 241-269.

Jiang, Y. & Liu, M., 2003. Granular elasticity without the Coulomb condition. *Physical Review Letters,* 91(14), p. 144301.

Jimenez-Herrera, N., Barrios, G. K. & Tavares, L. M., 2018. Comparison of breakage models in DEM in simulating impact on particle beds. *Advanced Powder Technology,* 29(3), pp. 692-706.

Jop, P., Forterre, Y. & Pouliquen, O., 2006. A constitutive law for dense granular flows. *Nature,* 441(7094), p. 727.

Kamrin, K., 2010. Nonlinear elasto-plastic model for dense granular flow. *International Journal of Plasticity,* Volume 26, pp. 167-188.

Kloss, C. & Goniva, C., 2011. LIGGGHTS-open source discrete element simulations of granular materials based on Lammps. *Supplemental Proceedings: Materials Fabrication, Properties, Characterosation, and Modeling,* Volume 2, pp. 781-788.

Kozicki, J., Teichman, J. & Muhlhaus, H. B., 2014. Discrete simulations of a triaxial compression test for sand by DEM. *International Journal for Numerical and Analytical Methods in Geomechanics,* 38(18), pp. 1923-1952.

Leica Microsystems, 2013. *Brief Introduction to Coating Technology for Electron Microscopy*. [Online] Available at: http://www.leica-microsystems.com/science-lab/brief-introduction-to-coating-technology-for-electron-microscopy/ [Accessed 18 August 2018].

Li, S., Li, D., Cao, L. & Shangguan, Z., 2015. Parameter estimation approach for particle flow model of rockfill materials using response surface method. *International Journal of Computational Materials Science and Engineering,* 4(01), p. 1550003.

Li, Y., Xu, Y. & Thornton, C., 2005. A comparison of discrete element simulations and experiments for 'sandpiles' composed of spherical particles. *Powder Technology,* Volume 160, pp. 219-228.

Lorenz, A., Tuozzolo, C. & Louge, M. Y., 1997. Measurements of impact properties of small, nearly spherical particles. *Experimental Mechanics,* 37(3), pp. 292-298.

Mack, S., Langston, P., Webb, C. & York, T., 2011. Experimental validation of polyhedral discrete element model. *Powder Technology,* Volume 214, pp. 431-442.

Malone, K. F. & Xu, B. H., 2008. Determination of contact parameters for discrete element method simulations of granular systems. *Particuology,* 6(6), pp. 521-528.

Marigo, M. & Stitt, E. H., 2015. Discrete element method (DEM) for industrial applications: Comments on calibration and validation for the modelling of cylindrical pellets. *KONA Powder and Particle Journal,* Volume 32, pp. 236-252.

Markauskas, D., Kacianauskas, R., Dziugys, A. & Navakas, R., 2010. Investigation of adequacy of multi-sphere approximation of elliptical particles for DEM simulations. *Granular Matter,* 12(1), pp. 107-123.

Maw, N., Barber, J. R. & Fawcett, J. N., 1976. The oblique impact of elastic spheres. *Wear,* 38(1), pp. 101-114.

McNulty, J. W., 1965. *An experimental study of arching in sand.* University of Illinois: Doctoral dissertation.

Mindlin, R. & Deresiewics, H., 1953. Elastic spheres in contact under varying oblique forces. *Journal of Applied Mechanics,* Volume 75, pp. 327-344.

Moreno-Atanasio, R., Xu, B. H. & Ghadiri, M., 2007. Computer simulation of the effect of contact stiffness and adhesion on the fluidisation behaviour of powders. *Chemical Engineering Science,* Volume 62, pp. 184-194.

Muir Wood, D., 2002. Some observations of volumetric instabilities in soils. *International Journal of Solids and Structures,* 39(13-14), pp. 3429-2449.

Nanoscience Instruments , 2018. *Scanning Electron Microscopy.* [Online]
Available at: http://www.nanoscience.com/techniques/scanning-electron-microscopy
[Accessed 17 August 2018].

Nassauer, B. & Liedke, T., 2013. Polyhedral particles for the discrete element method. *Granular Matter,* Volume 15, pp. 85-93.

National Highway Institute, 2006. *Soils and foundations: Reference manual - Volume 1,* Washington, D.C.: FHWA NHI-06-088.

NVIDIA, 2012. *NVIDIA KEPLER GK110 architecture whitepaper.* [Online]
Available at: http://www.nvidia.com/NVIDIA KEPLER GK110 Architecture Whitepaper
[Accessed 15 May 2018].

Oberholzer, B., 2018. *Trapdoor Experiments - Relative Densities* [Interview] (19 November 2018).

Oberholzer, B. M., 2017. *Investigating cavity propagation to the surface through centrifuge trapdoor experiments,* University of Pretoria: Masters dissertation.

Obermayr, M., Dressler, K., Vrettos, C. & Eberhard, P., 2011. Prediction of draft forces in cohesionless soil with the Discrete Element Method. *Journal of Terramechanics,* 48(5), pp. 347-358.

Oosthuizen, A. & Richardson, S., 2011. *Sinkholes and subsidence in South Africa,* Cape Town: Council for Geoscience.

O'Sullivan, C., 2011. Particle-based discrete element modeling: geomechanics perspective. *International Journal of Geomechanics,* 11(6), pp. 449-464.

Potyondy, D. O. & Cundall, P. A., 2004. A bonded-particle model for rock. *International Journal of Rock Mechanics and Mining Sciences,* 41(8), pp. 1329-1364.

Preciosa Ornela, 2011. *Glass beads as grinding media,* Desna, Czech Republic: Preciosa Traditional Czech Glass.

Renzo, A. & Maio, F. P., 2004. Comparison of contact-force models for the simulation of collisions in DEM-based granular flow codes. *Chemical engineering science,* 59(3), pp. 525-541.

Roessler, T. & Katterfeld, A., 2018. Scaling of the angle of repose test and its influence on the calibration of DEM parameters using upscaled particles. *Powder Technology,* Volume 330, pp. 58-66.

Roscoe, K., 1970. The influence of strains in soil mechanics. *Geotechnique,* 20(2).

Rui, R. et al., 2016. Investigation of soil-arching development in dense sand by 2D model tests. *Geotechnical Testing Journal,* 39(3), pp. 415-430.

Rui, R. et al., 2016. Evolution of soil arching: 2D DEM simulations. *Computers and Geotechnics,* Volume 73, pp. 199-209.

Rycroft, C. H., Kamrin, K. & Bazant, M. Z., 2009. Assessing continuum postulates in simulations of granular flow. *Journal of Mechanics and Physics of Solids,* Volume 57, pp. 828-839.

SANS 1936-1, 2012. *Development of dolomite land - Part 1: General principles and requirements,* s.l.: South African Bureau of Standards.

SANS 1936-2, 2012. *Development of dolomite land - Part 2: Geotechnical investigations and determinations,* s.l.: South African Bureau of Standards.

SANS 1936-4, 2012. *Development of dolomite land - Part 4: Risk management,* s.l.: South African Bureau of Standards.

Santichaianaint, K., 2002. *Centrifuge modelling and analysis of active trapdoor in sand.* University of Colorado, Boulder: Doctoral dissertation.

Santos, D. A. et al., 2016. Investigation of particle dynamics in a rotary drum by means of experiments and numerical simulations using DEM. *Advanced Powder Technology,* 27(2), pp. 692-703.

Schoning, W. L., 1990. *Distribution of sinkholes and subsidences in the dolomite areas south of Pretoria*. University of Pretoria: MSc Dissertation.

Siegmann, E. et al., 2017. Efficient discrete element method simulation strategy for analyzing large-scaled agitated powder mixers. *Chemie Ingenieur Tegnik,* 89(8), pp. 995-1005.

Sinnott, M. D. & Cleary, P. W., 2016. The effect of particle shape on mixing in a high shear mixer. *Computational Particle Mechanics,* 3(4), pp. 477-504.

Stanier, S. A., Blaber, J., Take, W. A. & White, D. J., 2015. Improved image-based deformation for geotechnical applications. *Canadian Geotechnical Journal,* 53(5), pp. 727-739.

Statistics South Africa, 2017. *Mid-year population estimates (2017).* [Online]
Available at: www.statssa.gov.za/publications/P0302/P03022017 [Accessed 5 August 2018].

Statistics South Africa, 2018. *Stats SA.* [Online]
Available at: http://www.statssa.gov.za/?p=11092 [Accessed 11 June 2018].

Stone, K. J. & Wood, D. M., 1992. Effects of dilatancy and particle size observed in model tests on sand. *Soil and Foundations,* 32(4), pp. 43-57.

Taylor, R. N., 1995. Centrifuges in modelling: principles and scale effects.. *Geotechnical centrifuge technology*, pp. 19-33.

Terzaghi, K., 1936. *Stress distribution in dry and saturated sand above a yielding trapdoor.* Harvard University, Cambridge (USA), Proc. 1st International Conference of Soil Mechanics.

Terzaghi, K., 1943. *Theoretical Soil Mechanics.* s.l.:John Wiley & Sons, Inc..

Thakur, S. C., Ooi, J. Y. & Ahmadian, H., 2016. Scaling of discrete element model parameters for cohesionless and cohesive solid. *Powder Technology,* Volume 293, pp. 130-137.

Tharp, T. M., 1999. Mechanics of upward propagation of cover-collapse sinkholes. *Engineering Geology,* Volume 52, pp. 23-33.

Thornton, C. & Randall, C. W., 1988. Applications of theoretical contact mechanics to solid particle system simulation. *Studies in Applied Mechanics,* Volume 20, pp. 133-142.

Tien, H. J., 1996. *A literature study of the arching effect.* Massachusetts Institute of Technology: MSc dissertation.

Trollip, N. Y., 2006. *The geology of an area south of Pretoria with specific reference to dolomite stability.* University of Pretoria: Doctoral Dissertation.

Vardoulakis, I., Graf, B. & Gudehus, G., 1981. Trapdoor problem with dry sand: A statistical approach based upon model kinematics. *International Journal for Numerical and Analytical Methods in Geomechanics,* Volume 5, pp. 57-58.

Wagener, F. M. & Day, P. W., 1986. Construction on dolomite in South Africa. *Environmental Geology and Water Sciences,* 8(1-2), pp. 83-89.

Waltham, A. C. & Fookes, P. G., 2003. Engineering classification of karst ground conditions. *Journal of Engineering Geology and Hydrogeology,* Volume 36, pp. 101-118.

Wang, G. S. & Kong, L. W., 2011. A non-coaxial and unbalanced plastic flow rule for geomaterials and its application to the shear band orientation prediction. *International Journal for Numerical and Analytical Methods in Geomechanics,* 35(6), pp. 668-693.

Wang, J., 2017. Force transmission modes of non-cohesive and cohesive materials at the critical state. *Materials,* 10(9), p. 1014.

Warren, J., 2000. Dolomite: occurence, evolution and economically important associations. *Earth-Science Reviews,* Volume 52, pp. 1-81.

Wensrich, C. M. & Katterfeld, A., 2012. Rolling friction as a technique for modelling particle shape in DEM. *Powder Technology,* Volume 217, pp. 409-417.

White, D. J. & Bolton, M. D., 2004. Displacement and strain paths during plane-strain model pile installation in sand. *Geotechnique,* 54(6), pp. 375-397.

White, D. J., Take, W. & Bolton, M., 2003. Soil deformation measurement using particle image velocimetry (PIV) and photogrammetry. *Geotechnique,* 53(7), pp. 619-631.

Wikipedia, 2018. *Regular polyhedron.* [Online]
Available at: https://en.m.wikipedia.org/wiki/Regular_polyhedron [Accessed 13 May 2018].

Windows-Yule, C. R., Tunuguntla, D. R. & Parker, D. J., 2016. Numerical modelling of granular flows: a reality check. *Computational Particle Mechanics,* 3(3), pp. 311-332.

Wood, D., 2004. *Geotechnical Modelling.* s.l.:Spon. Press.

Yan, Z., Wilkinson, S. K., Stitt, E. H. & Marigo, M., 2015. Discrete element modelling (DEM) input parameters: understanding their impact on model predictions using statistical analysis. *Computational Particle Mechanics,* Volume 2, pp. 283-299.

Yousefi, A. & Ng, T. T., 2017. Dimensionless input parameters in discrete element modelling and assessment of scaling techniques. *Computers and Geotechnics*, Volume 88, pp. 164-173.

Yuu, S., Abe, T., Saitoh, T. & Umekage, T., 1995. Three-dimensional numerical simulation of the motion of particles discharging from a rectangular hopper using distinct element method and comparison with experimental data. *Advanced Powder Technology*, 6(4), pp. 259-269.

Zhao, T., 2017. *Coupled DEM-CFD Analyses of Landslide -Induced Debris Flows.* Singapore: Springer.

Zhou, B., Huang, R., Wang, H. & Wang, J., 2013. DEM investigation of particle anti-rotation effects on the micromechanical response of granular materials. *Granular Matter*, 15(3), pp. 315-326.

Zhou, B., Wang, J. & Wang, H., 2018. Three-dimensional sphericity, roundness and fractal dimension of sand particles. *Geotechnique*, 68(1), pp. 18-30.

APPENDIX A

CENTRIFUGE TRAPDOOR EXPERIMENTS: INITIAL ANGLE OF PROPAGATION

Initial Shear Band Formation Analysis

Measured					
		CF01	CF02	CC11	CC12
Relative Density (I_D)		93%	94%	139%	119%
H (mm)		358.6	355.7	347.7	352.7
γ (kN/m^3)		16.6	16.6	18.2	17.8
σ_V (kPa)		297.8	295.7	316.4	313.5
Maximum arching	L	39.3	38.5	40	34.1
	R	39.6	38.5	39.4	35.8
	Average	**39.5**	**38.5**	**39.7**	**35.0**
5 mm	L	23.8	29.1	24	28.6
	R	28.1	31.4	27.7	19.9
	Average	**26.0**	**30.3**	**25.9**	**24.3**

Calculations					
Reference	Parameter	CF01	CF02	CC11	CC12
Iglesia, et al. (2013)	ϕ'_{Peak}	42.3	42.3	39	39
	ϕ'_{CS}	34.8	34.8	32	32
Rui, et al. (2016)	45° - $\phi_p/2$	23.85	23.85	25.5	25.5
	45° - $\phi_{cs}/2$	27.6	27.6	29	29
Dewoolkar, et al. (2007)	$0.8\Psi = \phi'_p - \phi'_{cs}$	9.4	9.4	8.8	8.8
	K_0	0.429	0.429	0.470	0.470
	p' (σ_H)	127.8	127.0	148.7	147.4
	I_R	3.79	3.85	5.95	4.96
	$5I_R$	18.94	19.23	29.74	24.79
	Ψ	23.68	24.04	37.17	30.99

$I_R = I_D(10-\ln(p'))-1$	Equation 4-1
$0.8\Psi = \phi'_p - \phi'_{cs}$	Equation 4-2
$0.8\Psi = 5I_R$	Equation 4-3

Percentage Difference (Measured vs Calculated)					
Maximum arching		CF01	CF02	CC11	CC12
Iglesia, et al. (2013)	ϕ'_{Peak}	-7%	-10%	2%	-12%
Dewoolkar, et al. (2007)	$0.8\Psi = \phi'_p - \phi'_{cs}$	76%	76%	78%	75%
	$0.8\Psi = 5I_R$	40%	38%	6%	11%
Rui, et al. (2016)	45 - $\phi_p/2$	40%	38%	36%	27%
	45 - $\phi_{cs}/2$	30%	28%	27%	17%

5 mm Displacement		CF01	CF02	CC11	CC12
Iglesia, et al. (2013)	ϕ'_{Peak}	-63%	-40%	-51%	-61%
Dewoolkar, et al. (2007)	$0.8\Psi = \phi'_p - \phi'_{cs}$	64%	69%	66%	64%
	$0.8\Psi = 5I_R$	9%	21%	-44%	-28%
Rui, et al. (2016)	45 - $\phi_p/2$	8%	21%	1%	-5%
	45 - $\phi_{cs}/2$	-6%	9%	-12%	-20%

APPENDIX B

DEM SIMULATION LOGS

B.1 CONTENTS OF APPENDIX B

Appendix B contains a detailed simulation log of the various stages of the Blaze-DEM trapdoor experiment, as listed below:

a) B.1 Pluviation log

b) B.2 Centrifuge “spin-up” log

c) B.3 Calibration and analyses

APPENDIX B

APPENDIX B.1: PLUVIATION LOG

	TD_P_Initial	TD_Initial2	TD_Initial3	TD_Initial4	TD_Initial5	TD_Initial6	TD_Initial7	TD_Initial8	TD_Initial9
World Setup									
Time Step (s)	5.00E-04	5.00E-04	1.00E-03	1.00E-03	1.00E-03	1.00E-03	1.00E-03	1.00E-03	1.00E-03
No. of Particles	339646	339646	260000	262000	290000	290000	290000	290000	290000
Gravity (cm^2/s)	-980	-19.6	-19.6	-19.6	-19.6	-19.6	-19.6	-19.6	-19.6
Launch Velocity (Y)	-500	-500	-500	-600	-600	-600	-600	-600	-600
Res_Height (cm)	34	32.8			33.1	26.3	33.2	30	31.14
Particle Setup									
Diameter (m)	0.1	0.1	0.1	0.1	0.1	0.1	0.1	0.1	0.1
Density (kg/m^3)	2500	2500	2500	2500	2500	2500	2500	2500	2500
COR	0.7	0.7	0.7	0.7	0.7	0.7	0.7	0.7	0.7
Stiffness (N/cm)	5.00E+05	5.00E+05	5.00E+05	5.00E+05	5.00E+05	5.00E+03	4.20E+05	8.00E+04	3.00E+04
Stiffness (N/m)	5.00E+07	5.00E+07	5.00E+07	5.00E+07	5.00E+07	5.00E+05	4.20E+07	8.00E+06	3.00E+06
Static Friction	0.45	0.45	0.6	0.5	0.3	0.3	0.3	0.3	0.3
Kinetic Friction	0.45	0.45	0.6	0.5	0.3	0.3	0.3	0.3	0.3
Cohesion	0	0	0.1	0.1	0	0	0	0	0
Rolling Res	0.01	0.01	0.01	0.01	0.01	0.01	0.01	0.01	0.01
Critical Time Step	7.88E-04	7.88E-04	7.88E-04	7.88E-04	7.88E-04	7.88E-03	8.60E-04	1.97E-03	3.22E-03
G	2.05E+05	2.05E+05	2.05E+05	2.05E+05	2.05E+05	2.05E+03	1.72E+05	3.28E+04	1.23E+04
v	0.22	0.22	0.22	0.22	0.22	0.22	0.22	0.22	0.22
Rayleigh Time Step	3.94E-03	3.94E-03	3.94E-03	3.94E-03	3.94E-03	3.94E-02	4.30E-03	9.86E-03	1.61E-02
Res_Density (kg/m^3)	1830	1622	1519	1533	1615	2082	1626	1652	1733

	TD_Initial10	TD_Initial11	TD_Initial12	TD_Initial13	TD_Initial14	TD_Initial15	TD_Initial16	TD_Initial17
World Setup								
Time Step (s)	1.00E-03	1.00E-03	1.00E-03	1.00E-03	1.00E-03	1.00E-03	1.00E-03	1.00E-04
No. of Particles	300000	305000	305000	302000	301000	300000	300000	300000
Gravity (cm^2/s)	-19.6	-19.6	-19.6	-19.6	-19.6	-19.6	-19.6	-19.6
Launch Velocity (Y)	-600	-600	-600	-600	-600	-600	-600	-600
Res_Height (cm)	32.95	33.13	33.19	33.05	33.19		33.1	36.5
Particle Setup								
Diameter (m)	0.1	0.1	0.1	0.1	0.1	0.1	0.1	0.1
Density (kg/m^3)	2500	2500	2500	2500	2500	2500	2500	2500
COR	0.7	0.7	0.7	0.7	0.7	0.7	0.7	0.5
Stiffness (N/cm)	5.00E+04	4.00E+04	4.70E+04	5.50E+04	6.00E+04	7.50E+04	9.00E+04	1.00E+07
Stiffness (N/m)	5.00E+06	4.00E+06	4.70E+06	5.50E+06	6.00E+06	7.50E+06	9.00E+06	1.00E+09
Static Friction	0.3	0.3	0.3	0.3	0.3	0.3	0.3	0.3
Kinetic Friction	0.3	0.3	0.3	0.3	0.3	0.3	0.3	0.3
Cohesion	0	0	0	0	0	0	0	0
Rolling Res	0.01	0.01	0.01	0.01	0.01	0.01	0.01	0.001
Critical Time Step	2.49E-03	2.79E-03	2.57E-03	2.38E-03	2.28E-03	2.04E-03	1.86E-03	1.76E-04
G	2.05E+04	1.64E+04	1.93E+04	2.25E+04	2.46E+04	3.07E+04	3.69E+04	4.10E+06
v	0.22	0.22	0.22	0.22	0.22	0.22	0.22	0.22
Rayleigh Time Step	1.25E-02	1.39E-02	1.29E-02	1.19E-02	1.14E-02	1.02E-02	9.29E-03	8.82E-04
Res_Density (kg/m^3)	1712	1733	1724	1716	1709	1703	1692	1620

	TD_Initial18	TD_Initial19	TD_Initial20	TD_Initial21	TD_Initial22	TD_Initial23	TD_Initial24	TD_Initial25
World Setup		Civil	Civil	Civil	Civil	Civil	Civil	Civil
Time Step (s)	3.00E-04	3.00E-04	3.00E-04	3.00E-04	5.00E-04	5.00E-04	6.00E-04	5.00E-04
No. of Particles	300000	300000	300000	300000	300000	300000	300000	300000
Gravity (cm^2/s)	-19.6	-19.6	-19.6	-19.6	-19.6	-19.6	-19.6	-19.6
Launch Velocity (Y)	-600	-600	-200	-100	-80	-80	-60	-100
Res_Height (cm)	34.5	35	34.8		34.96	34.69		34.6
Particle Setup								
Diameter (m)	0.1	0.1	0.1	0.1	0.1	0.1	0.1	0.1
Density (kg/m^3)	2500	2500	2500	2500	2500	2500	2500	2500
COR	0.5	0.8	0.8	0.2	0.2	0.95	0.95	0.95
Stiffness (N/cm)	2.00E+06	2.00E+06	2.00E+06	2.00E+06	1.50E+06	1.00E+06	7.00E+05	1.00E+06
Stiffness (N/m)	2.00E+08	2.00E+08	2.00E+08	2.00E+08	1.50E+08	1.00E+08	7.00E+07	1.00E+08
Static Friction	0.6	0.1	0.8	0.2	0.2	0.2	0.2	0.18
Kinetic Friction	0.6	0.1	0.8	0.2	0.2	0.2	0.2	0.18
Cohesion	0.1	0	0	0	0	0	0	0
Rolling Res	0.001	0.001	0.001	0.001	0.001	0.001	0.001	0.001
Critical Time Step	3.94E-04	3.94E-04	3.94E-04	3.94E-04	4.55E-04	5.58E-04	6.66E-04	5.58E-04
G	8.20E+05	8.20E+05	8.20E+05	8.20E+05	6.15E+05	4.10E+05	2.87E+05	4.10E+05
v	0.22	0.22	0.22	0.22	0.22	0.22	0.22	0.22
Rayleigh Time Step	1.97E-03	1.97E-03	1.97E-03	1.97E-03	2.28E-03	2.79E-03	3.33E-03	2.79E-03
Res_Density (kg/m^3)	1652	1648	1647	1652	1656	1669		1688

APPENDIX B

APPENDIX B.2: CENTRIFUGE “SPIN-UP” LOG

Standard Values	TD_SU01	TD_SU02	TD_SU03	TD_SU04	TD_SU05	TD_SU06	TD_SU07	TD_Initial26
Computer	Civil	Civil	Civil	Civil	Civil	Yugen	Yugen	Civil
GPU_Card	0	0	0	0	0	2	1	0
Sim_Stopped	10mm	10mm	10mm	10mm	10mm	10mm	10mm	10mm
World Setup								
Model	**L-D**	**L-D**	**L-D**	**L-D**	**L-D**	**L-D**	**L-D**	**L-D**
Time Step	1.00E-04	1.00E-04	1.00E-04	1.00E-05	1.00E-06	1.00E-04	4.00E-05	4.00E-05
No. of Particles	300000	300000	300000	300000	300000	300000	300000	300000
Gravity (cm/s)	-980	-980	-980	-980	-980	-980	-980	-980
V_limit	200	200	200	200	200	200	200	200
TD_Velocity	**2**	**2**	**2**	**2**	**2**	**2**	**2**	**2**
Particle Setup								
Diameter (cm)	10	10	10	10	10	10	10	10
Density (kg/m^3)	2500	2500	2500	2500	2500	2500	2500	2500
COR	0.7	0.7	0.7	0.7	0.7	0.95	0.95	0.95
Stiffness (N/cm)	5.50E+06	5.50E+07	5.50E+08	5.50E+08	5.50E+09	1.23E+07	1.23E+08	1.23E+08
Static Friction	0.2	0.2	0.2	0.2	0.2	0.18	0.18	0.18
Kinetic Friction	0.2	0.2	0.2	0.2	0.2	0.18	0.18	0.18
Rolling Res	0.01	0.01	0.01	0.01	0.01	0.001	0.001	0.001
DENSITY								
Initial File	I16_50	I16_50	I16_50	I16_50	I16_50	I16_50	I16_50	TD_I25_71
Initial Density	1692	1692	1692	1692	1692	1692	1692	1688
Density (kg/m^3) Final				1671		1685	1676	1677
Ymax				34.76		34.48	34.65	34.64
Density (kg/m^3) Initial				1691.7		1705.7	1686.9	1687.1
Y (H = 33.1cm)				2155		2155	2155	2155

APPENDIX B

APPENDIX B.3: CALIBRATION AND ANALYSES

	STANDARD	E: kn - Low	E: kn - Lower	kn & COR - Low	E: kn - High	μ: Higher	μs: higher	μk: Higher	TD_Speed: Faster	E: kn - Lower
Standard Values	**TD_C18**	**TD_C19**	**TD_C20**	**TD_C21**	**TD_C22**	**TD_C23**	**TD_C24**	**TD_C25**	**TD_C26**	**TD_C27**
Computer	Yugen	Yugen	Yugen	Yugen	Civil	Yugen	Yugen	Yugen	Yugen	Yugen
GPU_Card	0	1	2	1	0	2	1	2	2	1
Sim_Stopped	10mm	10mm	10mm	10mm	10mm	10mm	10mm	10mm	10mm	10mm
Active	16:50 (13/03/18):20mm	No	No	No	No	No	No	No	No	No
Time Start	00:41 (18/03/18):40mm	13:12(14/03/18)	11:12 (14/03/18)	15:30 (14/03/18)	16:00 (14/03/18)	16:19 (14/03/18)	23:00 (14/03/18)	23:00 (14/03/18)	08:43 (15/03/18)	08:55 (15/03/18)
Time End	15:53 (21/03/18):60mm	15:15(14/03/18)	16:10 (14/03/18)	17:30 (14/03/18)	17:27 (15/03/18)	21:03 (14/03/18)	08:41 (15/03/18)	08:40 (15/03/18)	14:56 (15/03/18)	16:29 (15/03/18)
World Setup	**LD**	**LD**	**LD**	**LD**	**LD**	**LD**	**LD**	**LD**	**LD**	**LD**
Critical Time Step	**1.19E-05**	**7.95E-05**	**2.51E-05**	**7.95E-05**	**7.95E-06**	**2.51E-05**	**1.19E-05**	**1.19E-05**	**1.19E-05**	**1.49E-05**
Time Step	1.00E-05	1.00E-04	4.00E-05	1.00E-04	1.00E-05	4.00E-05	2.00E-05	2.00E-05	2.00E-05	2.60E-05
Time Step (% of critical)	17%	25%	32%	25%	25%	32%	34%	34%	34%	35%
No. of Particles	300000	300000	300000	300000	300000	300000	300000	300000	300000	300000
Gravity (cm^2/s)	-980	-980	-980	-980	-980	-980	-980	-980	-980	-980
V_limit (cm/s)	200	200	200	200	200	200	200	200	200	200
TD_Velocity (cm/s)	**2**	**2**	**2**	**2**	**2**	**2**	**2**	**2**	**3**	**2**
Particle Setup										
Diameter (cm)	10	10	10	10	10	10	10	10	10	10
Density (kg/m^3)	2500	2500	2500	2500	2500	2500	2500	2500	2500	2500
COR	0.9	0.95	0.95	0.85	0.9	0.95	0.9	0.9	0.9	0.9
Stiffness (N/cm) Input	5.50E+08	1.23E+07	1.23E+08	1.23E+07	1.23E+09	1.23E+08	5.50E+08	5.50E+08	5.50E+08	3.50E+08
Stiffness (N/m)	5.50E+10	1.23E+09	1.23E+10	1.23E+09	1.23E+11	1.23E+10	5.50E+10	5.50E+10	5.50E+10	3.50E+10
Static Friction	0.18	0.18	0.18	0.18	0.18	0.3	0.4	0.18	0.18	0.18
Kinetic Friction	0.18	0.18	0.18	0.18	0.18	0.3	0.18	0.4	0.18	0.18
Rolling Res	0.001	0.001	0.001	0.001	0.001	0.001	0.001	0.001	0.001	0.001

	COR: Lower	TD_Speed: Faster	µs, µk: Higher	COR: Lower	TD_Speed: Slower	TimeStep: Greater	TimeStep: Greater	TD_Speed: Faster	E: kn - Lower	COR: Lower
Standard Values	**TD_C28**	**TD_C29**	**TD_C30**	**TD_C31**	**TD_C32**	**TD_C33**	**TD_C34**	**TD_C35**	**TD_C36**	**TD_C37**
Computer	Yugen	Civil	Yugen	Yugen	Yugen	Civil	Yugen	Civil	Yugen	Yugen
GPU_Card	1	0	2	1	2	0	1	0	2	1
Sim_Stopped	10mm	10mm	10mm	10mm	10mm	10mm	10mm	10mm	10mm	10mm
Active	No	No	No	No	No	No	No	No	No	No
Time Start	23:27 (15/03/18)	23:48 (15/03/18)	23:32 (15/03/18)	10:02 (16/03/18)	10:06 (16/03/18)	11:36 (16/03/18)	22:18 (16/03/18)	07:28 (17/03/18)	07:45 (17/03/18)	12:23 (17/03/18)
Time End	09:14 (16/03/18)	11:06 (16/03/18)	09:16 (16/03/18)	20:12 (16/03/18)	06:52 (17/03/18)	01:45 (17/03/18)	11:26 (17/03/18)	01:32 (18/03/18)	15:57 (17/03/18)	09:33 (18/03/18)
World Setup	**LD**	**LD**	**LD**	**LD**	**LD**	**LD**	**LD**	**LD**	**LD**	**LD**
Critical Time Step	**1.19E-05**	**1.19E-05**	**1.19E-05**	**1.19E-05**	**1.19E-05**	**1.19E-05**	**1.19E-05**	**1.19E-05**	**2.54E-05**	**1.19E-05**
Time Step	2.00E-05	2.00E-05	2.00E-05	2.00E-05	2.00E-05	2.00E-05	1.50E-05	1.00E-05	2.40E-05	1.00E-05
Time Step (% of critical)	34%	34%	34%	34%	34%	34%	25%	17%	19%	17%
No. of Particles	300000	300000	300000	300000	300000	300000	300000	300000	300000	300000
Gravity (cm^2/s)	-980	-980	-980	-980	-980	-980	-980	-980	-980	-980
V_limit (cm/s)	200	200	200	200	200	200	200	200	200	200
TD_Velocity (cm/s)	**2**	**2.5**	**2**	**2**	**1**	**2**	**2**	**3**	**2**	**2**
Particle Setup										
Diameter (cm)	10	10	10	10	10	10	10	10	10	10
Density (kg/m^3)	2500	2500	2500	2500	2500	2500	2500	2500	2500	2500
COR	0.6	0.9	0.9	0.75	0.9	0.9	0.9	0.9	0.9	0.7
Stiffness (N/cm) Input	5.50E+08	5.50E+08	5.50E+08	5.50E+08	5.50E+08	5.50E+08	5.50E+08	5.50E+08	1.20E+08	5.50E+08
Stiffness (N/m)	5.50E+10	5.50E+10	5.50E+10	5.50E+10	5.50E+10	5.50E+10	5.50E+10	5.50E+10	1.20E+10	5.50E+10
Static Friction	0.18	0.18	0.4	0.18	0.18	0.18	0.18	0.18	0.18	0.18
Kinetic Friction	0.18	0.18	0.4	0.18	0.18	0.18	0.18	0.18	0.18	0.18
Rolling Res	0.001	0.001	0.001	0.001	0.001	0.001	0.001	0.001	0.001	0.001

	Initial File	TD_Speed: Slower	µk: Higher	E: kn - Lower	COR: Higher	TD_Speed: Slower	TD_Speed & kn	µk: Higher	µs: Higher	µs: Higher
Standard Values	**TD_C38**	**TD_C39**	**TD_C40**	**TD_C41**	**TD_C42**	**TD_C43**	**TD_C44**	**TD_C45**	**TD_C46**	**TD_C47**
Computer	Yugen	Civil	Yugen	Yugen	Yugen	Yugen	Yugen	Civil	Yugen	Civil
GPU_Card	2	0	1	2	1	2	1	0	2	0
Sim_Stopped	10mm	10mm	10mm	10mm	10mm	10mm	10mm	10mm	10mm	10mm
Active	No	No	No	No	No	No	No	No	No	No
Time Start	18:05 (17/03/18)	08:40 (18/03/18)	10:18 (18/03/18)	22:54 (18/03/18)	07:36 (19/03/18)	07:36 (19/03/18)	09:42 (20/03/18)	13:31 (20/03/18)	06:25 (21/03/18)	11:54 (21/03/18)
Time End	15:45 (18/03/18)	07:01 (20/03/18)	03:35 (19/03/18)	05:54 (19/03/18)	01:47 (20/03/18)	23:28 (20/03/18)	00:00 (24/03/18)	11:54 (21/03/18)	03:36 (22/03/18)	10:57 (22/03/18)
World Setup	**LD**	**LD**	**LD**	**LD**	**LD**	**LD**	**LD**	**LD**	**LD**	**LD**
Critical Time Step	**1.19E-05**	**1.19E-05**	**1.19E-05**	**3.12E-05**	**1.19E-05**	**1.19E-05**	**1.52E-05**	**1.19E-05**	**1.19E-05**	**1.19E-05**
Time Step	1.00E-05	1.20E-05	1.20E-05	3.00E-05	1.20E-05	1.20E-05	1.53E-05	1.20E-05	1.20E-05	1.20E-05
Time Step (% of critical)	17%	20%	20%	19%	20%	20%	20%	20%	20%	20%
No. of Particles	300000	300000	300000	300000	300000	300000	300000	300000	300000	300000
Gravity (cm²/s)	-980	-980	-980	-980	-980	-980	-980	-980	-980	-980
V_limit (cm/s)	200	200	200	200	200	200	200	200	200	200
TD_Velocity (cm/s)	**2**	**1**	**2**	**2**	**2**	**1**	**0.5**	**2**	**2**	**2**
Particle Setup										
Diameter (cm)	10	10	10	10	10	10	10	10	10	10
Density (kg/m^3)	2500	2500	2500	2500	2500	2500	2500	2500	2500	2500
COR	0.9	0.9	0.9	0.9	0.96	0.9	0.9	0.9	0.9	0.9
Stiffness (N/cm) Input	5.50E+08	5.50E+08	5.50E+08	8.00E+07	5.50E+08	5.50E+08	3.35E+08	5.50E+08	5.50E+08	5.50E+08
Stiffness (N/m)	5.50E+10	5.50E+10	5.50E+10	8.00E+09	5.50E+10	5.50E+10	3.35E+10	5.50E+10	5.50E+10	5.50E+10
Static Friction	0.18	0.18	0.18	0.18	0.18	0.18	0.18	0.18	0.8	0.4
Kinetic Friction	0.18	0.18	0.4	0.18	0.18	0.18	0.18	0.8	0.18	0.18
Rolling Res	0.001	0.001	0.001	0.001	0.001	0.001	0.001	0.001	0.001	0.001

	μk: Higher	μs: Lower	COR: Lower	Everything	μk: Higher	μs: Lower (Surface)	Everything	μk: Higher	kn: Higher	Everything
Standard Values	**TD_C48**	**TD_C49**	**TD_C50**	**TD_C51**	**TD_C52**	**TD_C53**	**TD_C54**	**TD_C55**	**TD_C56**	**TD_C57**
Computer	Yugen	Yugen	Civil	Yugen	Yugen	Civil	Yugen	Yugen	Yugen	Yugen
GPU_Card	0	2	0	0	2	0	1	2	0	2
Sim_Stopped	10mm	10mm	10mm	10mm	10mm	10mm	10mm	10mm	10mm	20mm
Active	No	No	No	No	No	No	No	No	No	No
Time Start	22:21 (21/03/18)	06:39 (22/03/18)	12:50 (22/03/18)	23:10 (22/03/18)	07:09 (23/03/18)	15:11 (23/03/18)	06:39 (24/03/18)	12:01 (24/03/18)	06:13 (27/03/18	15:14 (26/03/18)
Time End	21:05 (22/03/18)	07:09 (23/03/18)	12:43 (23/03/18)	02:58 (25/03/18)	12:01 (24/03/18)	14:47 (24/03/18)	03:40 (29/03/18)	18:06 (25/03/18)	7:38 07/04/18 @	22:30 (29/03/18)
World Setup	**LD**	**LD**	**LD**	**LD**	**LD**	**LD**	**LD**	**LD**	**LD**	**LD**
Critical Time Step	**1.19E-05**	**1.19E-05**	**1.19E-05**	**1.49E-05**	**1.19E-05**	**1.19E-05**	**1.31E-05**	**1.19E-05**	**3.16E-06**	**1.31E-05**
Time Step	1.20E-05	1.20E-05	1.20E-05	1.45E-05	1.20E-05	1.20E-05	1.35E-05	1.20E-05	3.10E-06	1.35E-05
Time Step (% of critical)	20%	20%	20%	19%	20%	20%	21%	20%	20%	21%
No. of Particles	300000	300000	300000	300000	300000	300000	300000	300000	300000	300000
Gravity (cm^2/s)	-980	-980	-980	-980	-980	-980	-980	-980	-980	-980
V_limit (cm/s)	200	200	200	200	200	200	200	200	200	200
TD_Velocity (cm/s)	**2**	**2**	**2**	**1**	**2**	**2**	**2**	**2**	**2**	**2**
Particle Setup										
Diameter (cm)	10	10	10	10	10	10	10	10	10	10
Density (kg/m^3)	2500	2500	2500	2500	2500	2500	2500	2500	2500	2500
COR	0.9	0.9	0.6	0.96	0.9	0.9	0.7	0.9	0.9	0.94
Stiffness (N/cm) Input	5.50E+08	5.50E+08	5.50E+08	3.50E+08	5.50E+08	5.50E+08	4.50E+08	5.50E+08	7.80E+09	4.50E+08
Stiffness (N/m)	5.50E+10	5.50E+10	5.50E+10	3.50E+10	5.50E+10	5.50E+10	4.50E+10	5.50E+10	7.80E+11	4.50E+10
Static Friction	0.18	0.09	0.18	0.1	0.18	0.18	0.15	0.18	0.18	0.2
Kinetic Friction	0.8	0.18	0.18	0.1	0.4	0.18	0.4	0.09	0.18	0.1
Rolling Res	0.001	0.001	0.001	0.001	0.001	0.001	0.001	0.001	0.001	0.001

	Everything	Everything	Everything	Everything	Everything	Everything	Everything	Everything	Everything	Everything
Standard Values	**TD_C58**	**TD_C59**	**TD_C60**	**TD_C61**	**TD_C62**	**TD_C63**	**TD_C64**	**TD_C65**	**TD_C66**	**TD_C67**
Computer	Civil	Yugen	Civil	Yugen	Yugen	Civil	Civil	Civil	Civil	Civil
GPU_Card	0	2	0	1	0	0	0	0	0	0
Sim_Stopped	10mm	65mm	80mm	40mm	60mm	30mm	10mm	15mm	10mm	10mm
Active	No	No	No	No	No	No	No	No	No	No
Time Start	15:37(26/03/18)	22:37 (29/03/18)	22:41 (29/03/18)	03:43 (30/03/18)	14:48 (07/04/18)	20:45 (16/04/18)	09:07 (20/04/18)	15:00 (21/04/18)	08:15 (23/04/18)	11:09 (24/04/18)
Time End	22:30 (29/03/18)	22:45 (14/04/18)	08:00 (14/04/18)	10:00 (12/04/18)	16:34 (17/04/18)	09:07 (20/04/18)	12:30 (21/04/18)	08:00 (23/04/18)	11:00 (24/04/18)	5:30 (26/04/18)
World Setup	**LD**	**LD**	**LD**	**LD**	**LD**	**LD**	**LD**	**LD**	**LD**	**LD**
Critical Time Step	**1.09E-05**	**1.09E-05**	**9.56E-06**	**8.82E-06**	**1.31E-05**	**1.31E-05**	**1.31E-05**	**1.31E-05**	**1.31E-05**	**1.31E-05**
Time Step	1.10E-05	1.10E-05	9.50E-06	8.80E-06	1.35E-05	1.35E-05	1.35E-05	1.35E-05	1.35E-05	1.35E-05
Time Step (% of critical)	20%	20%	20%	20%	21%	21%	21%	21%	21%	21%
No. of Particles	300000	300000	300000	300000	300000	300000	300000	300000	300000	300000
Gravity (cm^2/s)	-980	-980	-980	-980	-980	-980	-980	-980	-980	-980
V_limit (cm/s)	200	200	200	200	200	200	200	200	200	200
TD_Velocity (cm/s)	**2**	**2**	**2**	**2**	**2**	**2**	**2**	**2**	**2**	**2**
Particle Setup										
Diameter (cm)	10	10	10	10	10	10	10	10	10	10
Density (kg/m^3)	2500	2500	2500	2500	2500	2500	2500	2500	2500	2500
COR	0.8	0.9	0.92	0.92	0.92	0.9	0.96	0.94	0.92	0.92
Stiffness (N/cm) Input	6.50E+08	6.50E+08	8.50E+08	1.00E+09	4.50E+08	4.50E+08	4.50E+08	4.50E+08	4.50E+08	4.50E+08
Stiffness (N/m)	6.50E+10	6.50E+10	8.50E+10	1.00E+11	4.50E+10	4.50E+10	4.50E+10	4.50E+10	4.50E+10	4.50E+10
Static Friction	0.1	0.1	0.1	0.1	0.15	0.18	0.18	0.25	0.1	0.12
Kinetic Friction	0.1	0.05	0.1	0.1	0.12	0.15	0.15	0.05	0.18	0.15
Rolling Res	0.001	0.001	0.001	0.001	0.001	0.001	0.001	0.001	0.001	0.001

	Everything	Everything	Everything	Everything	Everything	**CALIBRATED**	Unit_Check	Everything	Everything	Everything
Standard Values	**TD_C68**	**TD_C69**	**TD_C70**	**TD_C71**	**TD_C72**	**TD_C72_full**	**TD_C62_Units**	**TD_C73**	**TD_C73A**	**TD_C74**
Computer	Civil	Civil	Civil	Civil	Civil	Civil	Yugen	Yugen	Yugen	Yugen
GPU_Card	0	0	0	0	0	0	2	2	2	2
Sim_Stopped	10mm	10mm	10mm	10mm	10mm	80mm	10mm	10mm	10mm	10mm
Active	No	No	No	No	No	No	No	No	No	No
Time Start	6:15 (26/04/18)	9:50 (27/04/18)	14:50 (28/04/18)	18:10 (29/04/18)	13:20 (09/05/18)	10:00 (11/05/18)	13:20 (09/05/18)	21:00 (09/05/18)	06:05 (10/05/18)	13:40 (09/05/18)
Time End	9:50 (27/04/18)	14:50 (28/04/18)	18:10 (29/04/18)		10:00 (11/05/18)	05:51 (20/05/18)	Unstable - Units	02:06 (10/05/18)	13:00 (10/05/18)	15:00 (14/05/18)
World Setup	**LD**	**LD**	**LD**	**LD**	**LD**	**LD**	**LD**	**LD**	**LD**	**LD**
Critical Time Step	**1.31E-05**	**1.49E-05**	**1.31E-05**	**1.31E-05**	**1.31E-05**	**1.31E-05**	**1.31E-05**	**3.16E-05**	**3.16E-05**	**1.31E-05**
Time Step	1.35E-05	1.49E-05	1.35E-05	1.35E-05	1.35E-05	1.30E-05	1.35E-05	3.00E-05	2.30E-05	1.30E-05
Time Step (% of critical)	21%	20%	21%	21%	21%	20%	21%	19%	15%	20%
No. of Particles	300000	300000	300000	300000	300000	300000	300000	300000	300000	300000
Gravity (cm^2/s)	-980	-980	-980	-980	-980	-980	-980	-980	-980	-980
V_limit (cm/s)	200	200	200	200	200	200	200	200	200	200
TD_Velocity (cm/s)	**2**	**2**	**2**	**2**	**2**	**2**	**2**	**2**	**2**	**2**
Particle Setup										
Diameter (cm)	10	10	10	10	10	10	10	10	10	10
Density (kg/m^3)	2500	2500	2500	2500	2500	2500	0.0025	2500	2500	2500
COR	0.92	0.92	0.7	0.96	0.9	0.9	0.92	0.9	0.9	0.9
Stiffness (N/cm) Input	4.50E+08	3.50E+08	4.50E+08	4.50E+08	4.50E+08	4.50E+08	4.50E+08	7.80E+07	7.80E+07	4.50E+08
Stiffness (N/m)	4.50E+10	3.50E+10	4.50E+10	4.50E+10	4.50E+10	4.50E+10	4.50E+10	7.80E+09	7.80E+09	4.50E+10
Static Friction	0.18	0.18	0.18	0.18	0.18	0.18	0.15	0.18	0.18	0.2
Kinetic Friction	0.1	0.1	0.1	0.1	0.18	0.18	0.12	0.18	0.18	0.2
Rolling Res	0.001	0.001	0.001	0.001	0.001	0.001	0.001	0.001	0.001	0.001

	Lower StiffnessV1	Lower StiffnessV2	Lower StiffnessV3	Lower StiffnessV4	Lower StiffnessV5
Standard Values	**TD_C75_full**	**TD_C76_full**	**TD_C77_full**	**TD_C78_full**	**TD_C79_full**
Computer	Yugen	Yugen	Yugen	Yugen	Yugen
GPU_Card	0	1	1	0	2
Sim_Stopped	80mm	80mm	80mm	80mm	80mm
Active	No	No	No	No	No
Time Start	17:52 (14/05/18)	19:00 (14/05/18)	09:18 (16/05/18)	08:48 (17/05/18)	07:59 (18/05/18)
Time End	11:14 (16/05/18)	23:46 14/05/18)	13:47 (16/05/18)	23:20 (17/05/18)	11:00 (19/05/18)
World Setup	**LD**	**LD**	**LD**	**LD**	**LD**
Critical Time Step	**3.16E-05**	**3.16E-04**	**9.98E-04**	**9.98E-05**	**9.98E-05**
Time Step	3.10E-05	3.10E-04	9.00E-04	9.00E-05	5.00E-05
Time Step (% of critical)	20%	20%	18%	18%	10%
No. of Particles	300000	300000	300000	300000	300000
Gravity (cm^2/s)	-980	-980	-980	-980	-980
V_limit (cm/s)	200	200	200	200	200
TD_Velocity (cm/s)	**2**	**2**	**2**	**2**	**2**
Particle Setup					
Diameter (cm)	10	10	10	10	10
Density (kg/m^3)	2500	2500	2500	2500	2500
COR	0.9	0.9	0.9	0.9	0.9
Stiffness (N/cm) Input	7.80E+07	7.80E+05	7.80E+04	7.80E+06	7.80E+06
Stiffness (N/m)	7.80E+09	7.80E+07	7.80E+06	7.80E+08	7.80E+08
Static Friction	0.18	0.18	0.18	0.18	0.18
Kinetic Friction	0.18	0.18	0.18	0.18	0.18
Rolling Res	0.001	0.001	0.001	0.001	0.001

	Rolling_Friction_S1	Rolling_Friction_S2	Rolling_Friction_S3	Rolling_Friction_S4	TIME STEP
Standard Values	**TD_RF1**	**TD_RF2**	**TD_RF3**	**TD_RF4**	**TD_C72_TS**
Computer	Yugen	Yugen	Civil	Yugen	Yugen
GPU_Card	1	0	0	2	2
Sim_Stopped	80mm	80mm	80mm	80mm	80mm
Active	No	No	No	No	Half
Time Start	08:55 (17/05/18)	05:55 (18/05/18)	07:55 (21/05/18)	07:55 (28/03/18)	08:56 (21/05/18)
Time End	13:23 (25/05/18)	17:00 (25/05/18)	02:10 (31/05/18)	11:58 (09/06/2018)	175
World Setup	**LD**	**LD**	**LD**	**LD**	**LD**
Critical Time Step	**1.31E-05**	**1.31E-05**	**1.31E-05**	**1.31E-05**	**1.31E-05**
Time Step	1.30E-05	1.30E-05	1.30E-05	1.30E-05	6.50E-06
Time Step (% of critical)	20%	20%	20%	20%	10%
No. of Particles	300000	300000	300000	300000	300000
Gravity (cm^2/s)	-980	-980	-980	-980	-980
V_limit (cm/s)	200	200	200	200	200
TD_Velocity (cm/s)	**2**	**2**	**2**	**2**	**2**
Particle Setup					
Diameter (cm)	10	10	10	10	10
Density (kg/m^3)	2500	2500	2500	2500	2500
COR	0.9	0.9	0.9	0.9	0.9
Stiffness (N/cm) Input	4.50E+08	4.50E+08	4.50E+08	4.50E+08	4.50E+08
Stiffness (N/m)	4.50E+10	4.50E+10	4.50E+10	4.50E+10	4.50E+10
Static Friction	0.2	0.5	0.5	0.5	0.18
Kinetic Friction	0.2	0.5	0.5	0.5	0.18
Rolling Res	0.2	0.2	0.4	0.3	0.001

APPENDIX C

PYTHON SCRIPTS FOR DEM ANALYSES

```
###        --- Table of contents ---          ###
#   1: DEM_to_array.py                  Line   8
#   2: Contour_Lines10.py               Line  89
#   3: Create_Strain_Vector.py          Line 183
#   4: Max_Log_ShearStrain_GeoPIV.py    Line 461
###-----------------------------------------###

############################
# File 1: DEM_to_array.py #
############################

### This script converts the DEM output into a 2D array with 4 columns: Particle_ID, X, Y, Z Coordinates ###


Filename = input("what is the filename?")
#Filename = 'SS06'

def output_to_csv(Filename):

  FileExt = '/home/civilworkstation/Desktop/PythonPractice/%s' %Filename
  #FileExt = raw_input("what is the file extension?")
  #file = "/home/civilworkstation/Desktop/PythonPractice/SS06"
  infile = open(FileExt, 'r')
  #f = open(fname,'r')
  numbersfile = infile.readlines()[1:]


  mylist1 = []

  for line in numbersfile:
    fields = line.split("  ")
    mylist1.append(fields)

  mylist = []

  for item in mylist1:
    if item[0].isdigit():
      mylist.append(item)

  for sphere in mylist:
    sphere[4] = sphere[4].replace(" ", ", ")
    #print(sphere[4])


  ###Create a for loop that separates the Pos_COM into individual values

  Pos_COM = []

  for item in mylist:
    PC = item[4].split(",")
    #print(item[4])
    Pos_COM.append(PC)

  ##Work in arrays
  import numpy as np

  a = np.array(mylist)
  b = np.array(Pos_COM)

  #print(a)

  #This creates an array without the Pos_COM and the SPACES
  C = np.delete(a,
  np.s_[[1],[2],[3],[4],[5],[6],[7],[8],[9],[10],[11],[12],[13],[14],[15],[16]], 1)
  #print(C)
  #Adds Pos_COM array to C
```

```
    final = np.insert(C, [1], b, axis=1)

    #print(final)

    import numpy as np

    #makes all the values floats
    Y = final.astype(np.float)


    import numpy as np

    X = Y[np.argsort(Y[:,0])]
    print(X)

    np.savetxt('"%s".gz' %Filename, X)   # X is an array

    infile.close()

output_to_csv("%s" %Filename)



##############################
# File 2: Contour_Lines10.py #
##############################

File1 = raw_input('What is the name of the first file?')
File2 = raw_input('What is the name of the second file?')

#File1 = 'TD_SU04_Initial'
#File2 = 'TD_C18_10mm_SU04'

import gzip
import numpy as np
import math

#COM_initial is the initial COM and COM_final is the final (Format: ID,X,Y,Z)

COM_initial = np.loadtxt('"%s".gz' %File1)
COM_final = np.loadtxt('"%s".gz' %File2)
Displacement_Vector = np.subtract(COM_final, COM_initial)

#Create new Particle ID column
mylist = []

for i in range(0,len(COM_initial)):
    list = i
    mylist.append(list)

numbers = np.array(mylist)
Disp_Vector = np.delete(Displacement_Vector, np.s_[[0]], 1)

#Final3 is the displacement vector matrix (ID,X,Y,Z,U,V,W)
Final = np.insert(Disp_Vector, 0, numbers, axis=1)
Final2 = np.insert(Final, [1], COM_initial, axis=1)
Final3 = np.delete(Final2, np.s_[[1]],1)

F = Final3[Final3[:,3]>=85.0, :]

#print(F)
#print(Final3)

x = F[:,1]
y = F[:,2]
Z = F[:,3]
u = F[:,4]
```

```
v = F[:,5]
w = F[:,6]



#Create Resultant Displacement Vector
z = ((u**2)+(v**2))**(0.5)
z = np.array(z)
z[:, np.newaxis]

import numpy as np
from scipy.interpolate import griddata
import matplotlib.pyplot as plt
import numpy.ma as ma
from numpy.random import uniform, seed
from scipy.spatial import ConvexHull
import matplotlib.colors


# Rehaping and translating data
x=np.ravel(np.array(x))
y=np.ravel(np.array(y))
z_c=np.ravel(np.array(z))
x_c = x
y_c = y


# Mapping the irregular data onto a regular grid and plotting
xic = np.linspace(min(x_c), max(x_c), 1000)
yic = np.linspace(min(y_c), max(y_c), 1000)
zic = griddata((x_c, y_c), z_c, (xic[None,:], yic[:,None]))

fig, ax = plt.subplots()


levels = np.arange(0,55,5.5)
CS = plt.contour(xic,yic,zic,levels=levels,linewidths=1.0,cmap=plt.cm.jet)
#CS = plt.contourf(xic,yic,zic,9,cmap=plt.cm.rainbow)
plt.axis('equal')

#Code below adds a full colour bar to a line-only contour plot
norm= matplotlib.colors.Normalize(vmin=CS.vmin, vmax=CS.vmax)
sm = plt.cm.ScalarMappable(norm=norm, cmap = CS.cmap)
sm.set_array([])
fig.colorbar(sm, ticks=CS.levels)

plt.show()



###################################
# File 3: Create_Strain_Vector.py #
###################################

### Delaunay and Constant Strain Triangle Practice Script for Shear Strain Contours ###


#File1 = input('What is the name of the first file?')
File1 = 'TD_I26_75.gz'
File2 = input('What is the name of the second file?')

Filename1 = '%s_Strains' %File2
Filename2 = '%s_Nat_Strains' %File2

#File1 = 'TD_C18_50mm_SU04'
#File2 = 'TD_C18_60mm_SU04'

```

```
#File1 = 'TD_I26_75'
#File2 = 'TD_C54_10mm_I26'

import gzip
import numpy as np

#COM_initial is the initial COM and COM_final is the final (Format: ID,X,Y,Z)

COM_initial = np.loadtxt('%s' %File1)
COM_final = np.loadtxt('%s' %File2)
Displacement_Vector = np.subtract(COM_final, COM_initial)
#print COM_initial
#print COM_final

#Create new Particle ID column
mylist = []

for i in range(0,len(COM_initial)):
  list = i
  mylist.append(list)

numbers = np.array(mylist)
Disp_Vector = np.delete(Displacement_Vector, np.s_[[0]], 1)

#Final3 is the displacement vector matrix (ID,X,Y,Z,U,V,W)
Final = np.insert(Disp_Vector, 0, numbers, axis=1)
Final2 = np.insert(Final, [1], COM_initial, axis=1)
Final3 = np.delete(Final2, np.s_[[1]],1)
#print Final3

#F array format (ID,X,Y,U,V) - slice touching glass

F = Final3[Final3[:,3]>=85.0, :]
F = F[F[:,1]>=850, :]
F = F[F[:,1]<=2270, :]
F = F[F[:,2]<=2250, :]
F = F[F[:,2]>=450, :]
F = np.delete(F, np.s_[[3,6]],1)
#print(F)

XY = np.delete(F, np.s_[[0,3,4]],1)

#print XY

from scipy.spatial import Delaunay
tri = Delaunay(XY)

import matplotlib.pyplot as plt
#plt.triplot(XY[:,0], XY[:,1], tri.simplices.copy())
#plt.plot(XY[:,0], XY[:,1], 'o')
#plt.show()

#print len(tri.simplices)

TriCoord = XY[tri.simplices]
#print TriCoord


## Append node displacement from imported vector to the triangulated data ##

B = []

from itertools import product
for triangles, x in product(TriCoord, F):
  for Coord in triangles:
    if Coord[0] == x[1] and Coord[1] == x[2]:
      Coord = np.append(Coord,x[3:])
```

```
        B.append(Coord)
        break

#print B
TwoD = np.atleast_2d(B)
Full = TwoD.reshape(len(tri.simplices),3,4)
#print Full


## CONSTANT STRAIN TRIANGLE ##

DGM = []

for i in Full:
  x13 = i[0,0] - i[2,0]
  y12 = i[0,1] - i[1,1]
  y13 = i[0,1] - i[2,1]
  x21 = i[1,0] - i[0,0]
  x23 = i[1,0] - i[2,0]
  y23 = i[1,1] - i[2,1]
  x32 = i[2,0] - i[1,0]
  y31 = i[2,1] - i[0,1]

  detJ = (x13*y23)-(x23*y13)
  inv_detJ = float(1.0/detJ)
  #print inv_detJ


  u1 = i[0,2]
  v1 = i[0,3]
  u2 = i[1,2]
  v2 = i[1,3]
  u3 = i[2,2]
  v3 = i[2,3]

  q = np.zeros((6,1))

  q[0] = u1
  q[1] = v1
  q[2] = u2
  q[3] = v2
  q[4] = u3
  q[5] = v3

  B = np.zeros((2,2))

  B[0,0] = ((y23*u1)+(y31*u2)+(y12*u3))
  B[0,1] = ((x32*u1)+(x13*u2)+(x21*u3))
  B[1,0] = ((y23*v1)+(y31*v2)+(y12*v3))
  B[1,1] = ((x32*v1)+(x13*v2)+(x21*v3))

  B = np.multiply(B,inv_detJ)
  DGM.append(B)

#print DGM

I = np.identity(2)

#print I

FM = []

for L in DGM:
  J = L + I
  FM.append(J)

#print FM
```

```
334
335
336   from scipy.linalg import fractional_matrix_power
337
338   UM = []
339
340   for F in FM:
341     FT = np.transpose(F)
342     #print FT
343     UMI = np.dot(FT,F)
344     #print UMI
345     U = fractional_matrix_power(UMI,0.5)
346     #print U
347     UM.append(U)
348
349   #print UM
350
351   EBiot = []
352
353   for U in UM:
354     E = U - I
355     EBiot.append(E)
356
357   #print EBiot
358   from numpy import linalg as LA
359
360   PS = []
361
362   for E in EBiot:
363     w, v = LA.eig(np.array(E))
364     Eeng = np.zeros((1,2))
365     Eeng[0,1] = max(w)
366     Eeng[0,0] = min(w)
367     PS.append(Eeng)
368
369    ## Vector with [EengII EengI]
370
371   PS = np.reshape(PS,(len(tri.simplices),2))
372   #print PS
373
374   import math
375
376   E1 = np.add(PS,1)
377
378   ElogPS = np.log(E1)
379
380   #print ElogPS
381
382   ElogPS = np.nan_to_num(ElogPS)
383
384   #print ElogPS
385
386   ## ElogPS = Vector with [ElogII ElogI]
387   ## SSlogMax = ElogI - ElogII
388
389   SSlogMax = np.diff(ElogPS)
390
391   #print SSlogMax
392
393   SSLM = np.reshape(SSlogMax, (len(tri.simplices),1))
394   #print SSLM
395
396   LogStrains = []
397
398   for E in UM:
399     Elogxx = E[0,0]
400     Elogyy = E[1,1]
```

```
    A = np.zeros((1,2))
    A[0,0] = np.log(Elogxx)
    A[0,1] = np.log(Elogyy)
    LogStrains.append(A)

LogStrains = np.reshape(LogStrains, (len(tri.simplices),2))

#print LogStrains
## LogStrains = Vector with [Elogxx Elogyy]

### Remaining strains and Coordinates

Strains = []

for E in EBiot:
    Exx = E[0,0]
    Eyy = E[1,1]
    SSxy = E[0,1] + E[1,0]
    A = np.zeros((1,3))
    A[0,0] = Exx
    A[0,1] = Eyy
    A[0,2] = SSxy
    Strains.append(A)

#print Strains ## Array with format, IF: [Exx, Eyy, SSxy]


IF = np.reshape(Strains, (len(tri.simplices),3))
#print IF

#print TriCoord

Centroid = np.mean(TriCoord, axis=1)
#print Centroid

### STRAINS: Create array with indices corresponding to: [X, Y, Exx, Eyy, SSxy, EengII,
EengI, SSlogMax] ##

SC = np.insert(Centroid ,[2], IF, axis=1)
SC = np.append(SC,PS,axis=1)
STRAINS = np.append(SC,SSLM,axis=1)

## NAT_STRAINS: Create array with indices corresponding to: [X, Y, Elogxx, Elogyy,
ElogEngII, ElogEngI, SSlogMax] ##

NAT_STRAINS = np.delete(STRAINS, np.s_[[2],[3],[4],[5],[6]], 1)
NAT_STRAINS = np.insert(NAT_STRAINS, [2], LogStrains, axis=1)
NAT_STRAINS = np.insert(NAT_STRAINS, [4], ElogPS, axis=1)

#print NAT_STRAINS
#print STRAINS

#x = STRAINS[:,0]
#y = STRAINS[:,1]
#z = STRAINS[:,7]


np.savetxt('%s.gz' %Filename1, STRAINS)
np.savetxt('%s.gz' %Filename2, NAT_STRAINS)



########################################
# File 4: Max_Log_ShearStrain_GeoPIV.py #
########################################

### Delaunay and Constant Strain Triangle Practice Script for Shear Strain Contours ###
```

```
466
467
468   File1 = input('What is the name of the file?')
469   #File2 = raw_input('What is the name of the second file?')
470
471   #File1 = 'Strains'
472   #File2 = 'TD_P6_10mm'
473
474   import gzip
475   import numpy as np
476   import math
477
478   #Nat_Strains = np.loadtxt('%s.gz' %File1)
479   Nat_Strains = np.loadtxt('%s' %File1)
480
481   x = Nat_Strains[:,0]
482   y = Nat_Strains[:,1]
483   z = Nat_Strains[:,6]
484
485   ## Contour Plotting ##
486
487   import numpy as np
488   from scipy.interpolate import griddata
489   import matplotlib.pyplot as plt
490   import numpy.ma as ma
491   from numpy.random import uniform, seed
492   from scipy.spatial import ConvexHull
493
494   # Loading data
495
496   # Rehaping and translating data
497   x=np.ravel(np.array(x))
498   y=np.ravel(np.array(y))
499   z_c=np.ravel(np.array(z))
500   x_c = x
501   y_c = y
502
503   v = np.linspace(0, 2, 50, endpoint=True)
504
505   # Mapping the irregular data onto a regular grid and plotting
506   xic = np.linspace(min(x_c), max(x_c), 500)
507   yic = np.linspace(min(y_c), max(y_c), 500)
508   zic = griddata((x_c, y_c), z_c, (xic[None,:], yic[:,None]))
509   CS = plt.contour(xic,yic,zic,v,linewidths=0,colors='k')
510   CS = plt.contourf(xic,yic,zic,v,cmap=plt.cm.jet,extend='both')
511
512
513   plt.colorbar()#ticks=v) # draw colorbar
514   plt.savefig("'%s'.png" %File1, dpi=500)
515   #DPI controls the save, higher value, higher resolution
516   #plt.scatter(x_c, y_c, marker='o', s=5, zorder=10)
517   plt.axis('equal')
518   #plt.savefig('foo.pdf', bbox_inches='tight')
519   plt.show()
```

APPENDIX D

CALIBRATION: DISPLACEMENT TRAJECTORY RESULTS

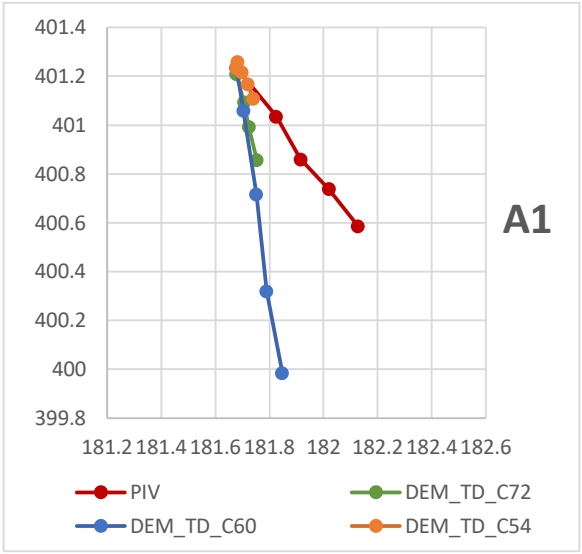

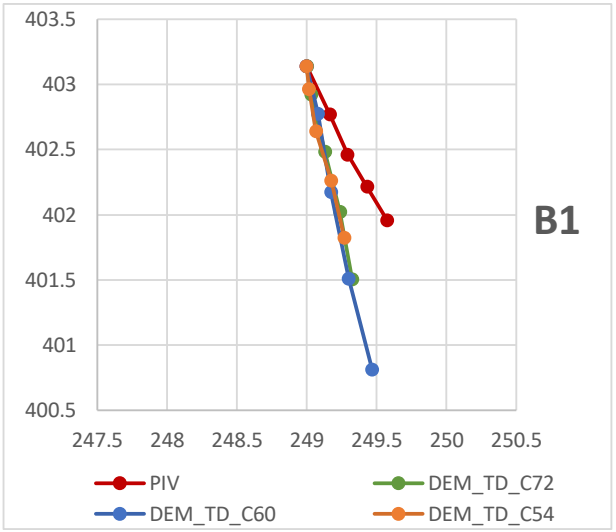

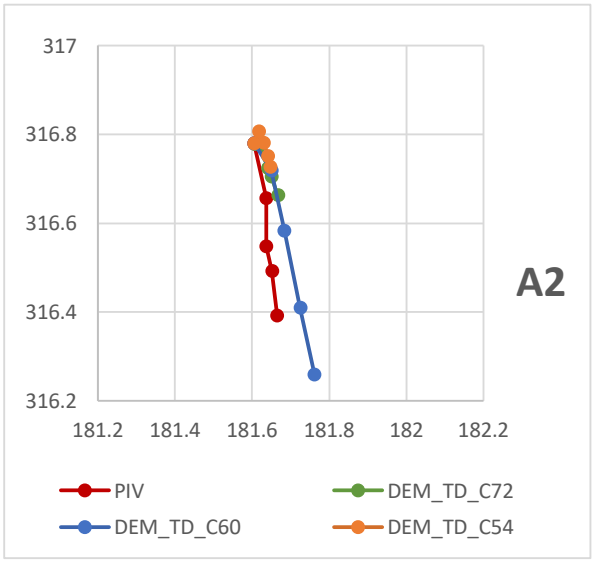

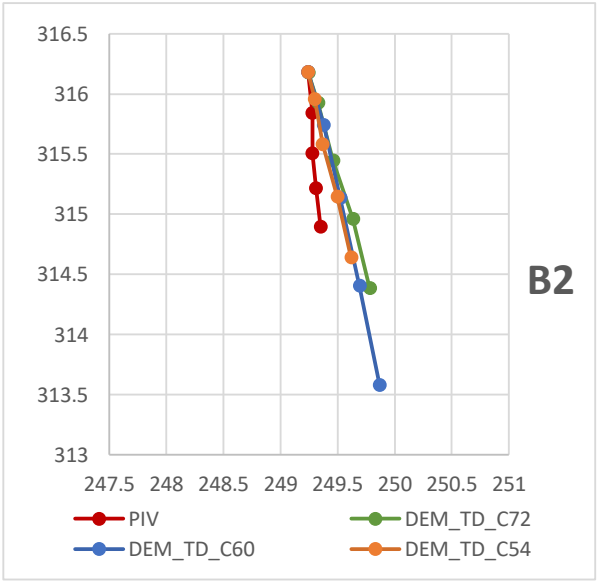

Appendix D: Page 1

All subset/particle displacements measured in millimetres (mm)

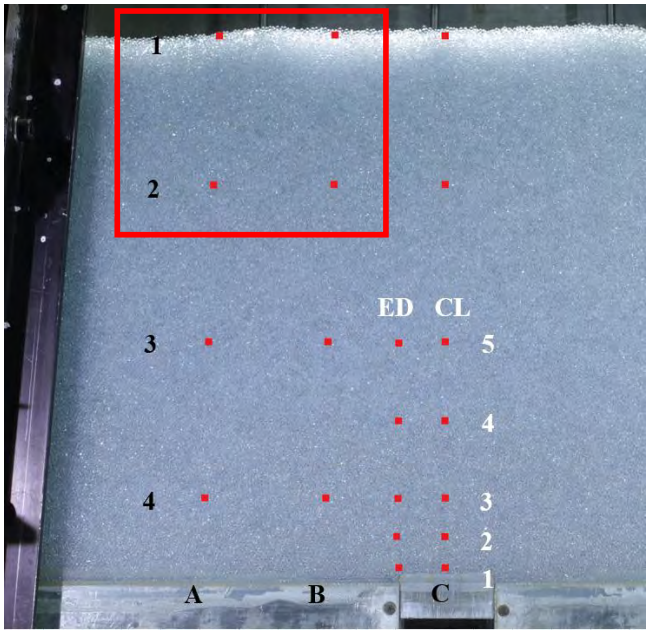

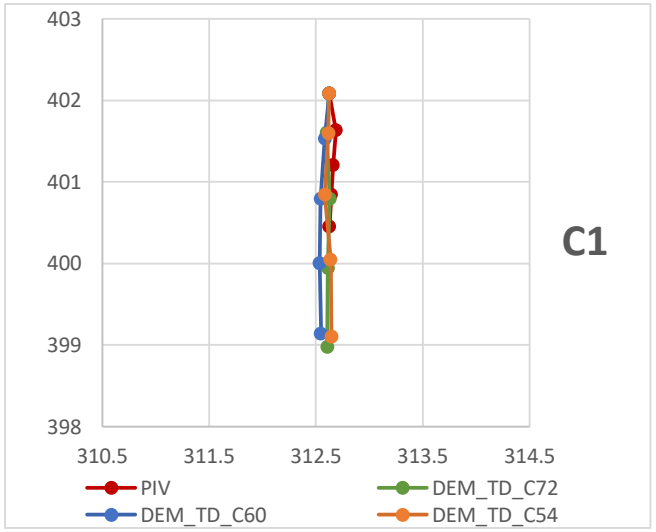

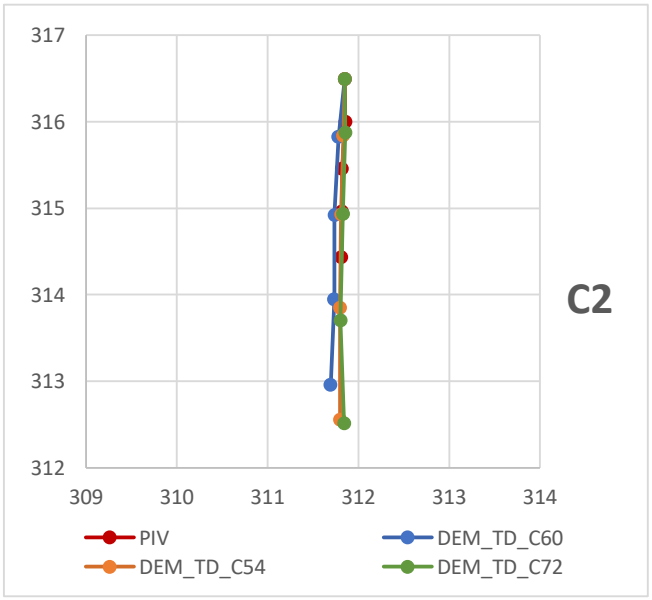

Appendix D: Page 2

All subset/particle displacements measured in millimetres (mm)

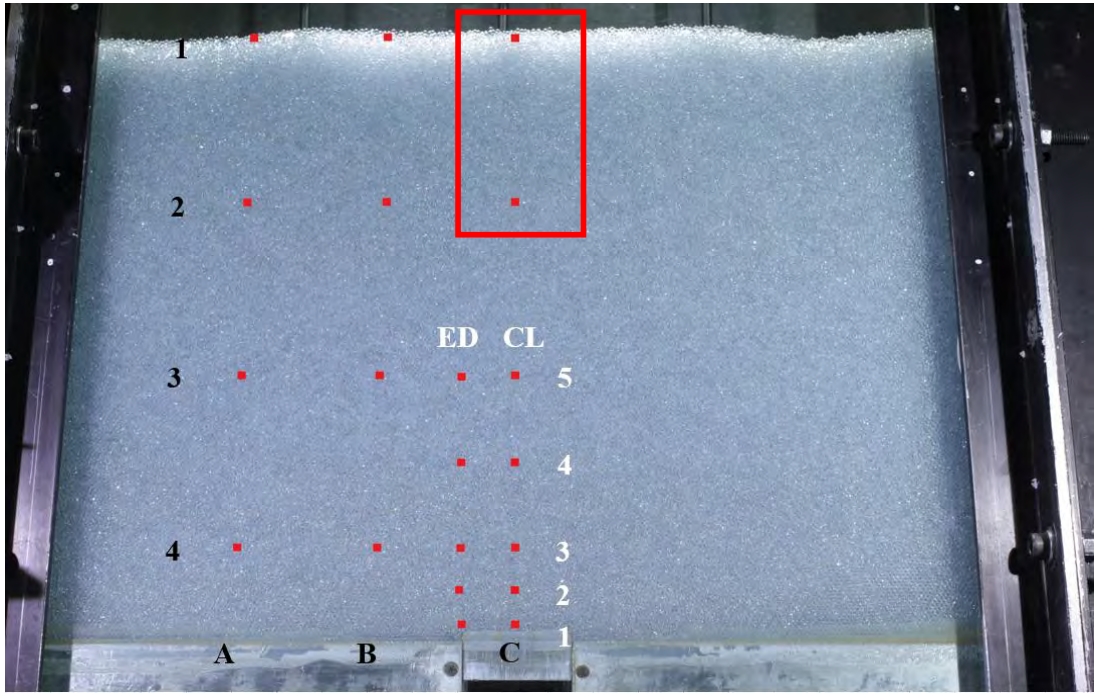

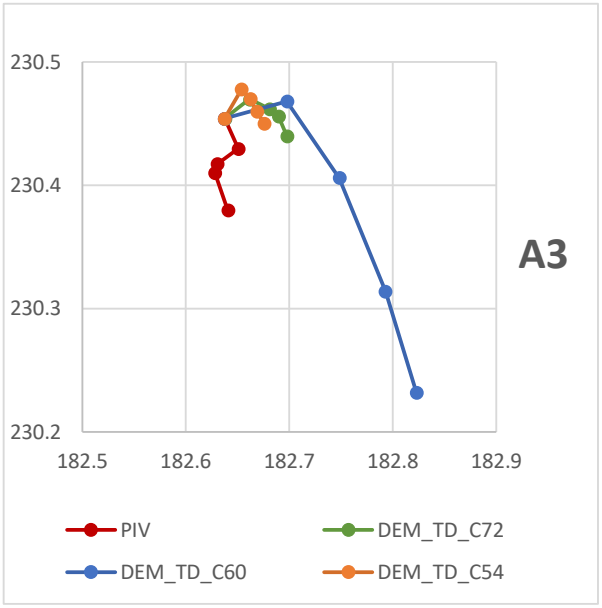

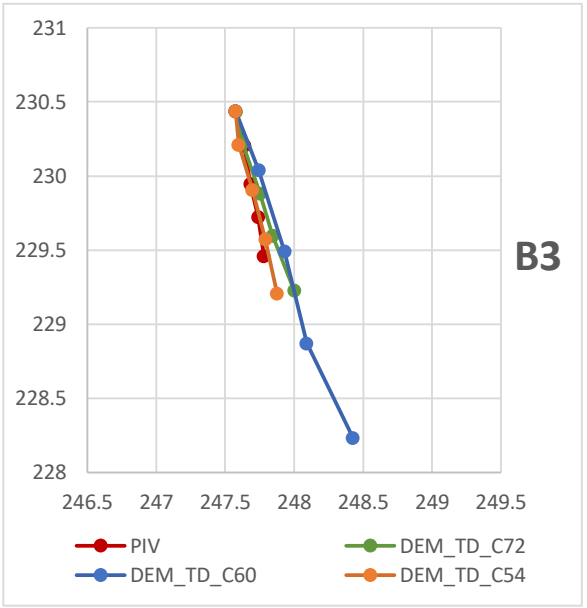

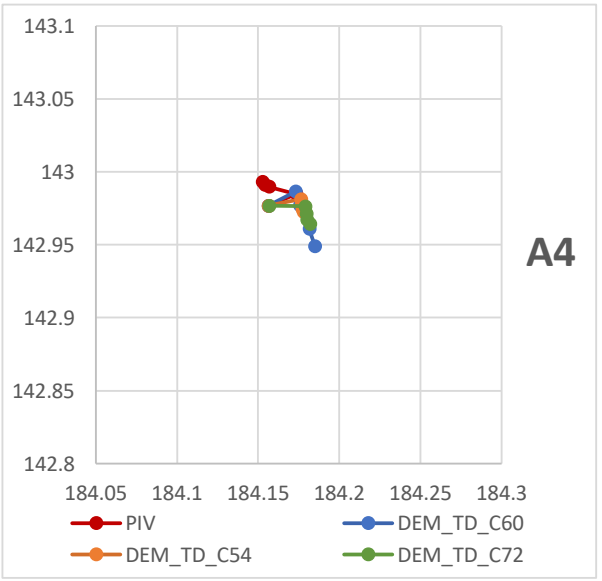

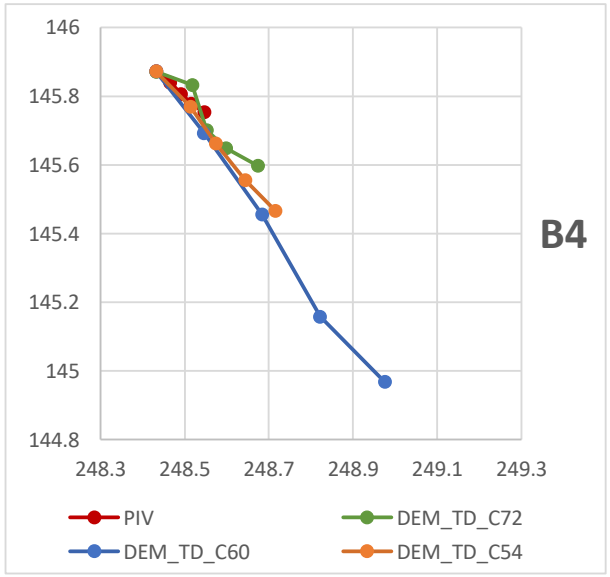

Appendix D: Page 3

All subset/particle displacements measured in millimetres (mm)

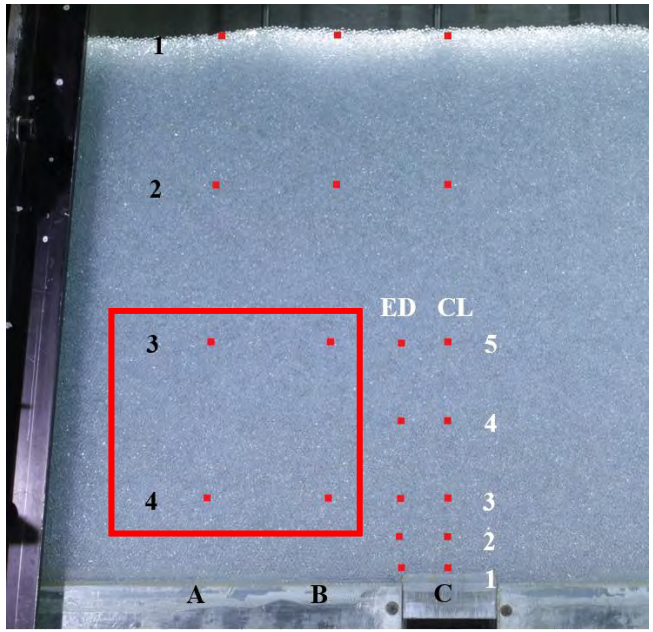

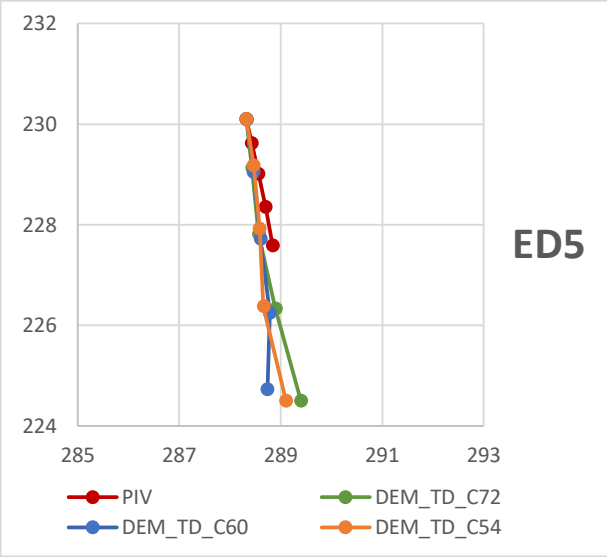

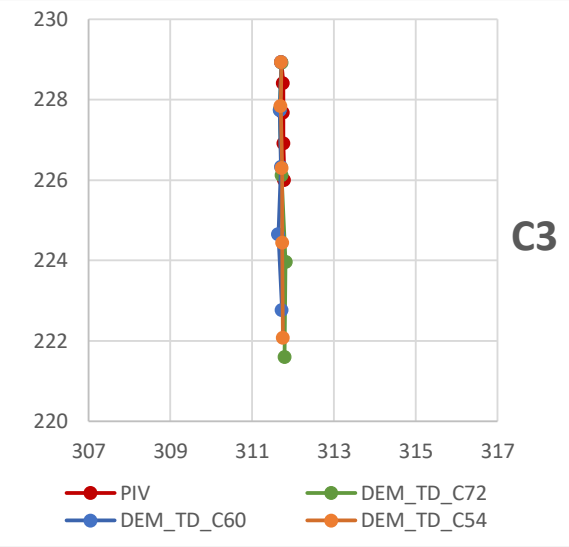

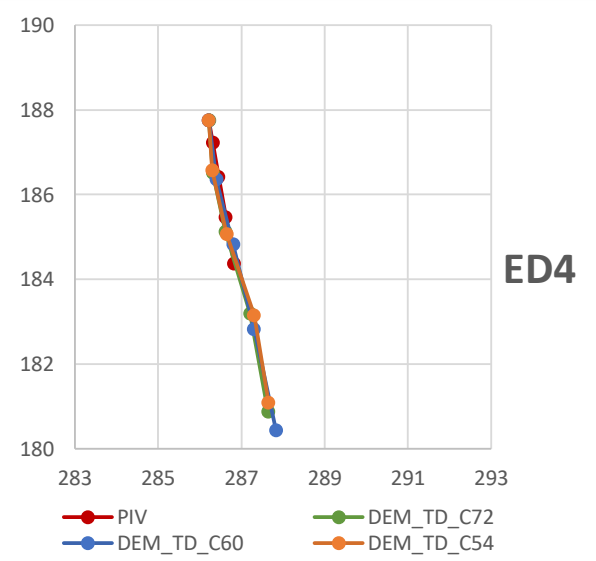

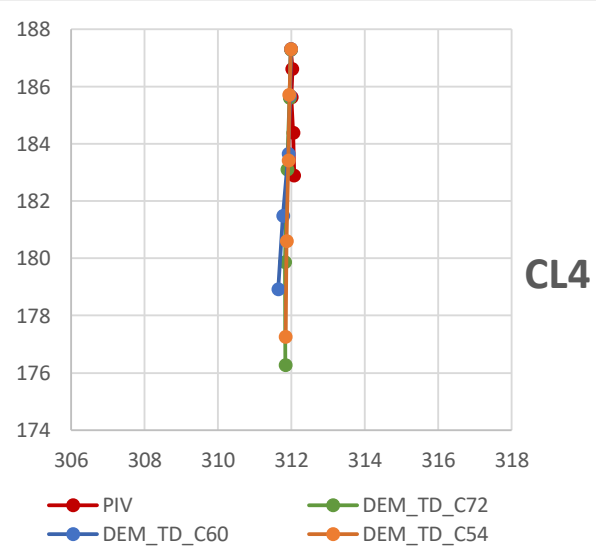

Appendix D: Page 4

All subset/particle displacements measured in millimetres (mm)

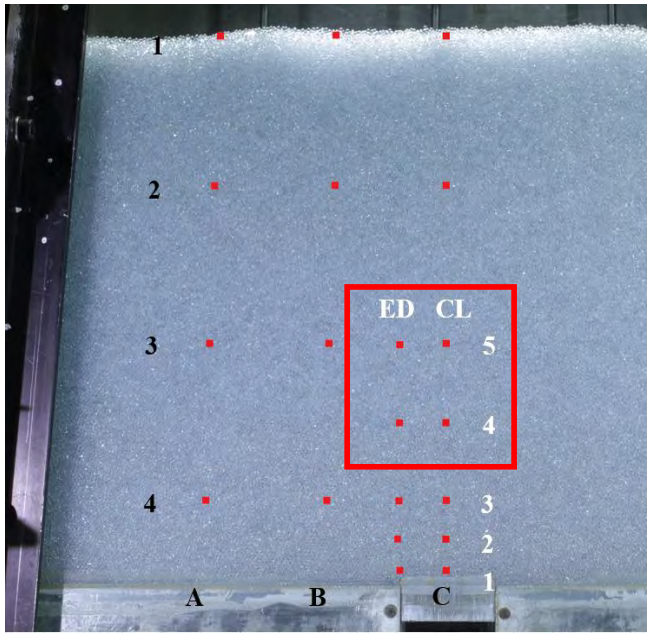

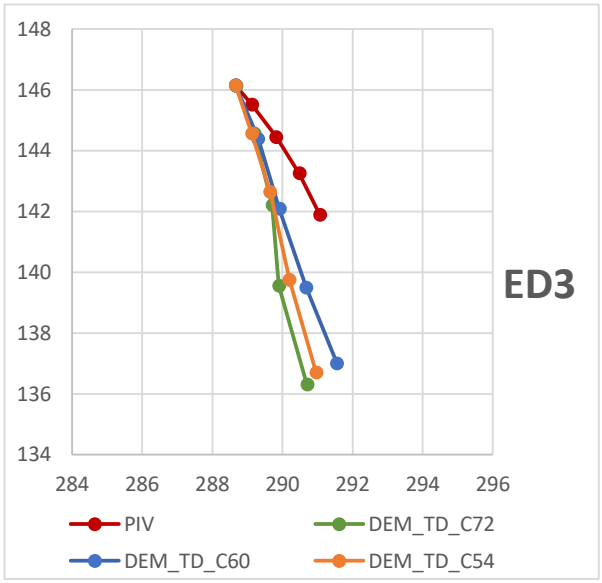

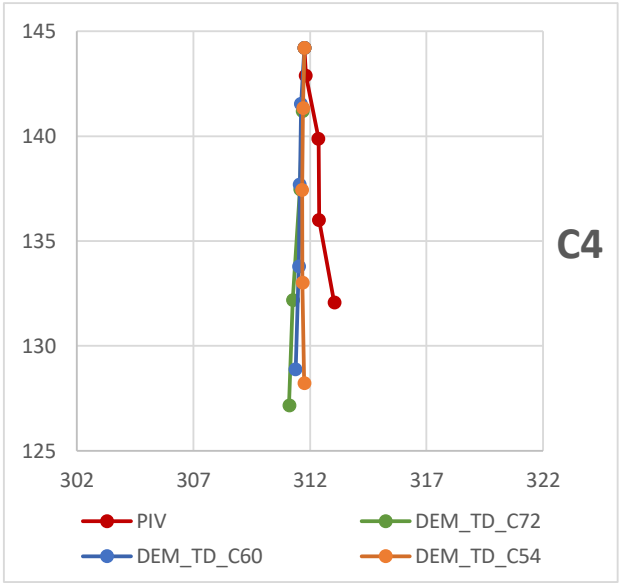

Appendix D: Page 5

All subset/particle displacements measured in millimetres (mm)

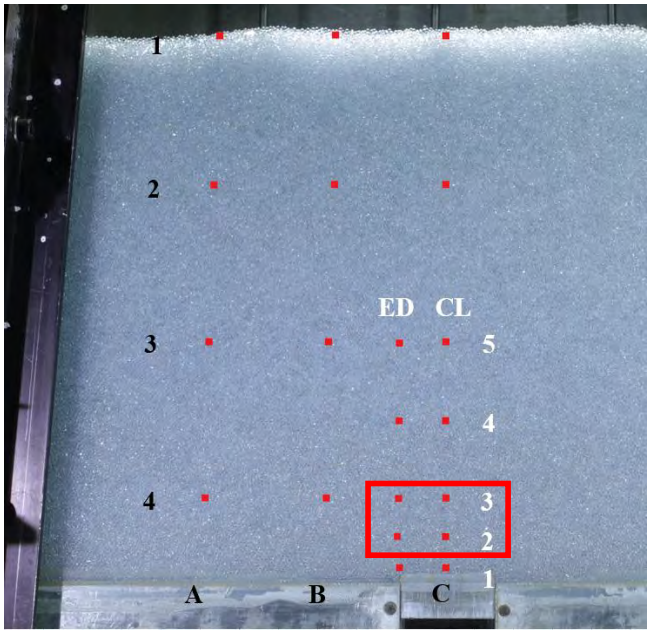

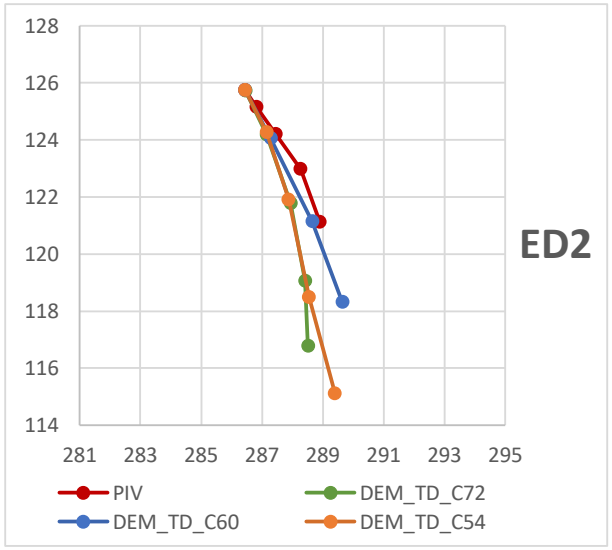

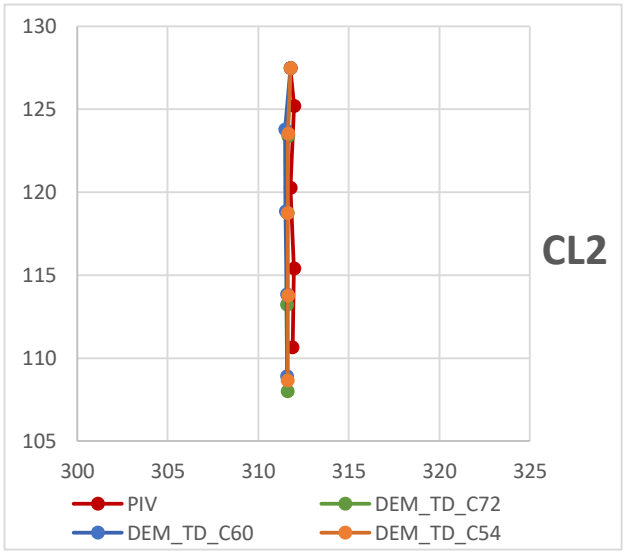

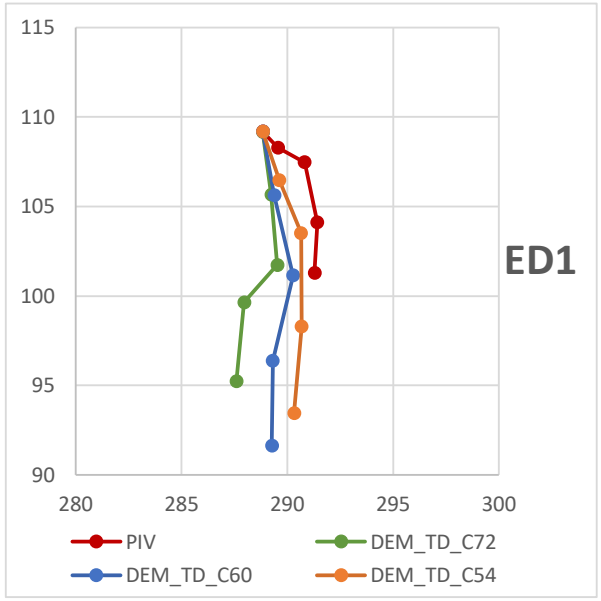

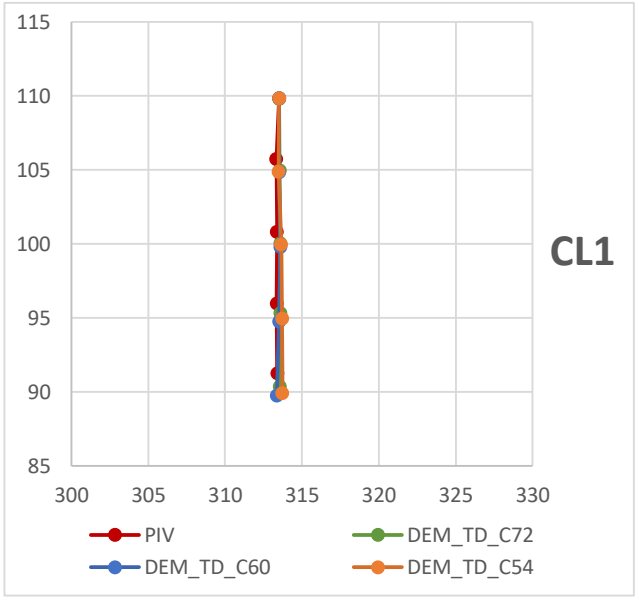

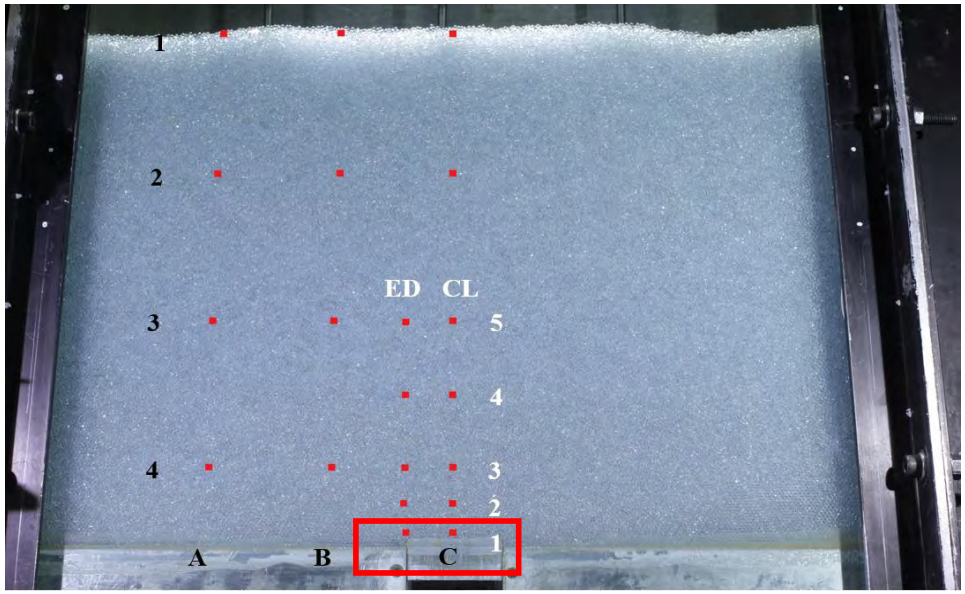

Appendix D: Page 6

All subset/particle displacements measured in millimetres (mm)